BIOLOGICAL STUDIES OF DIRHODIUM(II,II) COMPOUNDS AND THEIR APPLICATIONS AS PHOTOCHEMOTHERAPEUTIC AGENTS

A Dissertation

by

AMANDA DAVID LÓPEZ

Submitted to the Office of Graduate and Professional Studies of
Texas A&M University
in partial fulfillment of the requirements for the degree of

DOCTOR OF PHILOSOPHY

Chair of Committee,	Kim R. Dunbar
Committee Members,	Marcetta Y. Darensbourg
	James D. Batteas
	Jean-Philippe Pellois
Head of Department,	François Gabbaï

December 2015

Major Subject: Chemistry

ABSTRACT

The work contained in this dissertation focuses on the synthesis and characterization of dirhodium (II,II) compounds and studies of their anticancer activities against cervical and ovarian cancer cell lines. It has been demonstrated that tailoring the coordination environment of the dirhodium core and irradiation using low energy light (λ > 400 nm) dramatically affects the anticancer properties of the compounds.

In order to improve the anticancer activity of dirhodium compounds, a series of compounds containing two different bridging ligands was prepared and characterized. A new precursor was prepared from the reactions of dirhodium tetraacetate with *N,N'*-2,6-*o*-difluoroformamidinate to afford, $[Rh_2(F_2form)(\mu\text{-}O_2CCH_3)_3]$ (**1**). Compound **1** was reacted with diimine ligands phen (**2**) (1,10-phenathroline), dpq (**3**) (dipyrido[3,2-f:2',3'-h]-quinoxaline), dppz (**4**) (dipyrido[3,2-a:2',3'-c]phenazine) and (**5**) dppn (benzo[i]dipyrido[3,2-a:2',3'-h]quinoxaline) to obtain compounds of general formula $[Rh_2(F_2form)(\mu\text{-}O_2CCH_3)(NN)_2]^{2+}$. Compounds **2-5** exhibit significant photocytotoxic activities against HeLa, COLO-316, OVCAR-8 and NCI-ADR/RES. This new family of compounds is capable of depleting mitochondrial potential and inducing cell death on a short time scale (~ 10 min) after irradiation with compounds **4** and **5** being the most active of the series.

The ease of tuning dirhodium compounds prompted the study of another series of the mixed-bridging ligand compounds $[Rh_2(F_2form)(\mu\text{-}O_2CCH_3)(CH3CN)_6]^{2+}$ (**6**) and $[Rh_2(Ph_2P(C_6H_4))(\mu\text{-}O_2CCH_3)(CH3CN)_6]^{2+}$ (**7**). The presence of strong σ-donating

ligands renders the *trans* CH_3CN ligands labile in the dark, whereas the ones *trans* to the acetate are stable. These compounds were found not to exhibit significant anticancer activity against HeLa cells but they may be used as scaffolds for further functionalization with biologically or photocatalytically active ligands.

The antioxidant, antineoplastic molecule 2-pyrrolidinone was used as a bridging ligand in the partially solvated dirhodium complexes $[Rh_2(\mu\text{-}NOC_4H_6)_2(NOC_4H_7)_{ax}(CH_3CN)_5]^{2+}$ (**8**) and $[Rh_2(\mu\text{-}NOC_4H_6)_2(NOHC_4H_6)_{eq}(CH_3CN)_5]^{2+}$ (**9**). The aim of this chapter was to design a multifunctional drug that, upon irradiation, releases the anticancer drug 2-pyrrolidione and has open coordination sites that are available to bind to other biological molecules. Compound **8** does not exhibit anticancer properties upon irradiation, but **9** induces a 22-fold increase in cytotoxicity as compared to the dark control. These results are highly promising indicators that designer heteroleptic dirhodium compounds hold considerable potential as prodrugs for photochemotherapy.

DEDICATION

A mi querida madre, porque te sacrificaste para proveerme todo lo mejor e inculcarme los valores que formaron como persona. Porque me criaste para que fuera la mejor versión de mí, a ti te dedico cada uno de mis triunfos.

"*Haz de todos los obstáculos escalones para aquello que quieras alcanzar. Haz aquello que te gusta, siente lo que hay dentro de ti. Procura por encima de todo ser gente. Descubre aquello que es bueno dentro de ti. Busca lo bueno en todo y en todos a tu alrededor. Vive intensamente cada momento"*

M. Lo

ACKNOWLEDGEMENTS

The completion of this work could not have been accomplished without the help and support of many people in my life. I would like to express my deepest appreciation and gratitude to Dr. Dunbar, who was instrumental in the development of my scientific career. Her passion for science, motivation, support and guidance molded me into the independent researcher that I am today. Thank you for your friendship and being there when I needed guidance. Words cannot describe how thankful I am.

I would also like to thank Dr. Claudia Turro and her research group for the opportunity to collaborate and further the knowledge of dirhodium chemistry. I am also thankful to Dr. Pellois for the valuable research discussions and the opportunity to collaborate and work in his laboratories.

Thanks also to my coworkers and friends from the Dunbar and Pellois Groups, Andrew Brown, Codi Sanders, Zhanyong Li, Mohamed Saber, Jill Frank, Toby Woods and Co., Xuan Zhang, David Kempe, Francisco Birk, Sayan Saha, Ryan Coll, Briana Zamora, Stacy Lopez, James Hollas, Haomiao Xie, Dr. Hanhua Zhao, Dr. Sara Goberna-Ferrón, Dr. Ian Giles, Dr. Helen Chifotides, Sarah Lane, Dr. Heather Southerland, Dr. Maryfer Ballesteros, Dr. Silvia Gomez, Dr. Dawid Pinkowicz, Kelsey Schulte, Carolyn Gunthardt, Dr. Yuanzhu Zhang, Mayela Canales, Angie Wilson, Alfredo Erazo, Kristina Najjar, Ting-Yi Wang, Nandhini Muthukrishnan, Dakota Brock, Helena Kondow, Laila Dayani who made my time in TAMU a special journey.

My time in TAMU was full of great memories and valuable experiences. I would like to thank the many friends that I made in the Department of Chemistry. In addition, I want to give a shout out to the Brazos Runners Club-Boat of Fools for keeping me sane during the writing process by stimulating endorphin release through exercise and laughter.

Finally I want to thank my Puertorrican and Colombian family and close friends who believed in me and provided me with unconditional love and support. Thank you Mami, tití Minín, Wela, Gianfranco, Giancarlo, Catalina Mira, Clara González, Clara Mira, Marta Tamayo and my dearest friends Angel Martí, Meredith Vélez, Joel Rojas, Morgan Shirley, Michelle Lebo, Masato Hirai and Haifeng Yang.

TABLE OF CONTENTS

Page

LIST OF FIGURES

Page

LIST OF TABLES

Page

CHAPTER I

INTRODUCTION

Cancer

Cancer is characterized by the uncontrolled cell growth and impaired balance between new cell growth and old cell death and the ability of these cells to migrate to other areas in the body.[1] The disease is caused by inherent factors (mutations, hormones and immune conditions) as well as environmental factors (tobacco, diet, radiation, and infections organisms).[2] Cancer has become one of the leading causes of death worldwide and in the US it is second only to heart disease, accounting for 1 of every 8 deaths.[3-5] One of oldest reports of cancer dates back to the 1600 BC in ancient Egypt, but it has also been observed in animal and non-human primate fossils.[4-5]

The world's population in 2020 is expected to increase to ~7.5 billion and with it there will be more cancer diagnoses, an estimated ~15 million new cases.[6] In 2015 alone it is estimated that more than 1.67 million cases of cancer will be reported.[3] The increase in cancer incidence since the 19th century is mostly attributed to the change in diet and sedentary lifestyle which accounts to almost 90-95 % of all cases, the remaining 5-10 % is attributed to genetic factors (**Figure 1.1**).[5,7] Among all cancers, lung cancer is the leading cause of cancer mortality in both men and women, followed by prostate cancer in men and breast cancer in women (**Table 1.1**).[3] There has been an increase in survival rates since the 1970's mostly due to preventive care and early diagnosis, but there is a pressing need for new targeted therapies that improve the patient's quality of life during

treatment. Inorganic medicinal chemistry provides an excellent platform for new treatments against cancer.

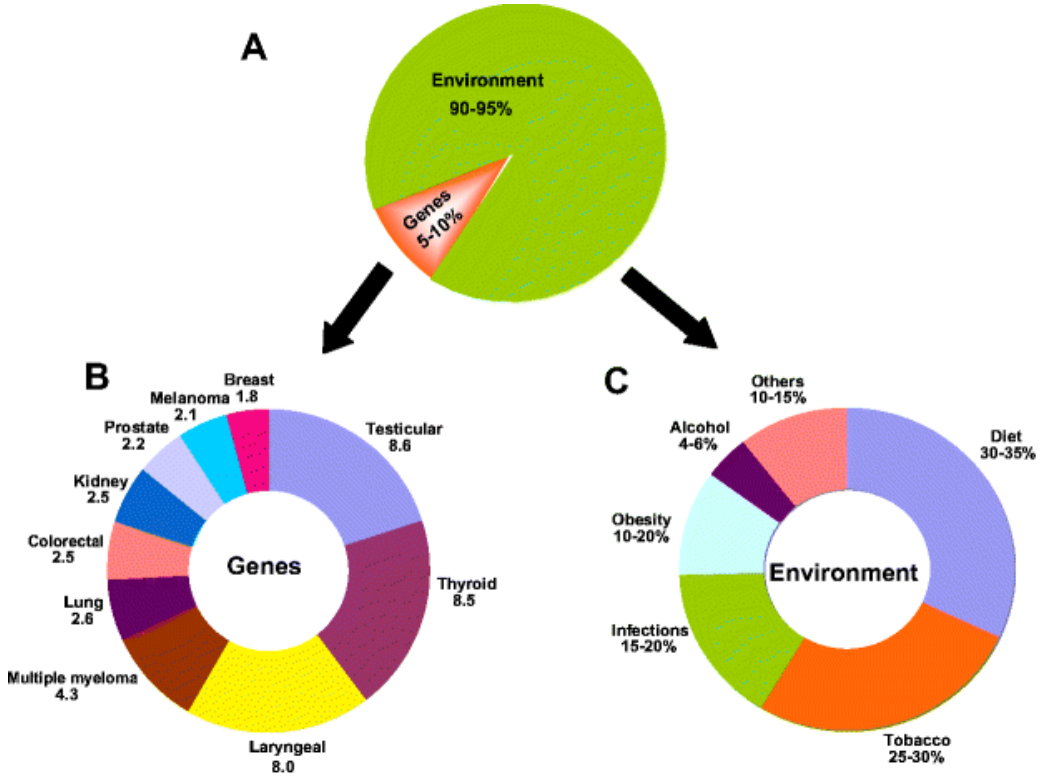

Figure 1.1 The role of genes and the environment in cancer development. **A)** Contribution of genetic and environmental factors to cancer. **B)** Family risk ratio for selected cancers. **C)** Contribution of environmental factors to cancer deaths due to a specified environmental risk factor. Adapted with permission from ref. 2. Copyright 2008 © Springer Science.

Table 1.1 Estimated Cancer Deaths in the US in 2015. Data obtained from ref. 3.

Men 312,150		Women 277, 280	
Lung & bronchus	28%	26%	Lung & bronchus
prostate	9%	15%	breast
Colon & rectum	8%	9%	Colon & rectum
Pancreas	7%	7%	Pancreas
Liver & intrahepatic bile duct	5%	5%	ovary
Leukemia	5%	4%	Liver & intrahepatic bile duct
Esophagus	4%	4%	Leukemia
Urinary Bladder	4%	3%	Esophagus
Non-Hodgkin lymphoma	3%	35	Urinary Bladder
All other sites	24%	2%	Non-Hodgkin lymphoma
		23%	All other sites

Cisplatin

It is well stablished that metal-based antitumor agents can target DNA by forming covalent interactions or by intercalating into the double helix of DNA.[8-9] The formation of DNA adducts is known to be an important aspect of the mechanism of activity of cisplatin [*cis*-diamine dichloroplatinum(II)] (*cis*-$Pt(NH_3)_2Cl_2$) which is one of the most potent anticancer agents that was approved for clinical use in the late 1970's. Cisplatin is routinely used in the treatment of testicular cancer, Hodgkin's lymphoma, ovarian, bladder, head/neck tumors and other malignancies.[10] Once inside the cell the original prodrug undergoes hydrolysis producing the positively charged complex *cis*-$[PtCl(NH_3)_2(H_2O)_1]^{2+}$ which first forms mono-adducts and then bis-adducts with DNA. This complex can also covalently bind to the DNA duplex forming 1,2-*cis*-$[Pt(NH_3)_2^{2+}$-d(GpG)] crosslinks which induce bending and unwinding of the DNA duplex.[11-12]

Cisplatin can also bind to cytoplasmic substrates that contains thiols like glutathione, methionine, metallothioneins and proteins.[13] The interaction of the drug with these molecules shifts the redox balance toward oxidative stress facilitating DNA damage, however it can also be deactivated in the same way due to decreased drug concentration in the cell.[14] Due to its ability to covalently bind the DNA duplex, cisplatin triggers the inhibition of replication and transcription, cell cycle arrest and attempted repair of damaged nucleotides which in turn cause programmed cell death.[11]

Drug Resistance

Despite the huge success of cisplatin in battling various forms of cancer, its use has many drawbacks including significant toxic side-effects and acquired drug resistance mostly.[15] The side-effects are result of the widespread systemic distribution of the drug in the body after administration; after 24 h 95% of the complex binds to plasma proteins and then localizes in the kidneys (0.4-2.9 μg/g), liver (0.5-3.7 μg/g) and prostate (1.6-3.6 μg/g).[16] It is believed that cisplatin enters the cells through passive diffusion or by active protein mediated transport systems such as the human organic cation transporter (hOCT2) (mostly for oxaliplatin) or the copper transport protein (Ctr1).[17] The mechanism by which the cell repairs the platinum lesions is unknown; it is believed, however that reduced drug uptake, increased drug efflux, increased intracellular detoxification, and increased DNA mismatch repair capacity and base excision are a few of the mechanisms that cause drug resistance.[18-21]

Cisplatin drug resistance is a result of many factors that are dependent on the type of tumor being treated. Several factors contributing to drug resistance are (1) reduced cisplatin accumulation in the cell due to changes in drug transport, (2) improved detoxification mechanism in the cell thought the upregulation of intracellular scavengers, (3) improved DNA repair mechanisms, (4) increased tolerance of DNA lesions and (5) changes in the signaling pathways that triggers programmed cell death or apoptosis.[14,16]

The decrease in drug accumulation in tumors has been attributed to the down regulation of the CTR-1 (plasma membrane copper transporter), which controls copper homeostasis and evidence suggest it is also involved in cisplatin uptake.[22-23] Copper export pump proteins ATP7A/ATP7B and MRP2 (plasma membrane transporter) have been found to be upregulated in cisplatin resistant cell lines, mostly in ovarian cancer.[24-25] The upregulation of these group of proteins increases drug efflux. Increased levels of intracellular scavengers like glutathione (GSH) and metallothioneins are responsible for deactivation of the drug inside the cell by decreasing the concentration of drug available in the cell milieu.[26-27]

Cisplatin resistant cells have the ability to remove DNA lesions by the nucleotide excision repair (NER) mechanism. The overexpression of ERCC1 (excision repair protein) increases the efficiency of the NER repair mechanism.[28] Another key mechanism into drug resistance is the deficiency in the mismatch repair (MMR) mechanism.[29] Defective MMR pathways prevent MMR proteins from repairing platinated DNA.[29-30] On target resistance is characterized by an increase in translesion synthesis in drug resistant tumors by the upregulation of DNA polymerases that bypasses DNA lesions caused by

cisplatin and increased proficiency of BRCA1/BRCA2 proteins (involved in regulation of transcription and cell cycle).[31-32] Deficiencies in the transduction signaling pathways interferes with the apoptotic response in the cell. The deficiency of proapoptogenic factors (BAX/BAK)[33], overexpression of antiapoptotic factors (BCL-2 proteins)[34], changes in activation of caspases (Caspases 3, 6, 7, 8 and 9)[35] and mutations to the tumor suppression protein p53[36] amongst others has been linked to carboplatin and cisplatin resistance as well.[28]

Non-Platinum Metal Based Anticancer Drugs

The structural and chemical modifications of cisplatin analogs have improved their cytotoxicity towards some resistant tumors but their mechanisms of action are fairly similar. Clearly there is a need for alternative chemotherapy agents that have different binding properties or mechanisms of actions from that of cisplatin. Therefore it is important to seek different types of antitumor agents that will not exhibit the same limitations as cisplatin and its derivatives.[37] Metal complexes have the ability to bind to different cell targets, including but not limited to DNA, disrupt enzymatic pathways or affect mitochondrial function.[16]

Ruthenium

Several examples of metal based anticancer compounds have been reported in the literature. Ruthenium based compounds have shown low systemic toxicity when compared to cisplatin.[38] Another key feature is that Ru based compounds show greater

accumulation through highly selective iron transport mechanisms (transferrin).[39] Two Ru(III) compounds have reached clinical trials, one of them is [H_2im][*trans*-Ru(Him) (S-DMSO)Cl_4] were Him = imidazole and DMSO = dimethyl sulfoxide (NAMI-A, phase II clinical trials) (**Figure 1.2a**). NAMI-A has shown to have selective activity against tumor metastases and it has the ability to bind DNA, induce cell cycle arrest (S phase), and it inhibits angiogenesis.[40] The second candidate in clinical trials is [H_2ind][*trans*-Ru(Hind)Cl_4] were Hind = indazole (KP1019, phase II clinical trials, **Figure 1.2b**). Even though KP1019 is structurally similar to NAMI-A, but its anticancer activity is significantly different. KP1019 binds to DNA and accumulates in the nucleus, thus inducing an intrinsic apoptotic response, characterized by the permeabilization of the mitochondria, triggering a release of cytochrome c which initiates the apoptotic cascade of events (activation of caspase-9).[41-42] The cytotoxic effects of KP1019 have been limited to solid tumors and no dose-limiting toxicity has been observed during phase I clinical trials.[43]

Gold

Gold compounds are of significant importance, Au(III) is isoelectronic with Pt(II) and it have similar chemistry.[16] Chelating nitrogen ligands (such as phen, bpy, terpyridine (tpy) and ethylenediamine) are needed to stabilize the Au(III).[44] Studies have shown that Au(III) diimine complexes (like $[AuCl(tpy)]^{2+}$) are stable in the presence of GSH and interact with DNA, they also exhibit good anticancer activity.[44-45] Of particular interest are Au(I) compounds, auranofin (Ridaura®, **Figure 1.2c**) has been used as medication for

rheumatoid arthritis, but it also exhibits antitumor activity in patients with bladder cancer.[46] The efficacy of auranofin as anticancer agents is related to its activity as inhibitor of thioredoxin reductase (TR, involved in ROS reduction).[47-48] Auranofin is currently in clinical trials (Phase II) for the treatment of lymphocytic leukemia and several solid cancers and it is also been investigated for its activity against skin melanoma.[48-49]

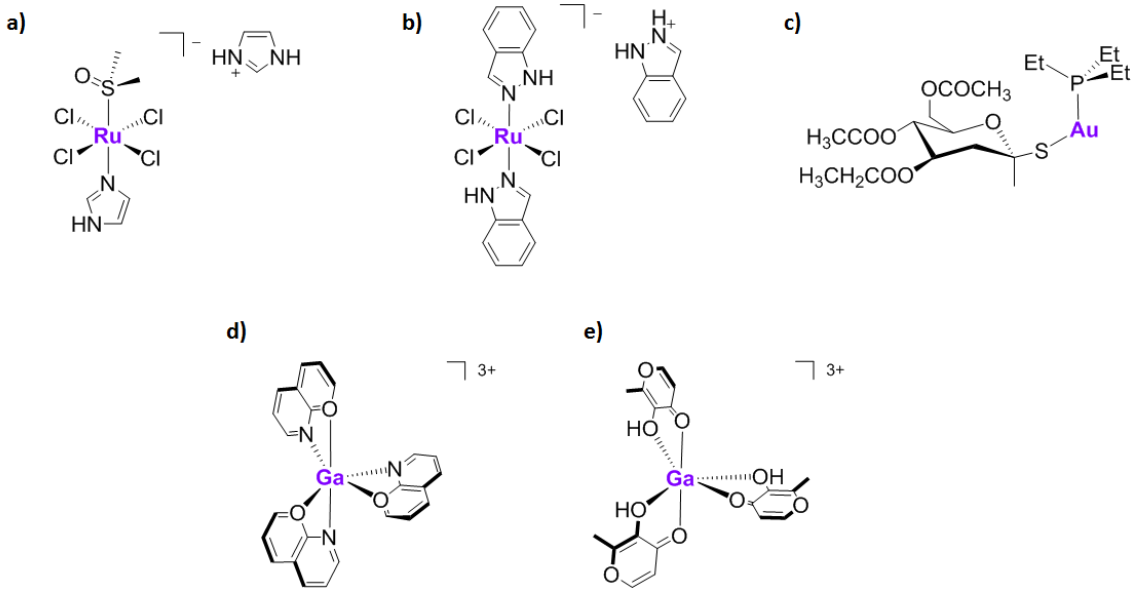

Figure 1.2 Schematic representation of the chemical structures of a) NAMI-A, b) KP1019, c) Auranofin, d) KP46 and d) tris(3-hydroxy-2-methyl-4H-pyran-4-onato)gallium(III).

Gallium

Main group element gallium as in the case of gold compounds, has been widely used in other applications (*e. g.* treatment of accelerated bone resorption, autoimmune and

infectious diseases and imaging) including cancer therapy.[16] The compound $Ga(NO_3)_3$ has been studied in clinical trials (Phase I and II) for the treatment of bladder cancer and non-Hodgkin's lymphoma with good outcomes.[50] Coordination of Ga^{3+} to organic ligands has proven an effective strategy to improve intestinal absorption when compared to $Ga(NO_3)_3$. Two oral Ga(III) treatments have been selected for preclinical trial namely *tris*(8-quinolinolato)-gallium(III) (KP46) and *tris*(3-hydroxy-2-methyl-4H-pyran-4-onato)gallium(III) (**Figure 1.2d-e**).[51] The higher activity of Ga(III) coordination compounds is mostly due to p53 activation facilitated by Ca^{2+}-signaling and generation of ROS.[52-53]

The examples provided here are just a small fraction of metal based compounds that exhibit anticancer properties and different mechanisms of action than cisplatin. It is evident that medicinal inorganic chemistry is an attractive field for the development of anticancer drugs that can circumvent drug resistance through different mechanisms and activation pathways that of cisplatin.

Dinuclear Metal-Metal Bonded Anticancer Compounds

Dinuclear metal-metal bonded compounds of rhodium are very promising non-platinum anticancer compounds for anticancer applications. The $Rh_2(\mu\text{-}O_2CCH_3)_4$ compound exhibits excellent anticancer activity against several cell lines including Ehrlich ascites tumor, sarcoma 180 and P388 lymphocytic leukemia.[54-55] It has been shown that dirhodium complexes have the ability to inhibit DNA replication, transcription and protein synthesis.[56-57] In addition, NMR studies have demonstrated the ability of the dirhodium

core to interact with DNA.[9,58-60] For example multinuclear NMR data have revealed that dirhodium compounds can bind to guanine, adenine and cytosine in a chelating fashion through *ax-eq*, *eq-eq* and *ax* positions thereby inducing changes in the base pair stacking and disrupting hydrogen bonding interactions of the DNA double helix.[58,61] Similarly to cisplatin, $Rh_2(\mu\text{-}O_2CCH_3)_4$ forms 1,2-d(pGpG) intrastrand crosslinks with DNA, but its efficacy as an anticancer agent is not limited to this binding mode.[60] Modifying the ligands around the rhodium centers at axial and equatorial positions offers a variety of possible binding sites for reactions with biomolecules. For example dirhodium compounds can be equipped with intercalative binding units, resulting in simultaneous covalent binding to the DNA and intercalation between the DNA base pairs (**Figure 1.3**).[62]

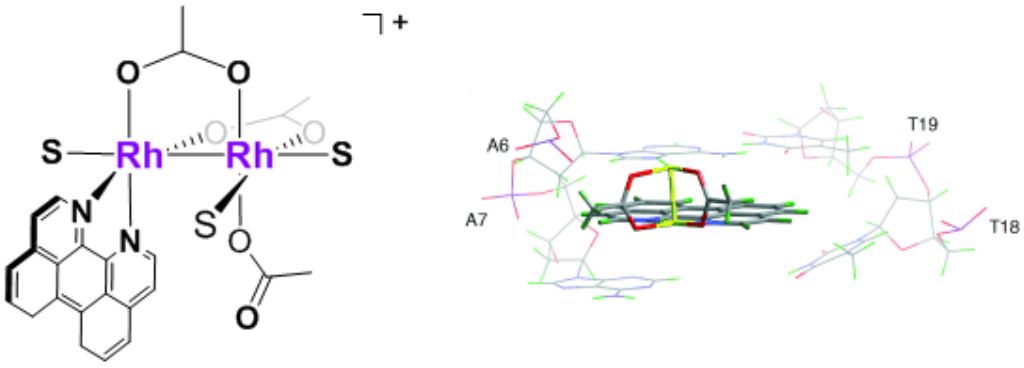

Figure 1.3 Example of combination binding, intercalative and coordinative, by *cis*-$[Rh_2(dap)(\mu\text{-}O_2CCH_3)_2(\eta^1\text{-}O_2CCH_3)(CH_3OH)](O_2CCH_3)]^+$ to adenine on a DNA AA12mer fragment, d(CTCTCAACTTCC). Adapted with permission from ref. 16. Copyright 2006 © Wiley Science.

Photodynamic Therapy

Photodynamic therapy (PDT) is a non-invasive treatment for endoscopically accessible tumors.[63-64] The localized action of PDT allows for the successful treatment of lung, bladder, gastrointestinal, esophageal, prostate and gynecological tumors.[63-65] This therapy uses photosensitizers and visible light (600-850 nm) in combination with molecular oxygen to cause damage to tumor cell membranes or tumor vasculature by the formation of $^1O_2$ and other reactive oxygen species, which in turn causes cell death by apoptosis or necrosis (**Figure 1.4**).[66-68]

One of the disadvantages of PDT is that it is dependent on the amount of oxygen present and the singlet oxygen generated can only diffuse by 0.02 μm therefore effectiveness of the treatment is restricted by $^1O_2$ formation (concentration of O_2 in the tumors) and its diffusion.[63] To date the PDT market is dominated by organic molecules, but the population of the triplet excited states upon irradiation (^{3}ES) is not efficient, thus limiting the generation of $^1O_2$.[69]

Metal based photosensitizes exhibit long lived ^{3}ES states that can generate $^1O_2$ in high yields. The literature is replete with examples of metal based photosensitizers that generate $^1O_2$ in good yields: Ru(II)[70-71], Os(II)[72], Ir(III)[73-74], Re(I)[75] are some of them. Our group has synthesized many dirhodium derivatives with the ability to act as PDT agents in both aerobic and anaerobic conditions with ^{3}IL life times in the range of 2.40-4.10 μs which makes these types of compounds suitable for PDT applications.[76]

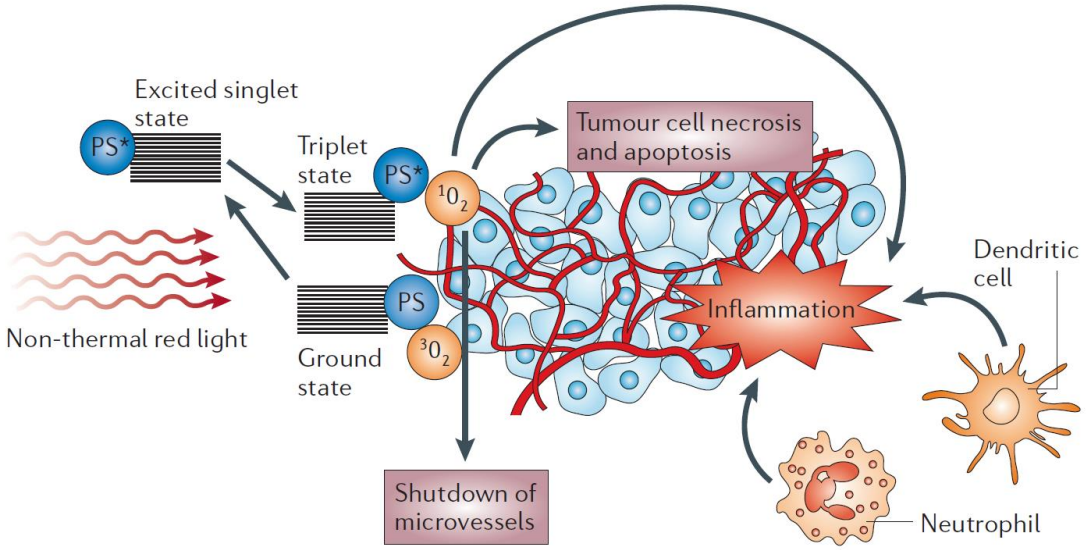

Figure 1.4 PDT mechanism of action in the cell. Adapted with permission from ref. 45. Copyright 2006 © Nature Publishing Group.

Oxygen Independent DNA Photocleavage of Dirhodium (II,II) Complexes

Tailoring the coordination environment around the dirhodium core provides means for the exploration of their reactivity and cytotoxic properties in cancer cells. One example of this is the photo-cisplatin analog $[Rh_2(O_2CCH_3)_2(CH_3CN)_6][BF_4]_2$ first synthesized by Garner and coworkers in 1986, it was found to be capable of binding to ds-DNA under visible light irradiation 20 years later by Turro and coworkers.[77] This new cisplatin analog was studied for its anticancer activity against Hs-27 human skin cells and it exhibits very promising anticancer properties with a 34-fold increase in toxicity upon irradiation. The activity of $[Rh_2(O_2CCH_3)_2(CH_3CN)_6][BF_4]_2$ is a result of the exchange of two of the equatorial CH_3CN ligands upon irradiation (λ = 355 nm and 509 nm), forming the active species $[Rh_2(O_2CCH_3)_2(CH_3CN)_2(H_2O)_4]^{2+}$ which upon irradiation can bind to 9-

ethylguanine, and linearized PUC18 plasmid and also inhibits transcription by the T7-RNA polymerazse.[57,77] This is the first dirhodium partial paddlewheel compound that can act as a photochemotherapeutic (PCT) agent in an oxygen independent fashion.[78] Ever since the discovery of the anticancer properties of $[Rh_2(O_2CCH_3)_2(CH_3CN)_6][BF_4]_2$ other derivatives have been pursued, such as: $[Rh_2(HNOCCH_3)_2(CH_3CN)_6]^{2+}$, $[Rh_2(DTolF)_2(CH_3CN)_6]^{2+}$, $[Rh_2(DTolF)_2(CH_3CN)_6]^{2+}$, $[Rh_2(DTolF)_2(CH_3CN)_6]^{2+}$ and $[Rh_2(Ph_2P(C_6H_4)](CH_3CN)_6]^{2+}$ ([F-form]$^-$: p-difluorophenylformamidinate, [NNN]$^-$: p-ditolyltriazenide, [DTolF]$^-$: p-ditolylformamidinate).[79-81]

Oxygen Dependent DNA Photocleavage of Dirhodium (II,II) Complexes

Another strategy being sought is the binding of electron acceptors to the dirhodium core. In the early 2000's Turro and coworkers studied the photophysical and photochemical properties of $Rh_2(\mu\text{-}O_2CCH_3)_4$ and observed that upon irradiation with light in the 395-600 nm region in the presence of an electron acceptor, the $Rh_2(\mu\text{-}O_2CCH_3)_4$ molecule is able to photocleave DNA by the formation of the mixed valence cation $[Rh_2(\mu\text{-}O_2CCH_3)_4{\cdot}2H_2O)]^+$.[82] This finding prompted the development of a new series of anticancer agents containing electron acceptors directly attached to the dirhodium core in order to study them for anticancer activity upon light activation.[8,76]

In this vein the monocationic series of compounds with formula $[Rh_2(O_2CCH_3)_2(\eta^1\text{-}O_2CCH_3)(N\text{-}N)_1(CH_3OH)]^+$ were N-N = bpy, phen, dpq, dppz and dppn, was investigated in the Dunbar and Turro labs.[83-84] This family of compounds showed anticancer activity against HeLa cells, but COLO-316 cells are more susceptible

to the effects of these compounds. The compounds that exhibited the most activity are $[Rh_2(O_2CCH_3)_2(\eta^1\text{-}O_2CCH_3)(dppz)_1(CH_3OH)]^+$ and $[Rh_2(O_2CCH_3)_2(\eta^1\text{-}O_2CCH_3)(dppn)_1(CH_3OH)]^+$ which are able to intercalate into DNA *in vitro* and cleave nuclear DNA as confirmed by the comet assay (a gel-electrophoresis method that measures DNA damage in individual cells).[85-86] Glutathione (GSH) which protects cells from oxidative damage generated by reactive oxygen species (ROS)[87] was modulated in the COLO-316 cells in order asses the effects of this tripeptide on the activity of the compounds. COLO-316 cells were incubated with the compounds in the presence of NAC (N-acetyl cysteine, increases cellular levels of GSH) and BSO (buthionine sulphoximine, depletes GSH levels in the cell) and their toxicity measured.[85] The results indicate that increased levels of glutathione in the cells do not inhibit the anti-proliferative activity of the compounds. This result is very important for the development of dirhodium based anticancer drugs, since the activity of these type of compounds is not hindered by the presence ROS scavengers in the cells.

Another series of compounds that was developed in our laboratories is the heteroleptic series of compounds of general formula $[Rh_2(O_2CCH_3)_2(dppn)(N\text{-}N)]^{2+}$. The most active of the series are $[Rh_2(O_2CCH_3)_2(dppn)(dppz)]^{2+}$ and $[Rh_2(O_2CCH_3)_2(dppn)_2]^{2+}$ which can generate $^1O_2$ upon irradiation with good yields (Φ = 0.4).[88] The addition of extended π structures to the dirhodium compounds confers greater anticancer activity when the compounds are irradiated, mostly due to the long lived $^3\pi\pi$ states due to the formation of ROS through O_2-dependent pathways.[88] It is worth noting that compounds $[Rh_2(O_2CCH_3)_2(dppn)(dppz)]^{2+}$ and $[Rh_2(O_2CCH_3)_2(dppn)_2]^{2+}$ still elicits

DNA photo-cleavage in the absence of oxygen.[78,88] These compounds exhibit toxicities in the lower micromolar range (Hs-27 cell line) upon irradiation, with phototoxicity indices (PI) of 21 and 24-fold respectively which is an improvement to current photodynamic therapy treatments (PDT) (**Figure 1.5**).[88]

A more systematic study of the anticancer activities of these compounds against HeLa and COLO-316 cells was performed and in the new study it was found that the complexes do not reach the nucleus although they exhibit good anticancer activities. It was also noted that changing the coordination environment around the dirhodium core triggers different responses in the cells; for example $[Rh_2(O_2CCH_3)_2(dppn)(dppz)]^{2+}$ induces programmed cell death whereas $[Rh_2(O_2CCH_3)_2(dppn)_2]^{2+}$ causes necrotic death.[37] By tuning the ligand environment, DNA photocleavage, $^1O_2$ or ROS generation can be enhanced, making these compounds attractive candidates for photodynamic therapy applications.

Photoactivated Chemotherapy

Photoactivated chemotherapy or photochemothreapy (PCT) consists on the release of a biologically active drug upon light irradiation to induce cell death.[78,89] The advantage of this type of therapy is that it is independent of the concentration of O_2 present in the cell and light is used as a trigger for drug release to elicit a toxic response. Ruthenium(II) compounds have been used for this application, *e. g.* $[Ru(tpy)(5\text{-cyanouracyl})_3]^{2+}$ reported by Turro and coworkers.[90] The prodrug upon irradiation with low energy light releases

a)

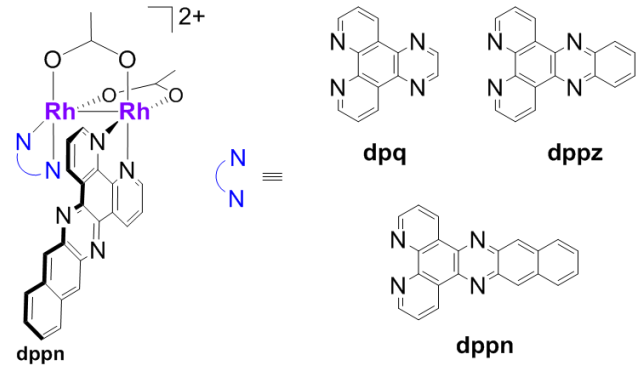

b)

Complex	f^1O_2	$LC_{50}/\mu M$ dark	irradiated	ratio
dpq	0.8	51 ± 5	9 ± 3	5.7
dppz	0.4	355 ± 18	17 ± 3	21
dppn	0.4	384 ± 24	16 ± 4	24
hematoporphyrin	0.2	22 ± 1	3.8 ± .2	5.7

Figure 1.5 Dirhodium compounds containing two different diimine ligands with sensitized $^1O_2$ quantum yields, cytotoxicity LC^{50} concentrations in the dark and upon irradiation against Hs-27 cells, and the phototoxicity index (ratio) obtained from ref. 88.

the bioactive 5-cyanouracil molecule which has been known to inhibit pyrimidine catabolism *in vivo*.[78,91] Studies *in cellulo* demonstrated that the toxicity of $[Ru(tpy)(5\text{-cyanouracyl})_3]^{2+}$ is attributed by the release of the 5-cyanouracil molecules and not the formation of Ru-aquo adducts.[78,90] A more recent report of two Ru(II) polypyridyl compounds (RuL_2(dppz-R) where R = CH_2NH_2 and L=bpy, phen or dipyridylamine) were conjugated to a photolabile linker (PLPG = N-OH-succinimidylester) which is covalently bound to a targeting peptide (BBN, L-Gln-L-Trp-L-Ala-L-Lys-$CONH_2$) or a nuclear localizing sequence (NLS, L-Arg-D-Arg-L-Arg-L-Lys-$CONH_2$) for PCT applications (**Figure 1.6**).[92] The Ru(II) prodrug bound to the targeting peptide showed increased drug

uptake and the conjugate bound to the nuclear targeting sequence showed preferential nuclear accumulation.[92] In addition light mediated release of the complexes induced a cytotoxic response against HeLa and MRC-5 cells.[92]

Partially solvated dirhodium compounds of the form $[Rh_2(O_2CCH_3)_2(CH_3CN)_6][BF_4]_2$ are good candidates for PCT. The substitution of the equatorial acetonitrile ligands for biologically active molecules poises $[Rh_2(O_2CCH_3)_2(CH_3CN)_6][BF_4]_2$ as a frontrunner in the PCT field. Dirhodium (II,II) acetamide compounds of the form $Rh_2(NHOCCH_3)_2(dppz)(CH_3CN)_4][BF_4]_2$ have been synthesized for this application.[93] The compound shows dual DNA binding upon irradiation namely, intercalation and covalent binding which is the first example of Dual DNA binding.[93] These are promising results that help further the understanding of dirhodium compounds and their interactions with DNA for better design of future drugs.

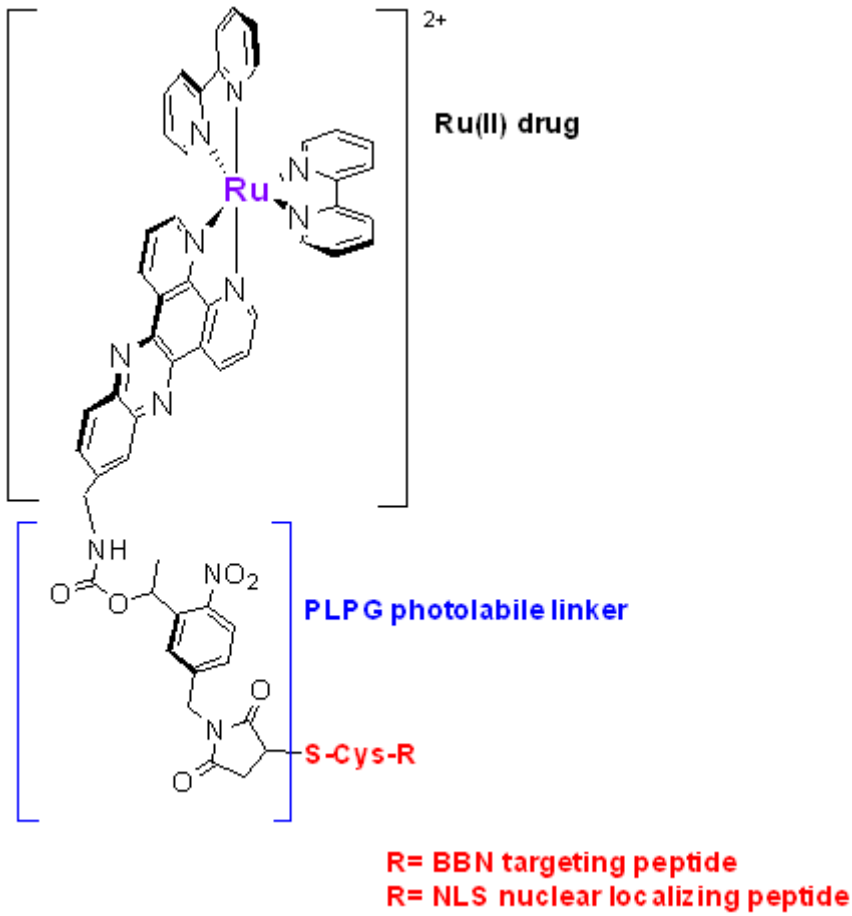

Figure 1.6 Schematic representation of Ru(II) prodrug for PCT applications, $[Ru(bpy)_2(dppz\text{-}PLGP\text{-}R)]^{2+}$.

Dissertation Objectives and Outline

Dirhodium compounds have shown interesting properties ranging from covalent binding to ss-DNA and ds-DNA, transcription inhibition and interactions with biologically relevant structure amongst others and activation by light. These metal-metal bonded compounds can be easily tailored to improve their photochemical properties and their anticancer activity, which makes them excellent candidates for future anticancer therapy.

In Chapter II the synthesis and characterization of a new class of dirhodium diimine compounds containing two bridging ligands will be discussed. The effects of the bridging ligands on cytotoxicity were evaluated against drug resistant cell lines and fluorescent probes were used to elucidate mechanisms of action.

Chapter III focuses on mixed-bridging ligand partially solvated dirhodium compounds and the rate of exchange of the equatorial CH_3CN molecules and how it affects the cytotoxicity of these molecules against HeLa cells.

Chapter IV describes the synthesis of a dirhodium partially solvated compounds with 2-pyrrolidinone as bridging ligands and their activity against HeLa cells for PCT applications.

Conclusions and future directions in dirhodium anticancer therapy will be discussed in Chapter V.

CHAPTER II

DIRHODIUM (II,II) MIXED-BRIDGED LIGAND COMPOUNDS CONTAINING ELECTRON ACCEPTING DIIMINE LIGANDS AND THEIR ACTIVITY AGAINST OVARIAN CANCER CELLS

Introduction

The discovery of the anticancer properties of cisplatin shepherded in the current modern era of medicinal inorganic chemistry.[94] Currently, many metal based compounds are being used as therapeutic and diagnostic agents.[16,94-95] Despite the considerable efficacy that the platinum based drugs cisplatin, carboplatin and oxaliplatin exhibit against various tumor, it is imperative to explore new metal based drugs in order to circumvent drug resistance and severe side effects.[96] Metal-metal bonded compounds constitute an excellent platform for new anticancer drugs due to their ease of tunability and functionalization. One example is dirhodium tetraacetate [$Rh_2(O_2CCH_3)_4$], which was shown by Bear and coworkers to exhibit anti-tumor activity against Ehrlich ascites L1210, sarcoma 180 and P388 with increased survival rates in mice.[55,97] Structure activity relationships have been established in order to understand mechanisms of action and possible targets.[54,98] In the early 2000's, NMR studies of $Rh_2(O_2CCH_3)_4$ reactions with DNA reported by Kang, Chifotides and Dunbar revealed that [$Rh_2(O_2CCH_3)_4$] can bind to double stranded DNA by generating DNA crosslinks at cytosine and adenine sites.[99] The Turro group demonstrated that reactions of dirhodium tetraacetate with electron acceptors in the presence of light induce DNA photocleavage.[82,100] Inspired by these results the

Dunbar and Turro groups initiated a collaboration to design dirhodium compounds with electron accepting ligands such as phen, dpq and dppz for therapeutic purposes. One example is the family of compounds of general formula $[Rh_2(O_2CCH_3)_2(\eta^1\text{-}O_2CCH_3)_1(CH_3OH)(L)]^+$ (L = phen, dpq, dppz or dppn) which were shown to intercalate to DNA *in vitro* and also bind to nuclear DNA *in cellulo* [85] Another series of compounds showing significant increase in toxicity against skin cancer cells is the heteroleptic series of compounds $[Rh_2(O_2CCH_3)_2(dppn)(L)]^{2+}$ with the dppz and dppn compounds exhibiting 21-fold and 24-fold increases in toxicity upon irradiation[88]

The ability of dirhodium compounds to induce a cytotoxic response upon irradiation poises them as good candidates for photodynamic therapy (PDT). PDT is a non-invasive technique that relies on the use of light in the presence of a photosensitizer as treatment for superficial tumors.[66] One of the limitations of current PDT agents is their dependence on oxygen concentration to be active which is a serious drawback for dense hypoxic tumors.[101] Once the oxygen in the tumor cell has been depleted the PDT agent loses its activity.[64] An important discovery for us is that the aforementioned dirhodium compounds do not require O_2 to exert a toxic response against cancer cells.[88]

Another aspect of the compounds that needs to be considered is that many anticancer drugs induce an apoptotic response (programmed cell death) in the cells.[102] In order to survive, cancer cells develop defense mechanisms and mutations against drug-induced apoptosis.[102-103] One of the advantages of PDT is that it induces a different cell death mechanism, namely necrosis.[101] Necrosis can be identified by changes in morphology like swelling of organelles and loss of plasma membrane integrity.[104]

Inducing necrotic cell death can be a strategy to circumvent acquired drug resistance.[103] Tumor death by necrosis elicits a pro-inflammatory response that is beneficial to the organism.[104] Recent reports suggest that in certain tumors the inflammatory response induced by necrotic death caused by an anticancer agent facilitates the production of cytokines that stimulates adaptive anti-tumor immunity.[105-107] These findings suggest that therapies should not be limited to apoptotic inducers.

Mixed bridge dirhodium compounds of the type $[Rh_2(DTolF)_2(O_2CCF_3)_2(H_2O)_2]$ (DTolF = p-tolyl formamidinate) first studied by Piraino showed similar anticancer activity to that of cisplatin and $[Rh_2(O_2CCH_3)_4]$ and exhibit increased survival rates in mice bearing Yoshida ascites and T8 sarcoma.[97] In light of these results, a new series of mixed-bridging ligand dirhodium compounds with electron acceptors has been prepared. The combination of two different bridging ligands on the dirhodium core and the presence of the diimine ligands render these compounds very different than any others that have been studies. The antineoplastic effects of these new family of compounds was investigated against cervical cancer cells (HeLa) and the ovarian carcinomas COLO-316, OVCAR-8 and multidrug resistant NCI-ADR/RES upon irradiation with visible light. The synthesis, characterization and biological activities of these new compounds will be discussed herein.

Experimental Section

Starting Materials

The compound $Rh_2(\mu\text{-}O_2CCH_3)_4\bullet 2CH_3OH$ was purchased from Pressure Chemicals or synthesized from $RhCl_3\bullet xH_2O$ from reported procedures.[108] The compounds *N,N'*-bis(2,6-difluorophenyl)formamidine (o-HF_2form) and $Rh_2((C_6H_5)_2P(C_6H_4))(O_2CCH_3)_3\bullet 2O_2CCH_3$ were synthesized by slightly modified published procedures.[109-110] Commercially available reagents, potassium tertbutoxide (K^tBuO) (Sigma Aldrich), sodium tetrafluoroborate ($NaBF_4$) (Sigma Aldrich) and 1,10-phenanthroline (phen) (VWR) were used as purchased and used as received. The ligands dpq (dipyrido[3,2-f:2',3'-h]-quinoxaline, dppz (dipyrido[3,2-a:2',3'-c]phenazine) and dppn (benzo[i]dipyrido[3,2-a:2',3'-h]quinoxaline)[111] were prepared according to published procedures. Analytical thin layer chromatography was carried out on aluminum-backed sheets coated with silica gel (SiO_2) 60 F254 adsorbent (0.20 mm thickness, EMD Chemicals). Flash chromatography was performed with SiO_2 60 (40-63 µm, BDH Chemicals). The solvents acetic acid (HOAc), acetone, hexanes (hex), tetrahydrofuran (THF), dichloromethane (CH_2Cl_2), diethyl ether (Et_2O), were of ACS grade and used as received. Acetonitrile (CH_3CN) was of ACS grade and was dried with 3Å molecular sieves and distilled under an inert atmosphere. Standard Schlenk-line techniques under a N_2 atmosphere were used, but work-up and isolation of products was performed in air unless otherwise stated.

Cell culture reagents Dubelco's modified Eagle medium (DMEM) (Invitrogen), fetal bovine serum (FBS) (Atlanta Biologicals), Leibovitz's L-15 Medium (L-15) without

phenol red (Life Technologies), Phosphate-Buffered Saline solution (DPBS) (Life Technologies), Resazurin (Sigma), Sytox Green® and Blue® (Invitrogen), Hoechst 33342 (Invitrogen), mitoTracker green (Invitrogen), Annexin V-FITC and propidium iodide (PI) apoptosis assay (biotool.com) and MitoProbe® JC-1 assay (Life Technologies) were used as received. The HeLa cell line was obtained from the American Type Culture Collection, cell line CCL-2. The COLO-316 cell line was kindly provided by Prof. Robert Burghardt (Texas A&M, Department of Veterinary Anatomy and Public Health) and the OVCAR-8 and NCI/ADR-RES cell lines were provided by Prof. James Sacchettini (Texas A&M, Department of Chemistry).

Preparation of $Rh_2(\mu\text{-o-}F_2\text{form})(\mu\text{-}O_2CCH_3)_3\bullet 2O_2CCH_3$ (1). A Schlenk flask was charged with o-HF_2form (72 mg, .26 mmol), K^{t}BuO (28 mg, 0.25 mmol) and THF (100 mL) and the reaction mixture was allowed to stir at room temperature for 4h under inert atmosphere until the reaction changed to a tan color. A purple solution of $Rh_2(\mu\text{-}O_2CCH_3)_4\bullet 2CH_3OH$ (123 mg, 0.24 mmol) in 100 mL of CH_2Cl_2:CH_3CN (1:1 v/v) was treated with deprotonated o-HF_2form in a dropwise form. The reaction mixture was stirred for 24 h at room temperature. The resulting maroon solution was filtered and the solvent was removed under reduced pressure to give a maroon solid which was washed with water and filtered to obtain a grey solid. The grey solid was purified by flash chromatography (SiO_2, hex/Acetone/HOAc 50:49:1) to afford **1** as a black solid which was recrystallized by slow diffusion of diethyl ether into a solution of **1** in acetonitrile from which X-ray quality crystals were obtained. Yield: 67 mg (36%). ^{1}H NMR (500 MHz, CD_3CN-d_3), δ

(ppm): 1.74 (s, 6H, O_2CCH_3), 1.85 (s, 3H, O_2CCH_3), 7.00 (t, 4H, o-2,6-difluorophenyl), 7.20 (m, 2H, o-2,6-difluorophenyl). Anal. Calcd. For $C_{23}H_{24}F_4N_4O_6Rh_2$ ($4H_2O$): C 34.38, N 6.97, H 3.98 %. Found C 35.31, N 6.00, H 3.12%.

Preparation of $[Rh_2(\mu\text{-o-}F_2form)(\mu\text{-}O_2CCH_3)_1(phen)_2](O_2CCH_3)_2$, (2). An acetonitrile solution (20 mL) of **1** (50 mg, 0.07 mmol) was prepared and combined with 10 mL of a CH_3CN suspension of the diimine ligand phen (29 mg, 0.16 mmol). The reaction mixture gradually changed color from maroon to orange and finally brown and then was refluxed under an inert atmosphere for 20 h. After stopping the reaction, the solvent was removed under reduced pressure and the brown solid that was recovered was dissolved in CH_2Cl_2 (5 mL) and the sample was precipitated with hexanes and collected by filtration through a fine frit. The product was washed with diethyl ether and dried under vacuum for 24 h. Yield: 30 mg (44%). ^{1}H NMR (500 MHz, CD_3OD-d_4), δ (ppm): 1.89 (s, 6H, O_2CCH_3), 2.68 (s, 3H, O_2CCH_3), 7.05 (t, 4H, o-2,6-difluorophenyl), 7.30 (m, 2H, o-2,6-difluorophenyl), 7.67 (m, 4H, phen), 7.71 (s, 4H, phen), 8.26-8.33 (dd, 6H, phen), 8.65 (d, 2H, phen), 9.19 (d, 2H, phen). ESI-MS: $[Rh_2(\mu\text{-o-}F_2form)(\mu\text{-}O_2CCH_3)_1(phen)_2]^{2+}$, 445.97. X-ray quality crystals were obtained from slow diffusion of diethyl ether into a CH_3CN solution of the compound.

Preparation of $[Rh_2(\mu\text{-o-}F_2form)(\mu\text{-}O_2CCH_3)_1(dpq)_2](O_2CCH_3)_2$ (3). A Schlenk flask was charged with **1** (38 mg, 0.05 mmol) along with 20 mL of CH_3CN to which was added a 5 mL of a suspension of dpq (23 mg, 0.10 mmol) in CH_3CN. The reaction mixture was

refluxed for 3 days under an inert atmosphere and the resulting brown solution was reduced to dryness under reduced pressure. The brown solid was dissolved in CH_3CN (~5 mL) and treated with diethyl ether to afford a light brown solid. The product was collected by filtration, washed with 3 x 10 mL of diethyl ether, and dried under vacuum for 24 h. Yield: 18 mg (32%). ESI-MS: $[Rh_2(\mu\text{-o-}F_2form)(\mu\text{-}O_2CCH_3)_1(dpq)_2]^{2+}$, 498.02. ^{1}H NMR (500 MHz, CD_3OD-d_4), δ (ppm): 1.87 (s, 6H, O_2CCH_3), 2.68 (s, 3H, O_2CCH_3), 7.07 (t, 4H, o-2,6-difluorophenyl), 7.31 (m, 2H, o-2,6-difluorophenyl), 7.85 (m, dpq), 8.33 (m, dpq), 8.79 (d, dppz), 9.02 (s, dpq), 9.07 (m, dpq) 9.36 (d, dpq). X-ray quality crystals were obtained by slow diffusion of hexanes into a CH_2Cl_2 solution of the compound.

Preparation of $[Rh_2(\mu\text{-o-}F_2form)(\mu\text{-}O_2CCH_3)_1(dppz)_2](O_2CCH_3)_2$ (4). A CH_3CN (5 mL) suspension of dppz (30 mg, 0.10 mmol) was added to a flask containing **1** (36 mg, 0.05 mmol). The reaction was refluxed for 48 h after which time the reaction had turned colors from maroon to red-brown. The reaction was stopped and a precipitate formed upon cooling to room temperature which was collected by filtration and dried under reduced pressure. Yield: 32 mg (58%). ESI-MS: $[Rh_2(\mu\text{-o-}F_2form)(\mu\text{-}O_2CCH_3)_1(dppz)_2]^{2+}$, 548.49. ^{1}H NMR (500 MHz, CD_3OD-d_4), δ (ppm): 1.87 (s, 6H, O_2CCH_3), 2.72 (s, 3H, O_2CCH_3), 7.12 (t, 4H, o-2,6-difluorophenyl), 7.35 (m, 2H, o-2,6-difluorophenyl), 7.93 (m, 4H, dppz), 7.95 (m, 5H, dppz), 8.40 (s, 1H, dppz), 8.84 (d, 2H, dppz), 9.29 (dd, 4H, dppz), 9.42 (d, 2H, dppz). Crystals suitable for X-ray were obtained from slow diffusion of diethyl ether into a CH_3CN solution of the compound. Anal. Calcd.

For $C_{55}H_{38}F_4N_{10}O_6Rh_2$ (2.95H_2O): C 51.66, N 10.76, H 3.71%. Found C 51.34, N 10.97, H 3.37%.

Preparation of [Rh_2(μ-o-F_2form)(μ-O_2CCH_3)$_1$(dppn)$_2$](O_2CCH_3)$_2$ (5). A CH_3CN (5 mL) suspension of dppn (27 mg, 0.08 mmol) was added to a flask containing **1** (30 mg, 0.04 mmol). The reaction was refluxed for 4.5 days after which time the reaction color had turned from maroon to dark brown. The reaction was stopped and a precipitate formed upon cooling to room temperature which was collected by filtration and dried under reduced pressure. Yield: 34 mg (32%). ESI-MS: [Rh_2(μ-o-F_2form)(μ-O_2CCH_3)$_1$(dppn)$_2$]$^{2+}$, 598.06. Anal. Calcd. For $C_{67}H_{46}F_4N_{12}O_6Rh_2$ (6.65H_2O): C 52.83, N 10.9, H 4.08%. Found C 52.26, N 10.32, H 3.5%.

Instrumentation

^{1}H NMR spectra were collected on a 500 MHz Inova spectrometer. The chemical shifts are reported in δ (ppm) and referenced relative to the residual proton impurities of the deuterated solvent (CD_3CN, d_3). Electrospray ionization (ESI) mass spectra were collected on an Applied Biosystem PE SCIEX QSTAR mass spectrometer (MDS Sciex). Elemental analyses were performed by Atlantic Microlab, Inc. X-ray data sets were collected for compounds **1**, **2** and **4** were collected on a Bruker CCD APEX diffractometer with graphite monochromated Mo Kα radiation (λ = 0.71073 Å) and compounds **3** and **5** X-ray data sets were collected at the Advanced Photon Source at Argonne National Laboratory using synchrotron radiation (λ = 0.41328 Å), beamline 15-ID-B. Live-cell

imaging was performed on an inverted epifluorescence microscope (Model IX81, Olympus, Center Valley, PA) equipped with a heating stage maintained at 37ºC. The images were collected using Rolera-MGI Plus back-illuminated EMCCD camera (Qimaging, Surrey, BC, Canada) mounted on the microscope with UplanFl 100x/ 1.3 NA oil, LCPlan 40x / 0.6 NA, or LCPlan 20x / 0.4 NA objectives.

Methods

Density functional theory. Molecular electronic calculations were performed by Density Functional Theory (DFT) methods using Gaussian09 (G09) program.[112] Correlation exchange functionals (MPW1PW91)[113-115] were utilized with the Stuttgart RSC 1997 Electron Core Potential (ECP)[116] basis set for the Rh atoms and the 6-31G(d') basis set for the C, N, O, F, H atoms[117-118]. Atomic coordinates were taken from the crystal structures and used as starting points for the geometry optimization excluding the $[BF_4]^-$ counter ions and solvent molecules. Time-Dependent Density Functional Theory (TD-DFT)[119-125] calculations were performed using the polarized continuum model (PCM) with CH_3CN or H_2O as the solvent[126-127]. The first twenty lowest singlet-state calculations were included for both CH_3CN and H_2O in the singlet state calculations. The graphic software 'agui'[128] was used to plot the molecular orbitals with iso-value of 0.04. The molecular orbital compositions was analyzed with the *Chemissian* Visualization Computer Program.[129]

Cell culture and *in vitro* cytotoxicity. Monolayers of HeLa cells were cultured in DMEM containing 10% FBS, 50 μg/mL of gentamicin, 4.5 mg/mL of glucose, and 4 mM of L-glutamine. The cells were incubated in a humidified atmosphere containing 5% CO_2 at 37ºC. The cells were allowed to grow to approximately 70% confluent for analysis. The viability of cervical cancer cells (HeLa) and the ovarian cancer cell lines COLO-316, OVCAR-8 and NCI/ADR-RES in the presence of compounds **4-5** was tested using the 7-Hydroxy-3*H*-phenoxazin-3-one 10-oxide (resazurin) assay. Cell monolayers at a 70% confluence 5000-1000 cell/mL were used, 100 μL of cells were seeded in 96-well sterile plates, and 100 μL of fresh medium was added to give a total volume of 200 μL. Cells were pre-incubated at 37 °C in a humidified atmosphere containing 5% CO_2. After 24 h, the medium was replaced by 100 μL of DMEM media containing different complex concentrations. The plates were incubated for 2h after which time the cells were washed three times with PBS and the medium was replaced by 100 μL and incubated for another 24 h. At the end of the exposure time, the plates were washed with PBS and the medium replaced with 80 μL/well of L-15 medium along with 20 μL of fresh Resazurin solution (0.4 mg/mL) followed by incubation for 6 h. After the 4 h incubation period the absorbance at 570 nm was measured using a Promega Glomax Multi microplate reader. Each experiment was performed in triplicate.

Sytox Green® assay. HeLa cells, at a concentration of 5000-10000 cell/μL, were harvested, 20 μL of cells were seeded in an 8-well sterile plate, and 180 μL of fresh medium was added to give a total volume of 200 μL. Cells were pre-incubated at 37 °C. After 48 h, cells were washed three times with sterile PBS and the medium was replaced by 200 μL/well of L-15 medium containing **5** at its LC_{50} concentration, 10 μM.

Eight well sterile plates with 80% cell confluency in each well were placed on an inverted epifluorescence microscope. Imaging was performed using the fluorescence filter set FITC (Ex=488 ± 10 nm/Em=520±20 nm). The fluorescence intensities of HeLa cells were measured with the SlideBook 4.2 software (Olympus, Center Valley, PA). The cells were irradiated for 2h inside a UV/vis photoreactor LZC-4 (LuzChem, Research, Inc.), equipped with 14 lamps (λ_{irr}>400 nm). After irradiation the cells were washed three times with sterile PBS and the medium was replaced with 90 μL of L-15 medium and treated with 10 μL of a 20 μM SYTOX® Green solution and incubated for 10 minutes before imaging. Cells were imaged with a 20X objective.

MitoProbe JC-1 assay. HeLa cells monolayers were cultured at a 70% confluence, 20 μL of the cells were plated in two 8-well sterile plates to which 180 μL of fresh DMEM was added to give a total volume of 200 μL. The cells were incubated for 24 h at 37 ºC after which time the cells were washed with DPBS and the medium was replaced by 200 μL of compound **5** at its LC_{50}^{*} concentration. One plate was incubated for 2h in the dark and the other plate was placed inside the UV/vis photoreactor for 30 min. The dark control was treated with 1 μL of a 2μg/mL JC-1® solution and incubated for 5 minutes before

imaging; the same procedure was followed with the irradiated sample. The same procedure was followed for compounds **2-5** with NIC-ADR/RES cell line, however irradiation time was only 10 min.

MitoTracker® green and Sytox Blue® staining. HeLa cells at a 70% confluency were harvested, 20 µL of cells were plated in two 8-well sterile plates to which 180 µL of fresh DMEM was added for a total volume of 200 µL. The 8-well dishes were pre-incubated for 24 h at 37 ºC, after 24 h they were washed with 200 µL of DPBS and the medium was replaced by 200 µL of L-15 medium containing compound **5** at its LC_{50}^{*} concentration, MitoTracker Green (50 nM) and Sytox Blue® (1 µM). The dark control was incubated for 2h in the dark and placed on an inverted epifluorescence microscope for imaging. The second plate was incubated for 2h with compound **5** in the dark and then irradiated with the confocal microscope using a 488 nm laser for 8 min. After irradiation, MitoTracker Green was added and allowed to incubate for 45 min and finally Sytox Blue® was added and incubated for 10 min before imaging. Imaging was performed at different time periods over a course of 1 h.

Annexing V-FITC and propidium iodide staining. Monolayers of ADR-res cells were cultured at 5000-10000 cells/ µL concentrations, then 20 µL of cells were transferred to a sterile 8-well dish and 180 µL of fresh DMEM was added for a total volume of 200 µL. The plate was pre-incubated for 24 h at 37 ºC, then it was washed with DPBS and the medium was replaced with 100 µL of L-15 medium containing **2-5** at their LC_{50}^{*}

concentration. The dish was incubated for 2h in the dark and then irradiated in the UV-vis photoreactor for 10 min. After irradiation the cells were treated with Annexin V-FITC (5 µL of stock) and propidium iodide (PI) (5 µM) and placed on the microscope's heating stage at 37 ºC for 15 min afterwards MES binding buffer was added (400 µL) and the cells were imaged.

Results and Discussion

Synthesis and Characterization

The compound $[Rh_2(F_2form)(O_2CCH_3)(CH_3CN)_2]$ (**1**) was synthesized by first deprotonating HF_2form with K^tBuO in THF for 4 h, the deprotonated HF_2from was added dropwise to a CH_3CN solution of $[Rh_2(O_2CCH_3)_4(CH_3OH)_2]$. The sample was filtered and the solvent removed. To remove any excess ligand and unreacted dirhodium acetate, the sample was purified by flash chromatography. X-ray quality crystals were obtained and the results will be discussed in more detail in the next section. ^1H NMR spectroscopy was used to confirm the purity of **1** (**Figure 2.1**) with two singlet resonances at 1.74 ppm and 1.85 ppm being observed in a ratio of 1:2 respectively. The singlet at 1.85 ppm corresponds to the acetate ligand located *trans* to the F_2form and the 1.74 ppm singlet resonance is due to the in-plane acetates *cis* to the F_2form. There are also two other multiplets at 7.04 ppm and 7.25 ppm in the aromatic region that belong to the F_2form ligand (**Figure 2.1**).

Compound **1** was reacted with two equivalents of the diimine ligands phen, dpq, dppz and dppn to afford $[Rh_2(F_2form)(O_2CCH_3)(phen)_2]^{2+}$ (**2**),

$[Rh_2(F_2form)(O_2CCH_3)(dpq)_2]^{2+}$ (**3**), $[Rh_2(F_2form)(O_2CCH_3)(dppz)_2]^{2+}$ (**4**), and $[Rh_2(F_2form)(O_2CCH_3)(dppn)_2]^{2+}$ (**5**), as acetate salts. A schematic representation of the syntheses of **2-5** is shown in (**Figure 2.2**). Upon reaction of **1** with the respective diimine ligands, there is an obvious color change from maroon to orange and at the end of the reaction the color is orange brown. The purity of compounds **2-4** was confirmed by ^1H NMR spectroscopy in CD_3OD; there is a characteristic triplet resonance of the protons on

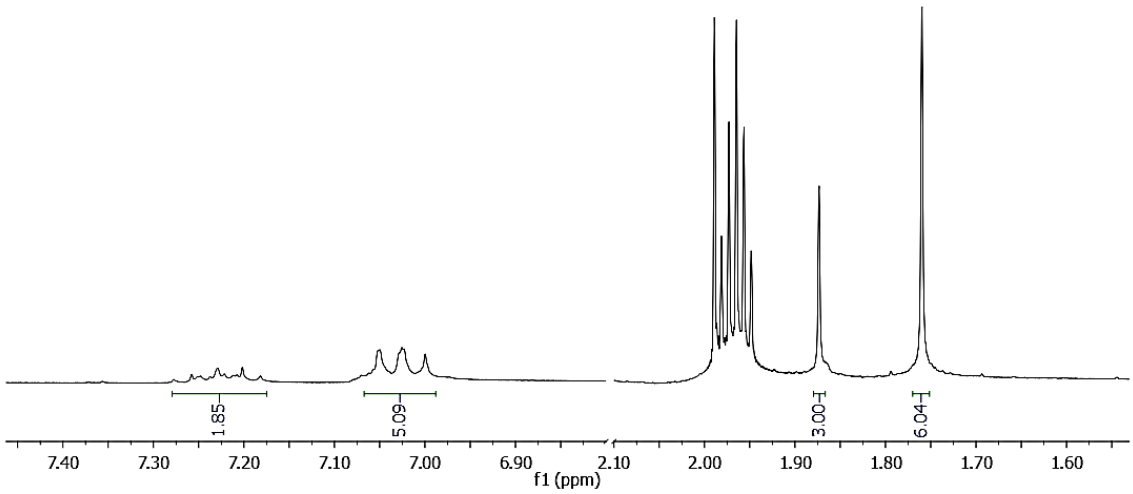

Figure 2.1 ^1H NMR spectrum of **1** in CD_3CN.

the $[F_2form]^-$ bridge at 7.04 ppm (J = 8.0 Hz), 7.07 (J = 8.9 Hz) and 7.12 ppm (J = 9.0 Hz) respectively. This triplet is shifted to lower fields upon coordination to the diimine ligands as compared to the starting material. In the solid state the axial positions of these compounds are occupied by acetate molecules, in solution they get replaced by the solvent

in this case CD_3OD and the free acetate resonance shows up as a singlet at 1.87 ppm, while the coordinated acetate shifts downfield to 2.69 ppm, hence the 1:2 ratio between the two. There is only one set of aromatic signals for the diimine ligands due to the C_{2h} symmetry of the compounds which renders them magnetically equivalent (**Figure 2.3a-c**).

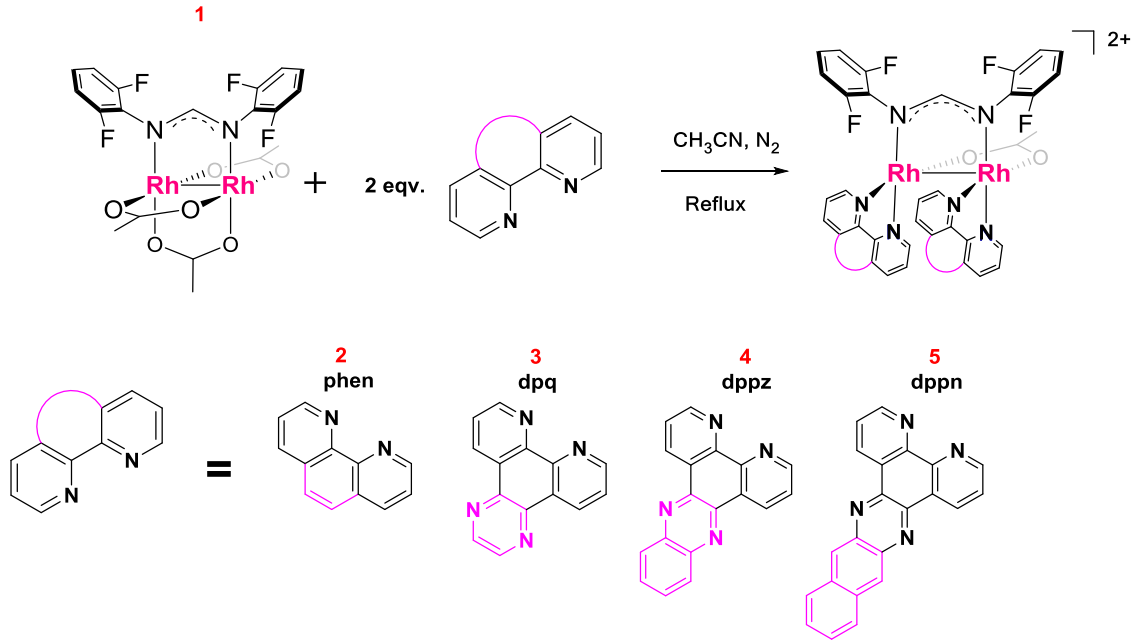

Figure 2.2 Schematic representation of the reaction of diimine ligands phen, dpq, dppz and dppn with **1** to form compounds **2-5**. Axial solvent molecules have been omitted for the sake of clarity.

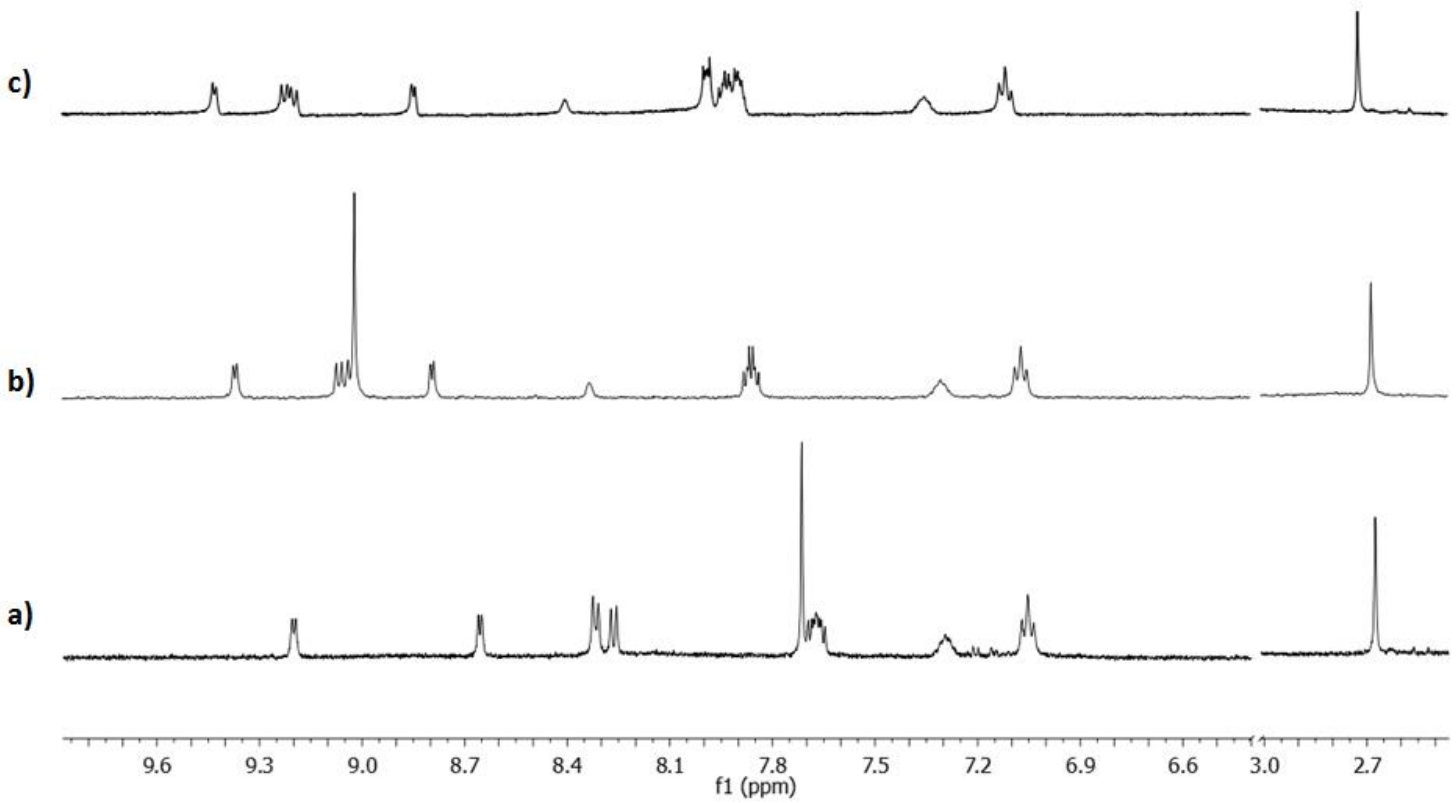

Figure 2.3 ^{1}H NMR spectra of compounds a) **2** b) **3** and b) **4** in CD_3OD.

In the case of compound **5** a ^{1}H NMR spectrum could not be obtained due to the π-π stacking interactions in solution which renders the solubility very low, however ESI-MS data show that the compound is pure. Compound **5** exhibits two mass signals, one at m/z = 598 amu and a second one at m/z = 1255 amu; the first peak corresponds to the $[Rh_2]^{2+}$ cationic unit ($[Rh_2(\mu\text{-o-}F_2form)(\mu\text{-}O_2CCH_3)_1(dppn)_2]^{2+}$) and the second one is the parent peak ($[Rh_2(\mu\text{-o-}F_2form)(\mu\text{-}O_2CCH_3)_1(dppn)_2]^{+}$) (**Figure 2.4**).

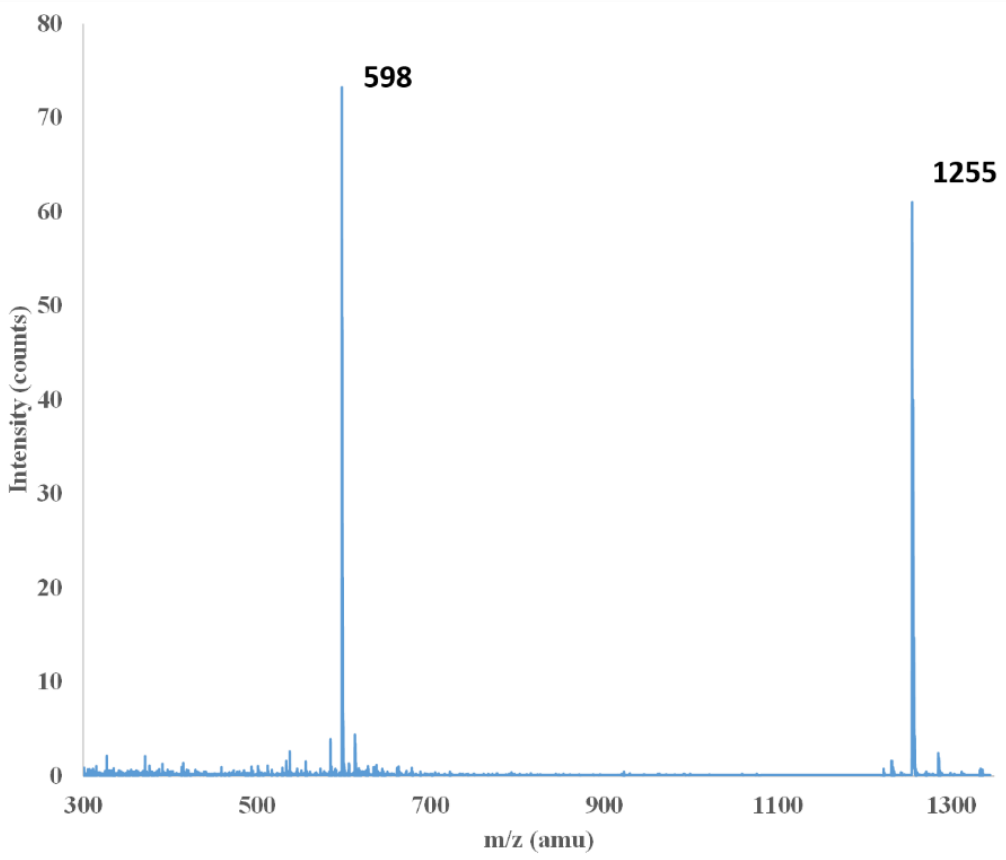

Figure 2.4 ESI-MS spectra of compound **5**.

X-ray Crystallographic Studies

[Rh_2(μ-o-F_2form)(μ-O_2CCH_3)$_3$(CH_3CN)$_2$], (1). Compound **1** crystallizes in the monoclinic space group $P2_1/c$. The cationic $[Rh_2]^{4+}$ unit is supported by three acetate bridge groups and one $[o\text{-}F_2form]^-$ ligand with the axial positions being occupied by CH_3CN ligands (**Figure 2.5a**). The Rh-Rh bond length is 2.4217(7) which is in range of other dirhodium carboxylate (2.35-2.45 Å) and formamidinate (2.37-2.45 Å) derivatives.[130] The average Rh-O (*trans* to $[F_2form]^-$) bond distances is 2.070(4) Å, which is slightly longer than that of the acetates *cis* to the $[F_2form]^-$ which is not surprising since the formamidinate is a σ-donating ligand. The Rh-N ($[F_2form]^-$) bond distances are in the range of 2.027(5)-2.035(5) Å.

a)

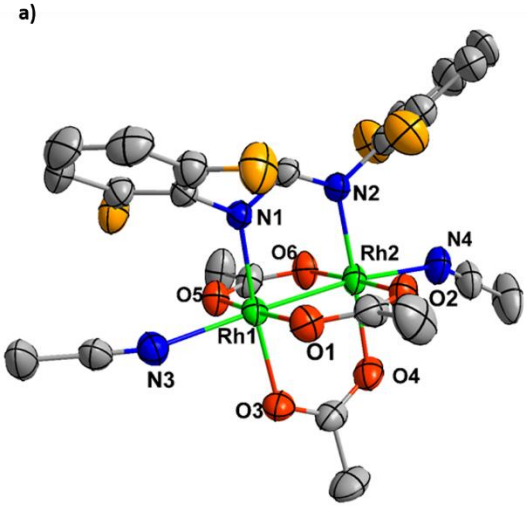

b)

1	
Bond	Å
Rh1-Rh2	2.4217(7)
Rh1-N1	2.027(5)
Rh1-O3	2.070(4)
Rh1-O5	2.046(5)
Rh1-O1	2.041(5)
Rh1-N3	2.264(5)
Rh2-N2	2.035(5)
Rh2-O4	2.070(4)
Rh2-O6	2.041(5)
Rh2-O2	2.032(5)
Rh2-N4	2.259(6)
Dihedral angles	°
N1-Rh1-Rh2-N2	0.9(2)
O3-Rh1-Rh2-O4	0.93(18)
O1-Rh1-Rh2-O2	0.56(16)
O5-Rh1-Rh2-O6	0.23(16)

Figure 2.5 a) Thermal ellipsoid plot for compound **1** at the 50% probability level; interstitial solvent and hydrogen atoms have been omitted for the sake of clarity. b) Table with important bond distances and dihedral angles for compound **1**.

[Rh_2(μ-o-F_2form)(μ-O_2CCH_3)$_1$(phen)$_2$](O_2CCH_3)$_2$, (2). The mixed-bridging ligand compound **2** crystalizes in the P-1 space group. The molecular structure of **2** consists of a bridging acetate and [F_2form]$^-$ ligand coordinated to the dirhodium (II,II) core along with two 1,10-phenantroline ligands in a *syn* configuration and two axial acetate molecules (**Figure 2.6**). The Rh-Rh distance is 2.5650(9) Å which is similar to the values for [$Rh_2(O_2CCH_3)_2(phen)_2][BF_4]_2$[131] and [$Rh_2$(DTolF)$_2$(phen)($CH_3CN$)$_3$][$BF_4$]$_2$,[132] which are 2.5808(2) Å and 2.5557(4) Å respectively. The Rh-N_{dpq} bond distances are in the range of 2.004(7)-2.044(6) Å. The complex adopts a twisted conformation which reduces repulsion between the two diimine ligands which adopt a dihedral angle of -18.3(3)° for N15-Rh1-Rh2-N19.

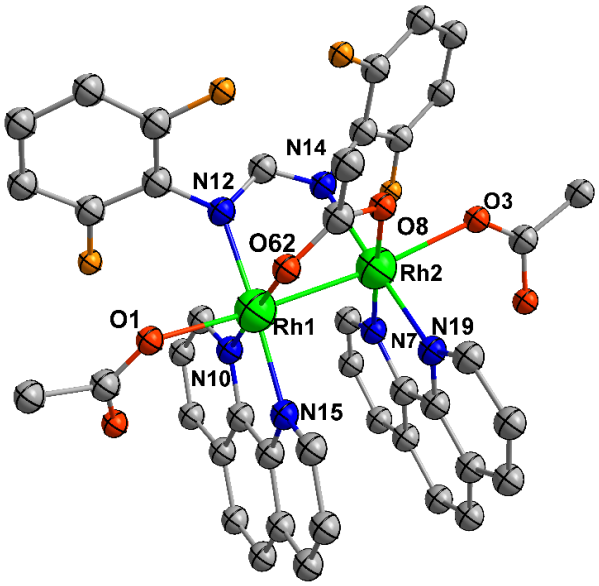

Figure 2.6 Thermal ellipsoid plot for compound **2** at the 50% probability level; interstitial solvent and hydrogen atoms have been omitted for the sake of clarity.

[Rh_2(μ-o-F_2form)(μ-O_2CCH_3)$_1$(dpq)$_2$]$(Cl)_2$, (3). The cationic structure of **3** is similar to that of **2** but the axial positions are occupied by Cl^- ligands (**Figure 2.7a**). The Rh-Cl_{ax} bond distances are in the range of 2.5145(16)-2.5337(16) Å which is not unusual for other dirhodium compounds reported in literature.[130,133] The Rh-Rh bond distance is 2.6086(6) Å which is ~ 0.04 Å longer than that of **2** and $[Rh_2(DTolF)(dpq)_2][BF_4]_2$.[134] The Rh-N (dpq *trans* to acetate) bond distances are 2.006(6) Å and 2.009(6) Å which are shorter than that of the Rh-N *trans* to the $[F_2form]^-$ which are 2.026(5) Å and 2.035(5) Å. The asymmetric unit of compound **3** contains two independent dirhodium units that engage in π-π interactions when viewed along the *a* axis (**Figure 2.7b**). The dirhodium metal unit causes the dpq ligands to come to close proximity, repulsions between the two dpq ligands causes splaying from the parallel alignment, therefore the planes between the two molecules cannot be determined. In order to determine the π-π stacking interactions the distance between the centroids of C23-C20-C18-C19-C25-C24 from one dpq and N9-C20-C23-N10-C22-C21 from the neighboring one was determined to be 3.52 Å (**Figure 2.7b**).

[Rh_2(μ-o-F_2form)(μ-O_2CCH_3)$_1$($dppz$)$_2$]$(O_2CCH_3)_2$, (4). Compound **4** crystallizes in the monoclinic space group $P2_1/n$. As in the case of compound **2**, both axial positions are occupied by acetate ligands **(Figure 2.8a)**. The Rh-Rh bond distance is 2.6089(8), which is longer than that observed for $[Rh_2(O_2CCH_3)_2(dppz)_2][O_2CCH_3]_2$ (2.5519(6) Å) and within the range of those found in $[Rh_2(DTolF)_2(dppz)_2][BF_4]_2$ and [Rh_2(F-

form)$_2$(dppz)$_2$][BF_4]$_2$ 2.597(1) Å and 2.6190(9) Å, respectively.[84,134] There are two dppz ligands coordinated to the dirhodium core in a *syn* orientation that are distorted from an eclipsed conformation due to steric repulsion. As in the case of **2** and **3** the Rh-N_{dpq} (*trans* to [F_2form]$^-$) bond distances are longer than the Rh-N_{dpq} (*trans* to acetate) distances due to the σ-donating character of the formamidinate. On the other hand, the bond distances for the Rh-O and Rh-N_{form} are comparable which is mainly attributed to the fact that the diimine ligands are electron acceptors.

[Rh_2(*μ*-o-F_2form)(*μ*-O_2CCH_3)(dppn)$_2$][Cl]$_2$, (5). The cationic structure of **5** is similar to that of **4**, but with two Cl^- ligands in the axial positions to complete the pseudo-octahedral coordination sphere (**Figure 2.8b**). The Rh-Rh bond distance is 2.582(11) Å, which is slightly shorter than those observed for **3** and **4**. There is a greater degree of distortion in the coordination sphere of the dirhodium (II,II) core due to a greater repulsion between the dppn ligands with dihedral angles defined by N14-Rh2-Rh1-N10 and N9-Rh1-Rh2-N15 being 18(3)° and 19(3)°, respectively. The Rh-N_{dppn} bond distances are in the range of 2.01(4)-2.05(4) Å. As in the case of **4**, compound **5** engages in π-π intermolecular interactions with neighboring molecules. The Rh-N ([F_2form]$^-$) distances are in the range of 2.09(6)-2.11(6) Å, which are significantly longer than those found in compounds **1-4**. The poor quality of the crystal in combination with the low resolution of the diffraction data (1.38 Å) accounts for the overestimated bond distances. in this compound.

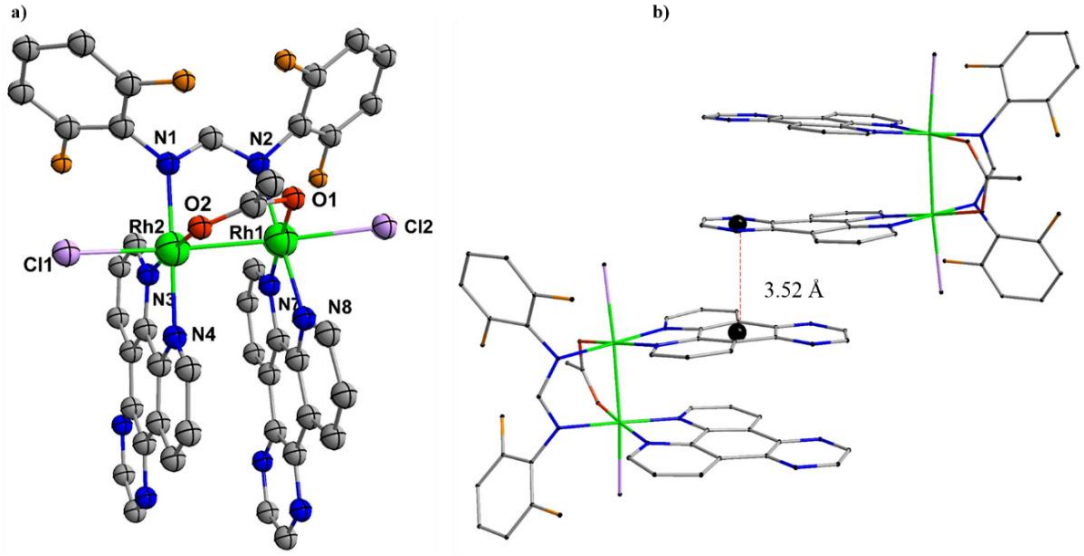

Figure 2.7. a) Thermal ellipsoid plot for compound **3** at the 50% probability level; interstitial solvent and hydrogen atoms have been omitted for the sake of clarity. b) Crystal packing of **3** showing intermolecular π-stacking.

Crystal data and refinement parameters for compounds **1-5** can be found in **Table 2.1**.

The detailed bond distances and dihedral angles for compounds **2-5** are compiled in **Table 2.2.**

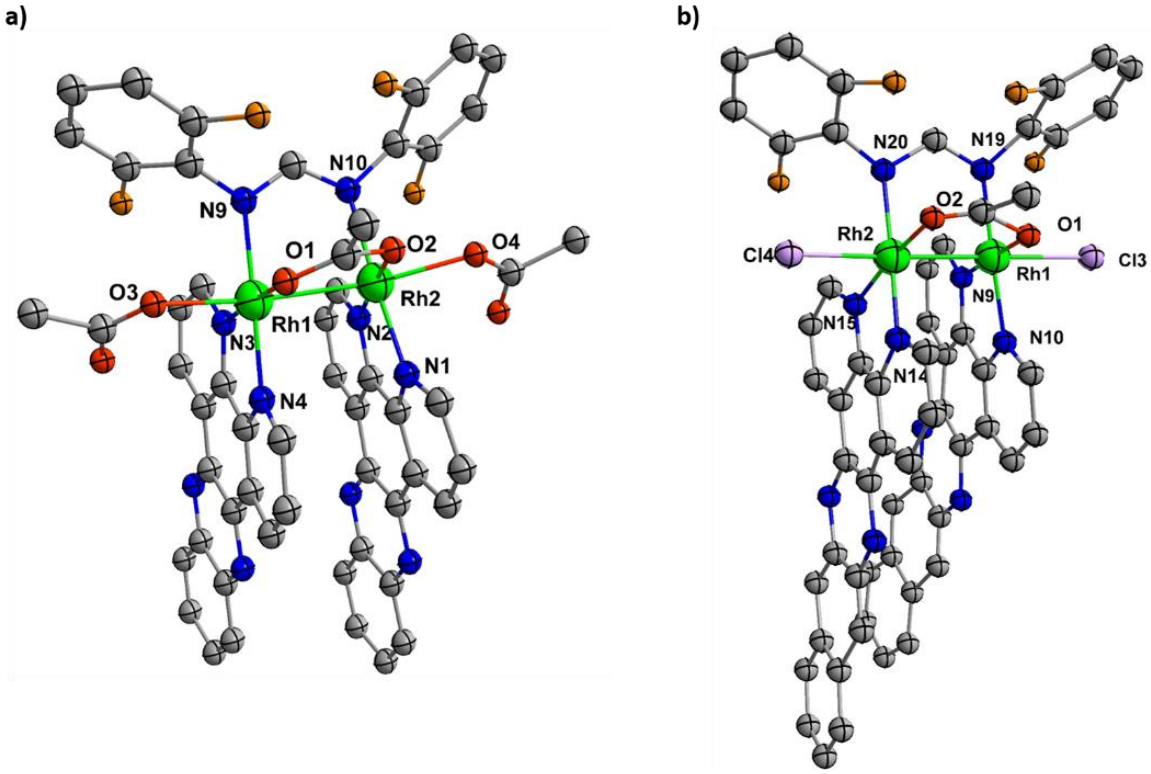

Figure 2.8. a) Thermal ellipsoid plot for compound **4** at the 50% probability level; interstitial solvent and hydrogen atoms have been omitted for the sake of clarity. b) Diamond generated representation of compound **5**.

Table 2.1 Crystal structural parameters and refinement data for compounds **1-5**.

	1	6•H_2O	3•CH_2Cl_2	4•H_2O	5•H_2O
Formula	$C_{23}H_{22}F_4N_4O_6Rh_2$	$C_{43}H_{32}F_4N_6O_9Rh_2$	$C_{44.5}H_{29}Cl_7F_4N_{11}O_2Rh_2$	$C_{55}H_{36}F_4N_{10}O_8Rh_2$	$C_{59}H_{34.5}N_{10}O_{3.5}F_4Rh_2Cl_2$
Mol. Wt. (g/mol)	732.26	1058.56	1279.76	1246.76	1257.43
Space group	$P2_1/c$	P-1	P-1	$P2_1/n$	$P2_1/n$
a, b, c/ Å	15.425(3)	9.5800(15)	13.3576(7),	12.0611(18)	17.90(1)
	10.138(2)	14.081(2)	14.5743(7)	13.413(2)	27.117(15)
	17.663(4)	16.276(3)	14.6593(7)	31.013(5)	26.327(15)
α, β, γ /°	90	96.531(2)	67.0260(10)	90	90
	103.23(3)	91.928(2)	66.4270(10)	98.064(2)	105.667(11)
	90	100.763(2)	83.1490(10)	90	90
Volume/ $Å^3$	2688.8(10)	2139.6(6)	2405.9(2)	4967.6(13)	12304(12)
Z	4	2	2	4	8
2Θ range for data collection	52.822°	51.038°	54.968°	48.944°	29.74°
R_{int}	0.0321	0.0582	0.0823	0.0597	0.2979
Goodness-of-fit (all data)[a]	1.268	1.046	1.004	0.985	1.832
R_1,[b] wR_2[c] [all data]	R_1 = 0.0462	R_1 = 0.0858	R_1 = 0.0925	R_1 = 0.0696	R_1 = 0.2921
	wR_2 = 0.1175	wR_2 = 0.2112	wR_2 = 0.1753	wR_2 = 0.1505	wR_2 = 0.5609

[a] $R = \sum \big| |F_o| - |F_c| \big| / \sum |F_o|$. [b] $wR = \{\sum[w(F_o^2 - F_c^2)^2] / \sum w(F_o^2)^2]\}^{1/2}$. [c] Goodness-of-fit = $\{\sum[w(F_o^2 - F_c^2)^2]/(n-p)\}^{1/2}$, where n is the number of reflections and p is the total number of parameters refined.

Table 2.2 Relevant bond distances and dihedral angles for compounds **1-5**.

Compound 2	Å	Compound 3	Å
Rh1-Rh2	2.5650(9)	Rh1-Rh2	2.6086(6)
Rh1-N10	2.004(7)	Rh1-N7	2.009(6)
Rh1-N15	2.028(7)	Rh1-N8	2.026(5)
Rh1-N12	2.044(6)	Rh1-O1	2.051(5)
Rh1-O62	2.061(5)	Rh1-N2	2.069(5)
Rh1-O1	2.207(5)	Rh1-Cl2	2.5337(16)
Rh2-N7	2.029(6)	Rh2-N1	2.056(5)
Rh2-N19	2.030(6)	Rh2-N3	2.006(6)
Rh2-O8	2.046(5)	Rh2-N4	2.035(5)
Rh2-N14	2.086(6)	Rh2-O2	2.047(5)
Rh2-O3	2.245(6)	Rh2-Cl1	2.5145(16)
Dihedral angles	°	Dihedral angles	°
N12-Rh1-Rh2-N14	-12.5(3)	N2-Rh1-Rh2-N1	-11.6(3)
O62-Rh1-Rh2-O8	-15.3(2)	O1-Rh1-Rh2-O2	-13.98(18)
N15-Rh1-Rh2-N19	-18.3(3)	N8-Rh1-Rh2-N4	-15.9(3)
N10-Rh1-Rh2-N7	-19.0(3)	N7-Rh1-Rh2-N3	-16.6(3)
Compound 4	Å	Compound 5	Å
Rh1-Rh2	2.6089(8)	Rh1-Rh2	2.582(11)
Rh1-N3	2.007(5)	Rh1-N19	2.09(6)
Rh1-N4	2.024(5)	Rh1-N9	2.04(4)
Rh1-O1	2.059(4)	Rh1-N10	2.01(4)
Rh1-N9	2.062(5)	Rh1-O1	2.09(5)
Rh1-O3	2.191(5)	Rh1-Cl3	2.57(2)
Rh2-N2	2.001(5)	Rh2-N20	2.11(6)
Rh2-N1	2.021(5)	Rh2-N14	2.02(4)
Rh2-O2	2.046(4)	Rh2-N15	2.05(4)
Rh2-N10	2.062(5)	Rh2-O2	2.01(6)
Rh2-O4	2.171(5)	Rh2-Cl4	2.52(2)
Dihedral angles	°	Dihedral angles	°
N9-Rh1-Rh2-N10	-7.6(2)	O1-Rh1-Rh2-O2	12(2)
O1-Rh1-Rh2-O2	-8.87(17)	N19-Rh1-Rh2-N20	7(2)
N4-Rh1-Rh2-N1	-9.7(2)	N14-Rh2-Rh1-N10	18(3)
N3-Rh1-Rh2-N2	-9.89(19)	N9-Rh1-Rh2-N15	19(3)

Electronic Absorption Spectroscopy

Electronic absorption spectroscopy data were obtained for compounds **1-5** in CH_3CN and the results are summarized in **Table 2.3**.

Table 2.3. Electronic absorption data for compounds **1-5** in CH_3CN collected at room temperature.

	λ (nm), (ε x 10^3 (M^{-1}•cm^{-1})) in CH_3CN
1	250 (15.9), 320 (2.6), 550 (0.22)
2	225 (59.8), 273 (46.5), 290 (32), 350 (5.1), 410 (0.44)
3	258 (10.6), 287 (59), 345 (14.0), 405 (6.6)
4	216 (59.0), 278 (134.3), 380 (18.4), 440 (0.27)
5	240 (71.2), 260 (61.3), 320 (107.3), 395 (18.4), 415 (19.8)

Compound **1** exhibits a transition at 320 nm which corresponds to Rh(π^*)→Rh-L_{eq}(σ^*) and a low energy transition at 550 nm ascribed to a metal centered transition originating from the Rh(π^*) →Rh(σ^*) as in the case of other carboxylates (**Figure 2.9**).[135-136] The spectral characteristics of compounds **2-5** in the region between 280-420 nm are very distinct. These bands in the higher energy range correspond to transitions originating from intramolecular $\pi\pi^*$ transitions from the diimine ligands.[88] Dirhodium compounds bearing 1,10-phenanthroline ligands have characteristic absorption bands around 260 nm and compound **2** has a distinctive band at 273 nm which is phen in origin (**Figure 2.10a**).[88] The free dpq ligand has an absorption maxima at 254 nm in chloroform which is in accord to that of **3** (287 nm, ε = 58950 $M^{-1}cm^{-1}$) (**Figure 2.10b**).[88] The ligands dppz and dppn in $CHCl_3$ solutions have absorption maxima at 370 nm and 414 nm respectively; these

maxima are also present in compounds **4** and **5** (**Figure 2.10c-d**). The electronic absorption spectrum characteristics from these series of compounds have also been observed in compounds previously synthesized in our laboratories; *e. g. cis*-$[Rh_2(O_2CCH_3)_2(L)(\eta^1\text{-}O_2CCH_3)(CH_3OH)]^+$(L= dpq, dppz, dppn), *cis*-$[Rh_2(F\text{-}form)_2(L)_2]^{2+}$ (L=dpq, dppz, dppn), *cis*-$[Rh_2(O_2CCH_3)_2(dppz)_2]^{2+}$ and *cis*-$[Rh_2(O_2CCH_3)_2(dppn)_2]^{2+}$ also exhibit these bands.[88,134] Formamidinate compounds like $[Rh_2(DTolF)_4]$ and $[Rh_2(F\text{-}form)_4]$ exhibit strong absorption features in the region between 230-280 nm in acetonitrile, the same is observed with compounds **2-5**.[134] These intense absorption bands in the high energy range of the spectrum for compounds **2-5** arise between 240-280 nm, namely 290 nm for **2**, 258 nm for **3**, 278 nm for **4** and 260 nm for **5** and are believed to be attributed to metal centered with the involvement of the diimine ligands.[134]Another important feature that can be observed for this new family of compounds is the presence of low energy absorption. Compounds **2-5** exhibit low energy absorptions that tail off in the region between 600-800 nm. This same feature has been observed for $[Rh_2(O_2CCH_3)_2(L)_2]^{2+}$ (L = dpq, dppz and dppn) and has been assigned as a charge-transfer transition originating from the $[F_2form]^-$ bridging ligand to the diimine ligand.[88]

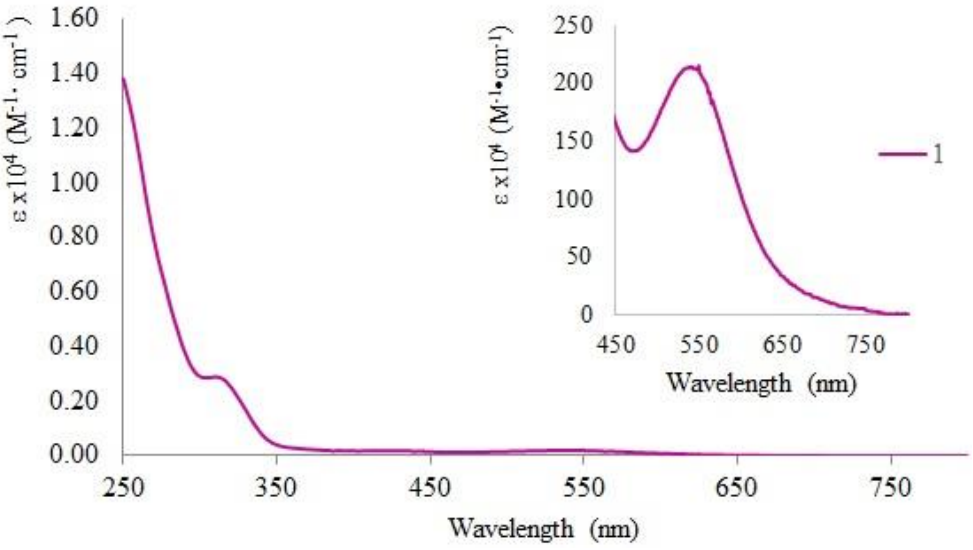

Figure 2.9 Electronic absorption spectrum of **1** in CH_3CN at room temperature.

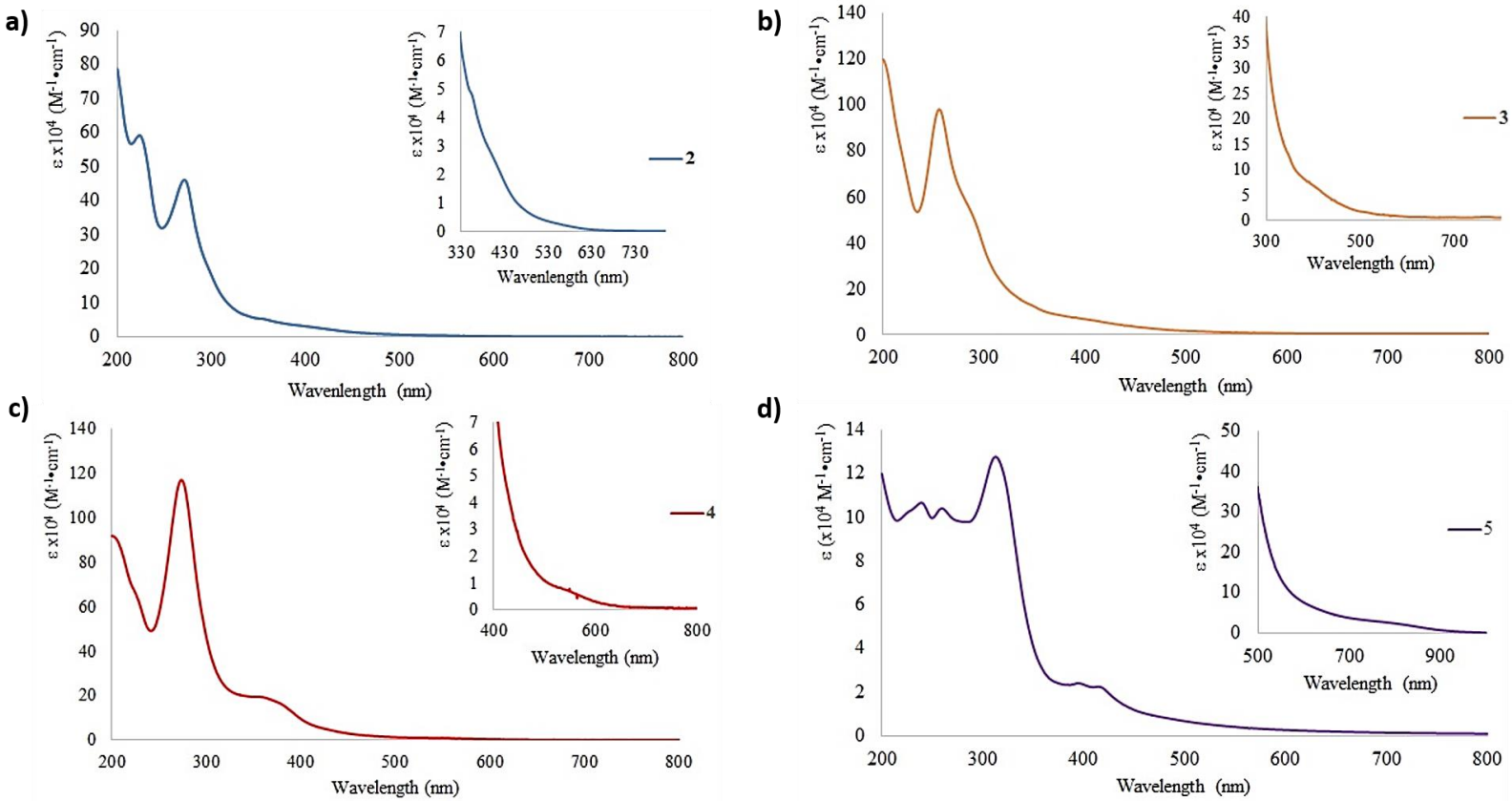

Figure 2.10 Electronic absorption spectra of compounds **2-5** in CH_3CN at room temperature.

Computational Studies

Geometry optimization in the gas phase was performed on compounds **2-5**. The optimization of these compounds was performed using the crystal structures as a starting point. Molecular orbital diagrams were constructed (**Figure 2.11**) and the contribution to the orbitals involved in the electronic transitions are listed in **Error! Reference source ot found.**. In compounds **2-4**, the MO composition of the HOMO is mainly from the bridging ligand $[F_2form]^-$ (~70 %) with some metal character (~30 %) as well. These findings are in accord with that of the analogous series of compounds *cis*-$[Rh_2(F\text{-}form)(L)_2]^{2+}$ and *cis*-$[Rh_2(DTolF)(L)_2]^{2+}$ where L = dpq, dppz and dppn.[134] On the other hand the HOMO as well as the HOMO-1-LUMO+1 orbitals of compound **5** are dppn based. The orbitals HOMO-3 through HOMO-1 in compounds **2-4** are mostly metal in character (~70%). The replacement of one $[F_2form]^-$ ligand does not seem to alter the electronic structure of this series of compounds as compared to that of *cis*-$[Rh_2(DTolF)(L)_2]^{2+}$.[134] In most of the molecular orbitals the contribution from the acetate is less than 5 %.

The LUMO to LUMO + 4 in compounds **3-5** are mostly diimine ligand centered as can be seen in **Error! Reference source not found.**. The LUMO of compound **5** lies .27 eV and 0.24 eV lower in energy than **3** and **4** respectively therefore compound **5** should be easier to reduce. The Rh(σ*) orbital for compounds **3** and **4** has been predicted to be the LUMO+6, LUMO+5 for compound **5**, while in compound **3** has been predicted to be LUMO+3 with Rh(σ*) contributions in the range of ~50-75%.

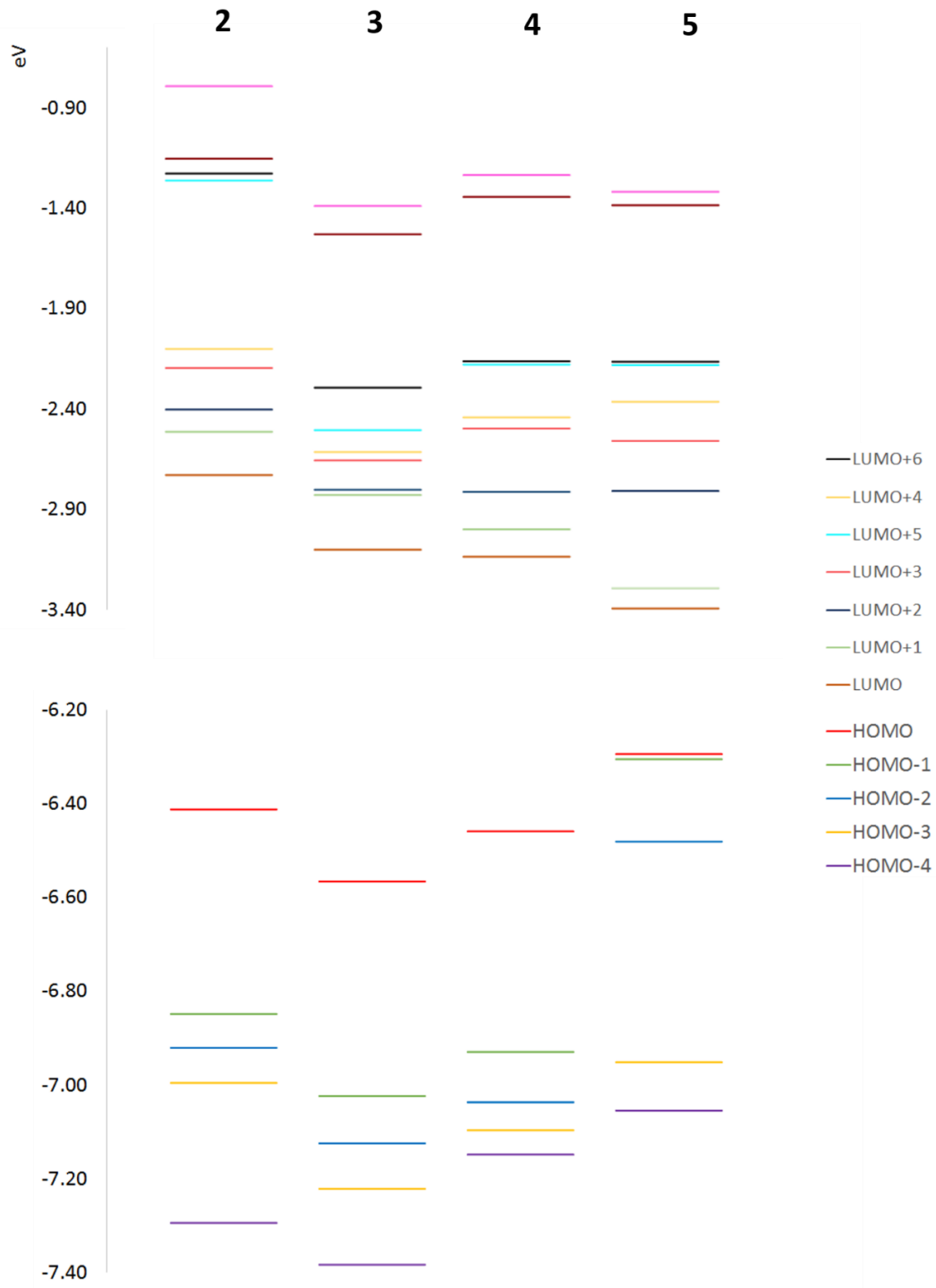

Figure 2.11 Molecular orbital diagrams for compounds **2-5**.

Table 2.4 Molecular orbital contributions for compounds **2-5** as predicted by DFT in CH_3CN.

	2	**3**	**4**	**5**
H-4	12 Rh 83 F_2form	5 Rh 93 F_2form	5 Rh 90 dppz	65 Rh 20 dppn 6 ax CH_3CN
H-3	72 Rh 21 phen	73 Rh 19 dpq	69 Rh 20 dppz	76 Rh 13 dppn
H-2	66 Rh 22 phen 8 ax CH_3CN	68 Rh 20 dpq 7 ax CH_3CN	68 Rh 17 dppz 6 ax CH_3CN	25 Rh 71 F_2form
H-1	73 Rh 17 F_2form	75 Rh 14 dpq 6 ax CH_3CN	77 Rh 13 dppz	99 dppn
H	28 Rh 68 F_2form	24 Rh 73 F_2form	26 Rh 71 F_2form	99 dppn
L	95 phen	96 dpq	90 dppz	95 dppn
L+1	99 phen	97 dpq	92 dppz	95 dppn
L+2	97 phen	98 dpq	84 dppz	4 Rh 72 dppn
L+3	76 Rh 5 F_2form 8 ax CH_3CN	99 dpq	87 dppz	3 Rh 74 dppn
L+4	51 Rh 21 F_2form 22 phen	99 dpq	86 dppz	2 Rh 81 dppn
L+5	89 phen	98 dpq	27 Rh 59 dppz	58 Rh 26 dppn
L+6	6 Rh 89 phen	75 Rh 5 F_2form 8 dpq 10 ax CH_3CN	51 Rh 33 dppz	54 Rh 20 F_2form 17 dppn 6 OAc
L+7	45 Rh 30 F_2form 19 phen	55 Rh 20 F_2form 19 dpq 6 OAc	55 Rh 21 F_2form 17 dppz 6 OAc	19 Rh 63 dppn
L+8	96 phen	47 Rh 30 F_2form 16 dpq 6 Oac	47 Rh 29 F_2form 17 dppz 6 OAc	90 dppn

a. H = HOMO, L = LUMO.

b. Fragment contributions that account for less than 5% have been omitted.

TD-DFT was also used to gain some insight into the composition of the electronic transitions observed for compounds **2-5**. The vertical energies and the orbitals that comprise the transitions are summarized in **Table 2.5**. The lowest energy transition for compounds **2** and **3** at 480 nm (f = 0.001) and 477 nm (f = 0.002) respectively, were predicted to be metal centered (MC, Rh(π^*) to Rh(σ^*)), compound **5**'s MC transition was predicted at 475 nm with a very low oscillator strength (f = 0.002). On the other hand compound **4** lowest energy transition corresponds to a ligand to ligand charge transfer band (^{1}LLCT) from $[F_2form]^-(\pi) \rightarrow dppz(\pi^*)$. Compound **5** is the exception where the lowest energy transition is mostly attributed to the intraligand (IL) π to π^* transition (~70 %) centered at 518 nm, this has also been observed for the homoleptic compounds $[Rh_2(DTolF)(dppn)_2]^{2+}$ and $[Rh_2(F\text{-}form)(dppn)_2]^{2+}$.[134] The HOMO in compounds **2-4** is ~30 % Rh and ~70 % $[F_2form]^-$ character while the LUMO is localized on the diimine ligand is >90 % this explains the LLCT bands observed for compounds **2-4** at 418 nm, 446 nm and 436 nm. The LLCT on compound **5** is not centered on the HOMO and LUMO orbitals but on the HOMO-3 and LUMO+5 and it is predicted at 457 nm.

Table 2.5 First eight electronic transitions predicted for **2-5** by TD-DFT calculations in CH_3CN as solvent.[a, b]

Excited State	2	3	4	5
1	480 nm, *f* = 0.001 H-1--> L+3 (74 %)	477 nm, *f* = 0.002 H-1--> L+6 (62 %)	478 nm, *f* = 0.001 H-1--> L+6 (48 %) H-1--> L+5 (27 %)	517 nm, *f* = 0.001 H--> L (70 %) H-1--> L+1 (26 %)
2	432 nm, *f* = 0.003 H--> L+3 (79 %)	446 nm, *f* = 0.002 H--> L (32 %) H-3--> L+6 (30 %)	436 nm, *f* = 0.002 H--> L (63 %) H--> L+1 (30 %)	516 nm, *f* = 0.03 H-1--> L (67 %) H--> L+1 (29 %)
3	418 nm, *f* = 0.002 H--> L (95 %)	442 nm, *f* = 0.002 H--> L (58 %)	431 nm, *f* = 0.004 H--> L+6 (52 %) H--> L+5 (29 %)	475 nm, *f* = 0.002 H-3--> L+5 (56%)
4	387 nm, *f* = 0.002 H-1--> L (35 %) H--> L+1 (22 %)	430 nm, *f* = 0.002 H-1--> L+6 (72%)	409 nm, *f* = 0.001 H--> L+2 (54 %) H-->L (32 %)	473 nm, *f* = 0.002 H--> L+1 (60 %) H-1--> L (26 %)
5	384 nm, *f* = 0.014 H-1--> L (42 %)	406 nm, *f* = 0.009 H-1--> L (82 %)	407 nm, *f* = 0.002 H--> L+1 (82 %)	457 nm, *f* = 0.001 H-2--> L (92 %)
6	380 nm, *f* = 0.002 H--> L+1 (35 %) H--> L+4 (23 %)	389 nm, *f* = 0.018 H-2--> L (58 %)	395 nm, *f* = 0.017 H-1--> L (44 %) H-1--> L+2 (44 %)	443 nm, *f* = 0.001 H-3--> L+5 (39 %) H-4--> L+5 (26 %)
7	376 nm, *f* = 0.004 H--> L+2 (87 %)	388 nm, *f* = 0.025 H--> L+7 (37 %)	383 nm, *f* = 0.02 H--> L+7 (48 %)	438 nm, *f* = 0.002 H-2--> L+1 (95 %)
8	371 nm, *f* = 0.034 H-2--> L (65 %)	379 nm, *f* = 0.025 H-3--> L (72 %)	380 nm, *f* = 0.059 H-2--> L (42 %) H-2--> L+2 (26 %)	429 nm, *f* = 0.004 H-2--> L+5 (63 %)

[a.] H = HOMO, L = LUMO, *f* = oscillator strength.

[b.] Only contributions greater than 20% have been listed.

In vitro *Cytotoxicity Studies*

Compounds **2-5** were screened for their anti-proliferative activity against four human cancer cell lines, namely HeLa, COLO-316, OVCAR-8 and NCI/ADR-RES and compared to that of cisplatin. The cell proliferation assay resazurin (7-Hydroxy-3*H*-phenoxazin-3-one 10-oxide) was used to evaluate the toxicity of **2-5** as their $[BF_4]^-$ salts. Resazurin, also known as Alamar Blue, is a water-soluble fluorescent dye that forms resorufin upon reduction by NADH by the cells, turning colors from blue to pink.[137-139] The formation of resorufin (pink) is indicative of enzymatic reduction by living cells and direct correlations to cell viability can be established (**Figure 2.12**).

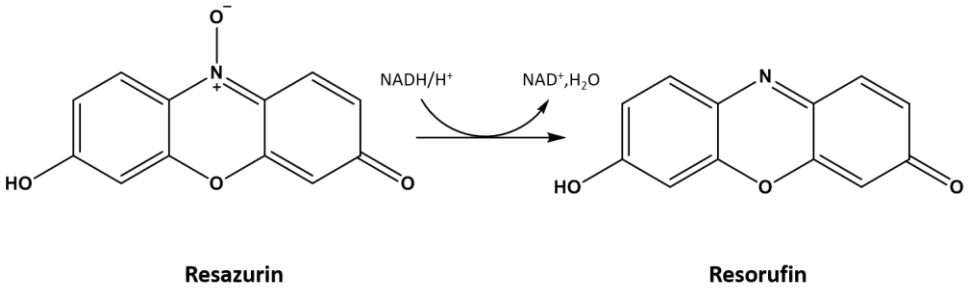

Figure 2.12 Schematic representation of the reduction of resazurin to resorufin.

The LC_{50} values (concentration required to kill 50 % of cell population) in the dark and upon irradiation (LC_{50}^*) were calculated for compounds **2-5** by measuring the survival of the cells in the presence of complex relative to the untreated control. The cells were incubated at different concentrations of complex for 2 h and then washed with phosphate

buffer, incubated for 24 h and their viability in the dark evaluated. A similar procedure was followed for the irradiated experiment; after the incubation and washing steps, the cells were irradiated ($\lambda_{irr} \geq 400$ nm) for 1 h. The phototoxicity index (PI) in another chapter was determined by calculating the ratio between LC_{50}^{*} and LC_{50}. The results of the cell proliferation assay for the different cell lines are summarized in **Table 2.6**.

Previous studies in our laboratories described the toxicity of a heteroleptic series of dirhodium compounds of the type $[Rh_2(O_2CCH_3)_2(dppn)(N\text{-}N)][O_2CCH_3]_2$ (N-N is bpy, phen, dpq, dppz or dppn) in the dark and upon irradiation. It was found that the compounds $[Rh_2(O_2CCH_3)_2(dppn)(dppz)]^{2+}$ and $[Rh_2(O_2CCH_3)_2(dppn)_2]^{2+}$ exhibit the greatest PI, 21 and 24 respectively.[88] The high toxicity of these compounds against human skin cancer cells (HS-27) is attributed to their ability to generate reactive oxygen species upon irradiation. In light of these results the cytotoxicity of compounds **2-5** was determined in the dark and upon irradiation. In these new series of compounds, **5** exhibits a 5.8-fold increase in toxicity upon irradiation unlike compounds **3** (PI = 1.8**)** and **4** (PI = 1). Although **2** also shows an estimated ~5-fold increase in toxicity upon irradiation, the LC_{50} values are very high for therapeutic purposes (LC_{50} >1 mM and LC_{50}^{*} >200 μM).
In addition the ovarian adenocarcinomas COLO-316, OVCAR-8 and NCI/ADR-RES were evaluated against compounds **2-5**. The ovarian carcinoma COLO-316 is an aneuploid cell line, meaning that it has multiple markers, deletions, additions and rearrangements of the chromosomes.[140] The OVCAR-8 line is the parent cell line of NCI/ADR-RES and the latter is a drug resistant (carboplatin, Adriamycin and paclitaxel) cell line characterized by the up regulation of P-glycoprotein (P-gp) an ATP-

Table 2.6 Cell viability data of compounds **2-5** in the dark and upon irradiation as determined by the resazurin assay.

	HeLa			COLO-316			OVCAR-8			NIC-ADR/res		
	LC_{50} µM[a]	**LC_{50}^{*} µM**[b]	**PI**[c]	**LC_{50} µM**[a]	**LC_{50}^{*} µM**[b]	**PI**[c]	**LC_{50} µM**[a]	**LC_{50}^{*} µM**[b]	**PI**[c]	**LC_{50} µM**[a]	**LC_{50}^{*} µM**[b]	**PI**[c]
***cis*-Pt**[d]	56 ± 4	56 ± 9	1	71 ± 11	63 ± 12	1	241 ± 10	170 ± 24	1.4	199 ± 7	143 ± 6	1.4
2	> 1mM	> 200 µM	5	> 300 µm	> 250 µM	~1.2	99 ± 18	44 ± 6	2.3	199 ± 5	192 ± 3	1
3	81 ± 15	45 ± 6	1.8	> 1mM	> 300 µM	3.3	86 ± 19	45 ± 20	1.9	149 ± 25	47 ± 10	3.2
4	151 ± 22	142 ± 25	1	80 ± 12	59 ± 7	1.4	41 ± 11	5 ± 2	8.2	76 ± 18	71 ± 15	1
5	64 ± 7	11 ± 4	5.8	246 ± 27	31 ± 6	7.9	353 ± 49	49 ± 8	7.2	336 ± 55	19 ± 4	17.7

a. Incubation time = 2 h. The results in this table are means of three independent experiments.
b. Irradiation time 1 h, λ_{irr} > 400 nm.
c. PI = phototoxicity index.
d. *cis*-Pt = cisplatin.

independent efflux pump that controls the extrusion of toxins and substances like anticancer drugs out of the cells.[141-143] As in the case of HeLa, **5** exhibits an LC_{50}^{*} value in the low micromolar range (19 ± 4 μM) with an increase in phototoxicity for COLO-316, OVCAR-8 and NCI/ADR-RES of 7.9, 7.2 and 17.7-fold respectively. It is worth noting that compound **4** exhibits good toxicity upon irradiation under the experimental conditions (2 h incubation + 1 h irradiation, LC_{50}^{*} = 5 ± 2 μM), with a PI of 8.2 which is even higher than that of compound **5**. The toxicity of compound **5** against the cell lines studied exceeds that of the FDA approved drug cisplatin and it also exhibits higher PI indices than Photofrin® (PI = 5.5)[76] as observed in **Table 2.6**. The greater toxicity of **5** in comparison to its congeners may be ascribed to the ability of the compound to generate reactive oxygen species upon irradiation as in the case of $[Rh_2(O_2CCH_3)_2(dppn)_2]^{2+}$ (Φ^1O_2 = 40 %) and subsequent photo-oxidation of membrane phospholipids as in the case of hematoporphyrin.[144-146]

Sytox Green® Staining: Effects of Light on Cell Health

In order to monitor the effects of compound **5** in cell morphology in the dark and upon irradiation confocal microscopy was utilized. The fluorescent probe Sytox Green® was utilized to stain dead cells. Sytox Green® is an impermeant fluorescent dye that translocates inside the cells once the plasma membrane has been compromised.[147] Once inside the cell, Sytox Green® intercalates nuclear DNA and shows a fluorescent response. Two plates of HeLa cells were incubated with compound **5** (11 ± 4 μM) for 2 h in the dark and one of them was irradiated for 1 h (λ > 400 nm) after incubation with the compound

in the dark. The experiment in the dark does not exhibit green fluorescent indicating that the cells were healthy under the experimental conditions as in the case of the dark control with no compound (**Figure 2.13a-b**). In contrast, after irradiation, the Sytox Green® staining can be detected and also a dramatic change in morphology is observed. Healthy cells show elongated structures, while cell membrane shrinkage and loss of membrane asymmetry is observed when **5** is followed by irradiation (**Figure 2.13c**). The irradiation alone is not harming the cells as can be observed from the data in **Figure 2.13d** where the cells were incubated in the dark for 2 h in the absence of compound followed by 1 h irradiation. The concentration (LC_{50}^{*}), incubation time (2 h) in combination with irradiation poses **5** as an excellent prospect for photochemotherapeutic applications.

Annexin V-FITC and Propidium Iodide Staining

Apoptosis or programmed cell death (PCD) is characterized by the activation of cysteine proteases (caspases), caspase mediated morphological changes (cell shrinkage, chromatin condensation, membrane blebbing, etc.) or caspase-independent pathways.[148] PCD is the best mechanism that the cell has to counteract tumor growth and most chemotherapeutic agents today work by triggering apoptosis via caspase dependent or independent pathways.[42] One key aspect of the apoptotic mediated cell death is the molecular changes induced during this process, specifically the exposure of phosphatidyl serine (PS) on the surface of the plasma membrane. The exposure of PS is used to detect apoptotic events, Annexin-V binds reversibly to the PS in the outer leaflet of the cell membrane and triggers a fluorescent response. Annexin V-FITC is used in combination

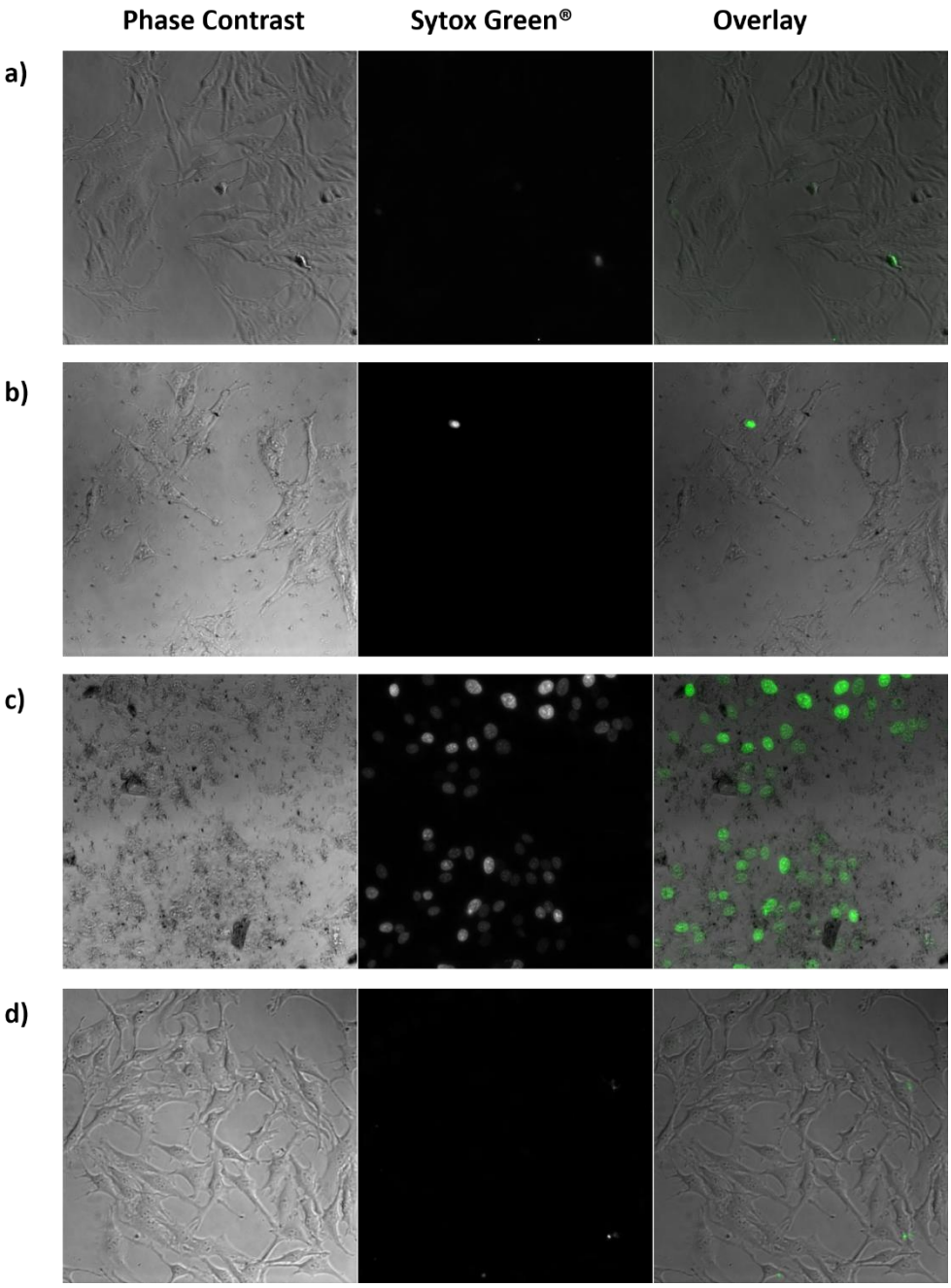

Figure 2.13 Confocal microscopy images of HeLa cells treated with a) no compound in the dark, b) 11 μM solutions of **5** for 2 h in the dark, c) 11 μM solutions of **5** for 2 h in the dark followed by irradiation for 1 h and d) no compound incubated for 2 h in the dark followed by irradiation for 1 h. The cells were treated with Sytox® Green and imaged. Left pane: phase contrast, middle pane: Sytox Green® fluorescence and right pane: overlay of phase contrast and Sytox Green® fluorescence, pseudo-colored green.

with the nuclear stain propidium iodide (PI). PI is impermeable to live cells, but once the cell integrity has been compromised it binds to nuclear DNA and there is a 20-fold increase in fluorescence.[149-150]

In order to determine the type of cell death induced by compounds **2-5**, NIC-ADR/RES cells were incubated with the compounds at their LC_{50}^{*} values in the dark for 2 h followed by irradiation for 10 min ($\lambda > 400$ nm). After treatment with the compounds, the cells were incubated with Annexin V-FITC and PI for 15 min. A control experiment was also performed wherein the cells were incubated with no compound and with staurosporine (5 μM) an apoptosis inducer (**Figure 2.14a and f**).[151] Compound **2** exhibits mostly green fluorescence and cell shrinkage can be observed, characteristic of an apoptotic death. In the case of compounds **3-5** the mechanism of cell death is not as evident - symmetric cell shrinking or nuclear fragmentation is observed. For compounds **3** and **4**, Annexin V and PI staining is observed but no cell symmetry is observed; this is most evident in **4**. Compound **5** exhibits membrane blebbing which is characteristic of an apoptotic mediated cell death, but the cell morphology is more characteristic of a necrotic type of cell death (**Figure 2.14f**). The time scale of the death induced by these compounds is too short (~10 min) for it to be apoptosis. Necrosis is characterized by the vacuolization of the cytoplasm, loss of membrane integrity and cellular swelling,[102]and this processes is observed with **5** along with membrane blebbing. These findings may suggest that the cell death mechanism may be a combination of apoptosis and a type of necrosis that has been recently identified in the literature as secondary necrosis. In secondary necrosis, in late stages of apoptosis, the dead cells may present necrotic features.[104] Another possibility

is that these compounds are causing endosomal lysis induced by irradiation which releases Ca^{2+} into the cytosol which in turns causes cell death. Porphyrin compounds have been widely used as PDT agents because upon light activation they can generate singlet oxygen. The generation of $^1O_2$ in cells by the porphyrins causes the release of endocytic vesicle contents casing cell death.[101] The compound $[Rh_2(O_2CCH_3)(dppn)_2]^{2+}$ had been previously studied in our laboratories for its anticancer activity upon irradiation and this compound can generate $^1O_2$ ($\Phi = 0.4$)[88], therefore it would be expected that **5** behaved in a similar fashion.

JC-1 Mitochondrial Potential Assay

Positively charged lipophilic cations have the ability to localize in the mitochondria due to the negative charge that this organelle bears in its membrane.[152-153] High lipophilicity decreases the desolvation energy required to penetrate the membrane and makes it easier to penetrate the mitochondrial membrane.[154-155] In this vein many efforts have been devoted to the development of organelle specific therapies against cancer and other malignancies and they are referred as "mitocans".[156-157]

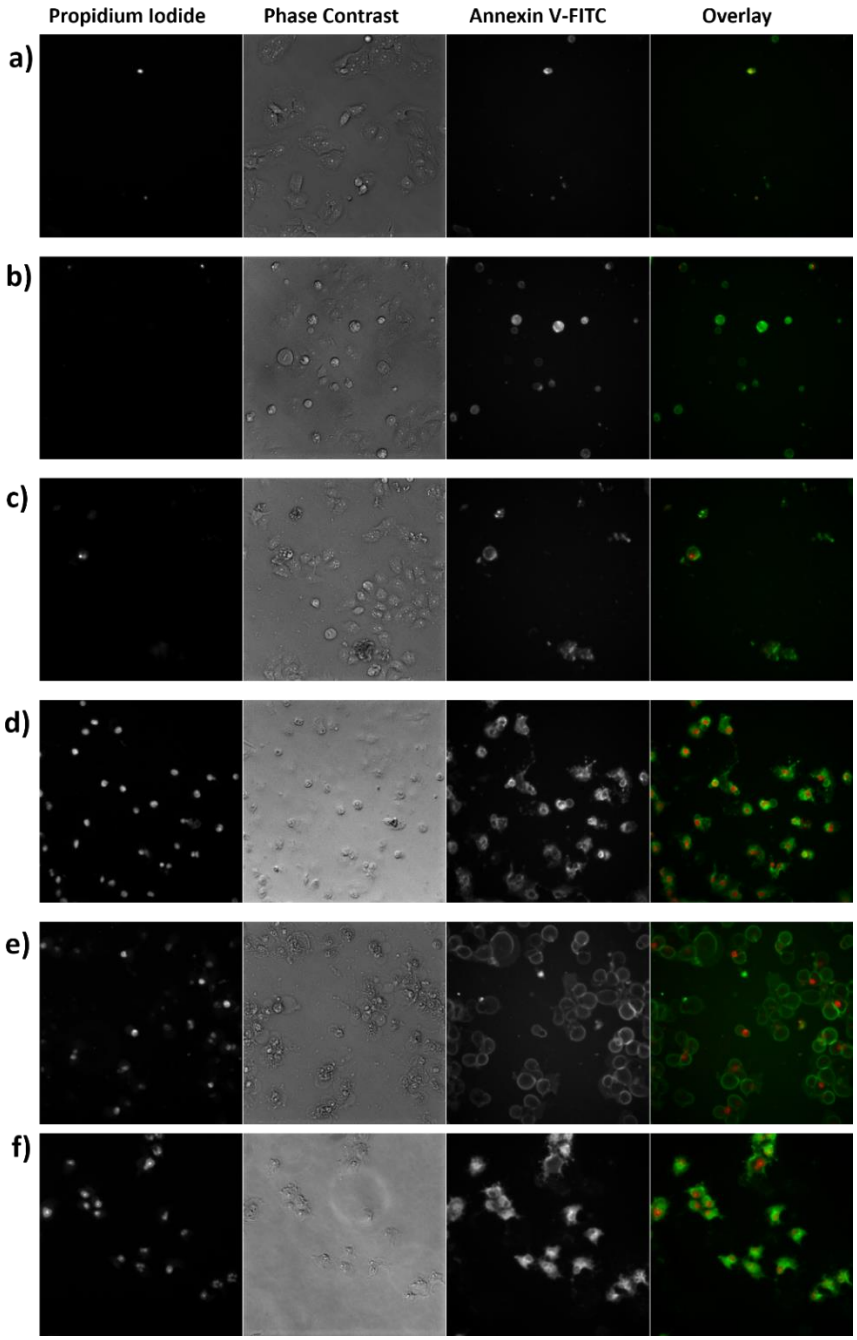

Figure 2.14 Confocal microscopy images of NCI-ADR/RES cells treated with a) no compound, b) **2**, c) **3** d) **4** e) **5** f) staurosporine for 2 h in the dark followed by irradiation for 10 min. The cells were treated with Annexin V-FITC and PI and imaged. **Left:** red fluorescence. **Center:** phase contrast. **Right:** green fluorescence. **Far right:** overlay of red and green fluorescence (pseudo-colored) images.

Recent studies indicate that fatty acid inhibitors (FAS-I) and vitamin E analogs exhibit excellent anticancer properties by preventing fatty acid synthesis or targeting the mitochondria in tumor cells. One example of this type of compound is Orlistat a FAS-I which is an FDA approved drug that is highly lipophilic and inhibits tumor growth in different types of cancer.[158] Another approach is the synthesis of metal complexes which are highly lipophilic and bear a positive charge in order to target this organelle, like the new family of dirhodium compounds **2-5**.

Reports have shown that accumulation of foreign substances in the mitochondria induces changes in the mitochondrial potential and the same observation has been made about some cancer drugs.[153] In order to monitor the changes in mitochondrial potential induced by compounds **2-5**, JC-1 (carbonyl cyanide 3-chlorophenylhydrazone) dye was utilized. The cationic dye JC-1, is a lipophilic compound that changes fluorescence emission from red to green, when there mitochondrial potential ($\Delta\Psi$) is depleted (**Figure 2.15**).[159] In healthy cells the fluorescence emission of JC-1 would be red (J-aggregates), cells whose mitochondria has been compromised show green fluorescence (J-monomers) which is an indication of decreased $\Delta\Psi$.

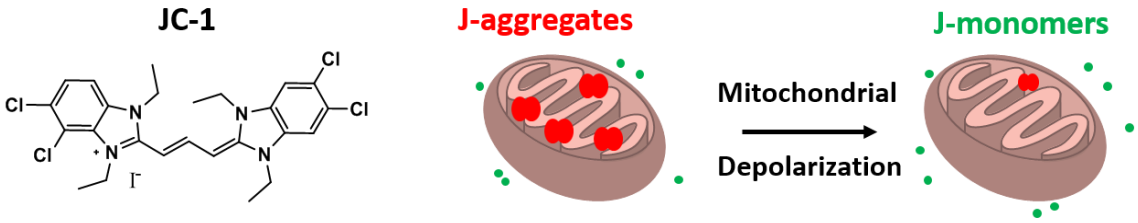

Figure 2.15 Schematic representation of mitochondrial depolarization and changes in fluorescence by JC-1.

Two independent experiments were performed with HeLa cells; the cells were incubated with compound **5** (11 μM) for 2 h in the dark and then stained with JC-1. The second experiment involved irradiation for 1 h after incubation with **5**. The cells incubated in the dark exhibit both red and green fluorescence after incubation with **5** in the dark. On the other hand, a significant decrease in red fluorescence and increase in green fluorescence is observed indicating depolarization of the mitochondria (**Figure 2.16**).

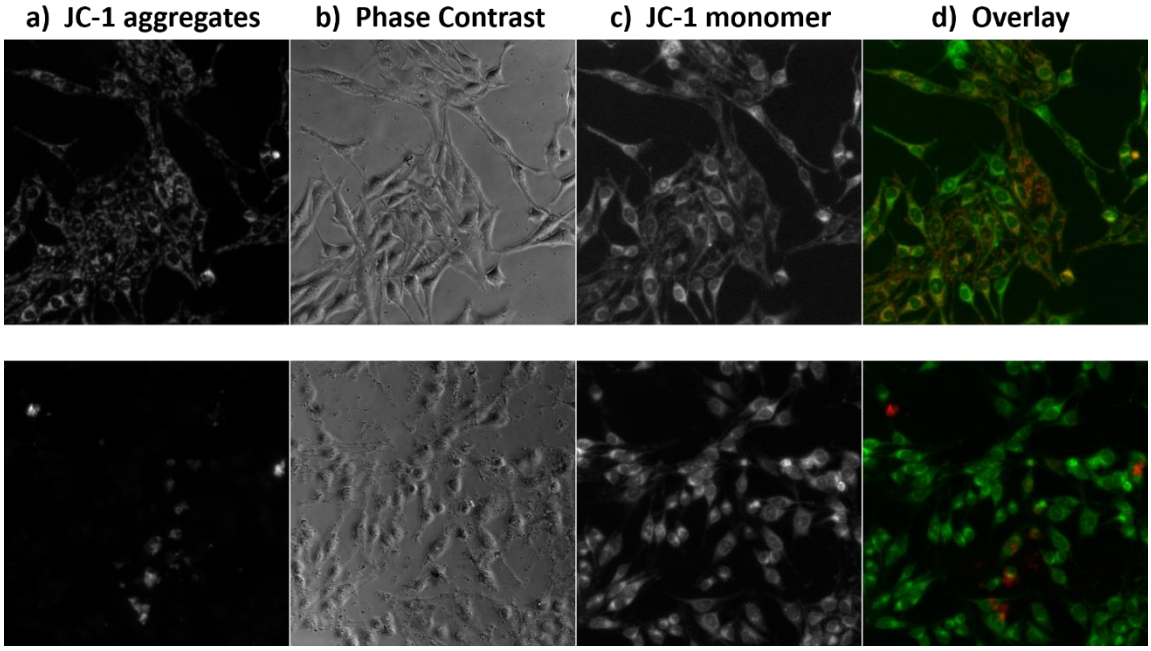

Figure 2.16 Confocal microscopy images of HeLa cells treated with 11 μM solutions of **5** for 2h in the dark followed by JC-1 staining (top panel) and irradiation experiment (bottom panel). a) Red fluorescence, b) phase contrast, c) green fluorescence and d) overlay of red and green fluorescence (pseudo-colored) images.

The same experiment was repeated with the drug resistant cells NIC-ADR/RES for compounds **2-5**, but the irradiation step was carried out for just 10 minutes. In addition, a positive control was performed with CCCP (carbonyl cyanide m-chlorophenylhydrazone) which is an inhibitor of oxidative phosphorylation that causes mitochondrial potential depletion (**Figure 2.17f**).[160] Compounds **2-5** show different degrees of mitochondrial depolarization as in the case of the positive control and most of the fluorescence observed for these compounds is green. Compound **2**, being the least cytotoxic one, shows mitochondrial potential depletion to a lesser extent while in **5** is more evident (**Figure 2.17b and e**). Even though the mitochondrial potential is depleted in each case, it is possible that the depletion in mitochondrial potential is triggered by the endosomal release of Ca^{2+} caused by our compounds upon irradiation which causes Ca^{2+} overload in the mitochondria. In order to prove this hypothesis more experiments need to be carried out, such as inhibiting PARP-1 or depleting the cell from Ca^{2+} in order to study its effect on cell viability and death mechanisms.[102-104,161]

Mitotracker Green & Sytox Blue®

The mitochondria are responsible for cell respiration and energy production in the cell and it is susceptible to oxidative damage. The accumulation of oxidative damage by the mitochondria is a contributing factor to mitochondrial dysfunction, disease and cell death.[162-163] The mitochondria are characterized by elongated tubules that form dynamic interconnecting networks; when mitochondrial health is compromised so is the morpho-

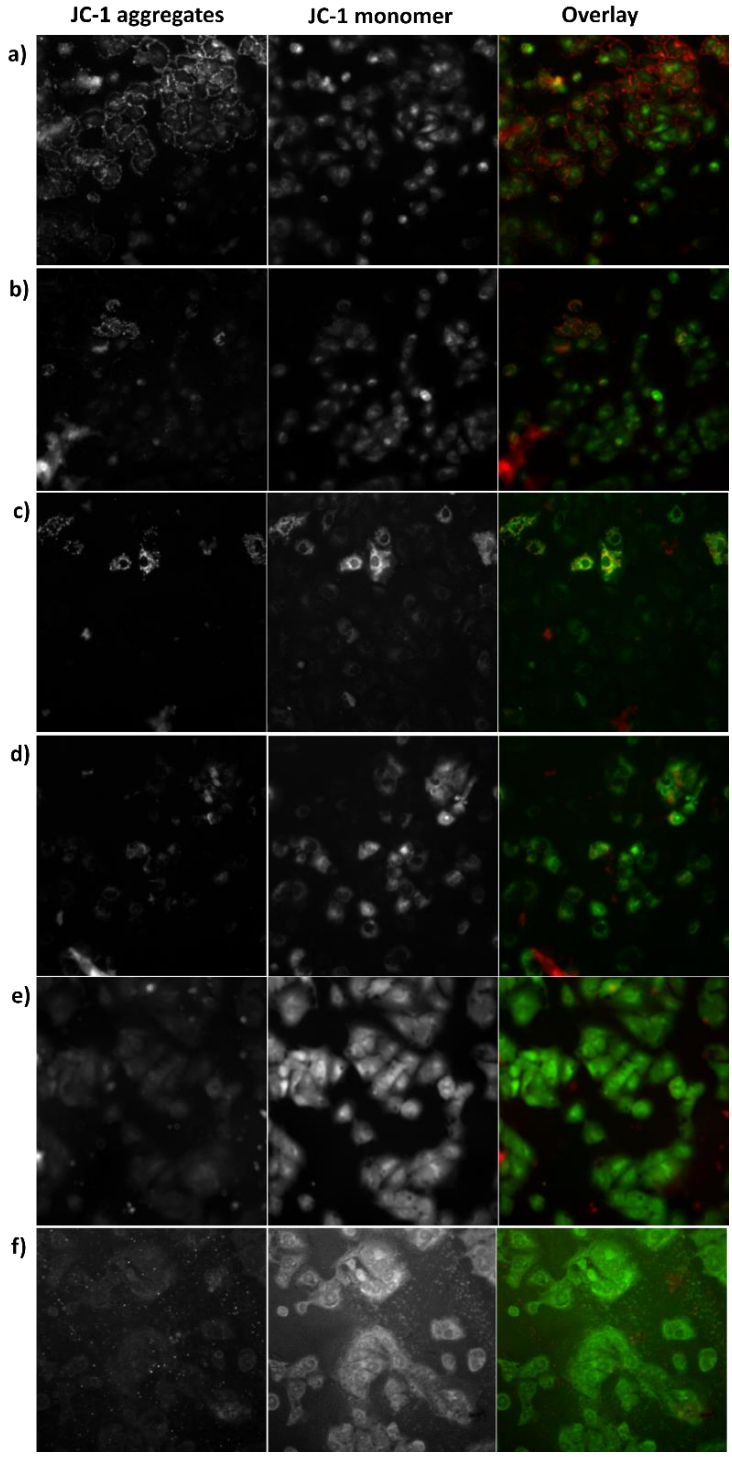

Figure 2.17 Confocal microscopy images of NCI-ADR/RES cells treated with a) no compound, b) **2**, c) **3** d) **4** e) **5** f) CCCP for 2 h in the dark followed by irradiation for 10 min. The cells were treated with JC-1 and imaged. **Left:** red fluorescence. **Center:** green fluorescence. **Right:** overlay of red and green fluorescence (pseudo-colored) images.

logy.[164] Monitoring the morphology of the mitochondria after the treatment of cells with anticancer agents can provide another piece of evidence about the effects of compound **5** on the cell. Mitotracker selectively binds to the mitochondria providing an easy avenue to monitor the morphology of the mitochondria after incubation with compound **5**. HeLa cells were treated with compound **5** for 2 h in the dark followed by treatment with Mitotracker green and Sytox Blue®. After incubation with **5**, the mitochondria still look healthy with the characteristic filamentous extended network as seen for the control (**Figure 2.18**). The cells were then irradiated for 8 min with the microscope and after this time the mitochondria had fragmented which was not observed with the negative control that had been irradiated. Also Sytox Blue® staining did not show up until 45 min after the cells were irradiated and cell shrinkage and chromatin condensation can be observed. These findings in combination with the JC-1 assay suggest that compound **5** may disrupt mitochondrial function thus triggering cell death.

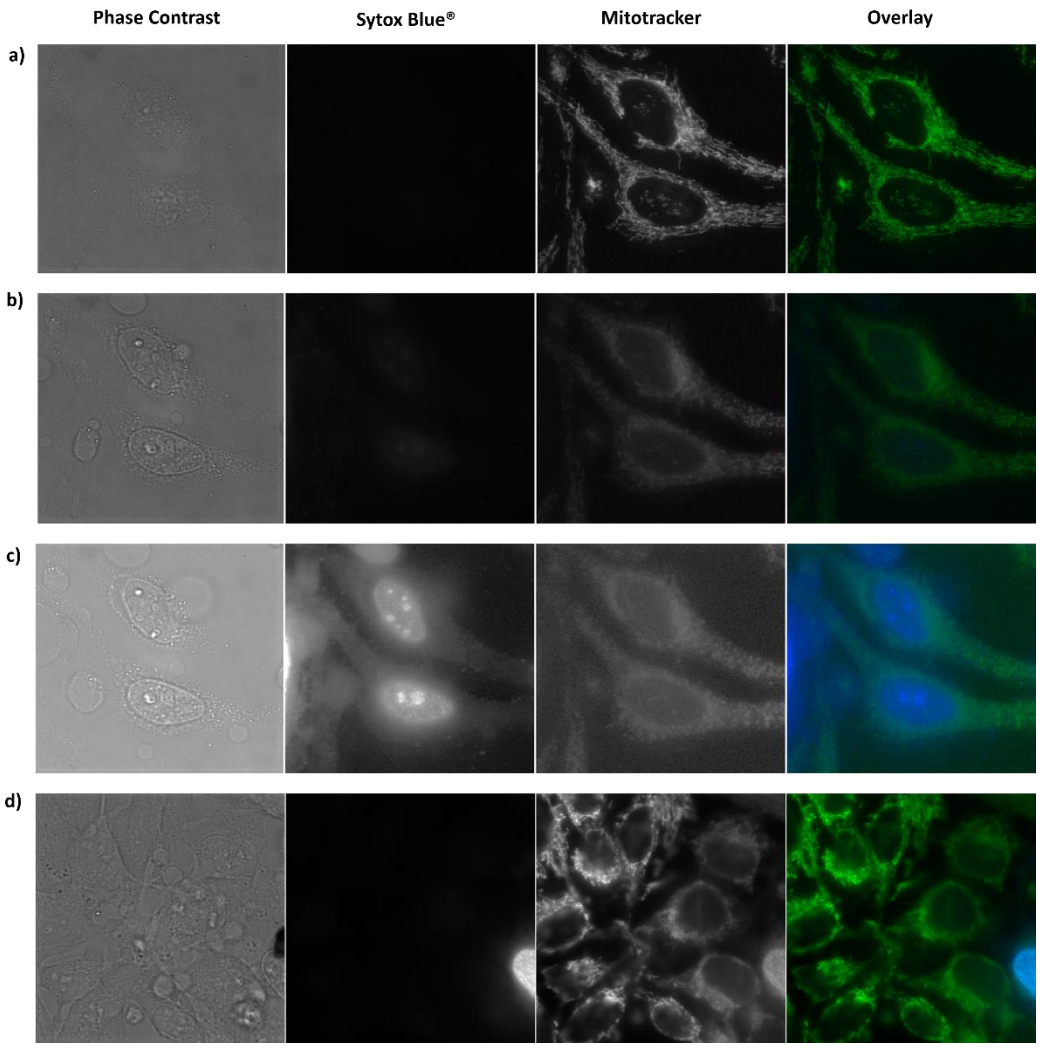

Figure 2.18 Confocal microscopy images of HeLa cells treated with 11μM solutions of **5.** a) **5** in the dark , b) **5** after 8 min irradiation, c) **5** after 45 min of treatment d) no compound after irradiation for 8 min. The cells were treated with Mytotracker and Sytox Blue® and imaged. **Left:** phase contrast. **Center:** blue fluorescence. **Right:** green fluorescence **Far right:** overlay of red and green fluorescence (pseudo-colored) images.

Concluding Remarks

A new family of dirhodium mixed bridging ligand compounds bearing electron accepting ligands phen, dpq, dppz and dppn was successfully synthesized and characterized and their anticancer activities against HeLa and ovarian cancer cell lines were evaluated. The DFT studies showed that the HOMO for compounds **2-4** is mostly $[F_2form]^-$ and the LUMO is diimine ligand in character, for which LLCT bands are observed between 415-440 nm in their electronic absorption spectra. The cell viability data show that compound **5** is most active against HeLa and NCI-ADR/RES, while **4** is most active against OVCAR-8 upon irradiation. The mechanism of cell death for this new series of compounds is not conclusive but it appears that compound **2** induces apoptotic cell death whereas compounds **3-5** trigger two different responses, namely dramatic cell morphology changes and Annexin V staining. These findings suggest that a combination apoptotic and necrotic cell death mechanisms are being triggered. The studies performed in this project provide insight into how changing the bridging ligand dramatically changes their anticancer activity and mechanisms of cell death and can help guide us in our quest to modulate the structure of dirhodium compounds in order to target preferential mechanisms of cell death.

CHAPTER III

MIXED-BRIDGING LIGAND PARTIALLY SOLVATED DIRHODIUM COMPOUNDS AS POTENTIAL ANTICANCER DRUGS

Introduction

The discovery of cisplatin as an anticancer drug by Barnett Rosenberg in the mid 1960's unveiled a new area of metal based treatments against cancer and other malignancies.[165] Although cisplatin is still widely used as a chemotherapeutic agent, new derivatives have been prepared and approved by the FDA to treat drug resistant tumors including oxaliplatin and carboplatin.[166] Other compounds are currently in the pipeline for approval; these include the Ru(III) based NAMI-A compound ([H_2im][*trans*-$RuCl_4$(S-dmso)-(Him)]; Him = imidazole, dmso = dimethyl sulfoxide) and KP1019 ([H_2ind][*trans*-$RuCl_4(Hind)_2$]; Hind = indazole) both of which are in phase II clinical trials with the latter being studied as a colorectal anticancer drug.[167] These metal complexes are just a handful of examples that mark the progress of the bioinorganic medicinal chemistry field in therapeutic applications. Among the known anticancer active compounds are dirhodium (II,II) based compounds including $Rh_2(O_2CCH_3)_4$, the mixed-bridging ligand compound *cis*-$[Rh_2(DTolF)_2(O_2CCF_3)_2 \bullet {}_2H_2O$ (DTolF= p-ditolylformamidinate), and $[Rh_2(O_2CCH_3)_3[(C_6H_3\text{-}2\text{-}O)P(C_6H_3\text{-}2\text{-}OMe)_2](HOAc)]$ which exhibit carcinostatic activity against mice bearing Ehrlich ascites tumors, Yoshida ascites sarcoma and oral carcinoma, bladder cancer, colon adenocarcinoma and breast cancer, respectively.[97,168-169] The mixed-bridging ligand compounds *cis*-$[Rh_2(DTolF)_2(O_2CCF_3)_2 \bullet {}_2H_2O$ and

$[Rh_2(O_2CCH_3)_3[(C_6H_3\text{-}2\text{-}O)P(C_6H_3\text{-}2\text{-}OMe)_2](HOAc)]$ have shown the most promise with anticancer activities similar to that of cisplatin but with an increased average life span in mice being treated with the drug.

In our laboratories, we are striving to develop dirhodium based anticancer agents that can be activated with low energy light for photodynamic therapy (PDT) applications. One avenue for this is the development of partially solvated compounds as example of which is $[Rh_2(\mu\text{-}O_2CCH_3)_2(CH_3CN)_6]^{+2}$, reported by Turro et *al.*[77] which covalently binds to biologically relevant molecules upon irradiation and loss of some of the acetonitrile ligands. Additional examples of this type of compound have been studied in our laboratories over the past decade.[77,79-81,170] Modifying the ligands around the rhodium centers at axial and equatorial positions offers a variety of possible binding sites for reactions with biomolecules in order to enhance the anticancer properties. Considering the anticancer activity exhibited by the mixed-bridge carboxylate compounds it is our aim to prepare partially solvated dirhodium mixed-bridging ligand compounds that combine the anticancer activity of the mixed-bridge carboxylates with that of the photocisplatin analog $[Rh_2(\mu\text{-}O_2CCH_3)_2(CH_3CN)_6]^{+2}$.

The present work focuses on the synthesis, characterization and anticancer evaluation of a new family of dirhodium mixed-bridging ligand partially solvated compounds of the type $[Rh_2(\mu\text{-o-}F_2form)(\mu\text{-}O_2CCH_3)(CH_3CN)_6](BF_4)_2$ and $[Rh_2(\mu\text{-}Ph_2P(C_6H_4))(\mu\text{-}O_2CCH_3)(CH_3CN)_6](BF_4)_2$. The full characterization and the anticancer properties of these compounds will be discussed in the following sections.

Experimental Section

Starting Materials

The compound $Rh_2(\mu\text{-}O_2CCH_3)_4\bullet 2CH_3OH$ was either purchased from Pressure Chemicals or synthesized from $RhCl_3\bullet xH_2O$ from a reported procedure.[108] The compounds *N,N'*-bis(2,6-difluorophenyl)formamidine (HF_2form) and $Rh_2((C_6H_5)_2P(C_6H_4))(O_2CCH_3)_3\bullet 2O_2CCH_3$ were synthesized by slightly modified published procedures.[109,171] The commercially available reagents potassium tertbutoxide (K^tBuO) (Sigma Aldrich), triphenylphosphine (PPh_3) (Sigma Aldrich), triethyloxonium tetrafluoroborate (Et_3OBF_4), 1M in CH_2Cl_2 (TCI America) were used as purchased. The solvents acetonitrile (CH_3CN), acetone, hexanes (hex), dichloromethane (CH_2Cl_2), and diethyl ether (Et_2O) were of ACS grade and used as received. Standard Schlenk-line techniques under a N_2 atmosphere were used but work-up and isolation of products was performed in air unless otherwise stated.

Cell culture reagents Dubelco's modified Eagle medium (DMEM) (Invitrogen), fetal bovine serum (FBS) (Atlanta Biologicals), Leibovitz's L-15 Medium (L-15) without phenol red (Life Technologies), Phosphate-Buffered Saline solution (DPBS) (Life Technologies), Sytox Green® (Invitrogen) and Hoechst 33342 (Invitrogen) were used as received. The HeLa cell line was obtained from the American Type Culture Collection, cell line CCL-2.

Preparation of $[Rh_2(\mu\text{-}o\text{-}F_2form)(\mu\text{-}O_2CCH_3)(CH_3CN)_6](BF_4)_2$ (6). An aliquot of 2 mL of Et_3OBF_4 (1M CH_2Cl_2) was added to 30 mL of an acetonitrile solution of $Rh_2(\mu$-o-

F_2form)(μ-O_2CCH_3)$_3$ (60 mg, 0.08 mmol) and the mixture was stirred at room temperature for 18 h. The maroon solution turned orange upon addition of the Et_3OBF_4. The reaction mixture was concentrated to ~3 mL and 30 mL of Et_2O was added which resulted in precipitation of the sample as an orange oil. The oil was washed three times with Et_2O and then recrystallized by slow diffusion of diethyl ether into a CH_3CN solution of the product from which X-ray quality crystals were obtained. Yield: 64 mg (84%). ^{1}H NMR (500 MHz, CD_3CN-d_3), δ (ppm): 2.02 (s, 3H, O_2CCH_3), 2.49 (s, 6H, eqCH_3CN), 2.53 (s, 6H, eqCH_3CN), 7.05 (t, 4H, o-2,6-difluorophenyl), 7.33(m, 2H, o-2,6-difluorophenyl). $C_{25}H_{25}B_2F_{12}N_7O_2Rh_2$•$3H_2O$: C, 3.43; N, 9.26; H, 3.11 %. Found: C, 3.42; N, 10.82; H, 2.71 %.

Preparation of [Rh_2(μ-$Ph_2P(C_6H_4)$)(μ-O_2CCH_3)($CH_3CN)_6$]($BF_4)_2$ (7). A 2 mL solution of Et_3OBF_4 (1M in CH_2Cl_2) was added to a brown solution of $Rh_2(Ph_2P(C_6H_4))(O_2CCH_3)_3$•$2O_2CCH_3$ (36 mg, 0.05 mmol) in CH_3CN (20 mL) which produced a color change from brown to orange. The reaction mixture was stirred for 1h at room temperature after which time the solvent was removed under reduced pressure to afford an orange oil. The orange oil was washed with copious amounts of Et_2O and the product was recovered as an orange solid. X-ray quality crystals were obtained by slow diffusion of diethyl ether into an CH_3CN solution of the product. Yield: 25 mg (51%). ^{1}H NMR (500 MHz, CD_3CN-d_3), δ (ppm): 1.64 (s, 3H, eqCH_3CN), 1.70 (s, 3H, eqCH_3CN), 1.88 (s, 3H, O_2CCH_3), 6.67 (m, 1H, bridging C_6H_4), 7.01 (m, 1H, bridging C_6H_4), 7.26

(m, 1H, bridging C_6H_4), 7.38-7.45 (m, 5H, PPh_2), 7.52-7.63 (m, 5H, PPh_2), 7.85 (q, 1H, bridging C_6H_4).

Instrumentation and Methods

Electrochemical data were collected using a HCH Electrochemical Analyzer model CH 1620A in dry CH_3CN. A BAS Pt disk working electrode, Pt wire auxiliary electrode, Ag/AgCl (3M KCl(aq)) reference electrode and 0.1 M tetra-n-butylammonium hexafluorophosphate ($[^nBu_4N][PF_6]$) as supporting electrolyte were utilized to carry out the measurements. X-ray data sets were collected for compounds **6** and **7** on a Bruker CCD APEX diffractometer with a graphite monochromated Mo Kα radiation (λ = 0.71073 Å), while **6b** X-ray data sets were collected from the APS-Argonne National Lab, beamline 15-ID-B.

Electrochemistry. The electrochemical studies were carried out at room temperature (298 K) in CH_3CN. The $E_{1/2}$ values were referenced against the Ag/AgCl electrode without correction for the junction potentials [$E_{1/2} = (E_{p,a} + E_{p,c})/2$]. Ferrocene was used as an internal standard in CH_3CN under the same experimental conditions as the compounds under study, $E_{1/2}$= 0.44 V vs Ag/AgCl for the Fc^+/Fc couple.

***In vitro* cytotoxicity.** The cell viability of HeLa cells in the presence of compounds **7** and **8** was tested using the fluorescent probe Sytox Green®. Multichannel sterile dishes were cultured with HeLa cells at a concentration of 5000-10000 cells/μL, each channel was

washed with DBPS and the medium was replaced with 200 µL of L-15 containing different concentrations of the compounds under study followed by incubation for 2h in the dark. After incubation of the compounds the second batch was irradiated inside a UV-visible photoreactor for 1 h. For each of the conditions both Hoechst (0.5 µg/mL) and Sytox Green® (1 µM) were added and incubated for 10 min in the dark on the confocal microscope's warming stage, 37 ºC before imaging.

Results and Discussion

Synthesis and Characterization

The synthesis of **6** involves the alkylation of the bridging acetate ligands of **1** with Et_3OBF_4 in dry acetonitrile, (**Figure 3.1a**). The trans influence that the $[F_2form]^-$ exerts on the *trans* acetate, ensures that the this is the second ligand to be alkylated to form the mixed bridging ligand compound and not the already known *cis*-$[Rh_2(O_2CCH_3)_2(CH_3CN)_6](BF_4)_2$.[77] The reaction mixture was stirred for 18 h at room temperature and was protected from the ambient light. The solvent was then removed *in vacuo* ~2 mL of acetonitrile was added to the red oil followed by 10 mL of diethyl ether to precipitate the product. The sample was filtered, washed with three 10 mL portions of Et_2O and dried overnight to afford **6** as a purple solid. ^1H NMR spectroscopy in CD_3CN was used to confirm the formation of **6** as a pure compound (**Figure 3.1b**). The ^1H NMR spectrum contains 4 singlet resonances in the aliphatic region at 1.98 ppm, 2.02 ppm, 2.49 ppm and 2.53 ppm which are assigned to the free CH_3CN, bridging acetate, eq CH_3CN^N *trans* to $[F_2form]^-$ and eq CH_3CN^O *trans* to the bridging acetate, respectively. In the

aromatic region the characteristic triplet resonance corresponding to the H atoms from the bridging $[F_2form]^-$ is observed at 7.05 ppm with a coupling constant of 8.4 Hz, which is slightly larger than for other dirhodium formamidinate compounds.[81,172] There is also a multiplet at δ = 7.33 ppm, which is attributed to the protons from the phenyl rings of the $[F_2form]^-$ ligand.

Compound **7** was synthesized in a similar manner as **6** (**Figure 3.2a**). The $[Rh_2(Ph_2P(C_6H_4))(O_2CCH_3)_3(CH_3CN)_2)]$ was dissolved in dry acetonitrile to afford a brown solution and treated with the alkylating which led to a color change from brown to orange. After 24 h of stirring the solvent was removed and the product was recovered from precipitation with diethyl ether and dried *in vacuo*. The purple solid recovered was characterized by ^{1}H NMR spectroscopy in D_2O (**Figure 3.2b**). Upon dissolution of **7** in D_2O the colors changes to purple which is attributed to the exchange of the axial acetonitrile ligands for the deuterated water which appears a singlet resonance at 2.06 ppm. There are three other singlet resonances at 1.72 ppm, 1.95 ppm and 2.17 ppm attributed to bridging acetate, eq CH_3CN^C *trans* to the orthometallated phenyl group of the phosphine, and the eq CH_3CN^P *trans* to the phosphorous atom from the phosphine. In the aromatic region there are four triplet resonances at 6.81 ppm, 7.06 ppm, 7.33 ppm and 7.81 ppm all of which that integrate to one proton which are due to the protons from the orthometallated phenyl ring of the phosphine. The remaining multiplet at 7.57 ppm integrates to twelve protons and has been assigned to the remaining phenyl rings of the phosphine.

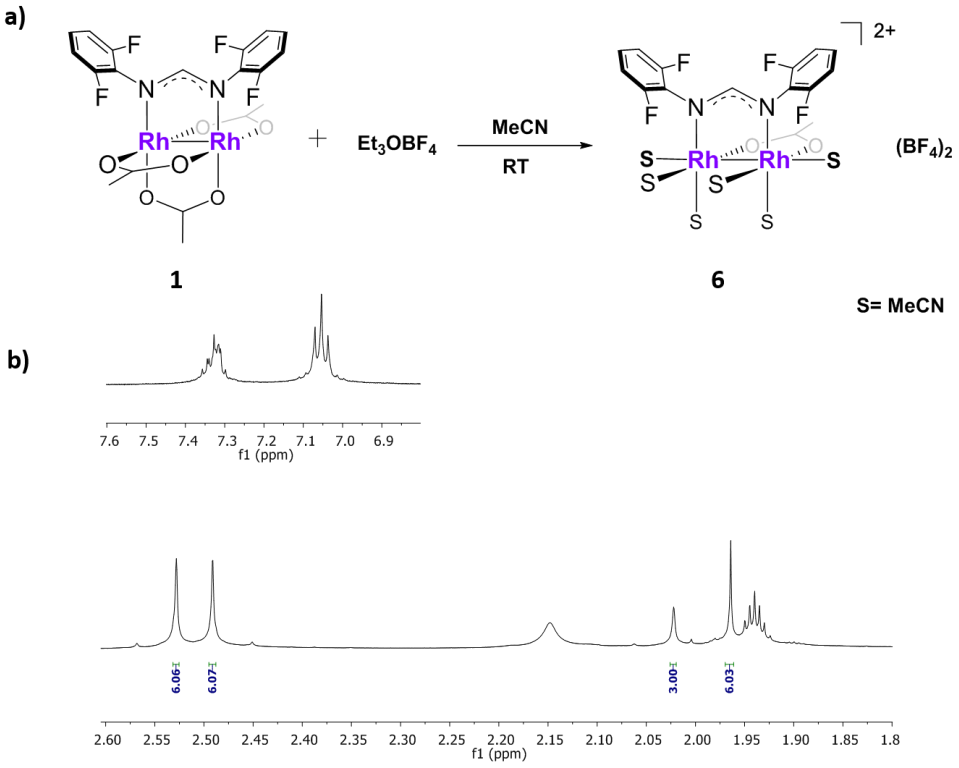

Figure 3.1 **a)** Synthetic scheme for the formation of **6** and **b)** ^{1}H NMR spectrum of **6** in CD_3CN.

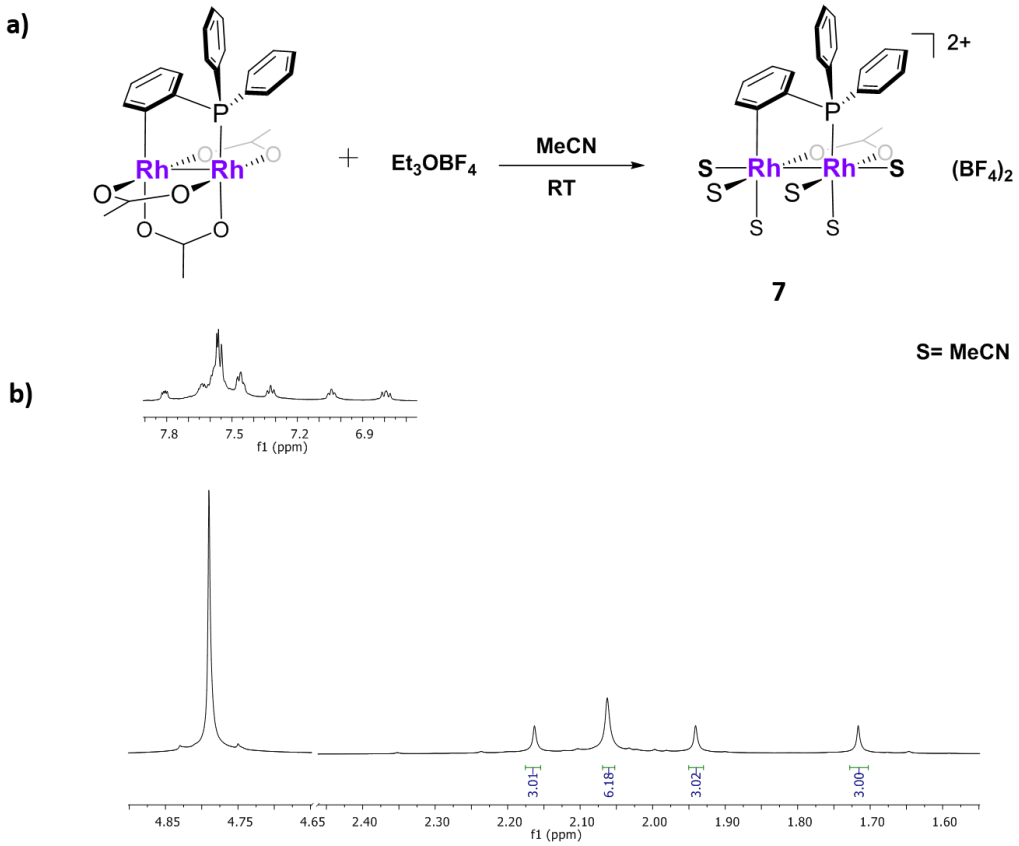

Figure 3.2 a) Synthetic scheme for the formation of **7** and **b)** ^{1}H NMR spectrum of **7** in D_2O.

X-ray Crystallography

Crystal data and structure refinement for compounds **6**, **6b** and **7** are summarized in

Table 3.1.

[Rh$_2$(μ-o-F$_2$form)(μ-O$_2$CCH$_3$)(CH$_3$CN)$_6$](BF$_4$)$_2$ (6). The mixed bridging compound **6** crystalizes in the monoclinic space group P2$_1$/c. The cation in **6** contains one acetate and one [F$_2$form]$^-$ bridging the dirhodium core. There are six acetonitrile ligands completing

the pseudo-octahedral coordination sphere around the dirhodium (II,II) core (**Figure 3.3**). The Rh-Rh bond distance is 2.5575(2) Å, which is comparable to other dirhodium partially solvated formamidinate complexes such as $[Rh_2[DTolF]_2(CH_3CN)_6]^{2+}$, $[Rh_2[F\text{-}form]_2(CH_3CN)_6]^{2+}$, and the lantern compound $Rh_2[DTolF]]_2(O_2CCF_3)_2$.[81,173] The Rh-N from the eq CH_3CN *trans* to the $[F_2form]^-$ bond distances are in the range of 1.840(2)-1.875(1) Å and are comparable to similar complexes (**Table 3.2**). On the other hand the Rh-N bond distances for the eq CH_3CN ligands *trans* to the acetate are between 2.408(2) Å and 2.436(2) Å, which is ~0.44 Å longer than that of the $Rh_2(O_2CCH_3)_2(CH_3CN)_6]^{2+}$.[174]

[Rh$_2$(μ-o-F$_2$form)(μ-O$_2$CCH$_3$)(CH$_3$CN)$_6$](BF$_4$)$_2$ (6b). The formation of this complex results from the poor stability of **6** in solution, crystals of **6b** were obtained from the slow diffusion of ether into an acetonitrile solution of **6** at room temperature. The cationic unit for compound **6b** crystalizes in a P-1 triclinic space group with two independent dirhodium units in the asymmetric unit and four outer-sphere $[BF_4]^-$ (**Figure 3.4**). The dirhodium (II,II) core is supported by one $[F_2form]^-$ and there are eight CH_3CN ligands occupying the remaining coordination sites. The Rh-Rh bond length is 2.58 Å, slightly longer than that of **6**, the $[F_2form]^-$ is twisted by 30.2(6)º from the eclipsed conformation. The eq CH_3CN ligands are also twisted from the ideal eclipsed conformation by 33.3(7)º, the splaying of the eq CH_3CN ligands has also been observed in other formamidinate compounds like $[Ir_2(DTolF)_2(CH_3CN)_6][BF_4]_2$[175], $[Rh_2(DTolF)_2(CH_3CN)_6][BF_4]_2$ and $[Rh_2(F\text{-}form)_2(CH_3CN)_6][BF_4]_2$,[81] but to a lesser extent. The Rh-N (eq CH_3CN) bond distances are in the range of 1.971-2.038 Å, which are in agreement with those of **6** and

$[Rh_2(F\text{-form})_2(CH_3CN)_6][BF_4]_2$.[81] The crystal structure of **6** showed that the Rh-O bond distances were 2.424(1) Å and 2.468(1) Å, remarkably long, the acetate group becomes labile to form **6b**.

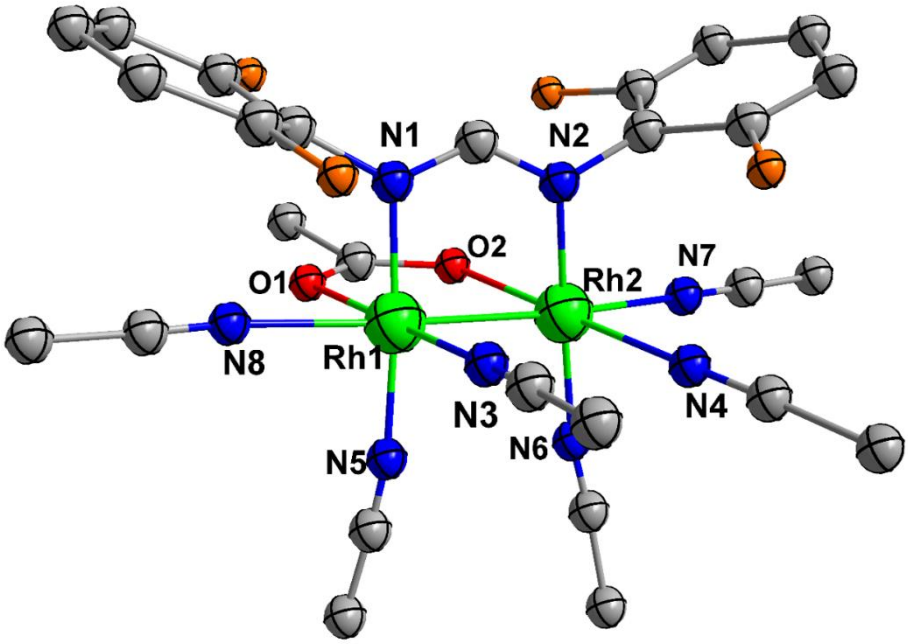

Figure 3.3 Thermal ellipsoid plot for the cationic unit **6** at the 50% probability level. The hydrogen atoms and counter ions have been omitted for the sake of clarity.

Table 3.1 Crystal and structural refinement data for **6** and **7**.

	6	**6b**	**7 • 2CH$_3$CN**
Empirical formula	$C_{29}H_{30}B_2ClF_{12}N_9O_2Rh_2$	$C_{29}H_{31}B_4F_{16}N_{10}Rh_2$	$C_{35.5}H_{38.75}B_2F_8N_{6.25}O_2PRh_2$
Formula weight (g/mol)	992.06	1072.7	995.39
Crystal system	monoclinic	triclinic	monoclinic
Crystal description, color	orange needle	red needle	orange plate
Space group	$P2_1/c$	P-1	$P2_1/n$
a, b, c/Å	15.204(3), 13.329(3), 22.242(4)	12.3599(18), 17.283(3), 19.791(3)	14.359(6), 13.513(5), 21.968(8)
α, β, γ /°	90, 90.98(3), 90	100.345(3), 95.826(3), 100.300(3)	90,707(5), 90
Volume/Å^3	4506.6(16)	4052.8(10)	4262(3)
Z	4	4	4
ρcalcg/cm^3	1.462	1.74	1.551
2Θ range for data collection/°	2.68 to 52.602	1.228 to 20.186	3.37 to 50.776
Independent reflections	6119 [R_{int} = 0.2261, R_σ = 0.1468]	4922 [R_{int} = 0.1527, R_σ = 0.0803]	7796 [R_{int} = 0.0567, R_σ = 0.0424]
Data/restraints/parameters	6119/3/256	4922/40/533	7796/3/527
Goodness-of-fit on F2	1.148	1.035	1.041
Final R indexes [I>=2σ (I)]	R_1 = 0.1245, wR_2 = 0.3165	R_1 = 0.0678, wR_2 = 0.1345	R_1 = 0.0484, wR_2 = 0.1235
Final R indexes [all data]	R_1 = 0.1950, wR_2 = 0.3558	R_1 = 0.1086, wR_2 = 0.1550	R_1 = 0.0642, wR_2 = 0.1348

[a] $R = \sum \big| |F_o| - |F_c| \big| / \sum |F_o|$. [b] $wR = \{\sum[w(F_o^2 - F_c^2)^2] / \sum w(F_o^2)^2]\}^{1/2}$. [c] Goodness-of-fit = $\{\sum[w(F_o^2 - F_c^2)^2]/(n-p)\}^{1/2}$, where n is the number of reflections and p is the total number of parameters refined.

Table 3.2 Summary of important bond distances in **6**.

Compound	Rh-Rh (Å)	Rh-L_{ax} (Å)	Rh-L_{eq} (Å)[a,c]	Rh-N (Å)	Rh-O (Å)
6	2.5575(2)	2.244(2), 2.164(2)[a]	1.840(2), 1.875(1), 2.408(2), 2.436(2)	1.852(2), 1.864(2)	2.424(1), 2.468(1)
$[Rh_2[DTolF]_2(CH_3CN)_6]^{2+}$ [(d)]	2.5594(8)	2.208(7), 2.235(7)[a]	2.020(6), 2.029(7)	2.026(6), 2.037(6)	-
$[Rh_2[F\text{-form}]_2(CH_3CN)_6]^{2+}$ [(d)]	2.571(1)	2.195(4), 2.251(4)[a]	2.032(5), 2.040(5)	2.038(5), 2.046(5)	-
$Rh_2[DTolF]]_2(O_2CCF_3)_2$ [(e)]	2.425(1)	2.311(3), 2.319(3)[b]	-	1.996(4), 1.998(4), 1.987(3), 1.990(3)	2.087(3), 2.079(3), 2.073(3), 2.092(4)

[a] L is CH_3CN. [b] Axial H_2O. [c] Axial and equatorial ligands are the same. [d] Ref. 125. [e] Ref. 126.

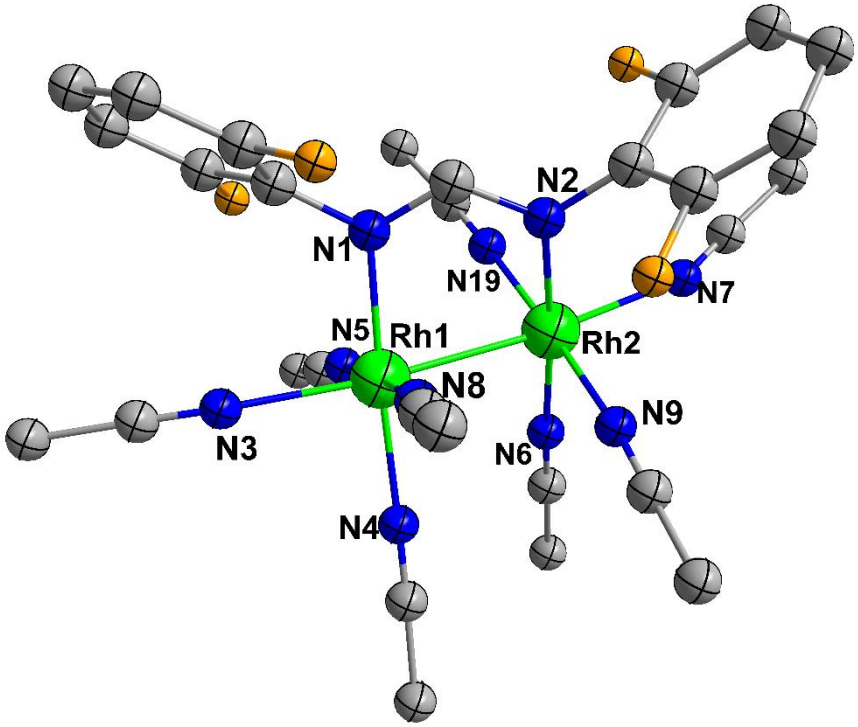

Figure 3.4 Thermal ellipsoid plot for the cationic unit **6b** at the 50% probability level. The hydrogen atoms and counter ions have been omitted for the sake of clarity.

$[Rh_2(\mu\text{-}Ph_2P(C_6H_4))(\mu\text{-}O_2CCH_3)(CH_3CN)_6](BF_4)_2$ (7). The cationic unit in **7** also crystallizes in the centrosymmetric monoclinic space group $P2_1/n$. The thermal ellipsoid plot shows that the dirhodium (II,II) core is bridged by one acetate and one orthometallated phosphine in a similar fashion to that of **6** (**Figure 3.5**). The Rh-Rh bond distance is 2.5591(9) Å, which is ~0.10 Å shorter than the $[Rh_2(\mu\text{-}Ph_2P(C_6H_4))_2(\mu\text{-}O_2CCH_3)(CH_3CN)_6](BF_4)_2$[81] and its isocyanide analogues and other dirhodium orthometallated phosphine compounds.[171] The phosphine is considerably twisted from an

eclipsed conformation, 28.88 º as the absence of a second phosphine on the dirhodium unit provides it with more flexibility which results in an increase in the Rh-Rh bond length.

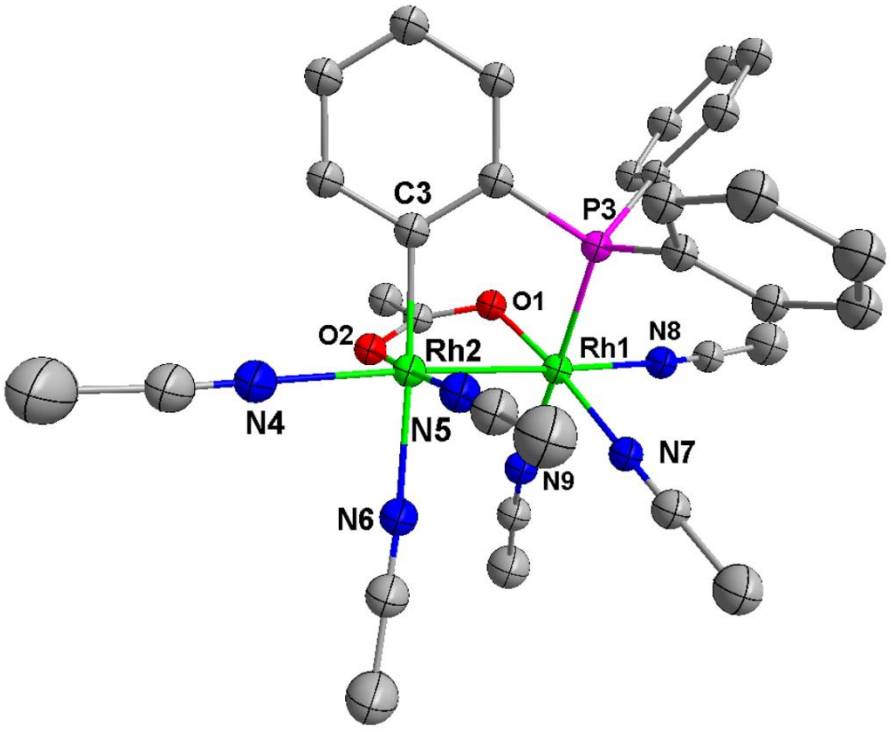

Figure 3.5 Thermal ellipsoid plot for the cationic unit **7** at the 50% probability level. The hydrogen atoms and counter ions have been omitted for the sake of clarity.

The Rh-N bond distances of the eq CH_3CN ligands that are *trans* to the acetate group are 1.980(4) Å and 1.985(4) Å which are similar to those of the $[Rh_2(O_2CCH_3)_2(CH_3CN)_6]^{2+}$ precursor (**Table 3.3**). The other two eq CH_3CN ligands *trans* to the phosphine exhibit more elongated Rh-N bond distances, 2.153(4)-2.127(4) Å which is attributed mainly to the trans influence from the phosphine since it is a good σ-donor. The Rh-C and Rh-P bond distances are comparable to those of the bis-cyclometallated compound $[Rh_2(\mu\text{-}PPh_2(C_6H_4))(\mu\text{-}O_2CCH_3)(CH_3CN)_6](BF_4)_2$.[81] The four eq CH_3CN ligands are splayed as one can see from the dihedral angles, 31.11(16)º and 30.43(18)º and are far from the ideal eclipsed conformation. Detailed bond distances and dihedral angles for compounds **6**-**7** are compiled in **Table 3.3**.

Table 3.3 Summary of important bond distances in **7**.

Compound	Rh-Rh (Å)	Rh-L_{ax} (Å)	Rh-L_{eq} (Å)[a,b]	Rh-C[c] (Å)	Rh-P (Å)	Rh-O[d] (Å)
7	2.5591(9)	2.184(5), 2.226(4)[a]	2.153(4), 2.127(4), 1.985(4), 1.980(4)	2.011(6)	2.2333(2)	2.035(4), 2.042 (3)
R-$[Rh_2[Ph_2P(C_6H_4)]_2(CH_3CN)_6]^{2+}$ [(e)]	2.656(1)	2.196(6)[a]	2.104(6), 2.142(6)	2.01(2)	2.232(7)	-
S-$[Rh_2[Ph_2P(C_6H_4)]_2(CH_3CN)_6]^{2+}$ [(e)]	2.655(1)	2.202(6)[a]	2.127(5), 2.131(5)	2.024(5)	2.228(2)	-
$Rh_2[Ph_2P(C_6H_4)]_2(O_2CCH_3)_2$ [(f)]	2.508(1)	2.342(5)	-	1.996(6)	2.210(2)	2.136(4), 2.190(4)
$Rh_2[Ph_2P(C_6H_4)]_1(O_2CCH_3)_3$ [(g)]	2.430(2)	2.336(4), 2.301(4)	-	1.999(5)	2.206(2)	2.025(4), 2.034(4), 2.218(4), 2.163(3)
$Rh_2(O_2CCH_3)_2(CH_3CN)_6$ [(h)]	2.534(1)	2.232(4)[a]	1.985(4), 1.980(3)	-	-	2.017(3), 2.012(3)

[a] L is CH_3CN. [b] Axial and equatorial ligands are the same. [c] C atoms from the orthometallated phosphine. [d] O atoms from the bridging acetate groups. [e] Ref. 81. [f] Ref. 171. [g] Ref. 109. [h] Ref. 174.

Table 3.4 Relevant bond distances and dihedral angles for compounds **6**-**7**.

6		**6b**		**7**	
Bond Distances	**Length/Å**	**Bond Distances**	**Length/Å**	**Bond Distances**	**Length/Å**
Rh1-Rh2	2.5575(2)	Rh1-Rh2	2.581(2)	Rh1-Rh2	2.5591(9)
Rh1-O1	2.424(1)	Rh1-N1	2.021(14)	Rh1-O1	2.035(4)
Rh2-O2	2.468(1)	Rh1-N3	2.169(17)	Rh2-O2	2.042(3)
Rh1-N1	1.852(2)	Rh1-N4	2.038(17)	Rh2-C3	2.011(6)
Rh2-N2	1.864(2)	Rh1-N5	1.971(17)	Rh1-P3	2.2333(2)
Rh1-N3	1.840(2)	Rh1-N8	2.013(19)	Rh2-N6	2.153(4)
Rh2-N4	1.875(1)			Rh1-N9	2.127(4)
Rh1-N5	2.408(2)			Rh2-N5	1.985(4)
Rh2-N6	2.436(2)			Rh1-N7	1.980(4)
Rh1-N7	2.244(2)			Rh2-N4	2.184(5)
Rh2-N8	2.164(2)			Rh1-N8	2.226(4)
Dihedral angles	**º**	**Dihedral angles**	**º**	**Dihedral angles**	**º**
N1-Rh1-Rh2-N2	-9.6(7)	N1-Rh1-Rh2-N2	27.2(6)	C3-Rh2-Rh1-P3	28.88(12)
O1-Rh1-Rh2-O2	-3.7(4)	N6-Rh2-Rh1-N4	33.3(7)	O1-Rh1-Rh2-O2	23.18(12)
N7-Rh1-Rh2-N8	-2.4(7)	N19-Rh2-Rh1-N5	37.9(6)	N6-Rh2-Rh1-N9	31.11(16)
N9-Rh1-Rh2-N10	-4.9(5)	N8-Rh1-Rh2-N9	36.2(7)	N7-Rh1-Rh2-N5	30.43(18)

Time Lapse ^{1}H NMR Spectroscopic Studies

The ^{1}H NMR spectra of compound **6** were measured in D_2O at different time intervals in the dark in order to monitor its stability in water. There are four singlet resonances in the spectrum of **6** in the aliphatic region, namely at 2.05 ppm, 2.13 ppm, 2.56 ppm and 2.58 ppm which are assigned as free CH_3CN, bridging acetate, eq CH_3CN^N and eq $CH3CN^O$ respectively. In the aromatic region one can observe the characteristic triplet resonance from the $[F_2form]^-$ bridging ligand ($^{3}J_{H\text{-}Rh}$ = 8.4 Hz) and the multiplet at 7.33 ppm. The time lapse experiment reveals how the eq $CH3CN^N$ singlet resonance at 2.56 ppm and that of the bridging acetate at 2.13 ppm decrease in intensity with time. There is also the appearance of new resonances at 2.15 ppm, 2.46 ppm and 2.63 ppm which are attributed to side products from the exchange of eq CH_3CN for D_2O which occurs upon dissolution and become more pronounced as time progresses (**Figure 3.6**).

The time lapse experiment was also performed on **7** and, in this case, the strong donating ability of the orthometallated phosphine promotes fast exchange of the *trans* eq CH_3CN ligands with D_2O in the dark. This process is monitored by the 2.06 ppm singlet resonance which integrates to twelve H with the other six H nuclei corresponding to the axial CH_3CN ligands which exchange readily in the dark with the solvent. The spectra taken over a period of 4 h indicate that the eq CH_3CN *trans* to the acetate are very stable and do not exchange during the time frame of the experiment (**Figure 3.7**).

Irradiation experiments were performed in an NMR tube located 18 inches away from a Vivitek D508 projector and spectra were collected at different time intervals. Compound **6** was irradiated for a period of 4 h and the ^{1}H NMR spectra look similar to

the time lapse experiment performed in the dark. Clearly irradiation of the sample does not aid in the exchange of the eq CH_3CN ligands for the D_2O solvent (**Figure 3.8**). The low stability of the eq CH_3CN in the dark makes this compound a poor candidate for PDT applications but it could be used as a scaffold for further functionalization due to the lability of the eq CH_3CN ligands *trans* to the $[F_2form]^-$.

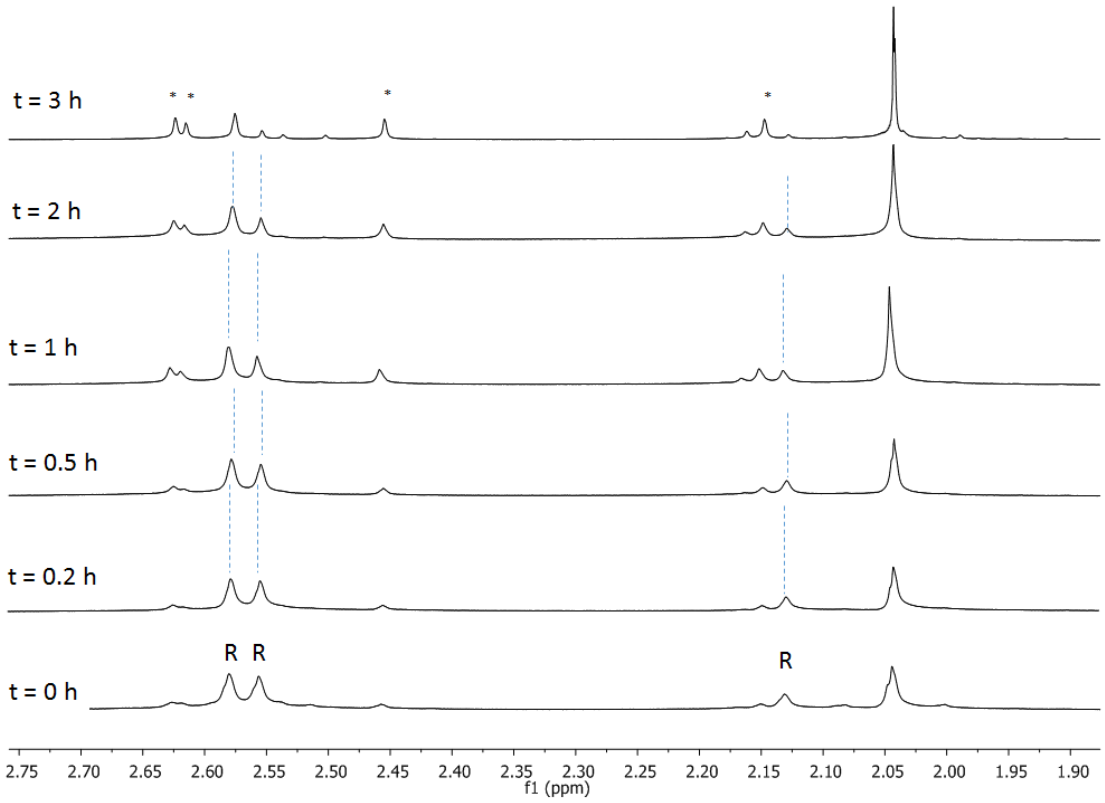

Figure 3.6 Changes in ^1H NMR spectra of **6** in D_2O as a function of time in the dark; only the region involving the changes in the spectra are shown. The labels R and * represent reagents and products, respectively.

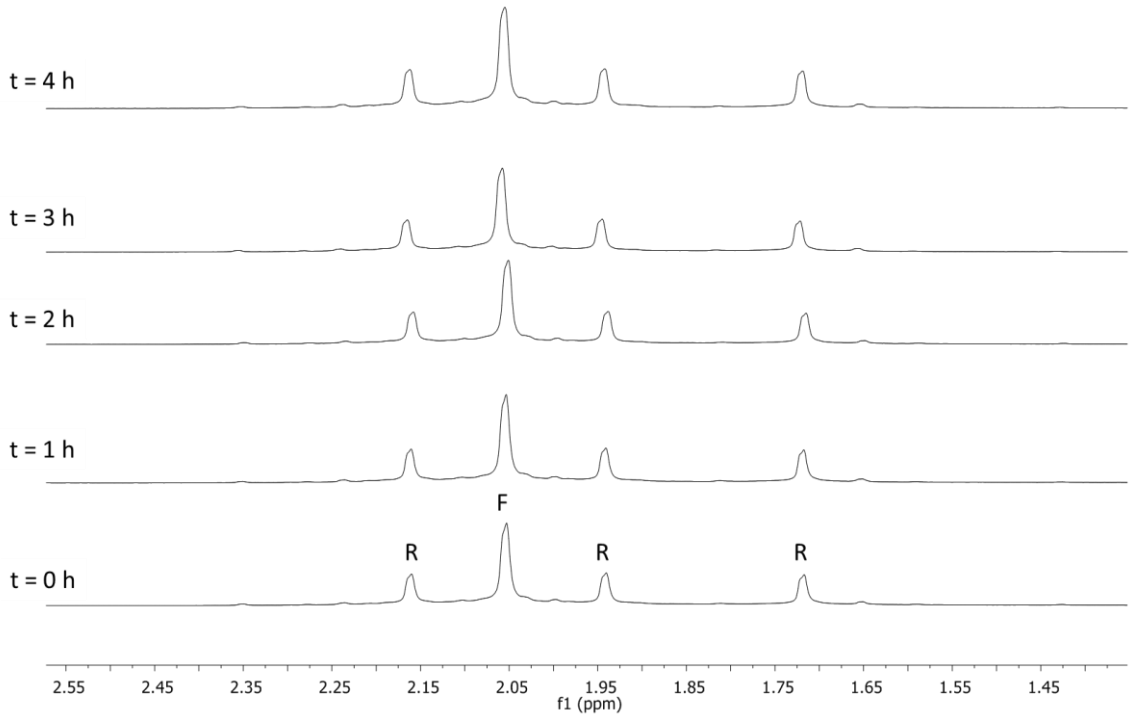

Figure 3.7 Changes in ^{1}H NMR spectra of **7** in D_2O as a function of time in the dark; only the region involving the changes in the spectra are shown. The labels R and F represent reagents and free CH_3CN, respectively.

The time lapse experiment for **7** was conducted for 4 h under irradiation with the projector. As in the case of **6**, the eq CH_3CN ligands do not exchange in the dark after photolysis for 4 h with white light (**Figure 3.9**). The eq CH_3CN ligands *trans* to the cyclometallated phosphine exhibit fast exchange in the dark upon dissolution in D_2O; this behavior is also observed in the case of $[Rh_2[Ph_2P(C_6H_4)]_2(CH_3CN)_6][BF_4]_2$ due to the strong σ-donating ability of the bridging phosphine ligand.[81]

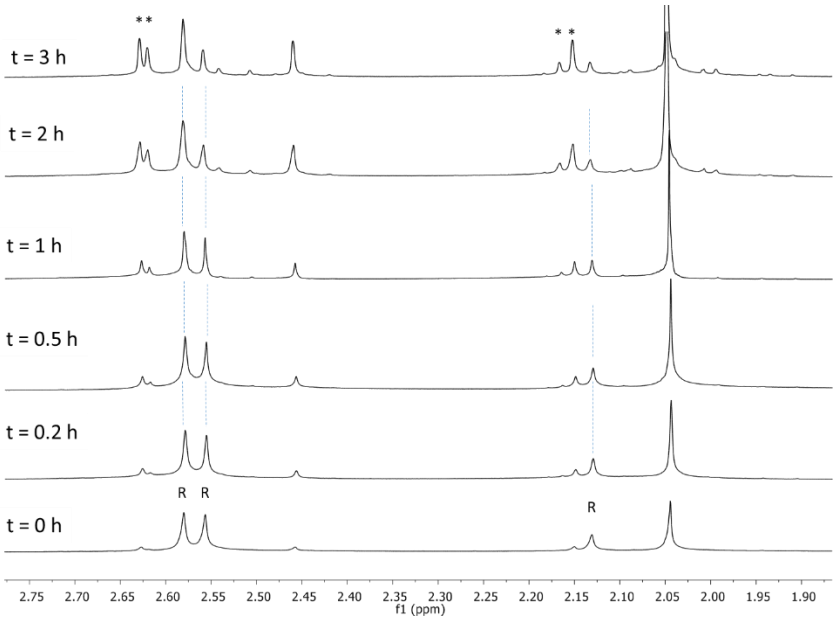

Figure 3.8 Changes in 1H NMR spectra of **6** in D2O as a function of irradiation time (λirr > 400-700 nm); only the region involving the changes in the spectra are shown. The labels R and * represent reagents and products, respectively.

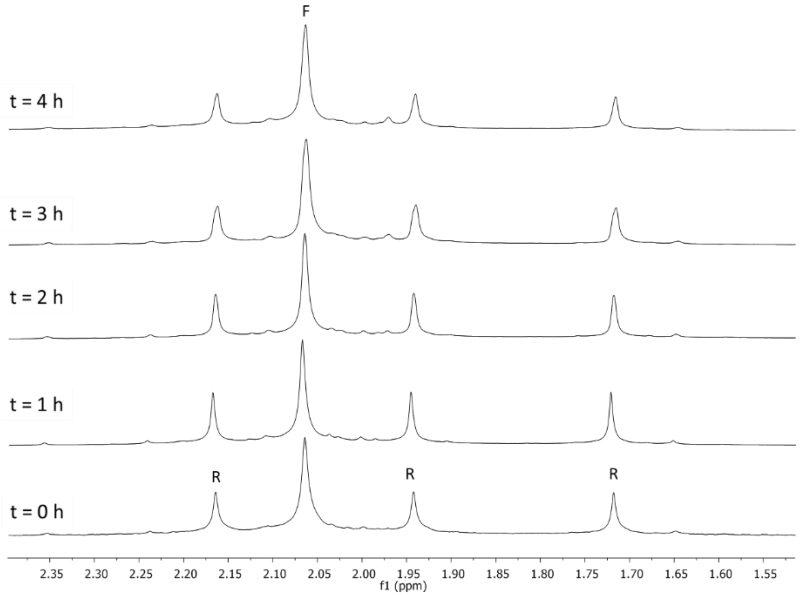

Figure 3.9 Changes in ^{1}H NMR spectra of **7** in D_2O as a function of irradiation time (λ_{irr} > 400-700 nm); only the region involving the changes in the spectra are shown. The labels R and F represent reagents and free CH_3CN, respectively.

Electronic Absorption Spectral and Electrochemical Studies

Electronic absorption spectra were obtained for compounds **6** and **7** in CH_3CN and H_2O; the data are summarized in **Table 3.5**.

Table 3.5 Electronic absorption data for complexes **6** and **7** in CH_3CN and H_2O at room temperature.

	λ (nm), (ε x 10^3 (M^{-1}•cm^{-1})) in CH_3CN	λ (nm), (ε x 10^3 (M^{-1}•cm^{-1})) in H_2O
6	220 (7.5), 260 (20.4), 360 (0.51), 500 (0.18)	250 (110), 360 (1.80), 510 (0.43)
7	243 (35.0), 290 (27.5), 485 (0.26)	234 (20.2), 290 (11.2), 535 (0.20)

The electronic absorption spectrum of **6** (**Figure 3.10a**) shows a strong absorption at ~ 260 nm ($\varepsilon = 2.0 \times 10^4$ M^{-1}•cm^{-1}) which is attributed to a metal-centered transition with some contributions from the $[F_2form]^-$ bridging ligand and the eq CH_3CN ligands. The spectrum in CH_3CN also displays a shoulder of moderate intensity at 360 nm ($\varepsilon = 5.1 \times 10^2$ M^{-1}•cm^{-1}) which becomes more prominent in H_2O. The lowest energy transition for **6** is observed at 500 nm with a bathochromic effect being observed in water at 510 nm. This transition is assigned as Rh(π*)-Rh(σ*). It is worth noting that in **6**, the lowest energy band is shifted to higher energies as compared to $[Rh_2(DTolF)_2(CH_3CN)_6][BF_4]_2$ and $[Rh_2(F\text{-}form)_2(CH_3CN)_6][BF_4]_2$ whose transitions occur at 521 nm and 534 nm respectively.[81] The hypsochromic shift exhibited by **6** underscores the effect on the electronic structure of the partial paddlewheel of merely substituting one formamidinate bridge for acetate.

In the case of **7** there is a shoulder of moderate intensity located at 243 nm (ε = 3.5 x 10^5 M^{-1}•cm^{-1}) which originates from the Rh(π*) to Rh-CH_3CN(eq)(σ*). There is also a band at 290 nm (ε = 2.7 x 10^5 M^{-1}•cm^{-1}) that does not shift with changes in solvent. The lowest energy transition is observed at 485 nm which is shifted to lower energies by ~ 10 nm as compared to $[Rh_2[Ph_2P(C_6H_4)]_2(CH_3CN)_6]^{2+}$ (478 nm).[81]

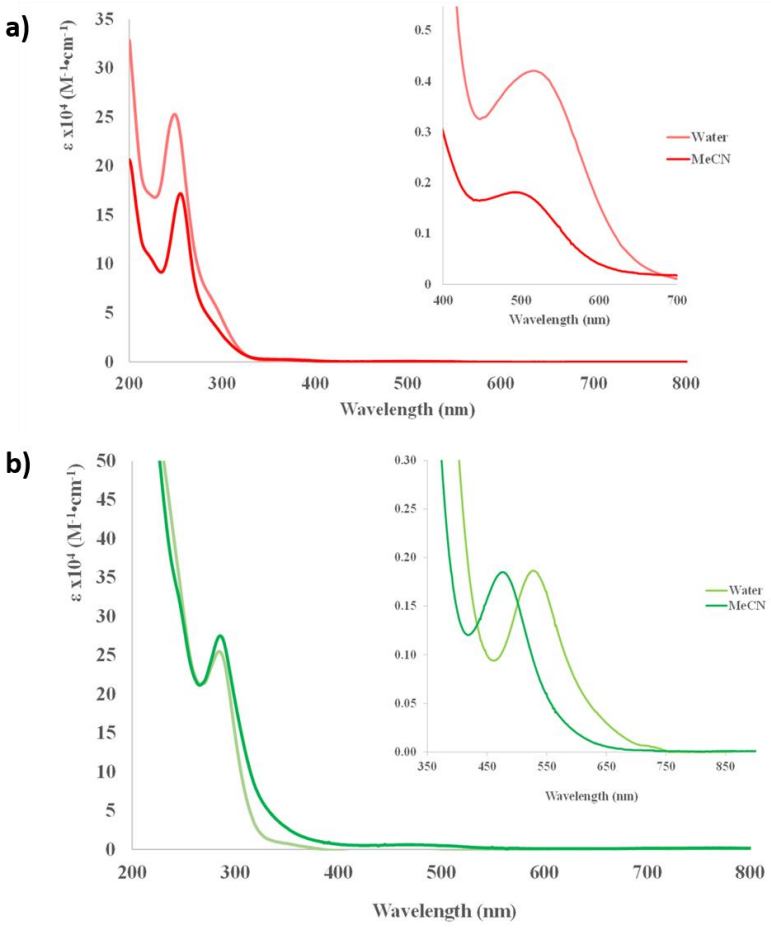

Figure 3.10 Electronic absorption spectra of compounds **a) 6** and **b) 7** in CH_3CN and H_2O at room temperature.

Dirhodium compounds are characterized by the facile exchange of the axial ligands with the solvent in which they are dissolved which causes the lowest energy transition to shift depending on their interaction with the Rh(σ*) orbital. Upon irradiation the compound $[Rh_2[O_2CCH_3)_2(CH_3CN)_6][BF_4]_2$ labilizes two of its eq CH_3CN ligands a process that is readily monitored by electronic absorption spectroscopy.[77] The lowest energy transition for **6** at 500 nm decreases in intensity over time and a slight shift to 515 nm was observed (**Figure 3.11a**). There is also a decrease in intensity in the band at 360 nm, which is Rh(π*) to Rh-$CH_3CN_{(eq)}$ (σ*) in character (**Figure 3.11b**). The thermal population of the Rh-$CH_3CN_{(eq)}$(σ*) level promotes the labilization of the eq CH_3CN which is mainly due to the strong σ-donation of the $[F_2form]^-$ bridging ligand.

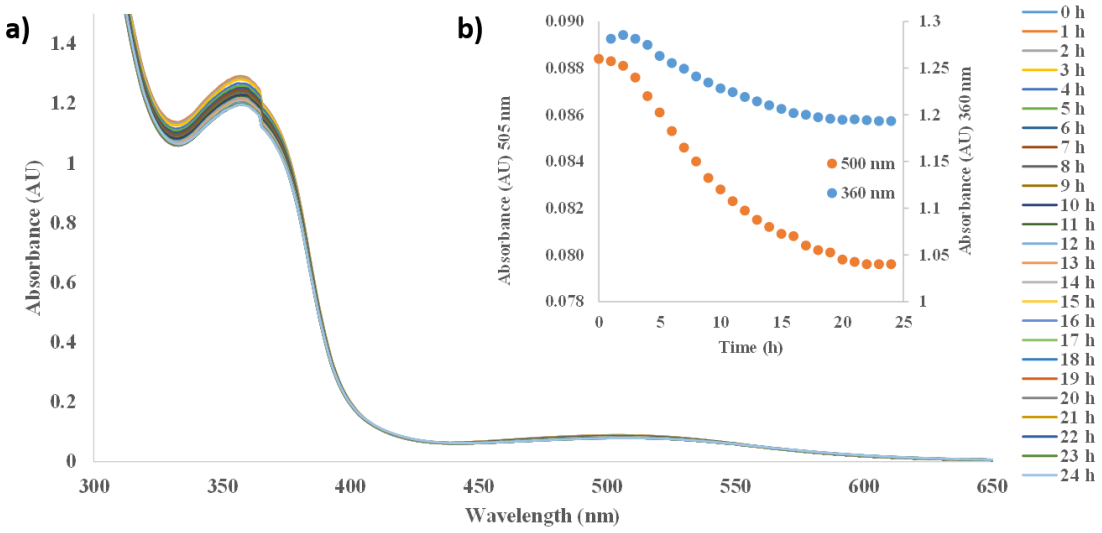

Figure 3.11 **a)** Electronic absorption spectra of **6** at room temperature in H_2O at different time intervals. **b**) Inset: absorbance values for the 500 nm and 360 nm absorption bands as a function of time.

The electronic absorption spectrum of **7** was also studied at different time intervals in H_2O. A slight decrease in intensity was observed in the lowest energy transition at 530 nm but no bathochromic shift was observed (**Figure 3.12a-b**). The behavior observed for **7** is mainly due to the *trans* influence that the $[PPh_3]^-$ exerts on the eq CH_3CN *trans* to it. Upon dissolution in H_2O the eq CH_3CN ligands *trans* to $[PPh_3]^-$ dissociate, thus the spectrum obtained in water corresponds to $[Rh_2[Ph_2P(C_6H_4)](O_2CCH_3)(H_2O)(CH_3CN)_2][BF_4]_2$ (**Figure 3.12c**).

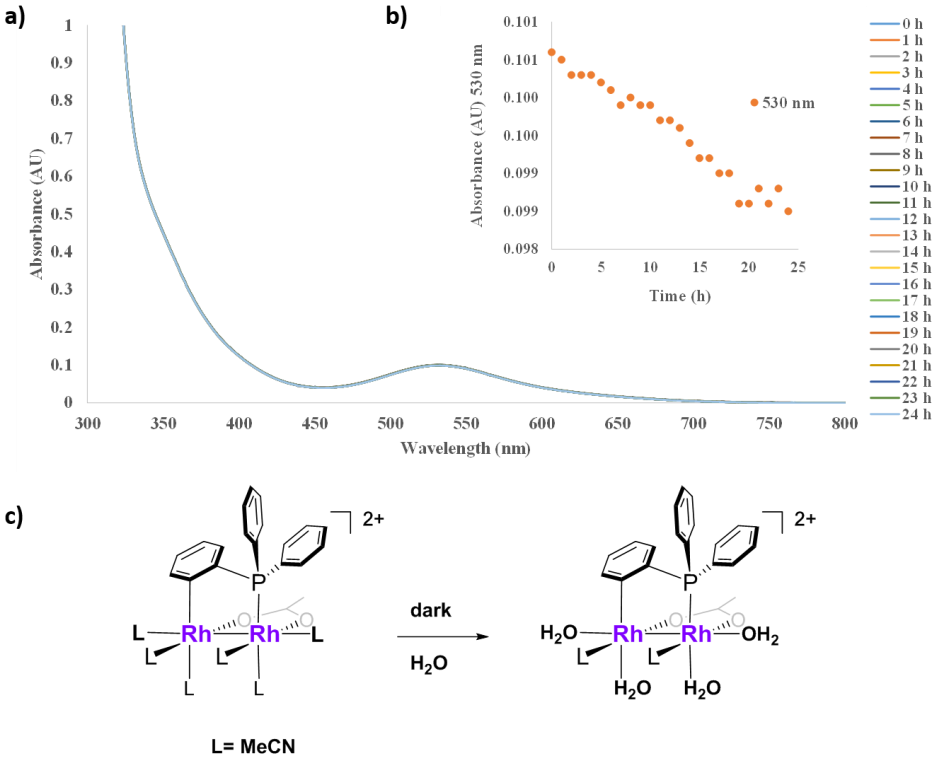

Figure 3.12 **a)** Electronic absorption spectra of **7** at room temperature in H_2O at different time intervals. **b**) Inset: absorbance values for the 530 nm absorption band as a function of time. **c)** Schematic representation of ligand exchange upon dissolution in water in the dark and at room temperature for compound **7**.

The redox potential for compounds **6** and **7** were measured and the results are summarized in **Table 3.6**.

Table 3.6 Electrochemical reduction potentials for compounds **6** and **7** and the free ligands.

Potential, V	$E_{pc,(red)1}$	$E_{pc,(red)2}$	$E_{1/2(ox)}$	$E_{pa,(ox)}$
$[Rh_2(O_2CCH_3)_1(F_2form)(MeCN)_6](BF_4)_2$	-0.84	-1.07	+1.75	
$[Rh_2(O_2CCH_3)_1[Ph_2P(C_6H_4)](MeCN)_6](BF_4)_2$	-0.87	-1.11	+1.51	
N,N'-2,6-difluoroformamidine[a]				+1.60
Triphenylphosphine[a]				+1.35

[a] Irreversible

The mixed bridge dirhodium compounds supported by $[F_2form]^-$ and $[PPh_3]^-$ ligands exhibit a reversible oxidation at +1.75 V and +1.51 V respectively attributed to the Rh(II)-Rh(II)→Rh(II)-Rh(III) couple. Ren *et al*. reported that the presence of electron donating groups on the formamidinates under study render the oxidation event more accessible and the opposite is true for electron withdrawing groups which can be observed in the reversible oxidation of compound **6** (+1.75 V).[176] The oxidation of compound **7** is in agreement with $[Rh_2[Ph_2P(C_6H_4)]_2(CH_3CN)_6][BF_4]_2$ (+1.54 V).[81] $[Rh_2[O_2CCH_3)_2(CH_3CN)_6][BF_4]_2$ displays two irreversible reduction waves at -0.56 V and -0.99 V vs SCE[79] and compounds **6** and **7** exhibit similar behavior. Compound **6** also displays two reductions at -0.84 V and -1.07 V, and **7** at -0.87 V and -1.11 V; in both cases the reduction waves are comparable to those of $[Rh_2[O_2CCH_3)_2(CH_3CN)_6][BF_4]_2$.

Computational Studies

A summary of important bond distances and molecular orbital contributions for **6** and **7** from the optimized structures are listed in **Table 3.7**and **Table 3.8**.

Table 3.7 Experimental bond distances obtained from X-ray diffraction data and the calculated ones derived from DFT gas phase optimization of the cationic structures of compounds **6** and **7**.

Compound 6	**Experimental**	**Calculated**	**Compound 7**	**Experimental**	**Calculated**
Bond	**Length/Å**	**Length/Å**	**Bond**	**Length/Å**	**Length/Å**
Rh1-Rh2	2.5575(2)	2.5565(5)	Rh1-Rh2	2.5591(9)	2.5791(0)
Rh1-O1	2.424(1)	2.0363(7)	Rh1-O1	2.035(4)	2.0509(9)
Rh2-O2	2.468(1)	2.0331(2)	Rh2-O2	2.042(3)	2.0455(4)
Rh1-N1	1.852(2)	2.0310(6)	Rh2-C3	2.011(6)	2.0158(5)
Rh2-N2	1.864(2)	2.0332(4)	Rh1-P3	2.2333(2)	2.2782(6)
Rh1-N3	1.840(2)	2.0448(7)	Rh2-N6	2.153(4)	2.2033(9)
Rh2-N4	1.875(1)	2.0455(5)	Rh1-N9	2.127(4)	2.1372(5)
Rh1-N5	2.408(2)	1.9955(1)	Rh2-N5	1.985(4)	1.9879(5)
Rh2-N6	2.436(2)	1.9957(0)	Rh1-N7	1.980(4)	1.9846(2)
Rh1-N7	2.244(2)	2.2231(5)	Rh2-N4	2.184(5)	2.1798(4)
Rh2-N8	2.164(2)	2.2199(8)	Rh1-N8	2.226(4)	2.2585(0)
Dihedral		**º**	**Dihedral**		**º**
N1-Rh1-Rh2-N2	-9.6(7)	16.76(8)	C3-Rh2-Rh1-P3	28.88(12)	27.12(5)
O1-Rh1-Rh2-O1	-3.7(4)	16.597	O1-Rh1-Rh2-O2	23.18(12)	22.65(5)
N7-Rh1-Rh2-N8	-2.4(7)	20.78(2)	N6-Rh2-Rh1-N9	31.11(16)	31.64(7)
N9-Rh1-Rh2-N10	-4.9(5)	21.42(9)	N7-Rh1-Rh2-N5	30.43(18)	30.83(6)

Table 3.8 Orbital contribution of selected molecular orbitals for compound **6** in CH_3CN and H_2O derived from TD-DFT.

	6 in CH_3CN			**6 in H_2O**			**7 in CH_3CN**			**7 in H_2O**	
HOMO-2	13 Rh 84 F_2form 1 OAc	1 eq CH_3CN 1 ax CH_3CN	HOMO-2	77 Rh 11 F_2form 2 OAc	7 eq CH_3CN 3 ax H_2O	HOMO-2	80 Rh 4 PPh_3 6 OAc	7 eq CH_3CN 3 ax CH_3CN	HOMO-2	84 Rh 2 PPh_3 5 OAc	8 eq CH_3CN 1 ax H_2O
HOMO-1	63 Rh 23 F_2form 5 OAc	6 eq CH_3CN 3 ax CH_3CN	HOMO -1	85 Rh 4 OAc	8 eq CH_3CN 3 ax H_2O	HOMO-1	69 Rh 17 PPh_3 2 OAc	5 eq CH_3CN 7 ax CH_3CN	HOMO-1	76 Rh 2 PPh_3 5 OAc	5 eq CH_3CN 3 ax H_2O
HOMO	67 Rh 28 F_2form	2 OAc 3 eq CH_3CN	HOMO	28 Rh 67 F_2form	2 OAc 3 eq CH_3CN	HOMO	46 Rh 48 PPh_3 2 OAc	3 eq CH_3CN 2 ax CH_3CN	HOMO	47 Rh 47 PPh_3 2 OAc	3 eq CH_3CN 1 ax H_2O
LUMO	78 Rh 5 F_2form 3 OAc	5 eq CH_3CN 9 ax CH_3CN	LUMO	80 Rh 5 F_2form 3 OAc	4 eq CH_3CN 8 ax H_2O	LUMO	72 Rh 11 PPh_3 4 OAc	5 eq CH_3CN 8 ax CH_3CN	LUMO	75 Rh 11 PPh_3 3 OAc	4 eq CH_3CN 7 ax H_2O
LUMO+1	56 Rh 21 F_2form	7 OAc 15 eq CH_3CN	LUMO+1	53 Rh 26 F_2form	7 OAc 14 eq CH_3CN	LUMO+1	44 Rh 37 PPh_3	7 OAc 11 eq CH_3CN	LUMO+1	42 Rh 41 PPh_3	6 OAc 10 eq CH_3CN
LUMO+2	50 Rh 26 F_2form	7 OAc 16 eq CH_3CN	LUMO+2	50 Rh 28 F_2form	7 OAc 15 eq CH_3CN	LUMO+2	4 Rh 92 PPh_3 3 eq CH_3CN		LUMO+2	3 Rh 93 PPh_3 3 eq CH_3CN	

In order to gain more insight into the structural and electronic absorption characteristics of compounds **6** and **7**, DFT calculations were conducted. The geometry optimization results for both compounds are comparable to that of the experimental findings. The Rh-Rh bond distance in **6** is in close agreement with that of the crystal structure and in the case of **7** it is slightly longer than the experimental value, ca. ~0.02 Å. The crystal structure of **6** exhibits remarkably long Rh-O bond distances, differing by ~0.43 Å from the calculated structure. Dirhodium partially solvated compounds bearing acetate and acetamides typically exhibit bond distances in the range of 1.98-2.02 Å,[79,174] however **6** has unusually long Rh-N_{eq} CH_3CN^O from the X-ray diffraction data, 2.408(2) Å. The optimization of **6** provides a Rh-N_{eq} CH_3CN^O bond distance that resembles more that of the reported values, 1.875(1) Å. Also the dihedral angles for the optimized cationic structure of **6**, shows big distortions and splaying of the four eq CH_3CN molecules which is not observed on the crystallographic structure. The geometry optimization results for compound **7** confirmed that the Rh-N_{eq} (*trans* to P) and Rh-N_{eq} (*trans* to C) are longer than that of the Rh-N_{eq} *trans* to the acetate groups which is not surprising since the orthometallated phosphine exerts a stronger trans effect than the acetate group on the eq CH_3CN monodentate ligands. Also the dihedral angles for **7** defined by the eq CH_3CN and the dirhodium core are in good agreement with the X-ray diffraction data. The dihedral angles from the bridging ligands, $[PPh_3]^-$ and $[O_2CCH_3]^-$ and the dirhodium core calculated by DFT are ~1.5º and ~0.5º shorter than the X-ray structure, but are still in good agreement with the experimental results.

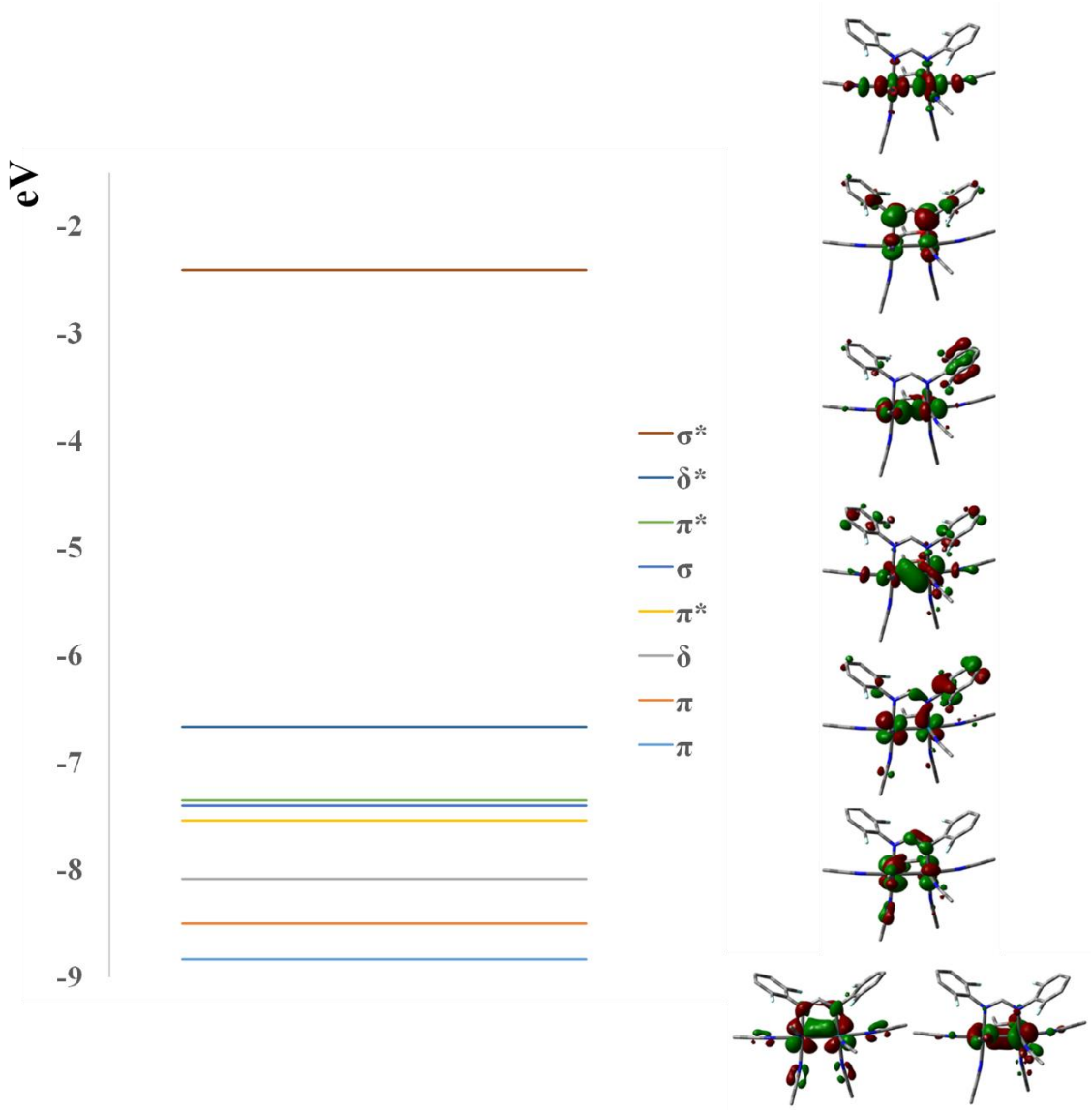

Figure 3.13 MO diagram involving the dirhodium core unit in **6** obtained by DFT calculations (iso-value=0.04).

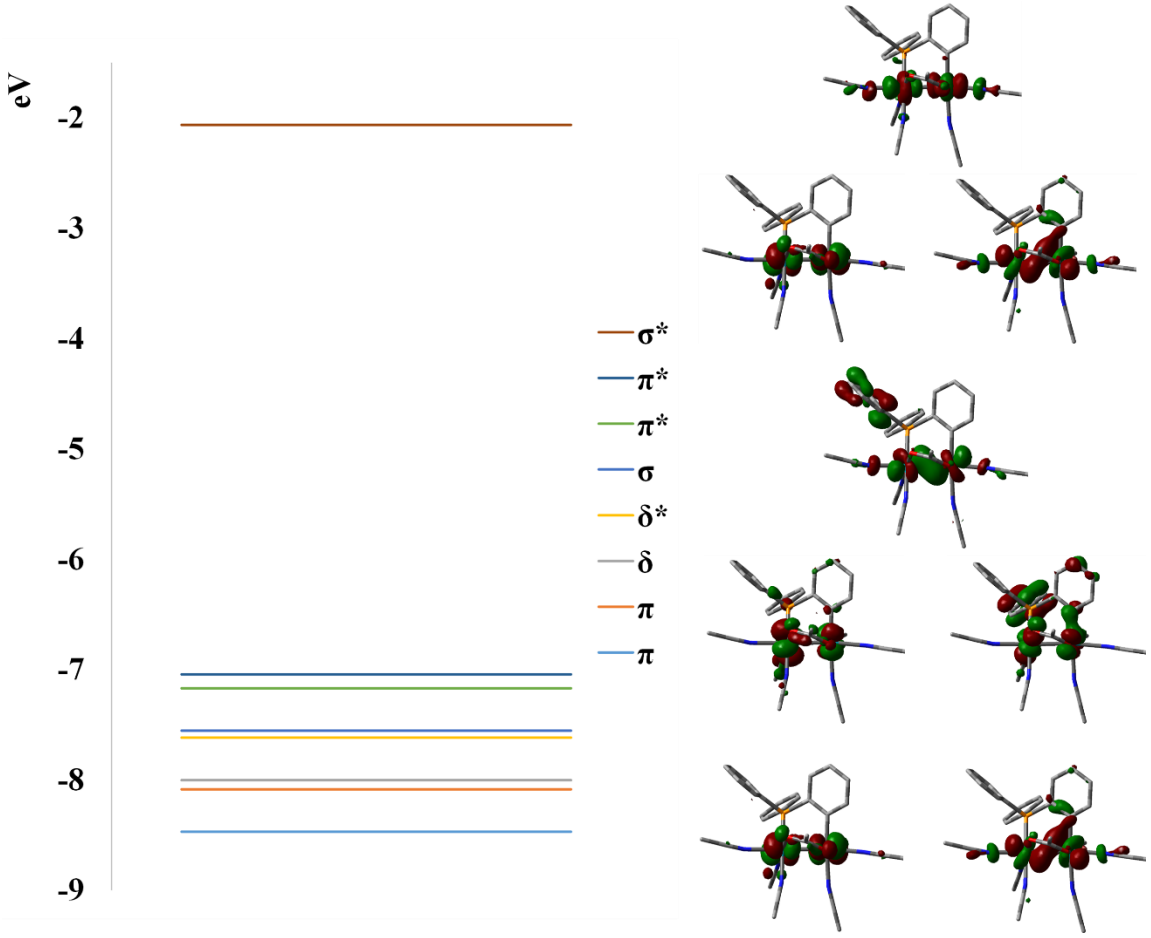

Figure 3.14 MO diagram involving the dirhodium core unit in **7** obtained by DFT calculations (iso-value=0.04).

DFT calculations were performed on the optimized cationic structures of **6** and **7** in CH_3CN and H_2O**.** The results from this study indicate that the molecular orbital contributions are very similar in both solvents (**Table 3.8**). The HOMO in **6** is mostly $[F_2form]^-$ (pπ bridging) based (71%) with some contribution from the acetate bridge (~2%). The LUMO is a rhodium based orbital corresponding to the Rh(σ*) orbital, whereas the LUMO+1 and LUMO+2 have considerable antibonding character between the Rh and eq CH_3CN ligands, with equal contributions to the eq CH_3CN *trans* to the acetate and to the $[F_2form]^-$. The Rh(σ) level is higher in energy by 0.68 eV that the Rh(δ) level which is lower in energy than the Rh(π*). The stabilization of the Rh(π*) is mainly due to the bonding interactions of the rhodium with the $[F_2form]^-$ bridging ligand (**Figure 3.13**).

The metal-based orbitals for **7** exhibit the configuration $\pi^4\delta^2\delta^{*2}\ \sigma^2\pi^{*4}\sigma^{*0}$ (**Figure 3.14**). The HOMO for **7** has a 1:1 contribution from Rh and $[PPh_3]^-$ (π Phenyl). The Rh(δ) and Rh(δ*) are stabilized due to its interaction with the bridging phosphine ligand, while the Rh(σ) lies at higher energies due to the antibonding interactions with the axial CH_3CN ligands. The LUMO is mostly a rhodium based orbital with 72% contributions and visualization of this orbital indicates that it corresponds to the Rh(σ*). The LUMO+1 and LUMO+2 have significant Rh-CH_3CN_{eq} character which corresponds to the Rh-L_{eq}(σ*) orbitals responsible for the labilization of the equatorial acetonitrile ligands.

To gain more insight into the origin of the electronic transitions of compounds **6** and **7**, TD-DFT/PCM calculations were conducted. The lowest energy band (λ = 465 nm, f = 0.001) for **6** corresponds to the HOMO-1 to LUMO ligand-to-metal charge-transfer

(LMCT) transition (**Table 3.9**) from the $[F_2form]^-$ (pπ) to the Rh(σ*) orbital. The absorption band at 435 nm involves the transition from HOMO-6 to LUMO which have been ascribed to the Rh(π*) to Rh(σ*) transition due to the rhodium contribution which makes this a metal centered transition (MC). The transition at 326 nm has orbital contributions from the HOMO-1 to the LUMO+1 and is ascribed as the transition from Rh(π*) to Rh-L_{eq} (σ*). This transition is responsible for the labilization of the eq CH_3CN monodentate ligands upon irradiation. The strong absorptions from 311-318 nm are a combination of MC and LMCT and originate from the HOMO-5 and HOMO-8 levels with a 1:3 Rh:F_2form character and major contributions from the Rh(δ) orbitals respectively.

Compound **7** displays a low energy band at 463 nm (f = 0.001) that corresponds to transitions originating from the HOMO-2 to LUMO orbitals. This electronic transition is a metal centered transition composed mainly of Rh(π*) and Rh(σ*) character and it correlates well with the experimental results. The absorptions between 290-310 nm are charge transfer bands (LMCT) that have been attributed to transitions involving the phosphine bridging ligand and the metal center, HOMO-12 to LUMO and HOMO-2 to LUMO+2 and are LMCT/MC in character. The transitions in the region between 340-360 nm have contributions from the HOMO-2 to L+1 orbitals, which have Rh(π*) and Rh-L_{MeCN} (σ*) in character, this is the band that decreases in intensity due to the labilization of the equatorial ligands as shown in the time lapse experiments. Visualization of the frontier orbitals for **6** and **7** are depicted in **Figure 3.15** and **Figure 3.16**.

Table 3.9 First ten electronic transitions predicted for **6** and **7** by TD-DFT calculations in CH_3CN and H_2O as solvent. H = HOMO, L = LUMO and *f* = oscillator strength.

6 in CH_3CN				**6 in H_2O**			
E/ (nm)	*f*	Excitations		E/ (nm)	*f*	Excitations	
465	0.001	H-1 -->L	58%	509	0.001	H-1 -->L	82%
454	0.002	H-->L	79%	495	0.001	H --> L, H-2 --> L	34%, 48%
435	0.002	H-6-->L	50%	477	0.002	H --> L, H-2 --> L	42%, 30%
392	0.002	H-->L	65%	386	0.005	H --> L+1	61%
378	0.002	H-->L+2	56%	374	0.002	H -->L	52%
347	0.010	H-10-->L	22%	346	0.002	H-8-->L	30%
331	0.010	H-1-->L+1	29%	335	0.004	H-8 --> L	54%
326	0.003	H-1-->L+1	23%	329	0.002	H-1 --> L+1	63%
318	0.013	H-8-->L	52%	319	0.013	H-2 --> L+2	27%
311	0.013	H-5-->L	30%	308	0.015	H-1 -->L+2, H-6 -->L	25%, 22%

7 in CH_3CN				**7 in H_2O**			
E/ (nm)	*f*	Excitations		E/ (nm)	*f*	Excitations	
463	0.001	H-2 -->L	77%	520	0.001	H-2 -->L	79%
444	0.008	H-1-->L, H-->L	35%, 22%	502	0.003	H-1 --> L, H->-L	41%, 34%
390	0.001	H-->L, H-1-->L	39%, 37%	423	0.001	H --> L, H-1-->L	48%, 34%
361	0.001	H-2 --> L+1	39%	373	0.001	H-2 --> L+1	25%
349	0.004	H-1-->L+1, H-->L+1	46%, 20%	350	0.006	H-1 -->L+1, H-->L+1	37%, 20%
338	0.003	H-7-->L+1, H-10-->L+1	29%, 25%	339	0.003	H-7-->L+1, H-10-->L+1	23%, 20%
321	0.006	H-11-->L	30%	336	0.004	H-2 --> L+1, H-9-->L	29%, 23%
314	0.019	H-4-->L+1	26%	328	0.024	H-10 --> L, H-7-->L	23%, 20%
311	0.030	H-->L+2	29%	306	0.0053	H-3 --> L	37%
301	0.030	H-12-->L	34%	298	0.006	H-3 --> L+1	20%

*$2|\text{coefficient}|^2 > 0.2$

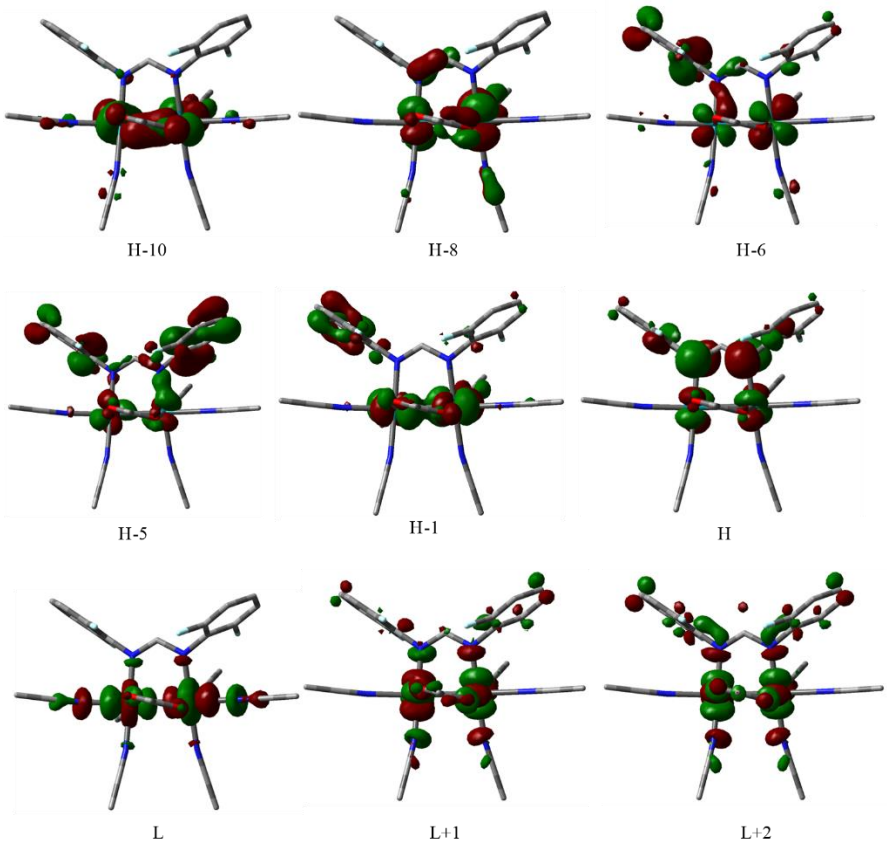

Figure 3.15 MO depiction of **6** generated by TD-DFT calculations in solvation model (CH_3CN) generated by agui with iso-value = 0.04; H = HOMO, L = LUMO.

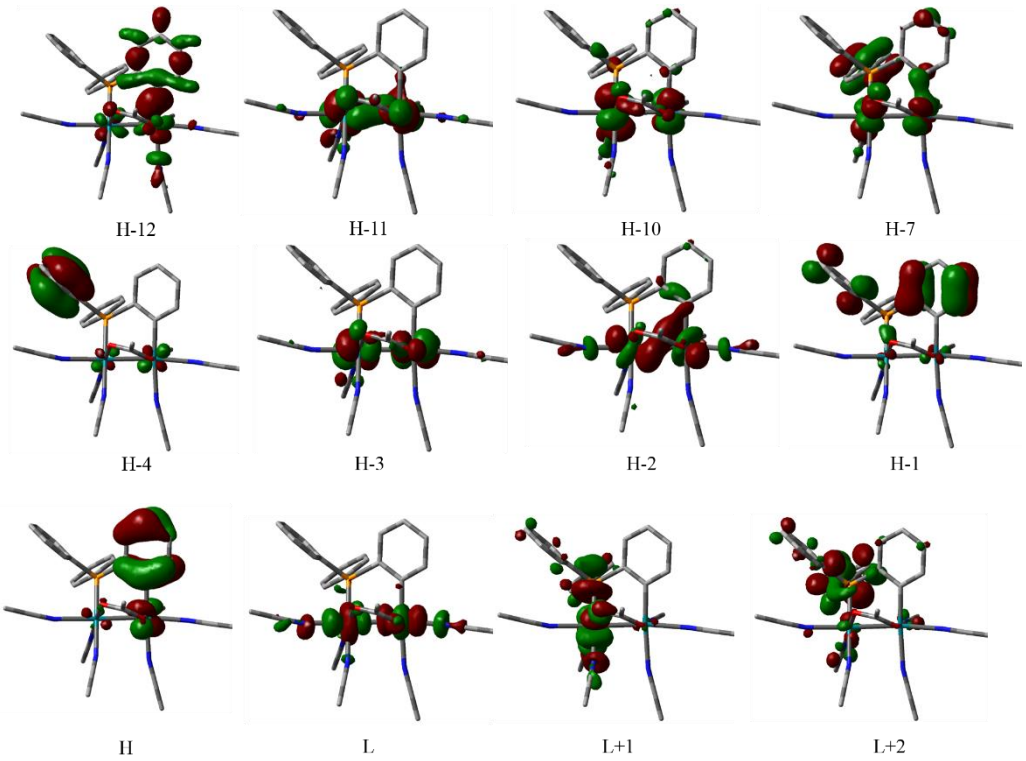

Figure 3.16 MO depiction of **7** generated by TD-DFT calculations in solvation model (CH_3CN) generated by agui with iso-value = 0.04; H = HOMO, L = LUMO.

In-vitro *Cytotoxicity Studies*

The cytotoxicities of compounds **6** and **7** were determined against HeLa cells with the aid of fluorescent probes, Sytox Green® and Hoechst 33342. The blue fluorescent dye, Hoechst 33342 indiscriminately binds to DNA in both dead and live cells, while Sytox Green® selectively stains dead or dying cells, exhibiting green fluorescence.[147,177] The cells were incubated with compounds **6** and **7** for 4 h in the dark at different concentrations, followed by treatment with Sytox Green® and Hoechst for 10 min. The dark experiments showed that for both compounds, mostly blue fluorescence was observed, meaning that the cells were still alive (**Figure 3.17 and Figure 3.18**). Since no green fluorescence was observed under the experimental conditions, the LC_{50} values could not be determined but have been estimated to be >>200 µM.

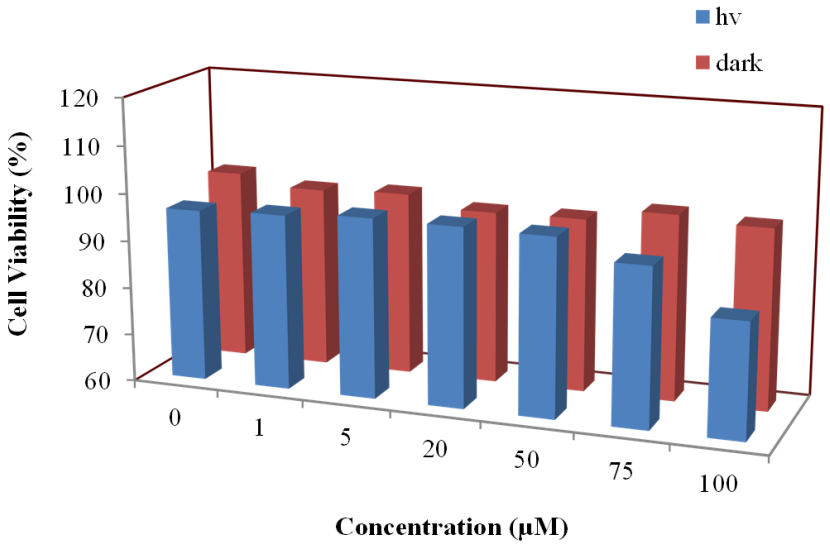

Figure 3.17 Cell viability plot for compound **6** in the dark (red) and upon irradiation (blue).

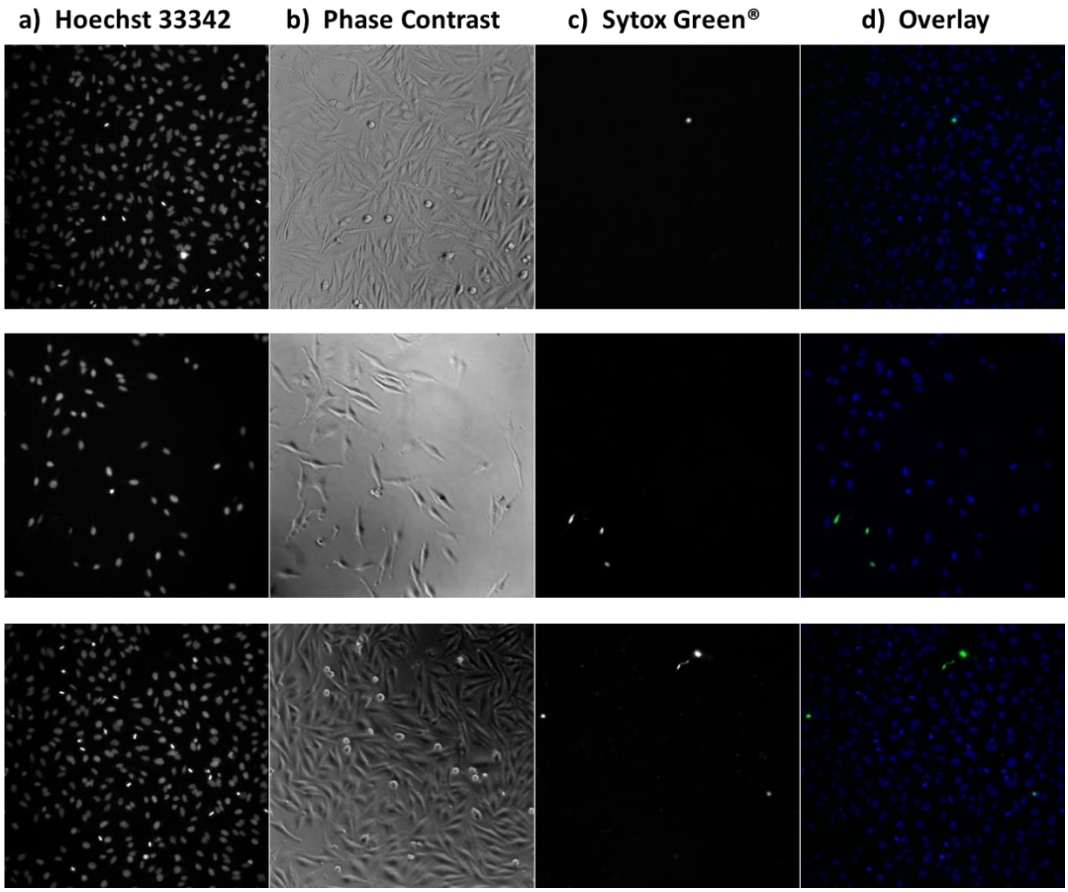

Figure 3.18 Confocal microscopy images of HeLa cells treated with 50 μM solutions of **6** and **9** for 4 h in the dark followed by treatment with Sytox® Green and Hoechst. Top control in the dark, middle pane compound **6** and bottom compound **7**. a) Hoechst 33342, blue fluorescence, b) phase contrast, c) SYTOX® Green fluorescence, and d) overlay of blue and green fluorescence.

The photocytotoxicities of **6** and **7** were also studied. These cells were incubated in the dark for 2 h followed by irradiation with white light (λ = 400-700 nm) for a period of 1 h. After staining with Sytox Green® and Hoechst it was observed that, as in the case of the dark experiment and the control with no compound, only blue fluorescence was observed (**Figure 3.19**). Clearly the mixed bridge partially solvated compounds are not

toxic against HeLa cells. These results are not surprising considering the low stability of **6** in aqueous soliton; moreover the compound may not be entering the cell or it could be decomposing before reaching its target. Compound **7** exhibits rapid exchange of the eq CH_3CN (*trans* to PPh_3) for H_2O in the dark but the eq CH_3CN ligands *trans* to acetate are not released upon irradiation which may be a contributing factor to the lack of toxicity upon irradiation.

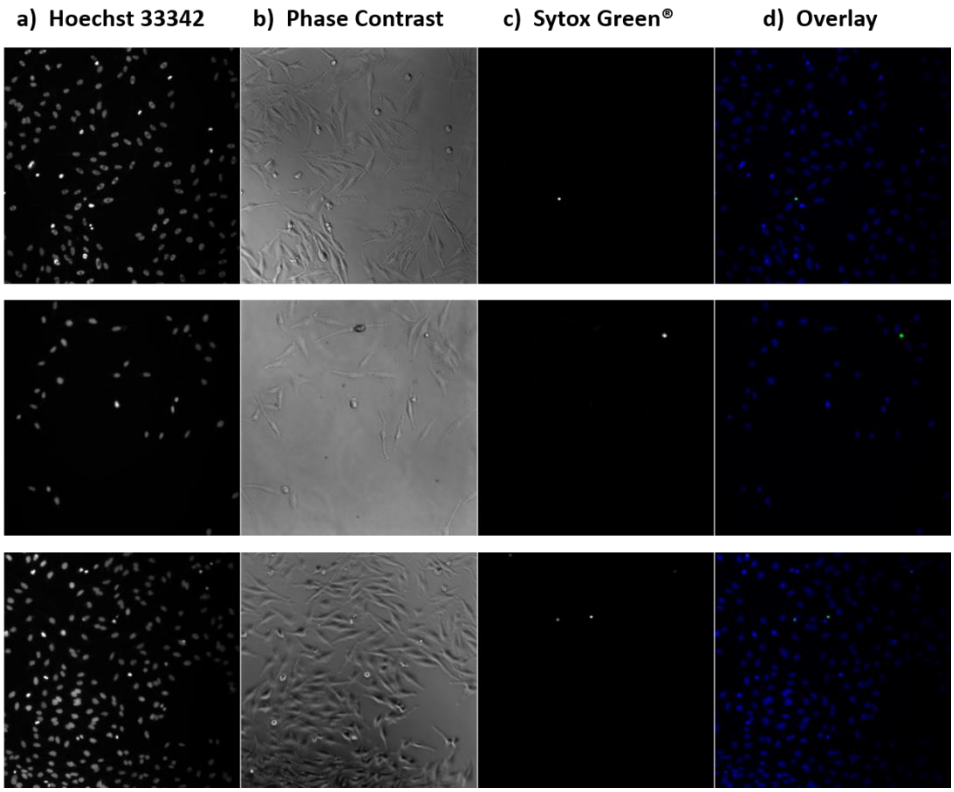

Figure 3.19 Confocal microscopy images of HeLa cells treated with 50 μM solutions of **6** and **7** for 4 h in the dark, irradiated for 30 min, and followed by treatment with Sytox® Green and Hoechst. Top control after irradiation, middle pane compound **6** and bottom compound **7**. a) Hoechst 33342, blue fluorescence, b) phase contrast, c) SYTOX® Green fluorescence, and d) overlay of blue and green fluorescence.

Concluding Remarks

The partial paddlewheel dirhodium compounds bearing mixed-bridging ligands $[Rh_2(\mu\text{-o-}F_2form)(\mu\text{-}O_2CCH_3)(CH_3CN)_6](BF_4)_2$ and $[Rh_2(\mu\text{-}Ph_2P(C_6H_4))(\mu\text{-}O_2CCH_3)(CH_3CN)_6](BF_4)_2$ were successfully prepared and characterized and their anti-proliferative activity tested against HeLa cells. Compounds **6** and **7** have strong sigma donating bridges along with one acetate group. The eq CH_3CN ligands *trans* to the σ-donating bridgeheads exchange readily with the H_2O molecules upon dissolution with the opposite being observed for the eq CH_3CN *trans* to the acetate group. The time lapse ^1H NMR spectra of compound **6** shows that the eq CH_3CN ligands exchange at the same rate in the dark and upon light irradiation, this may be due to the light source utilized for this experiments. Also **6** is not stable for long periods of time as evidence by the isolation of the by-product **6b** and subsequent X-ray analysis that shows that the acetate bridge has been lost which may be due to the remarkably long Rh-O (bridging acetate) bond distances. In the case of **7**, the orthometallated phosphine group causes strains in the dirhodium unit with a 29 ° torsion angles which had also been observed for $[Rh_2(C_6H_4(Ph_2))_2(CH_3CN)_6]^{2+}$.

The DFT calculations helped in the interpretation of the transitions in the electronic absorption spectrum. Compound **6** has a low energy transition that is $[F_2form](p\pi)$ to $Rh(\sigma^*)$ in character while in **7** it is $Rh(\pi^*)$ to $Rh(\sigma^*)$. The presence of only one strong σ-donor bridging ligand does not improve the lability of the eq CH_3CN ligands *trans* to the acetate. The time lapse ^1H NMR studies indicate that the eq CH_3CN ligands *trans* to the acetate do not exchange upon light irradiation over a period of 5 h. The cell viability data

indicate that the compounds studied in this chapter do not show anti-proliferative properties under the experimental conditions. To our knowledge this is the first report of partial paddlewheel dirhodium compounds bearing mixed bridging ligands. Additional bridging ligands should be pursued in order to improve the dark stability of these compounds and render the photolability of the eq CH_3CN ligands *trans* to acetate more facile.

CHAPTER IV

DIRHODIUM (II,II) PYRROLIDINATO COMPOUNDS AND THEIR APPLICATIONS AS ANTICANCER AGENTS

Introduction

Despite the great success of cisplatin in battling various forms of cancer, its efficacy has been compromised by drug resistance mechanisms and a plethora of side effects.[15,178] This situation has prompted the development of new and improved drugs that interact with targets other than DNA, including proteins,[98] enzymes,[179] histones,[95] and which induce a cascade of events that ultimately leads to cell death.[180-181] Although cisplatin and other platinum complexes are widely viewed as the gold standards for metal chemotherapeutic agents, other transition metal compounds exhibit impressive anti-carcinostatic properties and deserve to be explored.

One major drawback of current traditional therapies is the lack of targeted action. A much more effective alternative approach is photodynamic therapy (PDT). PDT is a non-invasive treatment for endoscopically accessible tumors[63-64] which involves the use of photosensitizers and visible light in combination with molecular oxygen to cause damage to tumor cell membranes by generation of singlet oxygen and other reactive oxygen species (ROS).[66-67] The fact that the photosensitizer relies on the oxygen present in the cell, however, is disadvantageous because once the oxygen is depleted in dense tumor tissue, the drug becomes ineffective.[63] To circumvent this problem, "photo-cisplatin" analogs that do not rely on oxygen are being studied in our laboratories and others. Turro and co-workers studied the photophysical properties of [Rh_2(μ-

$O_2CCH_3)_2(CH_3CN)_6]^{+2}$ and, upon irradiation with low energy light, two equatorial CH_3CN monodentate ligands are labilized and exchanged for H_2O molecules.[77] The photo-aquation product $[Rh_2(\mu\text{-}O_2CCH_3)_2(H_2O)_4(CH_3CN)_2]^{+2}$ becomes the active species and induces a 34-fold increase in toxicity when tested against skin cancer cells. A number of related compounds have been synthesized and their photophysical properties investigated examples of which are the H,H and H,T isomers of $[Rh_2(HNOCCH_3)_2(CH_3CN)_6](BF_4)_2$[79], $[Rh_2$(6-chloro-oxo-pyridinate)$(CH_3CN)_6](BF_4)_2$[170] that photocleave DNA *in vitro* and exhibit an increase in toxicity against HeLa cells upon irradiation with low energy light respectively. In order to improve antiproliferative activity of these type of compounds we set out to tune the properties by studying different bridging ligands.

Dirhodium tetrakis-pyrrolidinato and valerolactamate complexes were reported in the late 1980's but their biological applications were not investigated until 2012.[182-184] Che and coworkers reported the antiproliferative properties of a series of dirhodium tetracarboxylates and Rh_2(3-butyl-2-pyrrolidinato)$_4$ and their studies revealed that it exhibits anticancer activity with LC_{50} values in the range of 0.5-1.60 μM on the different cancer cell lines tested. The compound 2-pyrrolidinone is known for a wide range of applications ranging from tablet binders, and as a food additive, our interest in the molecule lies in the fact that it shows antioxidant and anticancer activities.[185-186] The aim of the work in this chapter is the synthesis and characterization of a new family of dirhodium (II,II) partially solvated compounds equipped with 2-pyrrolidinate bridging ligands and the study of their anticancer activity upon white light irradiation.

Experimental Section

Starting Materials

The compound $Rh_2(\mu\text{-}O_2CCH_3)_4\bullet 2CH_3OH$ was purchased from Pressure Chemicals or synthesized from $RhCl_3\bullet xH_2O$ from reported procedures.[108] The compound $Rh_2(\mu\text{-}NOC_4H_6)_4(CH_3CN)_2$ was prepared following reported procedures.[183] The commercially available reagents 2-pyrrolidinone (pyrro) and ferrocenium hexafluorophosphate were purchased from Sigma Aldrich and triethyloxonium tetrafluoroborate (Et_3OBF_4), 1M in CH_2Cl_2 was purchased from TCI America; all of them were used as purchased. Analytical thin layer chromatography was carried out on aluminum-backed sheets coated with aluminum oxide (Al_2O_3) neutral 60 F254 adsorbent (0.20 mm thickness, EMD Chemicals). Flash chromatography was performed with Al_2O_3 (activated, basic, Brockmann I, Sigma Aldrich). The solvents acetonitrile (CH_3CN), toluene and diethyl ether (Et_2O) were of ACS grade quality and used as received. Standard Schlenk-line techniques (under N_2 atmosphere) were used and work-up and isolation of products was performed in air unless otherwise stated.

Cell culture reagents Dubelco's modified Eagle medium (DMEM) (Invitrogen), fetal bovine serum (FBS) (Atlanta Biologicals), Leibovitz's L-15 Medium (L-15) without phenol red (Life Technologies), Phosphate-Buffered Saline solution (DPBS) (Life Technologies) and Sytox Green® (Invitrogen), Hoechst 33342 (Invitrogen) were used as received. The HeLa cell line was obtained from the American Type Culture Collection, cell line CCL-2.

Preparation of *cis*-2,2-[$Rh_2(\mu\text{-}NOC_4H_6)_2(NOC_4H_7)(CH_3CN)_5](BF_4)_2$ (8). The reagent Et_3OBF_4 (1 mL, 1 mmol) was added to a CH_3CN:CH_3OH (1:1 v/v) solution of $Rh_2(\mu\text{-}NOC_4H_6)_4(CH_3CN)_2$ (28.2 mg, 0.045 mmol) and the mixture was stirred for 18 h in the absence of light. The reddish/purple colored solution was concentrated to ~3 mL and diethyl ether was added to precipitate a purple solid which was collected by filtration. The solid was purified by flash chromatography (Al_2O_3, toluene:CH_3CN 70:30) to afford **9** as a light purple solid. X-ray quality crystals were obtained from slow diffusion of diethyl ether into a solution of the product in acetonitrile. Yield 15 mg (40%). ^{1}H NMR (500 MHz, CD_3CN-d_3), δ (ppm): 1.96 (s, 6H axCH_3CN), 2.40 (m, pyrro), 2.46 (s, eqCH_3CN^N), 2.49 (s, 6H, eqCH_3CN^O), 3.29 (m, pyrro), 3.40 (m, pyrro), 3.48 (m, pyrro), 5.93 (s, Hpyrro). ESI-MS: m/z = 665.97 ($[Rh_2(\mu\text{-}NOC_4H_6)_2(NOC_4H_7)(CH_3CN)_5]^+$), 533.86 ($[Rh_2(\mu\text{-}NOC_4H_6)_2(CH_3CN)_4]^+$), 498.96 ($[Rh_2(\mu\text{-}NOC_4H_6)_2(CH_3CN)_3]^+$), 490.93 ($[Rh_2(\mu\text{-}NOC_4H_6)_2(CH_3CN)_1]^+$), 449.88 ($[Rh_2(\mu\text{-}NOC_4H_6)_2(NOC_4H_7)]^+$).

Preparation of *cis*-2,2-[$Rh_2(\mu\text{-}NOC_4H_6)_2(NOHC_4H_6)(CH_3CN)_5](BF_4)_2$ (9). A solution of **2** (20 mg, .030 mmol) in acetonitrile was stirred at room temperature in the absence of light for 18 h. The pink solution was reduced in volume to ~5 mL and the product was precipitated by adding diethyl ether to afford a reddish solid. The solid was purified by flash chromatography (Al_2O_3, toluene:CH_3CN 50:50) to afford **10** as a light red-purple solid. X-ray quality crystals were obtained from slow diffusion of diethyl ether into a solution of the product in acetonitrile. Yield: 12 mg (48 %). ^{1}H NMR (500 MHz, CD_3CN-d_3), δ (ppm): 1.96 (s, 6H axCH_3CN), 2.05 (m, pyrro), 2.34 (s, eqCH_3CN), 2.42 (s, pyrro),

2.45 (t, 2H, eq OH-pyrro), 2.49 (s, 3H, eqCH_3CN), 3.32 (m, pyrro), 3.43 (m, pyrro), 3.53 (m, pyrro), 3.72 (m, pyrro), 10.87 (s, 3,4-dihydro-2*H*-pyrrol-5-ol). ESI-MS: m/z = 539.90 ($[Rh_2(\mu\text{-}NOC_4H_6)_2(CH_3CN)_4]^{+2}$), 498.88 ($[Rh_2(\mu\text{-}NOC_4H_6)_2(CH_3CN)_3]^{+2}$), 457.89 ($[Rh_2(\mu\text{-}NOC_4H_6)_2(CH_3CN)_2]^{+2}$). Anal. Calcd. for $C_{20}H_{34}B_2F_8N_7O_4Rh_2 \bullet 1.15H_2O$: C, 28.78; N, 11.75; H, 4.14%. Found: C, 28.19; N, 12.33; H, 3.65%.

Preparation of *cis*-2,2-[$Rh_2(\mu\text{-}NOC_4H_6)_4(CH_3CN)_2$]$(PF_6)_1$ (10). A solution of $Rh_2(\mu\text{-}NOC_4H_6)_4(CH_3CN)_2$ (17 mg, .027 mmol) in acetonitrile was treated with $[FeCp_2](PF_6)$ (8.8 mg, .027 mmol) and the mixture was stirred for 1 h. After this time the solvent was removed under reduced pressure and the resulting dark purple solid was washed with diethyl ether and warm toluene and collected by filtration. X-ray quality crystals were obtained from slow diffusion of diethyl ether into a solution of the product in acetonitrile. Yield: 18 mg (84%). The compound is NMR silent. (ESI-MS: m/z = 541.97 ($[Rh_2(\mu\text{-}NOC_4H_6)_4]^+$), 583.02 ($[Rh_2(\mu\text{-}NOC_4H_6)_4(MeCN)]^+$).

Instrumentation and Methods

X-ray data sets were collected for compounds **8** and **9** on a Bruker CCD APEX diffractometer with graphite monochromated Mo Kα radiation (λ = 0.71073 Å). X-ray data for **10** was collected at beamline 15-ID-B at the Advanced Photon Source at Argonne National Laboratory using synchrotron radiation (λ= 0.41328 Å).

Results and Discussion

Synthesis and Characterization of the Dirhodium Pyrrolidinato Complexes

The synthesis of **8** involves the reaction of neutral *cis*-2,2-$Rh_2(\mu$-$NOC_4H_6)_4(CH_3CN)_2$ with a slight excess of alkylating agent Et_3OBF_4 in order to replace two 2-pyrrolidinato ligands for CH_3CN molecules according to a published procedure by Turro *et al*[79] (**Figure 4.1**). A similar procedure was followed for compound **9** by using the starting material *cis*-2,2-$Rh_2(\mu$-$NOC_4H_6)_4(CH_3CN)_2$. In both reactions, compounds **8** and **9** turned color from reddish-pink to magenta upon contact with the alkylating agent. Both compounds were purified by flash chromatography using Al_2O_3 as the solid phase and a mixture of toluene:CH_3CN as the mobile phase; in both cases a dark purple band was recovered. The dark purple fraction was reduced in volume and recrystallized. The purity of **8** and **9** was confirmed by ^{1}H-NMR spectroscopy and ESI mass spectrometry. Compounds **8** and **9** adopt H-H conformations and only one isomer was observed. Compound **8** contains an axial 2-pyrrolidonone whereas **9** has an equatorial pyrrol ligand *trans* to the *O* which is a result of the alkylation of one of the 2-pyrrolidinone bridging ligands followed by protonation *in situ*. X-Ray analysis of the dark purple fraction recovered from the flash chromatography of **8** and **9** indicated that it was the oxidized starting material crystallized as the tetrafluoroborate salt. Bear and coworkers[183] reported the electrochemical generation of the Rh_2(II,III) compound in bulk via controlled potential electrolysis of $Rh_2(\mu$-$NOC_4H_6)_4(CH_3CN)_2$. We prepared compound **10** by chemical oxidation of *cis*-2,2-$Rh_2(\mu$-$NOC_4H_6)_4(CH_3CN)_2$ with [FeCp](PF_6) in acetonitrile to afford a dark purple solution which was purified by TLC (toluene: CH_3CN, 1:1) and whose

identity was confirmed by ESI-MS; no ^{1}H NMR spectrum was obtained for this compound due to its paramagnetic nature.

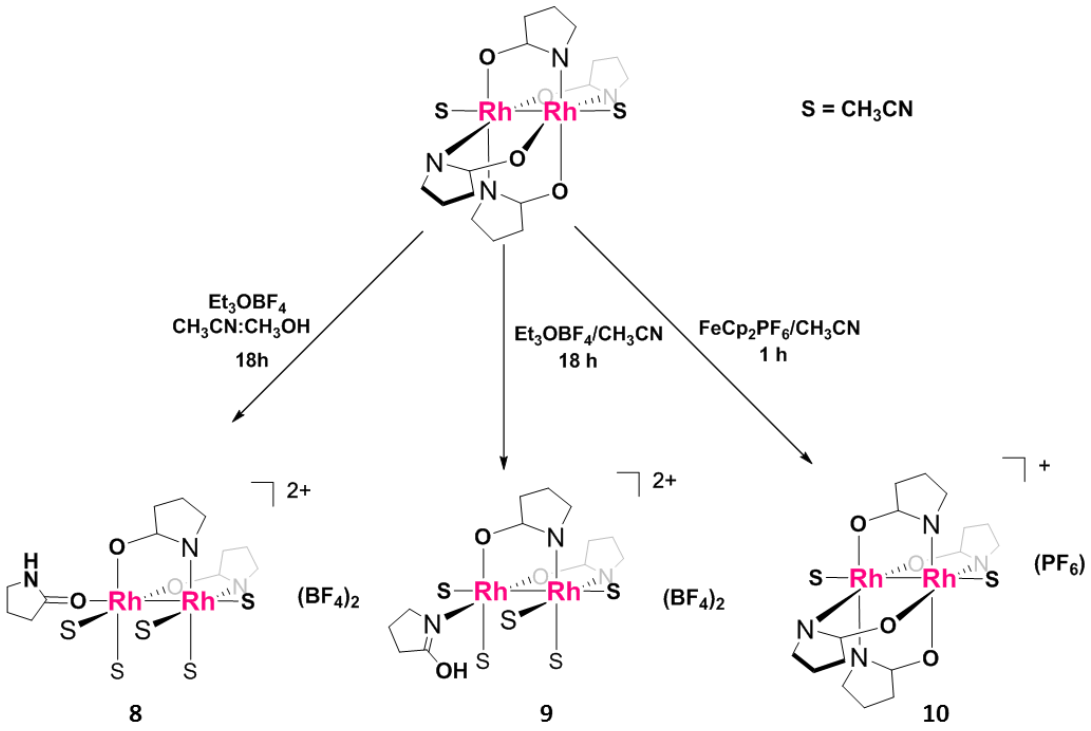

Figure 4.1 Schematic representation of the synthesis of compounds **8-10**.

X-ray Crystallographic Studies

Crystal data and structure refinement for compounds **8** and **9** are summarized in **Table 4.1**.

Table 4.1 Crystal and structural refinement data for **8-10**.

	8	**9**	**10**
Formula	$C_{22}H_{34}N_8O_3Rh_2B_2F_8$	$C_{26}H_{40}B_2F_8N_{10}O_3Rh_2$	$C_{20}H_{30}N_6O_4F_6PRh_2$
Mol. Wt. (g/mol)	838.01	920.12	769.29
Space group	$P2_12_12_1$	P-1	C2/c
a, b, c/ Å	11.6660(17)	11.931(10)	19.720(3)
	14.141(2)	12.430(10)	8.1009(10)
	18.853(3)	12.489(10)	16.911(2)
α, β, γ /°	90	93.696(11)	90
	90	97.323(12)	98.055(4)
	90	98.120(11)	90
Volume/Å^3	3110.1(8)	1812(3)	2674.8(6)
Z	4	2	4
2Θ range for data collection/°	54.204	46.502	29.558
R_{int}	0.061	0.0346	0.0397
Goodness-of-fit (all data)[a]	1.105	1.037	1.048
R_1,[b] wR_2[c] [all data]	R_1 = o.0453	R_1 = 0.0876	R_1 = 0.0748
	wR_2 = 0.1308	wR_2 = 1601	wR_2 = 0.1890

[a] $R = \sum \big| |F_o| - |F_c| \big| / \sum |F_o|$. [b] $wR = \{\sum[w(F_o^2 - F_c^2)^2] / \sum w(F_o^2)^2]\}^{1/2}$. [c] Goodness-of-fit = $\{\sum[w(F_o^2 - F_c^2)^2]/(n-p)\}^{1/2}$, where n is the number of reflections and p is the total number of parameters refined.

***cis*-2,2-[Rh_2(μ-NOC_4H_6)$_2$(NOC_4H_7)(CH_3CN)$_5$](BF_4)$_2$ (8)**. A pink needle was selected for the X-ray crystallographic analysis which was grown from slow diffusion of diethyl ether into a solution of **8** in CH_3CN. Compound **8** crystallizes in the chiral space group $P2_12_12_1$ and the cationic unit contains a dinuclear Rh_2(II,II) core coordinated to two bridging [2-pyrrolidinato]$^-$ ligands in a *cis*-2,2 arrangement with four CH_3CN ligands occupying the equatorial positions with another CH_3CN molecule in the axial position proximal to the N bridge head. There is a 2-pyrrolidinone molecule in the axial position of the Rh center coordinated to the O atom from the bridgehead with H-bonding interactions involving the NH group of the axial 2-pyrrolidione and the O atom of the bridge (N-H···O = 1.98 Å, 145.72(6)º) are observed (**Figure 4.2**). The Rh-Rh bond distance is 2.5752(4) Å which is longer than that of dirhodium paddlewheel complexes with four bridging ligands such as *cis*-2,2-[Rh_2(μ-NOC_4H_6)$_4$][183] but comparable to the partially solvated *cis*-[Rh_2($OC(O)CH_3$)$_2$(CH_3CN)$_6$][BF_4]$_2$.[77] The Rh-N [2-pyrro]$^-$ distances are in the range of 2.0014(2)-2.0190(2) Å which is longer than that of the *cis*-2,2-[Rh_2(μ-NOC_4H_6)$_4$][183]; the Rh-O [2-pyrro]$^-$ distances range between 2.0105(2)-2.0114(2) Å which is longer than for the parent compound. The Rh-N^N (eq CH_3CN) and Rh-N^O (eq CH_3CN) bond distances are in the range of Å and 2.0260(2)-2.0494(2) Å and 1.9763(2)-1.99414(2) respectively which are comparable to the corresponding parameters for the acetamide H,H and H,T isomers of *cis*-[Rh_2($HNOCCH_3$)$_2$(CH_3CN)$_6$][BF_4]$_2$[79]. The Rh-N (ax CH_3CN) distance is ~0.20 Å longer than that of the eq CH_3CN ligands and the Rh-O (ax Hpyrro) has a bond distance of 2.2460(3) Å which is ~0.40 Å longer than that

of the bridging ligands. Compound **8** adopts an eclipsed configuration of the eq CH_3CN with very minor distortions to the octahedral coordination sphere of the rhodium atoms.

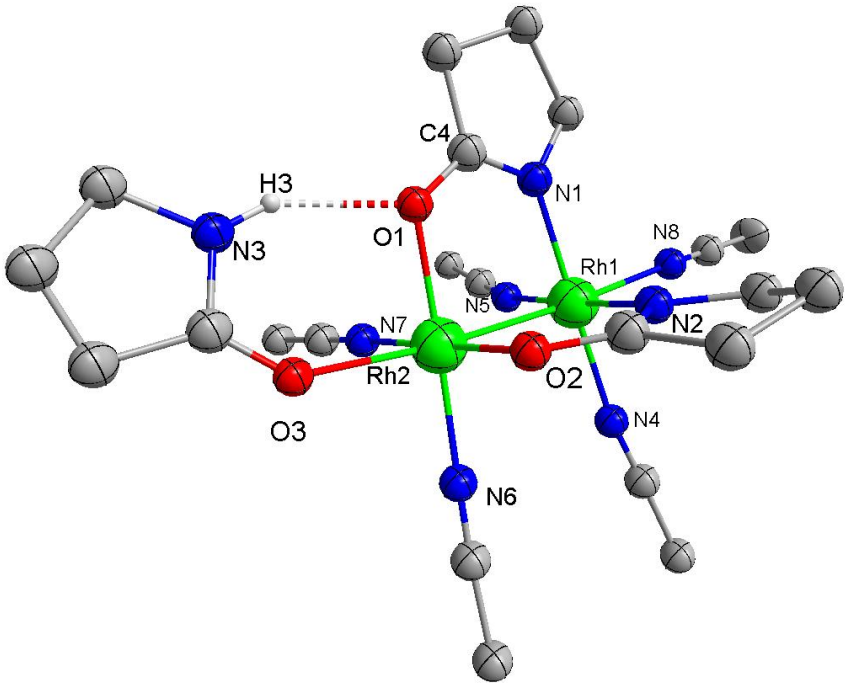

Figure 4.2 Thermal ellipsoid plot for the cationic unit **8** at the 50% probability level. The hydrogen atoms and counter ions have been omitted for the sake of clarity.

***cis*-2,2-[Rh_2(μ-NOC_4H_6)$_2$(η^1-$NOHC_4H_7$)(CH_3CN)$_5$](BF_4)$_2$ •2CH_3CN (9).** Compound **9** crystallizes in the space group P-1. The thermal ellipsoid plot in **Figure 4.3** shows that the cationic unit consists of a dirhodium core with two *cisoid* bridging 2-pyrrolidionato ligands in a H-H fashion and unlike the other partially solvated compounds, **9** bears four

eq CH_3CN monodentate ligands and one 3,4-dihydro-2*H*-pyrrol-5-ol in the equatorial position *trans* to the O from the bridge head and two axial CH_3CN molecules. The Rh-Rh bond distance is 2.547(2) Å, slightly shorter than that in **8**. The Rh-N (ax CH_3CN) bond distance are in the range of 2.198(9)-2.209(9) Å which is shorter than **8**. The Rh-N^N (eq CH_3CN) bond distances fall in the range of 2.018(8)-2.033(8) Å, similar to those of **8** and $[Rh_2(HNOCCH_3)_2(CH_3CN)_6][BF_4]_2$.[79] The Rh-$N^O$ bond distance is 1.973(9) Å, also comparable to the acetate and acetamide analogs. The 3,4-dihydro-2*H*-pyrrol-5-ol in the equatorial position is engaged in H-bonding with the O from the bridge (O-H⋯O = 1.781(6) Å, 160.2(6)º). Small distortions form the eclipsed configuration of the 2-pyrro bridging ligands, with the dihedral angle defined by O4-Rh2-Rh1-N2 being 6.2(3)º which is not observed in **8**. The equatorial 3,4-dihydro-2*H*-pyrrol-5-ol is positioned outside of the eq CH_3CN plane by 10.2(7)º; this displacement is mostly due to its ability to H-bond with the O6 from the bridgehead.

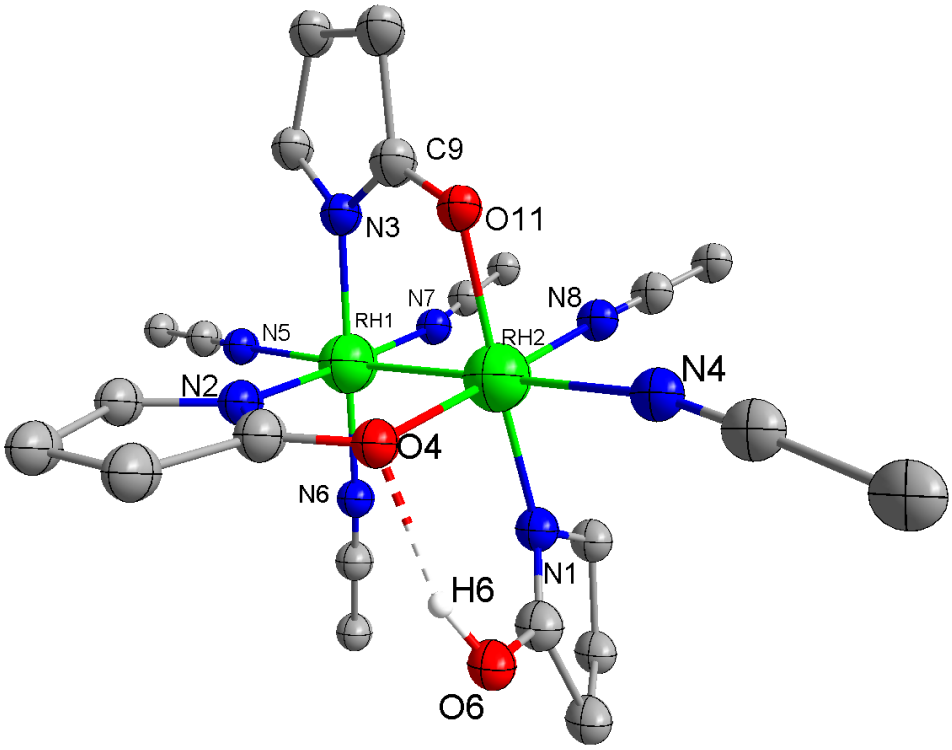

Figure 4.3 Thermal ellipsoid plot for the cationic unit **9** at the 50% probability level. The hydrogen atoms and counter ions have been omitted for the sake of clarity.

***cis*-2,2-[$Rh_2(\mu\text{-}NOC_4H_6)_4(CH_3CN)_2](PF_6)_1$ (10).** The oxidized compound [$Rh_2(\mu\text{-}NOC_4H_6)_4$ crystallizes in the space group C2c. The thermal ellipsoid plot shows that the cationic unit consists of a dirhodium core which lies on an inversion center and is bound to two *cis* N and two *cis* O atoms as in the case of [$Rh_2(\mu\text{-}NOC_4H_6)_4$ reported by Bear (**Figure 4.4**).[183] The dirhodium compound contains two acetonitrile molecules occupying the axial positions instead of the 2-pyrrolidinone molecules. The Rh-N_{ax} distances are 2.214(6) Å which are in agreement with other structures of the same type. The Rh-Rh bond distance is 2.4436(10) Å which is comparable to the neutral analog. Important bond

distances for this unit have been summarized in **Table 4.2**. The counter ion $[PF_6]^-$ lies on a C_2 axis and is disordered. The presence of the counter ion taken together with spectroscopic data confirms that the dirhodium compound is positively charged and that the Rh units are mixed-valence with a Rh_2(II,III) oxidation state.

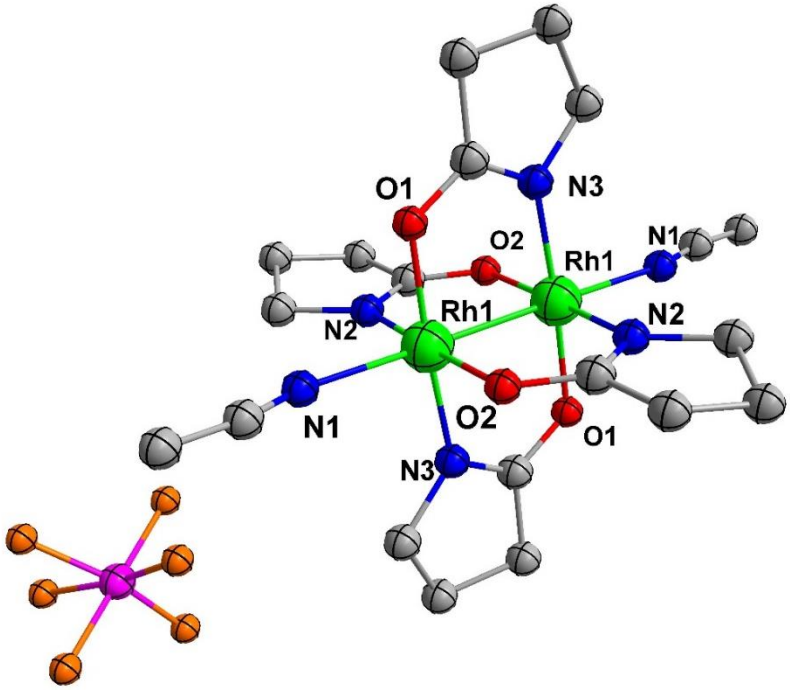

Figure 4.4 Thermal ellipsoid plot of the cationic unit **10** at the 50% probability level. The hydrogen atoms have been omitted for the sake of clarity.

Detailed bond distances and dihedral angles for compounds **8-10** are compiled in **Table 4.2**.

.

Table 4.2 Relevant bond distances and dihedral angles for compounds **8-10**.

8		**9**		**10**	
Bond Distances	**Length/Å**	**Bond Distances**	**Length/Å**	**Bond Distances**	**Length/Å**
Rh1-Rh2	2.5752(8)	Rh1-Rh2	2.547(2)	Rh1-Rh1'	2.4436(10)
Rh1-N1	2.019(7)	Rh1-N3	1.995(7)	Rh1-O1	2.033(5)
Rh1-N2	2.001(6)	Rh1-N2	2.000(7)	Rh1-N1	2.214(6)
Rh1-N5	2.049(7)	Rh1-N6	2.018(8)	Rh1-O2	2.033(5)
Rh1-N8	2.206(7)	Rh1-N7	2.033(8)	Rh1-N2	1.983(6)
Rh1-N4	2.026(7)	Rh1-N5	2.208(8)	Rh1-N3	1.978(6)
Rh2-O2	2.010(6)	Rh2-N1	2.011(8)		
Rh2-O2	2.011(5)	Rh2-N8	1.973(8)		
Rh2-N7	1.976(6)	Rh2-O11	2.020(7)		
Rh2-N6	1.994(7)	Rh2-O4	2.020(6)		
Rh2-O3	2.246(7)	Rh2-N4	2.198(9)		
O1-H3	1.951(6)	O4-H6	1.7803(12)		
Dihedral	**°**	**Dihedral**	**°**	**Dihedral**	**°**
N2-Rh1-Rh2-O2	-1.4(2)	O4-Rh2-Rh1-N2	6.168(5)	N2-Rh1-Rh1'-O2	1.15
O1-Rh2-Rh1-N1	-3.6(3)	O11-Rh2-Rh1-N3	8.385(7)	N3-Rh1'-Rh1-O1	0.48
N7-Rh2-Rh1-N5	-0.1(3)	N7-Rh1-Rh2-N8	6.467(5)		
N4-Rh1-Rh2-N6	-1.5(3)	N6-Rh1-Rh2-N1	6.811(5)		
Rh2-O3-C12-N3	-12.3(11)	N1-C1-O6-Rh2	-5.197(5)		
O1-C4-N1-C1	176.6(8)	C6-C5-N2-C8	0.7801(7)		
C5-N2-C8-O2	-179.5(6)	O11-C9-N3-C12	-176.851(3)		

NMR Spectroscopic Studies of Compounds **8** *and* **9**

The ^{1}H NMR spectrum of **8** shows two multiplets at δ = 2.02 ppm and δ = 2.39 ppm corresponding to the protons from the 2-pyrrolidinato bridging ligands and that of the axially bound 2-pyrrolidionone (**Figure 4.5**). There are two unique multiplets at δ = 3.39 ppm and 3.47 ppm corresponding to the 2-pyrrolidinato ligands, each integrating to 4 protons. The triplet resonance at δ = 3.29 ppm integrates to two protons and is assigned as the axially bound 2-pyrrolidione molecule. The two singlet resonances at δ = 2.46 ppm and δ = 2.49 ppm correspond to the equatorial CH_3CN molecules. The eq CH_3CN molecules were integrated against the bridging 2-pyrrolidinate ligand resonance at δ = 3.39 ppm, the δ = 2.46 ppm but does not integrate to six protons which indicates fast exchange of the monodentate ligand with the NMR solvent CD_3CN in the dark. Compound **9** also has four multiplets which are not as resolved as in the case of **8** located at δ = 2.02 ppm, δ = 3.32 ppm, δ = 3.43 ppm and δ = 3.53 ppm that correspond to the 2-pyrrolidinato bridging ligand (**Figure 4.6**). There are three singlet resonances at δ = 2.34 ppm, δ = 2.42 ppm and δ = 2.49 ppm and a triplet at δ = 2.45 ppm. Also there three multiplets at δ = 2.66 ppm, δ = 2.81 ppm and δ = 3.69 ppm that are ascribed as the equatorial 3,4-dihydro-2*H*-pyrrol-5-ol ligand and a singlet at δ = 10.87 ppm corresponding to the hydroxyl proton which is not observed in **8**.

The X-Ray crystallographic data for these compounds shows that the Rh centers are supported by two *cis* $[NOC_4H_6]^-$ groups in a head-to-head conformation and that the third 2-pyrrolidinone in **8** resides in the axial position. Unlike **8**, compound **9** bears a 3,4-dihydro-2*H*-pyrrol-5-ol in an equatorial position *trans* to the *O* atom from the bridging

group which explains the triplet resonance at $\delta = 2.45$ ppm. The fast exchange of the eq CH_3CN ligands for **8** and **9** prompted the ^1H NMR study of these in D_2O in the dark and after irradiation with white light at different time intervals the results of which will be discussed in the following section.

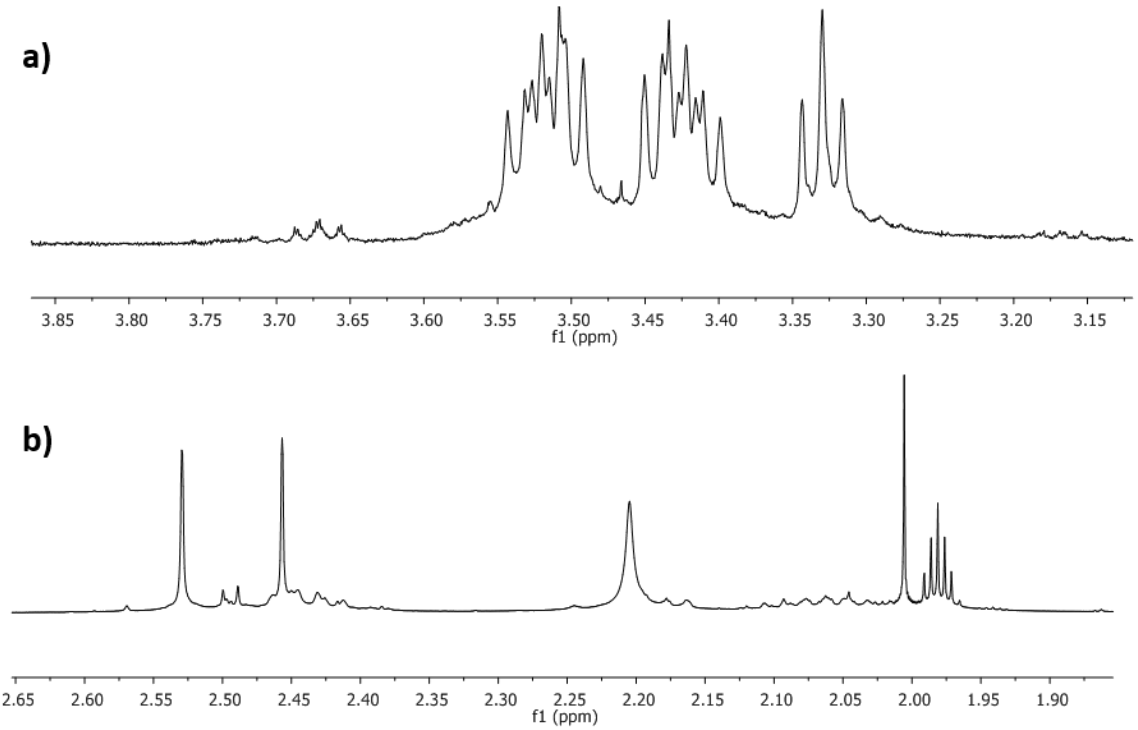

Figure 4.5 a) ^1H NMR spectrum of compound **8** in CD_3CN, bridging 2-pyrrolidinate signals b) ^1H NMR spectrum of eq CH_3CN signals of compound **8**.

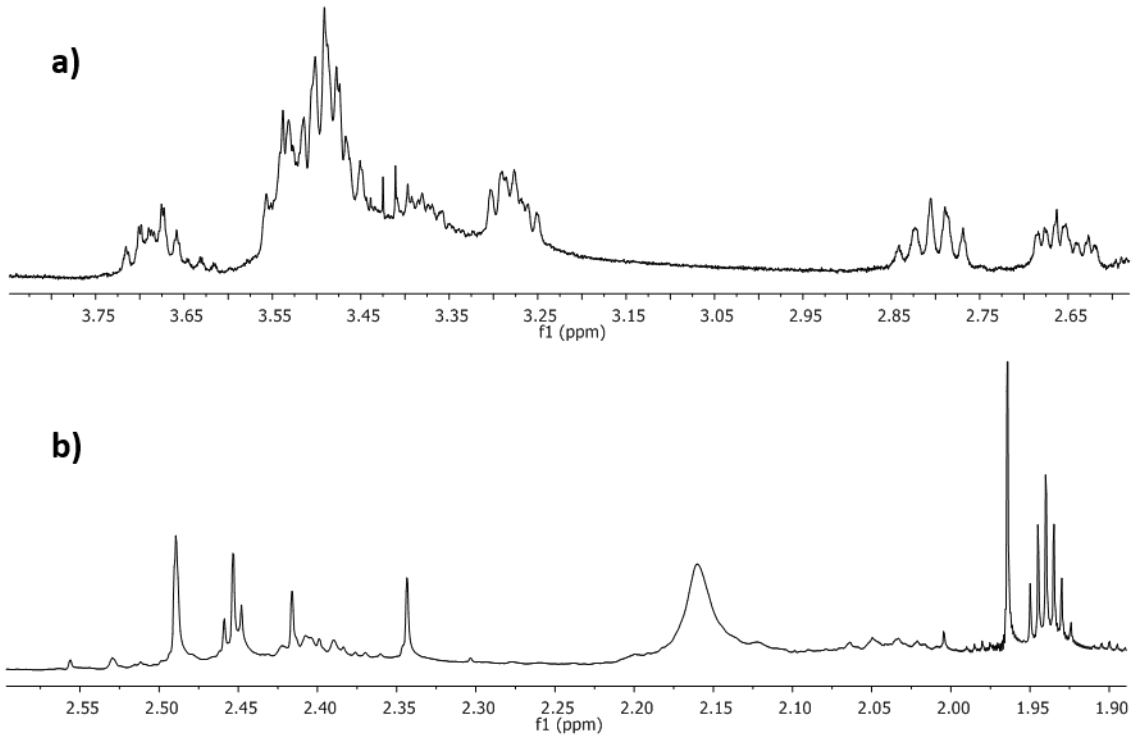

Figure 4.6 a) ^{1}H NMR spectrum of compound **9** in CD_3CN, bridging 2-pyrrolidinate signals b) ^{1}H NMR spectrum of eq CH_3CN signals of compound **9**.

*Time Lapse ^{1}H-NMR Studies of **8** and **9***

In order to study the exchange of the equatorial CH_3CN ligands in **8** and **9**, ^{1}H-NMR spectroscopy was utilized. The ^{1}H NMR spectrum of compound **8** in D_2O exhibits two singlets of equal intensity at δ = 2.50 ppm and δ = 2.57 ppm and a triplet at δ = 2.34 ppm assigned to the eq CH_3CN^{N}, eq CH_3CN^{O} and 2-pyrrolidinate ligands respectively (**Figure 4.7**). The ^{1}H NMR resonances were assigned by comparison with the *cis*-2,2-$[Rh_2(HNOCCH_3)_2(CH_3CN)_6]$ compound.[79] The eq CH_3CN ligands were integrated against the 2.34 ppm resonance since it does not change with time. After 30 min in the dark, a decrease in intensity for the 2.50 ppm and 2.57 ppm resonances is observed which

is due to the exchange of the eq CH3CN^{N} and eq CH3CN^{O} ligands respectively. The lability of eq CH_3CN with D_2O was also studied for compound **9** in the dark (**Figure 4.8**). There are three singlet resonances at 2.39 ppm, 2.53 ppm and 2.56 ppm. The features at 2.39 ppm and 2.53 ppm correspond to the eq CH_3CN molecules *trans* to N. The resonance at 2.53 ppm decreases in intensity as the reaction progresses whereas the one at 2.39 ppm does not change during the time investigated. The resonance at 2.56 ppm is assigned as the eq CH_3CN t*rans* to O by comparison to **8** which has a resonance at 2.56 ppm as well and exchanges slowly in the dark as in the case of **9**. There are two multiplet resonances at 2.51 ppm and 3.49 ppm that are assigned as the eq pyrrol; these two resonances decrease in intensity after 3 h which indicates that the ligand is labile in the dark.

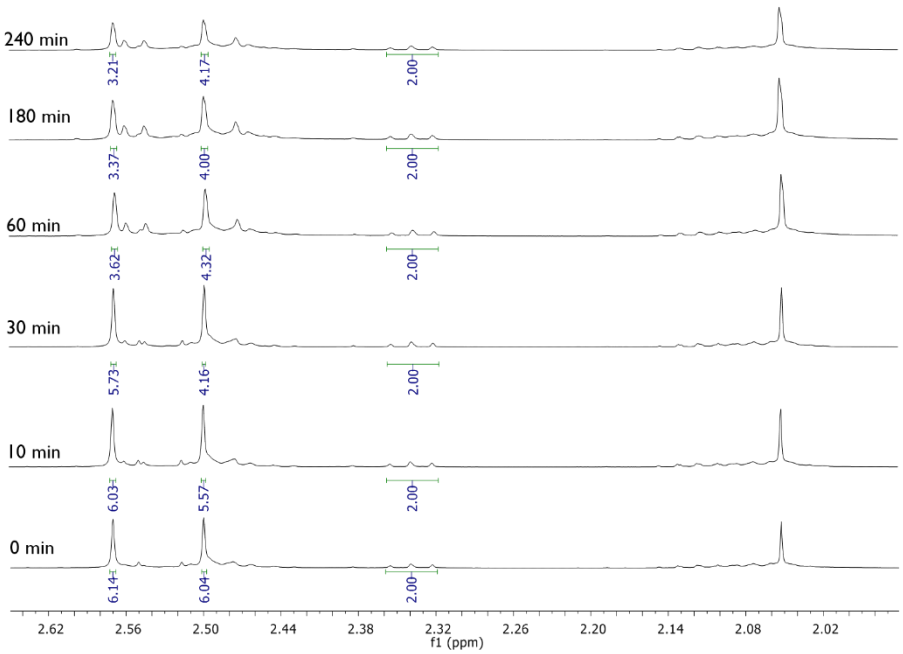

Figure 4.7 Changes in ^{1}H NMR spectra of 8 in D_2O as a function of time in the dark; only the region involving the changes in the spectra are shown.

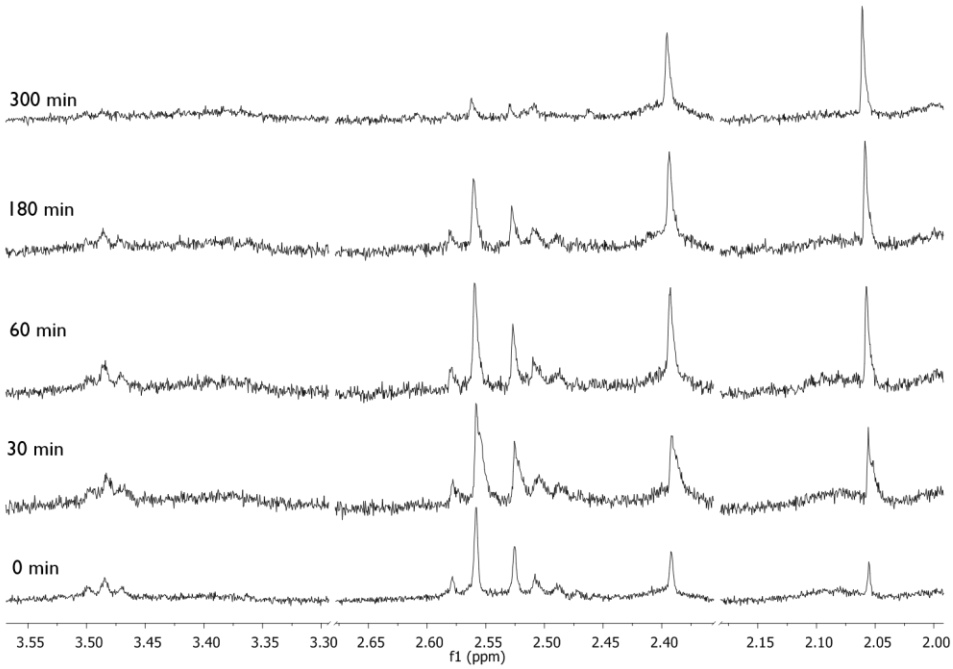

Figure 4.8 Changes in ^{1}H NMR spectra of **9** in D_2O as a function of time in the dark; only the region involving the changes in the spectra are shown.

A time lapse experiment was also performed for compounds **8** and **9** after irradiation. This experiment reveals that the eq CH_3CN^{O} exchange takes more than 1 h of irradiation to take place and that release of eq CH_3CN^{N} is very slow. There is also an increase in intensity in the resonance at δ = 2.06 ppm which corresponds to free CH_3CN. Both exchange processes are much slower as compared to the acetamide compounds reported by Turro *et* al.[79] which could be due to the power dependence of the photoaquation process (**Figure 4.9**).[77] As in the case of **8**, compound **9** was irradiated with white light (>400-700 nm) and a ^{1}H NMR spectrum was taken at different time intervals in order to determine the lability of the eq CH_3CN ligands and that of the eq pyrrole molecule. The eq pyrrole resonance is observed at 2.10 ppm and 3.49 ppm and

these signals decrease in intensity with increasing irradiation times (**Figure 4.10**). The eq CH_3CN^O resonance at 2.39 ppm disappears upon irradiation and the eq CH_3CN^N resonances at 2.53 ppm and 2.56 ppm also decrease in intensity with time. The 2.06 ppm resonance increases in intensity which corresponds to free CH_3CN. Several new singlet resonances can be observed after 5 h of irradiation, namely 2.16 ppm, 2.46 ppm and 2.61 ppm, which correspond to various photoaquation products as in the case of other compounds of this type such as the dirhodium acetamides and oxopyridinates, *cis*-$[Rh_2(HNOCCH_3)_2(CH_3CN)_6][BF_4]_2$ and *cis*-$[Rh_2(mhp)_2(CH_3CN)_6][BF_4]_2$ respectively.[79,170]

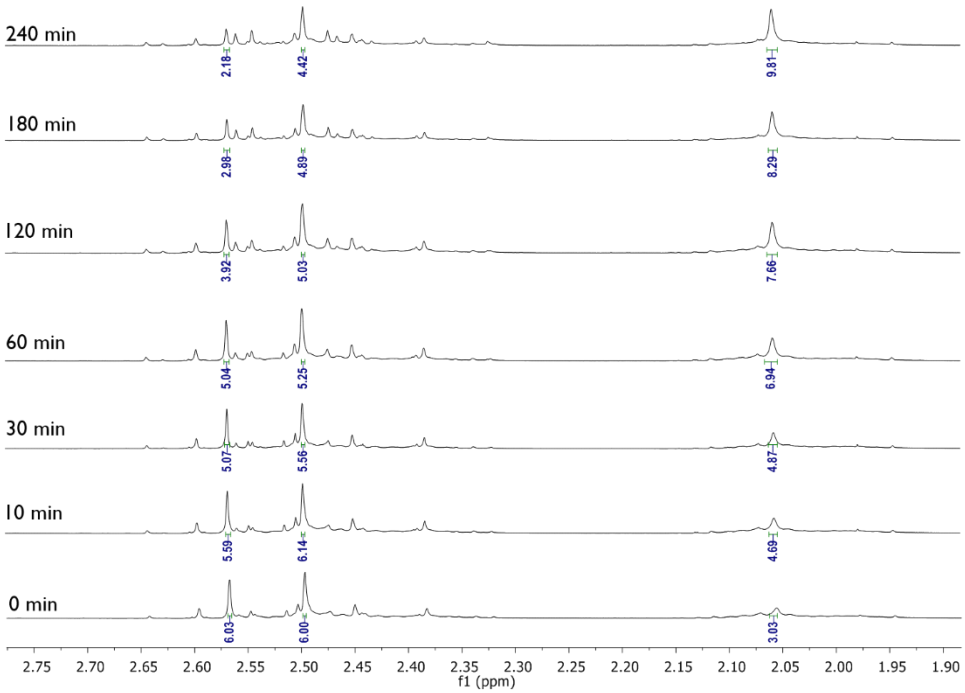

Figure 4.9 Changes in ^1H NMR spectra of 8 in D_2O as a function of irradiation time (λ_{irr} > 400-700 nm); only the region involving the changes in the spectra are shown.

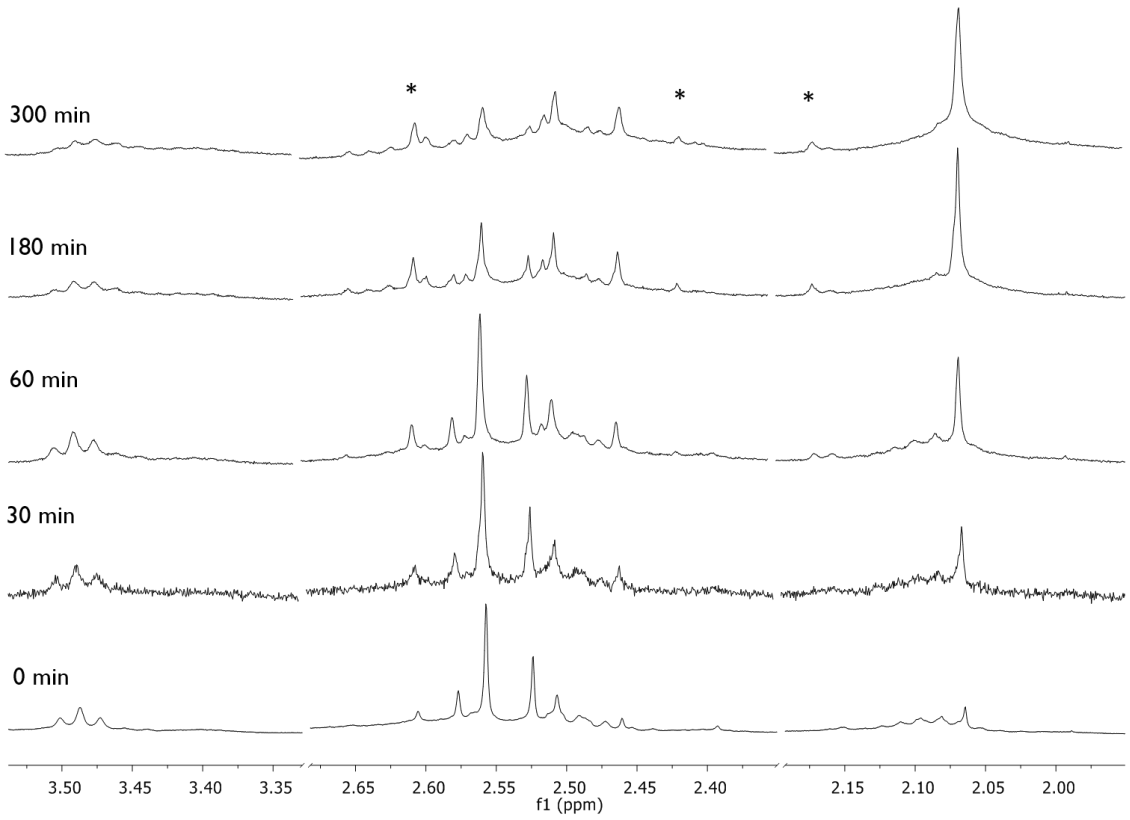

Figure 4.10 Changes to the ^{1}H NMR spectra of **9** in D_2O as a function of irradiation time (λ_{irr} >400-700 nm), where * denotes product; only the region involving the changes in the spectra are shown.

Electronic Absorption and Electrochemical Studies

Electronic absorption spectra were obtained for compounds **8-10** in CH_3CN and H_2O; the data is summarized in **Table 4.3**.

Table 4.3 Electronic absorption data for complexes **8-10** in CH_3CN and H_2O at room temperature.

	λ (nm), (ε x 10^3 (M^{-1}•cm^{-1})) in CH_3CN	λ (nm), (ε x 10^3 (M^{-1}•cm^{-1})) in H_2O
8	277 (5.8), 330 (0.75), 515 (0.33)	273 (1.0), 370 (0.76), 555 (0.51)
9	275 (13.2), 359 (0.42), 525 (0.25)	275 (36.3), 380 (0.25), 550 (0.17)
10	245 (12.4), 335 (0.82), 490 (3.86), 530 (3.63), 1033 (2.05), ~1410 (0.03)	250(7.53), 330 (0.22), 475 (4.05), 520 (3.87), 1050 (1.62)

The electronic absorption spectra of **8** and **9** exhibit similar behavior in CH_3CN. There is a transition at 515 nm for **8** and 525 nm for **9**, which are ascribed as metal center transitions of the type $Rh_2(\pi^*) \rightarrow Rh(\sigma^*)$ with some bridging ligand character (**Figure 4.11a**). Both compounds exhibit absorptions between 330-360 nm; these features have been observed for the partially solvated compounds $[Rh_2(HNCOCH_3)_2(CH_3CN)_6]^{2+}$(~350 nm),[170] $[Rh_2(6\text{-R-oxo-pyridinate})_2(CH_3CN)_6]^{2+}$ (~380 nm)[170] and $[Rh_2(OOCCH_3)_2(CH_3CN)_6]^{2+}$ (~363 nm).[77] The transitions in this region are characterized by contributions from the $Rh(\pi^*)$ to Rh-$CH_3CN_{eq}(\sigma^*)$ and $Rh(\sigma^*)$ molecular orbitals and are weak as indicated by molar absorptivity coefficients (**Table 4.3**). The bands at 275 nm for both **8** and **9** correspond to metal-centered transitions with contributions from both bridging ligands and the equatorial ligands. Electronic absorption spectra were obtained

in water for both **8** and **9** and, as expected, there is a bathochromic shift of the lowest energy transition in accordance with the behavior of analogous compounds under the same experimental conditions (**Figure 4.11b**).

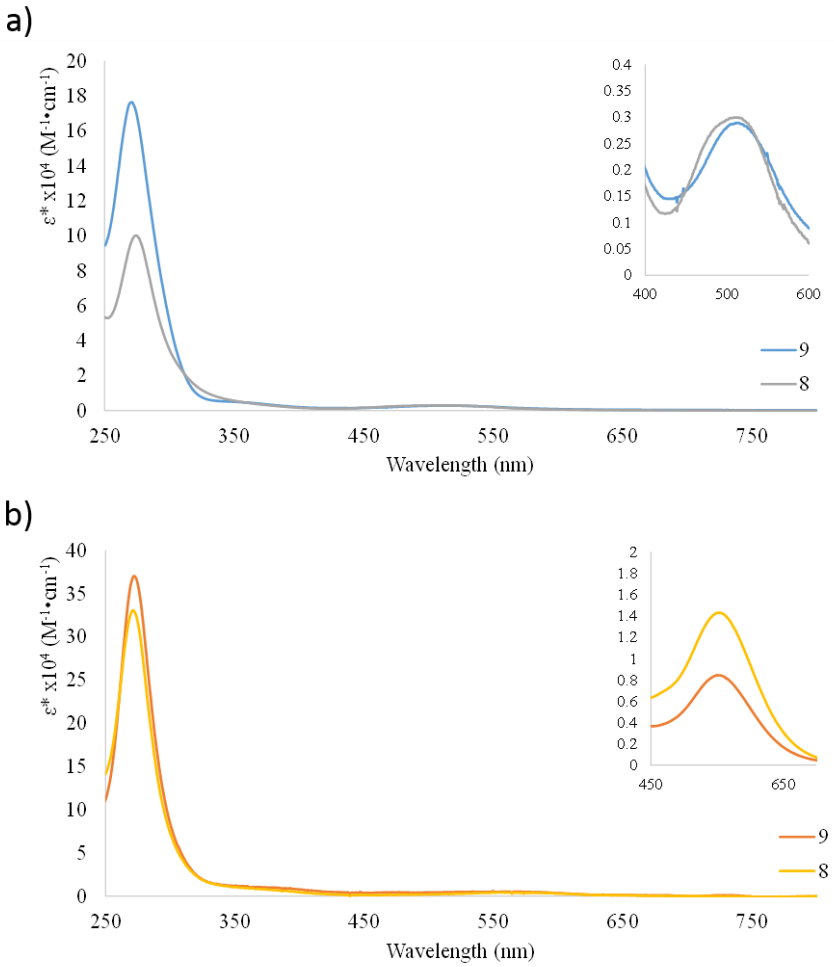

Figure 4.11 Electronic absorption spectra of compounds **8** and **9** in (a) CH_3CN and (b) H_2O at room temperature.

The electronic absorption spectrum of compound **10** had been reported in the late 1980's by Bear *et* al. and it was noted that the compound has a weak band at 490 nm and 530 nm that do exhibit a bathochromic shift when the solvent is changed unlike previous compounds (**Figure 4.12**).[109] There are also two other transitions in the low energy region of the UV and NIR area of the spectrum in acetonitrile, at 1033 nm and 1410 nm (**Figure 4.12a**, inset) which were not reported by Bear

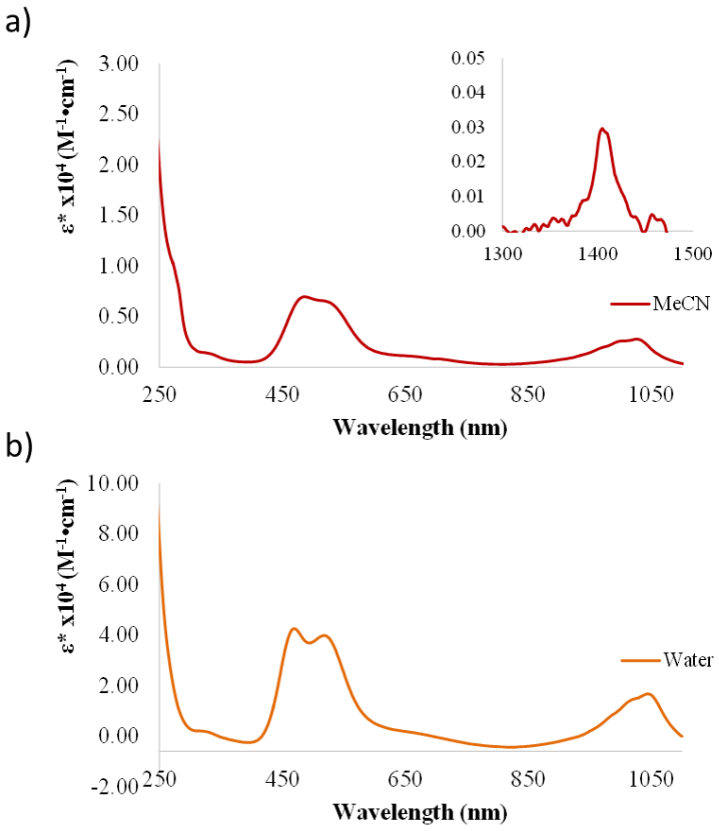

Figure 4.12 Electronic absorption spectra of compounds **10** in (a) CH_3CN and (b) H_2O at room temperature.

The stability of compounds **8** and **9** in H_2O was assessed by measuring the electronic absorption spectra in the dark at different time intervals over a period of 24 h. The lowest energy transition for partially solvated compounds as **8** and **9** are characterized by a decrease in intensity over time when eq CH_3CN molecules are being labilized, with a concomitant increase in intensity and a bathochromic shift of this band. This is not the case for **8** over the course of the experiment; there is a decrease in intensity (**Figure 4.13a**) in the band at 555 nm and a small bathochromic shift is observed which is not as prominent as in the case of the model compound $[Rh_2(OOCCH_3)_2(CH_3CN)_6]^{2+}]$[77] (**Figure 4.13b**). This experiment supports the time lapse ^1H NMR studies in the dark for this compound in that **8** is stable in the dark as evidenced by the minimal decrease in intensity of the 555 nm band.

Compound **9** has its lowest energy transition at 550 nm. The time lapse experiment showed a decrease in the absorption and, unlike **8**, a bathochromic shift is observed to 575 nm as the time progresses and the band increases in intensity. An isobestic point is observed at 565 nm at t = 5 h. The inset in **Figure 4.14** shows the decrease in absorbance of the band at 550 nm and the increase in absorbance of the band at 575 nm. These results are in agreement with the ^1H NMR data obtained during the time lapse experiments in the dark, namely that **9** exchanges the eq CH_3CN ligands in the dark.

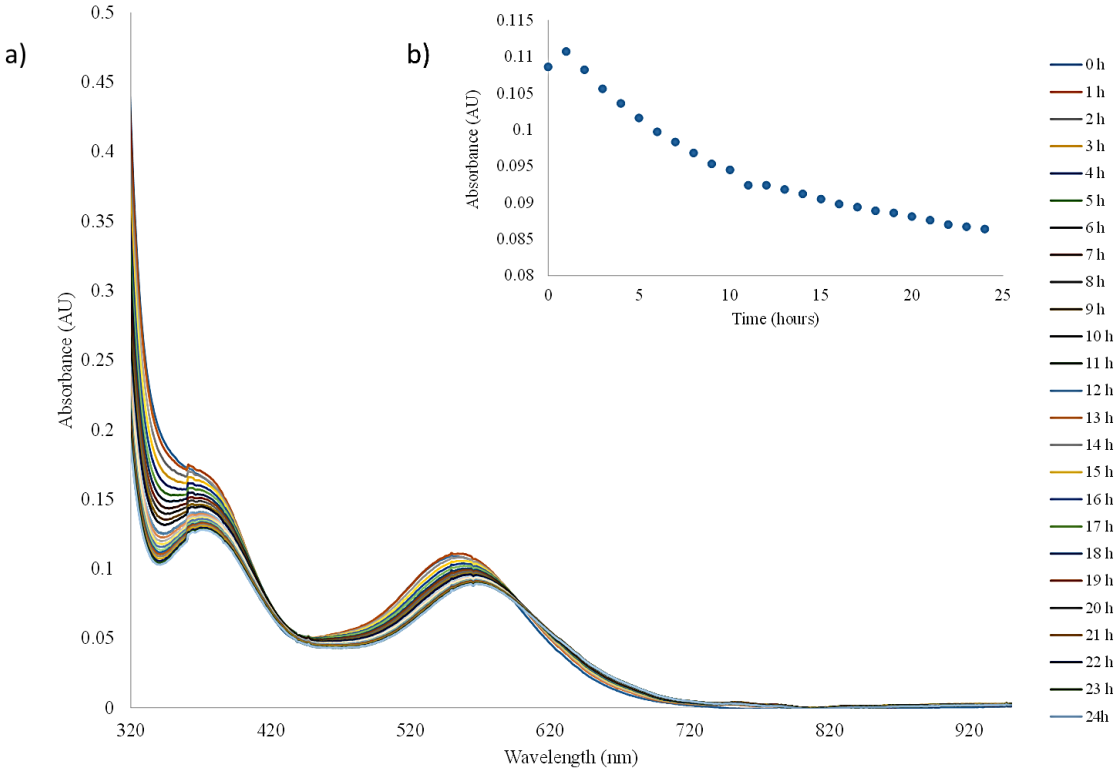

Figure 4.13 a) Electronic absorption spectra of **8** at room temperature in H_2O at different time intervals. **b**) Inset absorbance values for the 555 nm absorption band as a function of time.

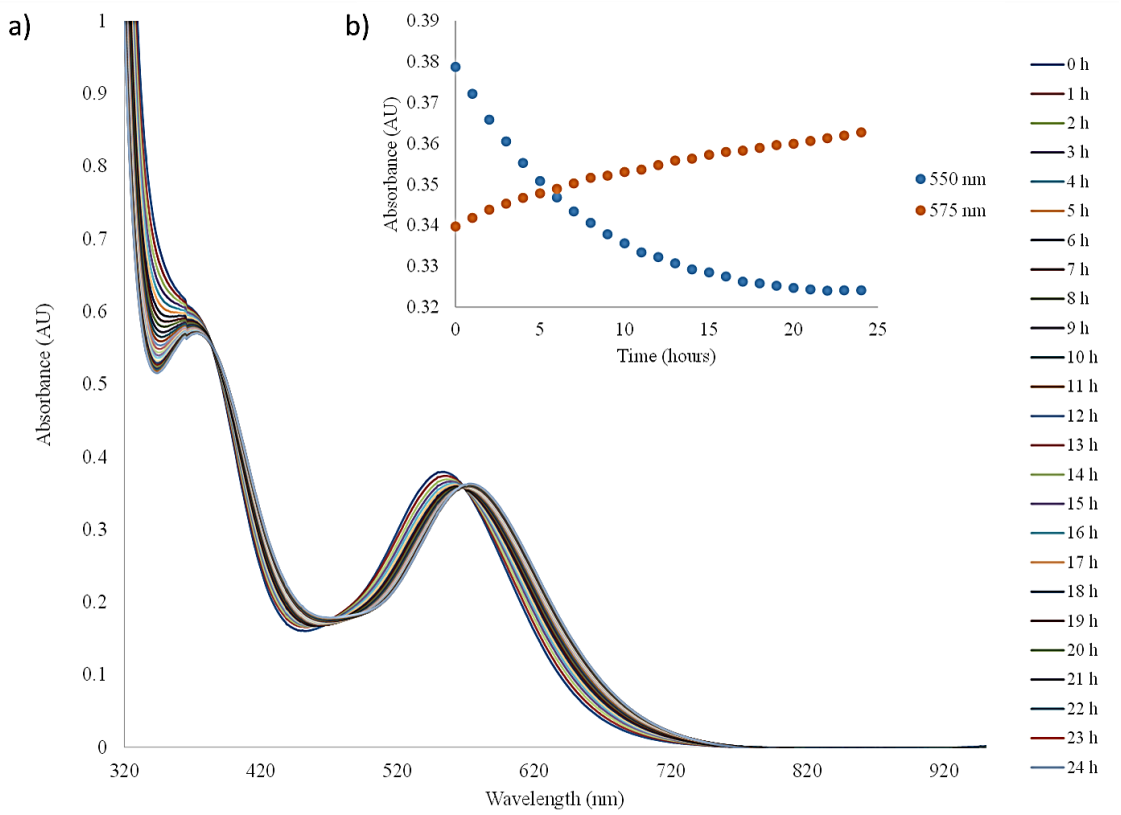

Figure 4.14 a) Electronic absorption spectra of **9** at room temperature in H_2O at different time intervals. **b**) Inset absorbance values for the 550 nm and 575 nm absorption bands as a function of time.

The redox potentials of **8-10**, $[Rh_2(pyrro)_4]$ and 2-pyrrolidinone were obtained by cyclic voltammetry measurements in acetonitrile and are listed in **Table 4.4**. The free ligand 2-pyrrolidinone ligand does not exhibit any electrochemical reactions within the limits of the solvent stability. Compounds **8** and **9** exhibit similar electrochemical behavior in that both exhibit a reversible oxidation event at +1.58 V which is consistent with the $Rh_2(II,II) \rightarrow Rh_2(II,III)$ couple as in the case of the acetamide partial paddlewheel complexes and the *cis*-2,2-$[Rh_2(pyrro)_4]$ compound of Bear *et* al. and *cis*-$[Rh_2(HNCOCH_3)(CH_3CN)_6](BF_4)_2$.[79,109,182] There is an irreversible reduction for **8** and **9** located at -1.23 V and -1.44 V, an event that is also observed for the partially solvated acetamide compounds reported by Turro, but which is absent for *cis*-$[Rh_2(OCOCH_3)_3(CH_3CN)_6][BF_4]_2$. There is an additional reduction for **8** and **9** at -1.02 V and -0.92 V respectively. In the case of **8** there is an additional oxidation at +0.20 V that is not present in **9** and by comparing it to the starting material it appears to be metal based as well. With regards to the irreversible oxidation at ~0.89 V, this is a chemical reaction that occurs after the compound has been oxidized from $Rh_2(II,II)$ to $Rh_2(II,III)$ as in the case of $[Rh_2(pyrro)_4]$**.** Compound **10** had been previously reported by Bear *et.* al.,[109] and once the compound oxidizes to the $Rh_2(II,III)$ analog, an irreversible chemical reaction occurs which is also observed for compounds **8** and **9**. It is important to note that **10** decomposes after several scans and the same is observed if the compound is left in solution for prolonged periods of time.

Table 4.4 Electrochemical reduction potentials for compounds **8-10**as well as the free ligands.

Potential, V	$E_{1/2}$ ox(1)	$E_{1/2}$ ox(2)	E_{pc} red(1)	E_{pc} red(2)	E_{pc} red(3)
$Rh_2(\mu\text{-pyrro})_2(MeCN)_5(Hpyrro)1](BF_4)_2$	1.58	0.20	0.87[a]	-1.02[a]	-1.28[a]
$Rh_2(\mu\text{-pyrro})_2(MeCN)_5(NOHC_4H_6)1](BF_4)_2$	1.58	-	0.87[a]	-0.92[a]	-1.24[a]
$[Rh_2(pyrro)_4(MeCN)_2](PF_6)_1$	1.37	0.17	0.89[a]	-	-
$[Rh_2(pyrro)_4(MeCN)_2]$	1.38	0.18	0.89[a]	-	-
2-pyrrolidinone	[b]				

[a] Irreversible [b] Not active within the limits of the solvent.

Computational Studies

Density functional theory calculations were conducted on compounds **8** and **9** in order to aid in the assignment of the electronic transitions in the UV spectra and to augment the electrochemistry results. The optimizations of **8** and **9** were performed based on the crystal structures as a starting point for the geometry optimization. The results of these optimizations are in close agreement with the X-ray structures (**Table 4.5**). The bond distances from the calculated cationic structures of **8** and **9** are comparable to that of the crystal structures, although the dihedral angles vary slightly from the experimental data which may result from the splaying of the eq CH_3CN ligands upon optimization of the cationic structures under the solvation model. The TD-DFT calculations were conducted on the optimized structures of compounds **8** and **9** in both CH_3CN and H_2O.

Table 4.5 Experimental bond distances obtained from X-ray crystallography data and the calculated distances derived from DFT gas phase optimization of the cationic structures of compounds **8** and **9**.

8			**9**		
Bond	**Experimental**	**Calculated**	**Bond**	**Experimental**	**Calculated**
	Length/Å	**Length/Å**		**Length/Å**	**Length/Å**
Rh1-Rh2	2.5752(8)	2.5900(3)	Rh1-Rh2	2.547(2)	2.5774(3)
Rh1-N1	2.019(7)	2.0162(8)	Rh1-N3	1.995(7)	2.0151(6)
Rh1-N2	2.001(6)	2.0170(1)	Rh1-N2	2.000(7)	2.0232(9)
Rh1-N5	2.049(7)	2.0452(4)	Rh1-N6	2.018(8)	2.0471(7)
Rh1-N8	2.206(7)	2.2761(5)	Rh1-N7	2.033(8)	2.0399(1)
Rh1-N4	2.026(7)	2.0426(3)	Rh1-N5	2.208(8)	2.22716(8)
Rh2-O1	2.010(6)	2.0328(4)	Rh2-N1	2.011(8)	2.0575(2)
Rh2-O2	2.011(5)	2.0144(2)	Rh2-N8	1.973(8)	1.9923(2)
Rh2-N7	1.976(6)	2.0044(1)	Rh2-O11	2.020(7)	2.0514(2)
Rh2-N6	1.994(7)	1.9969(1)	Rh2-O4	2.020(6)	2.0387(9)
Rh2-O3	2.246(7)	2.2259(4)	Rh2-N4	2.198(9)	2.1952(1)
O1-H3	1.951(6)	1.9633(1)	O4-H6	1.7803(12)	1.6394(1)
Dihedral	**º**	**º**	**Dihedral**	**º**	**º**
N2-Rh1-Rh2-O2	-1.4(2)	-5.7(1)	O4-Rh2-Rh1-N2	6.168(5)	16.183(6)
O1-Rh2-Rh1-N1	-3.6(3)	-4.9(8)	O11-Rh2-Rh1-N3	8.385(7)	16.723(8)
N7-Rh2-Rh1-N5	-0.1(3)	-6.2(5)	N7-Rh1-Rh2-N8	6.467(5)	21.035(4)
N4-Rh1-Rh2-N6	-1.5(3)	-7.2(9)	N6-Rh1-Rh2-N1	6.811(5)	19.615(1)
Rh2-O3-C12-N3	-12.0(2)	-10.7(4)	N1-C1-O6-Rh2	-5.197(5)	-10.782(3)
O1-C4-N1-C1	176.6(8)	178.3(2)	C6-C5-N2-C8	0.7801(7)	1.549(9)
C5-N2-C8-O2	-179.5(6)	-177.4(1)	O11-C9-N3-C12	-176.851(3)	-175.439(9)

The electronic configuration of $Rh_2(O_2CCH_3)_4(L)_2$ in the ground state is $\sigma^2 \pi^4\delta^2\pi^{*4}\delta^{*2}\sigma^*$ with the HOMO being the Rh-Rh(δ*) orbital.[187-188] Coordination of the donating ligand 2-pyrrolidinate to the dirhodium core causes a destabilization of the Rh(δ*) by antibonding interactions of the 2-pyrrolidinate ligands with the metal based orbital, raising it in energy and making it the HOMO, as observed for other compounds such as $Rh_2(DTolF)_4$.[189] The electronic configuration for this new family of dirhodium compounds is $\pi^4\delta^2\pi^{*4}$ $\sigma^2\delta^{*2}\sigma^*$ for compounds **8** and **9**. On the other hand, the LUMOs for **8** and **9** have Rh(σ*) character which is consistent with the well-studied compounds $Rh(O_2CCH_3)_4(L)_2$ and $Rh_2(O_2CCH_3)_2(CH_3CN)_6]^{2+}$. The LUMO+1 orbitals have Rh-Leq(σ*) antibonding character with electron density concentrated on the acetonitrile ligand positioned *trans* to the oxygen atom from the 2-pyrrolidinato bridging ligand as in the case of the $[Rh_2(HNOCCH_3)_2(CH_3CN)_6]^{2+}$ reported by Turro. The MO diagram involving the Rh_2(II,II) unit for compounds **8** and **9** was constructed and the visualization of the frontier orbitals depicted with Agui (**Figure 4.15** and **Figure 4.16**); energy and orbital contributions have been summarized in **Table 4.6**. In the case of the oxidized compound **10** the electronic configuration becomes π^4 $\sigma^2\pi^{*4}\delta^2\delta^{*1}\sigma^*$. The HOMO and SOMO orbitals of $[Rh_2(NOC_4H_6)_4]^+$ are the Rh(δ) and Rh(δ^*) orbitals, respectively. The LUMO as in the case of other dirhodium carboxylates and **8** and **9** is the metal based orbital Rh(σ^*). The δ orbital is higher in energy than that of the π^* orbitals, this may be attributed to the destabilization of the δ orbital through interactions with the N_π that raises the energy of both δ and δ^* orbitals.

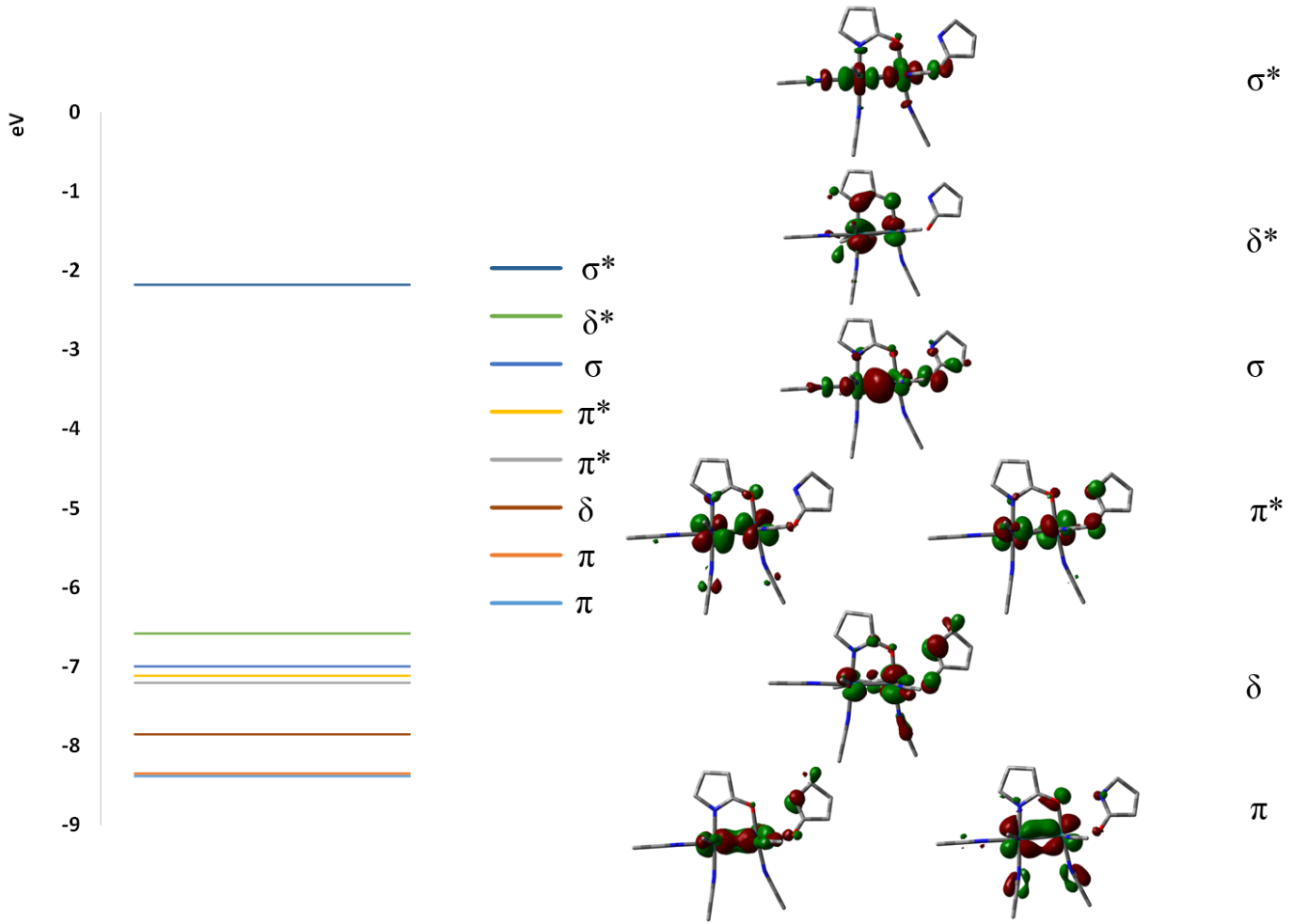

Figure 4.15 MO diagram involving the dirhodium core unit in **8** obtained by DFT calculations (iso-value=0.04).

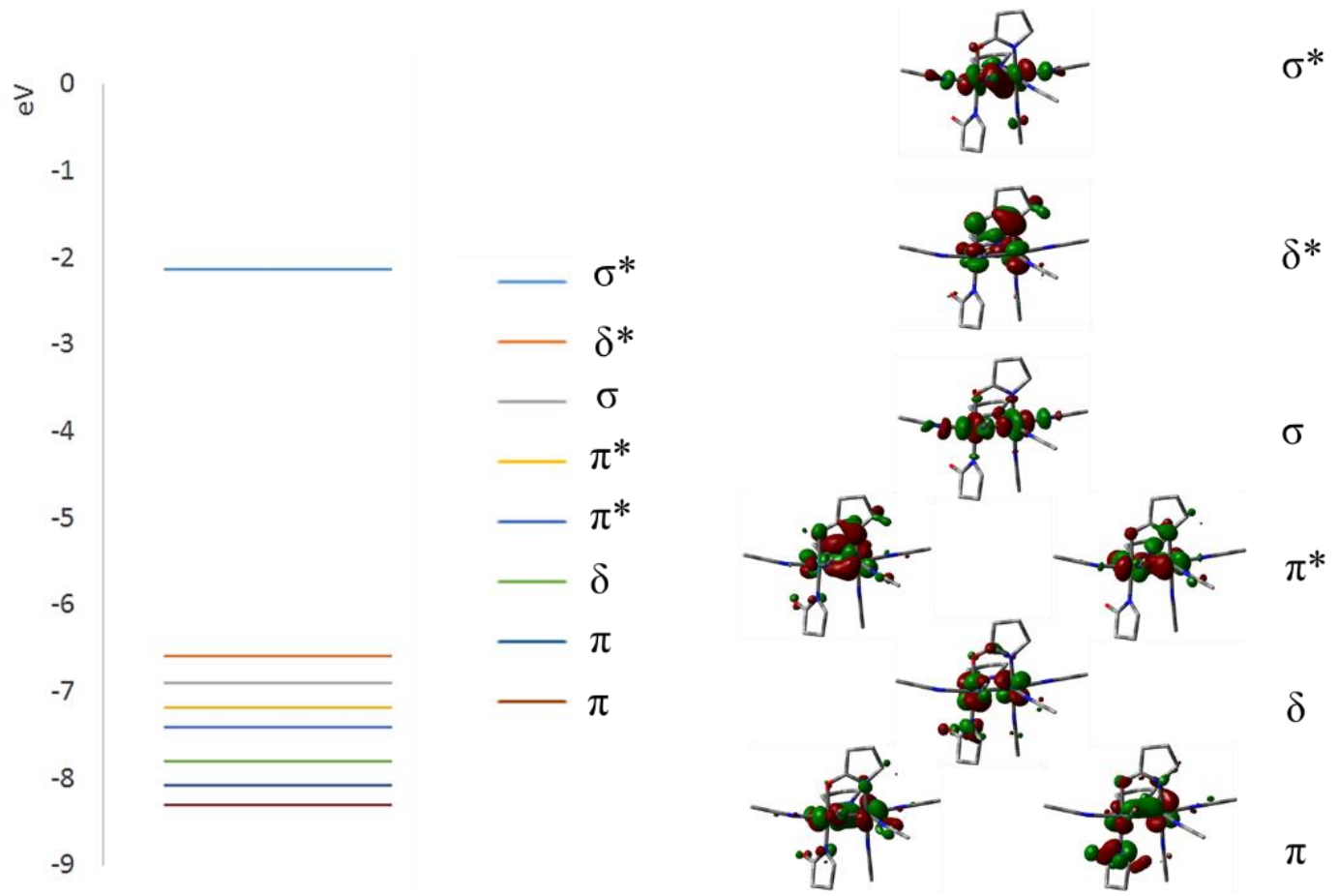

Figure 4.16 MO diagram involving the dirhodium core unit in **9** obtained by DFT calculations (iso-value=0.04).

Table 4.6 Orbital contributions, energy levels and bond characters for the dirhodium units in **8** and **9**.

	8		**9**	
	Orbital and Energy	Contribution (%)	Orbital and Energy	Contribution (%)
π	HOMO-8, -8.358 eV	66 Rh 10 Pyrro Bridge 11 ax Pyrro 10 eq CH_3CN	HOMO-7, -8.308 eV	70 Rh 11 Pyrro Bridge 6 eq Pyrro 9 eq CH_3CN
π	HOMO-7, -8.308 eV	75 Rh 10 eq CH_3CN 9 Pyrro Bridge	HOMO-6, -8.082 eV	56 Rh 11 Pyrro Bridge 26 eq Pyrro
δ	HOMO-6, -7.835 eV	57 Rh 10 Pyrro Bridge 12 eq CH_3CN 20 ax Pyrro	HOMO-5, -7.806 eV	71Rh 10 Pyrro Bridge 8 eq CH_3CN 10 eq Pyrro
π*	HOMO-3, -7.192 eV	81 Rh 10 Pyrro Bridge 7 eq CH_3CN	HOMO-4, -7.412 eV	37 Rh 53 Pyrro Bridge
π*	HOMO-2, -7.102 eV	75 Rh 6 Pyrro Bridge 6 eq CH_3CN 11 ax Pyrro	HOMO-3, -7.187 eV	65 Rh 27 Pyrro Bridge 5 eq CH_3CN
σ	HOMO-1, -6.987 eV	63 Rh 7 Pyrro Bridge 21 ax Pyrro 5 ax CH_3CN	HOMO-1, -7.146 eV	78 Rh 9 ax CH_3CN 6 Pyrro Bridge 6 eq CH_3CN
δ*	HOMO, -6.574 eV	43 Rh 51 Pyrro Bridge 4eq CH_3CN	HOMO, -6.595 eV	41 Rh 54 Pyrro Bridge
σ*	LUMO, -2.216 eV	80 Rh 7 Pyrro Bridge 5 ax Pyrro	LUMO, -2.137 eV	79 Rh 7 Pyrro Bridge 9 ax Pyrro

The MO diagram involving the Rh_2(II,II) unit for compound **10** was constructed and the visualization of the frontier orbitals depicted with Agui (**Figure 4.17**); energy and orbital contributions have been summarized in **Table 4.7**.

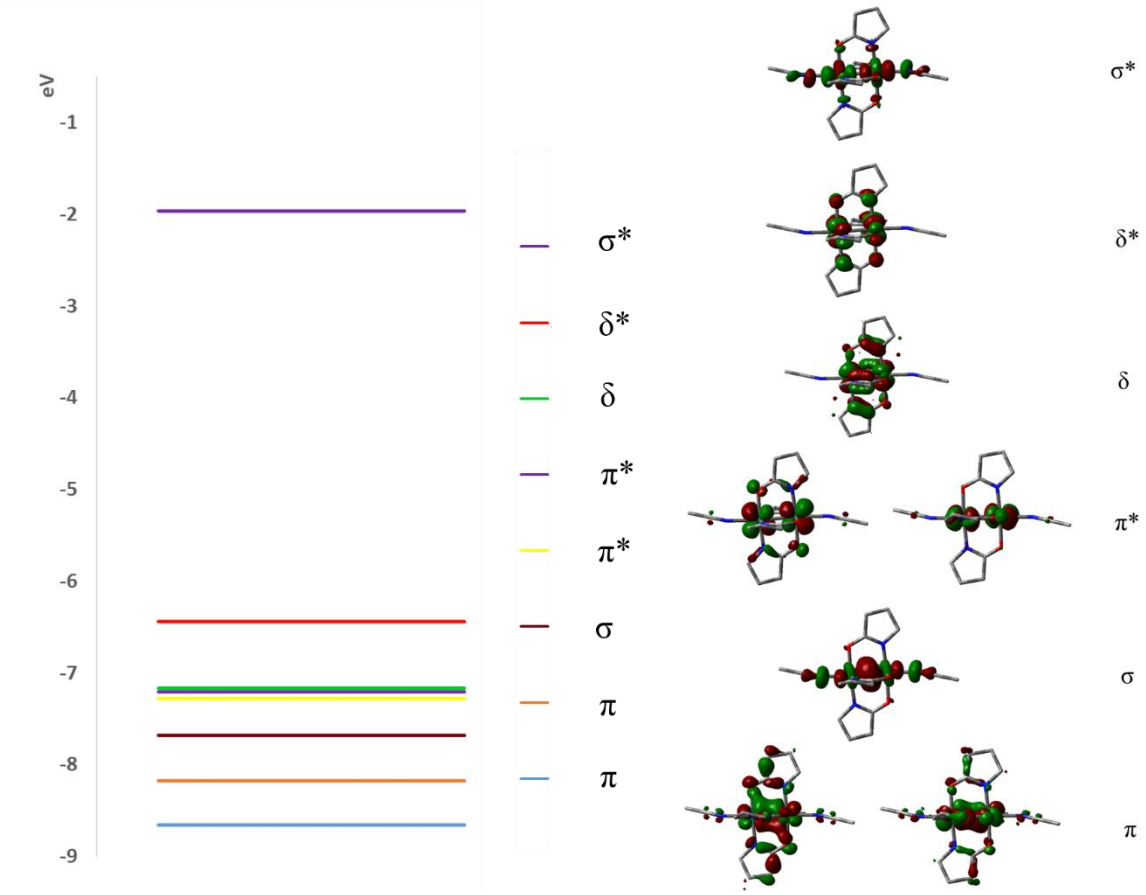

Figure 4.17 MO diagram involving the dirhodium core unit in **10** obtained by DFT calculations (iso-value=0.04).

Table 4.7 Orbital contributions, energy levels and bond characters for the dirhodium units in **10**.

10			
	Orbital	**Energy (eV)**	**Orbital Contribution (%)**
π	HOMO-10	-8.391	52 Rh 46 Pyrro Bridge 5 ax CH_3CN
π	HOMO-9	-8.979	48 Rh 46 Pyrro Bridge 6 ax CH_3CN
σ	HOMO-5	-7.681	76 Rh 7 Pyrro Bridge 16 ax CH_3CN
π*	HOMO-3	-7.052	25 Rh 74 Pyrro Bridge 1 ax CH_3CN
π*	HOMO-2	-7.023	78 Rh 4 ax CH_3CN 18 Pyrro Bridge
δ	HOMO	-6.774	76 Rh 20 Pyrro Bridge 4 ax CH_3CN
δ*	SOMO	-6.444	58 Rh 42 Pyrro Bridge
σ*	LUMO	-1.961	77 Rh 13 Pyrro Bridge ax CH_3CN

The MO compositions related to the electronic transitions for compounds **8-10** in CH_3CN are listed in **Table 4.8** orbital contributions for compounds **8** and **9** in water are listed in **Error! Reference source not found.**. The orbital contributions for **8** and **9** in oth solvents are very similar so only the results from the CH_3CN experiment will be discussed. The Rh based orbitals span from HOMO-8 to HOMO-1 with minor contributions from the 2-pyrrolidinate bridging ligand. The HOMO is evenly distributed between bridging ligand character in **8** (~51% HOMO, 4% eq CH_3CN) and Rh, whereas in **9** it is composed of 2-pyrrolidinate, pyrrol and the eq CH_3CN ligand in nature accounting for 59% of the HOMO with the remaining being Rh based; in both cases the HOMO corresponds to the Rh(δ*) orbital and 2-pyrrolidinato (π*) character. The LUMO for both compounds is mostly Rh in character, which has been assigned as the Rh(σ*) level. The orbitals LUMO+1 and LUMO+2 engage in significant antibonding interactions between the Rh core and the eq CH_3CN ligands and have been ascribed to Rh-L_{eq}(σ*); the same has been observed for the analogous compound *cis*-H-H-$[Rh_2(HNOCCH_3)_2(CH_3CN)_6]^{2+}$ and *cis*-2,2-$[Rh_2(O_2CCH_3)_2(CH_3CN)_6]^{2+}$.[79] Compound **10**'s HOMO is Rh(δ) in character, the SOMO corresponds to the Rh(δ*) and the LUMO is Rh(σ*) in character.

Table 4.8 Orbital contribution of selected molecular orbitals for compounds **8-10** in CH_3CN derived from TD-DFT.

8 in CH_3CN		**9 in CH_3CN**		**10 in CH_3CN**	
HOMO-6	57 Rh 10 Pyrro Bridge 12 eq CH_3CN 20 ax Pyrro	HOMO-6	56 Rh 11 Pyrro Bridge 26 eq Pyrrol	HOMO-6	75 Rh 9 Pyrro Bridge 16 ax CH_3CN
HOMO -4	13 Rh 82 Pyrro Bridge	HOMO-4	37 Rh 53 Pyrro Bridge	HOMO -5	7 Rh 93 Pyrro Bridge
HOMO-3	81 Rh 10 Pyrro Bridge 7 eq CH_3CN	HOMO-3	65 Rh 27 Pyrro Bridge 5 eq CH_3CN	HOMO-3	25 Rh 74 Pyrro Bridge
HOMO-2	75 Rh 6 Pyrro Bridge 6 eq CH_3CN 11 ax Pyrro	HOMO-2	78 Rh 6 Pyrro Bridge 6 eq CH_3CN 9 ax CH_3CN	HOMO-2	80 Rh 17 Pyrro Bridge
HOMO-1	63 Rh 7 Pyrro Bridge 21 ax Pyrro 5 ax CH_3CN	HOMO-1	67 Rh 7 Pyrro Bridge 20 eq Pyrrol 5 ax CH_3CN	HOMO-1	76 Rh 20 Pyrro Bridge
HOMO	43 Rh 51 Pyrro Bridge	HOMO	41 Rh 54 Pyrro Bridge	HOMO	78 Rh 20 Pyrro Bridge 4 ax CH_3CN
LUMO	80 Rh 7 Pyrro Bridge 5 ax Pyrro	LUMO	79 Rh 7 Pyrro Bridge 9 ax CH_3CN	SOMO	58 Rh 42 Pyrro Bridge
LUMO+1	62 Rh 21 eq CH_3CN 17 Pyrro Bridge	LUMO+1	62 Rh 17 Pyrro Bridge 12 eq Pyrrol 9 eq CH_3CN	LUMO	77 Rh 9 ax CH_3CN 13 Pyrro Bridge

Table 4.9 Orbital contribution of selected molecular orbitals for compounds **8** and **9** in H_2O derived from TD-DFT.

8 in H_2O		**9 in H_2O**	
HOMO-6	69 Rh 14 eq CH_3CN 12 Pyrro Bridge 5 ax Pyrro	HOMO-6	57 Rh 10 Pyrro Bridge 28 eq Pyrrol 5 eq CH_3CN
HOMO-4	16 Rh 77 Pyrro Bridge	HOMO-4	57 Rh 31 Pyrro Bridge 5 eq CH_3CN 5 ax H_2O
HOMO-3	80 Rh 10 Pyrro Bridge 6 eq CH_3CN	HOMO-3	36 Rh 56 Pyrro Bridge 6 ax H_2O
HOMO-2	66 Rh 21 ax Pyrro 5 Pyrro Bridge	HOMO-2	85 Rh 6 Pyrro Bridge 7 eq CH_3CN
HOMO-1	75 Rh 21 ax Pyrro 5 Pyrro Bridge	HOMO-1	71 Rh 5 Pyrro Bridge 20 eq Pyrrol
HOMO	44 Rh 51 Pyrro Bridge	HOMO	45 Rh 50 Pyrro Bridge
LUMO	80 Rh 7 Pyrro Bridge 6 ax Pyrro	LUMO	81 Rh 7 pyrro Bridge 7 ax H_2O
LUMO+1	63 Rh 17 Pyrro Bridge 20 eq CH_3CN	LUMO+1	63 Rh 16 Pyrro Bridge 11 eq Pyrrol 9 eq CH_3CN

The TD-DFT calculations were as a tool to assign the origin of the electronic transitions in the UV-visible spectrum. The lowest energy transition at λ = 474 nm and 471 nm have been assigned as charge-transfer transitions with a minor contribution from the Rh(δ*)→Rh(σ*) originating from the HOMO, HOMO-3 to LUMO for **8** and HOMO-1, HOMO-2 and HOMO-3 to LUMO for **9** respectively (Error! Reference source not found. and **Table 4.11**). Population of the Rh-Leq(σ*) orbital (namely LUMO+1 and LUMO+2) upon irradiation promotes labilization of the eq CH_3CN ligands whose signature is observed in the region of 320-420 nm. There is a very distinct feature at 275 nm which corresponds to the HOMO-6 and HOMO to the LUMO+1 which is mostly metal centered and has been ascribed to Rh(π*)→Rh-Leq(σ*). The electronic transitions derived from the TD-DFT calculations in CH_3CN and H_2O and the frontier orbitals involved in the electronic transitions are summarized in Error! Reference source not ound. and **Table 4.11**, **Figure 4.18** and **Figure 4.19** show the visualization of the orbitals involved in the electronic transitions for compounds **8** and **9**.

Compound **10**'s electronic absorption spectrum shows a band with two distinct absorptions comprised of two peaks at 490 and 530 nm originating from the HOMO-5 and HOMO to LUMO and HOMO-6 to LUMO, respectively. These two absorptions have been assigned as a combination of pyrro(π*)→Rh(σ*) and Rh(π*)→ Rh(σ*). The low energy absorption at 1033 nm is a charge transfer band originating from the HOMO-4 (pyrro(π*)) to the SOMO (Rh(δ*)) which corresponds to ta LMCT transition. The transition at 1410 nm has been assigned as a metal centered transition, Rh(π*)→Rh(δ*), with contributions from the HOMO-2 and SOMO which explains the low absorptivity

coefficient of this transition ($\varepsilon = 0.3 \times 10^2$ $M^{-1} \bullet cm^{-1}$). The first ten electronic transitions for **10** have been summarized in **Table 4.12** and the depiction of orbitals involved in the electronic transitions in **Figure 4.20**.

Table 4.10 First ten electronic transitions predicted for **8** by TD-DFT calculations in CH_3CN and H_2O as solvent. H = HOMO, L = LUMO.

8 in CH_3CN				**8 in H_2O**			
E (nm)	*f*	Excitations	Contribution	E (nm)	*f*	Excitations	Contribution
474	0.001	H-3 -->L	48%	507	0.001	H-1 --> L	56%
		H-->L	26%	497	0.001	H-3 --> L	36%
351	0.004	H-2-->L+1	30%			H-2--> L	23%
347	0.005	H-->L+2	52%	362	0.004	H-4 --> L	25%
345	0.005	H-3 -->L +1	25%			H-1 --> L+1	25%
317	0.029	H-7-->L	42%	353	0.008	H-7 --> L	29%
314	0.049	H-8-->L	25%			H-3 --> L+1	20%
		H-4-->L	22%	340	0.001	H-4 --> L	27%
289	0.356	H-2-->L	35%			H-1 --> L+1	27%
		H-3-->L+2	22%			H-6 --> L	22%
284	0.013	H-3-->L+2	46%	304	0.001	H-2--> L+1	61%
281	0.176	H-2-->L+2	27%			H-3 --> L+1	27%
273	0.015	H-->L+1	37%	290	0.141	H-1 --> L+2	42%
				288	0.162	H-3 --> L+2	27%
		H-6-->L+1	35%	281	0.105	H-3 --> L+1	41%
				279	0.079	H --> L+1	34%

Table 4.11 First ten electronic transitions predicted for **9** by TD-DFT calculations in CH_3CN and H_2O as solvent. H = HOMO, L = LUMO.

9 in CH_3CN				**9 in H_2O**			
E (nm)	*f*	Excitations	Contribution	E (nm)	*f*	Excitations	Contribution
471	0.001	H-1 -->L	69%	539	0.001	H-1 -->L	85%
456	0.001	H-3-->L	50%	517	0.001	H-2 --> L	81%
		H-2-->L	23%	380	0.001	H --> L+1	48%
354	0.001	H-1-->L +1	54%	365	0.002	H-4 --> L	35%
347	0.001	H-->L+2	69%	353	0.001	H-7 --> L	25%
341	0.005	H-4-->L	42%			H-1 -->L+1	23%
323	0.002	H-5-->L	84%			H-5 --> L	20%
311	0.002	H-6-->L	24%	349	0.001	H-5 --> L	50%
304	0.082	H-2-->L	20%	346	0.001	H --> L+2	25%
		H-3-->L	20%	322	0.025	H-3 --> L	44%
300	0.009	H-2-->L+1	38%			H-5 --> L+1	23%
		H-3-->L+1	27%	313	0.009	H-2 --> L+1	48%
289	0.018	H-1-->L+2	35%	292	0.005	H-1 --> L+2	52%

Table 4.12 First ten electronic transitions predicted for **10** by TD-DFT calculations in CH_3CN and H_2O as solvent. H = HOMO, L = LUMO.

10 in CH_3CN			
E (nm)	*f*	Excitations	Contribution
1556	0.001	H-2-->S	87%
1126	0.018	H-4-->S	24%
626	0.061	H-4-->S	100%
546	0.037	H-6-->S	100%
504	0.005	H-5-->L	39%
		H -->L	32%
501	0.001	H-5 -->L	60%
		H-->L	14%
425	0.001	H -->L	100%
417	0.004	H -->L	72%
416	0.003	H-1-->L	76%
353	0.004	H-11-->S	100%

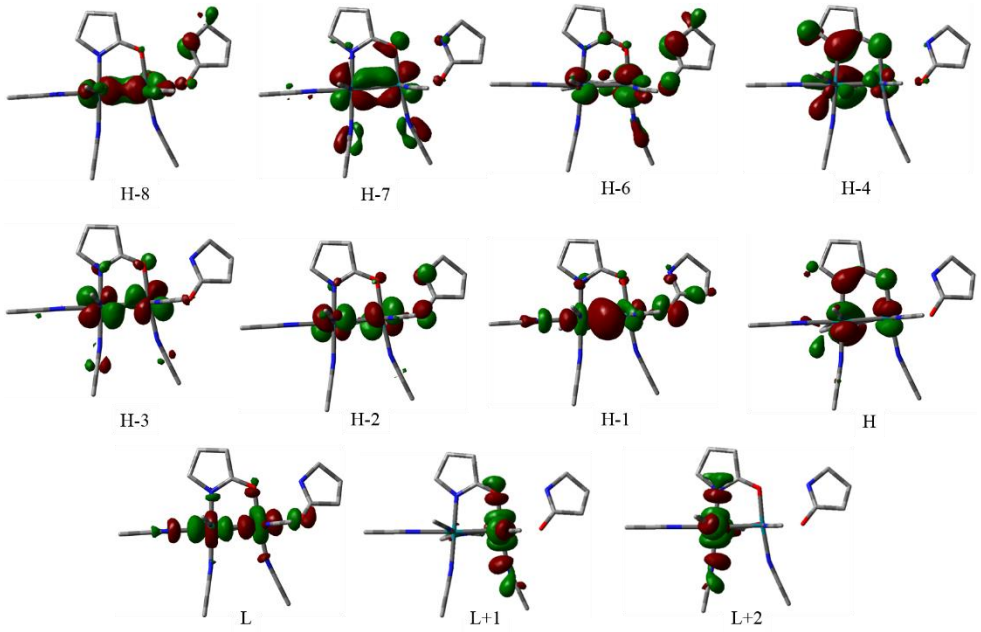

Figure 4.18 MO depiction of **8** generated by TD-DFT calculations in the solvation model (CH_3CN) generated by agui with iso-value = 0.04; H = HOMO, L = LUMO.

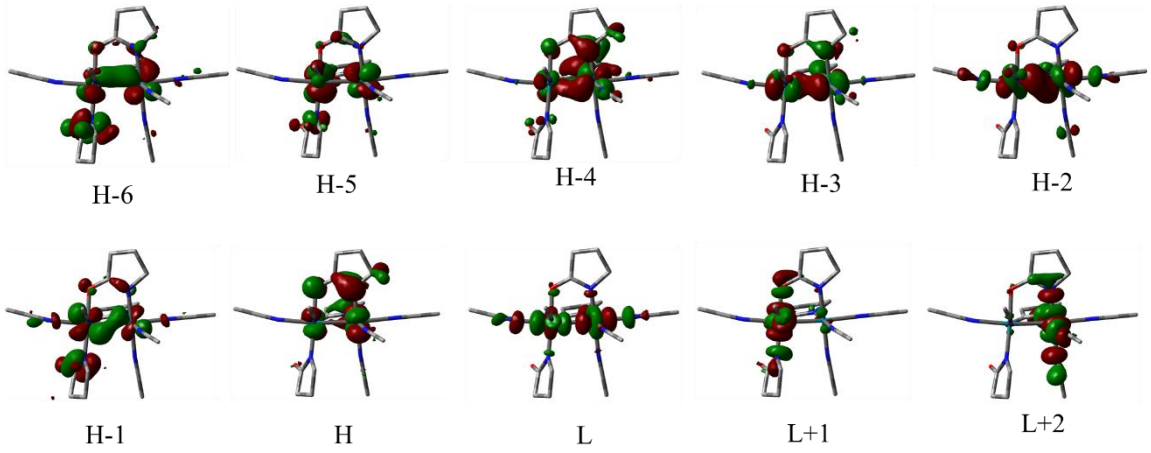

Figure 4.19 MO depiction of **9** generated by TD-DFT calculations in the solvation model (CH_3CN) generated by agui with iso-value = 0.04; H = HOMO, L = LUMO.

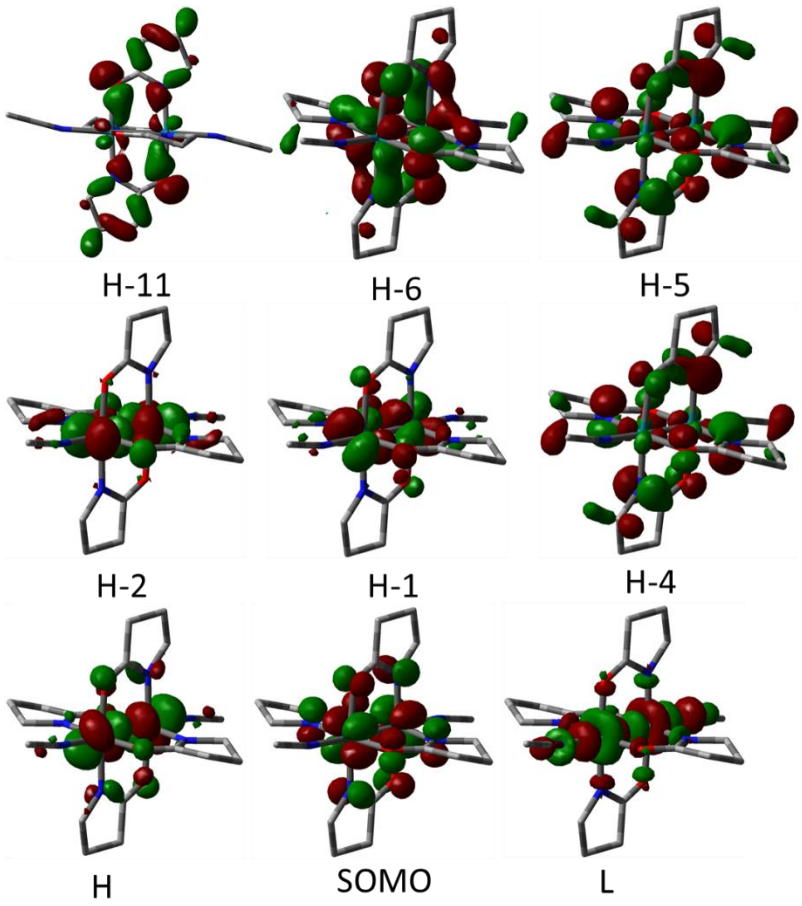

Figure 4.20 MO depiction of **10** generated by TD-DFT calculations in the solvation model (CH_3CN) generated by agui with iso-value = 0.04; H = HOMO, L = LUMO.

In Vitro *Cytotoxicity Studies*

Cell viability studies were performed on compounds **8** and **9** and their toxicities were evaluated in the dark and upon irradiation with visible light using SYTOX® Green and Hoechst 33342 fluorescent staining performed on HeLa cells, whereas **10** was evaluated by the resazurin assay. Sytox Green® is a cell impermeable dye that increases its fluorescence signal by 100-fold when the cells have been compromised or are dead.[147] Hoechst 33342 is a permeable blue fluorescence probe that stains both live and dead cells

by binding to the minor groove of double-stranded DNA rich in adenine and thymine.[177] On the other hand resazurin is a fluorescent cell viability assay analogous to the formazan-based assays (MTT/XTT) as it measures cell viability via the irreversible reduction of resazurin to resorufin which is directly proportional to aerobic respiration.[138-139] For the dark experiments, the cells were incubated with different concentrations of compounds **8-10** for 2 h followed by treatment with Sytox® Green and Hoechst 33342 staining for 10 min or resazurin in the case of **10**. The cells incubated with **8** and **9** in the dark exhibited mostly blue fluorescence (**Figure 4.21**). Compound **10**, like **8** and **9**, exhibits no toxicity in the dark with an LC_{50} value >> 1mM. The absence of green fluorescence indicates that the cells are not dying upon exposure to **8** and **9** up to concentrations in the mM range. The LC_{50} in the dark for **8** is 913 ± 51 μM; this result is comparable to the dark control experiments where no compound is present thus indicating the low toxicity of **8** in the dark. The toxicity of compounds **8-10** is significantly lower than that of cisplatin under the same conditions, results which have been summarized in **Table 4.13**.

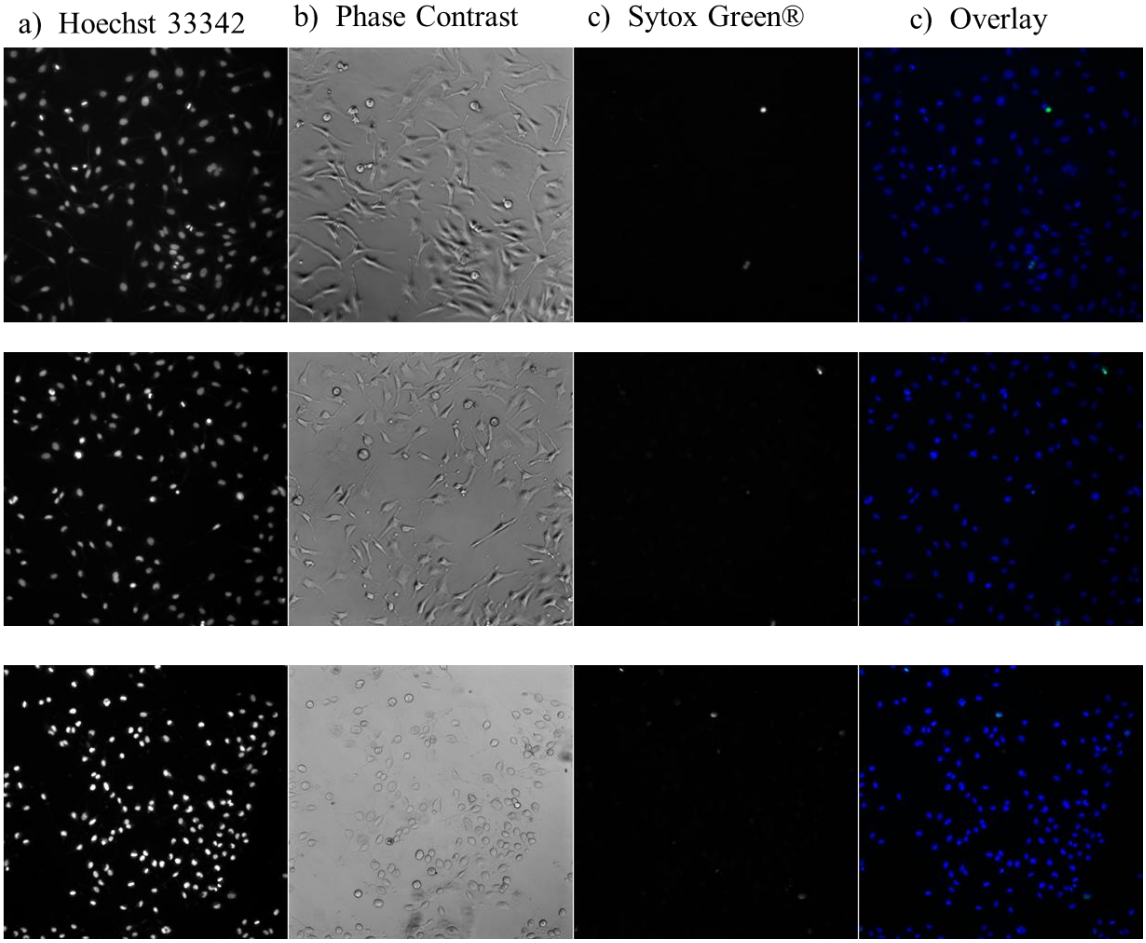

Figure 4.21 Confocal microscopy images of HeLa cells treated with 50 μM solutions of **8** and 100 μM solutions of **9** for 2 h in the dark followed by treatment with Sytox® Green and Hoechst. Top control in the dark, middle pane compound **8** and bottom compound **9**. a) Hoechst 33342, blue fluorescence, b) phase contrast, c) SYTOX® Green fluorescence, and d) overlay of blue and green fluorescence.

Table 4.13 Cytotoxicity and phototoxicity data for compounds **8-10**, cisplatin and Hematoporphyrin in the dark and upon irradiation.

	LC_{50} µM	LC_{50}^{*} µM	Phototoxicity Index
cisplatin	58 ± 4	47 ± 3	1.2[a]
Hematoporphyrin	21 ± 1	3.8 ± 0.2	5.5[b]
8	913 ± 51	483 ± 41	2
9	4115± 72	186 ± 30	22
10[c]	>>1 mM	868 ± 99	NA

a. Ref 170
b. Ref 190
c. Measured with resazurin assay.

The toxicities of **8**-**10** were evaluated after irradiation for 1 h (**Figure 4.22** and **Table 4.13**). Compounds **8** and **10** do not show increase activity upon light activation. The low toxicity of **8** is ascribed to the relative stability of the eq CH_3CN ligands in aqueous solution as it takes more than 4 h for these to exchange as demonstrated by ^1H NMR studies. The mixed-valence compound **10** does not exhibit cell toxicity in the dark or upon irradiation; the LC_{50}^{*} is 868 ± 99 µM. The most active of this new family of dirhodium compounds is **9** with an LC_{50}^{*} of 186 ± 30 µM with an increase in phototoxicity index (PI) of LC_{50}/LC_{50}^{*} = 22. The toxicity of this compound is still lower than that of cisplatin, but it's PI is superior than that of hematoporphyrin the main ingredient in the FDA approved PDT agent Photofrin®, PI = 5.5. Dirhodium aqua species can bind to biomolecules and other cellular targets in an analogous way to cisplatin therefore the increased toxicity of **9** may be due to the generation of the active aqua species and the release of the eq pyrrole molecule upon light irradiation as evidenced by the ^1H NMR studies.[77,79,170]

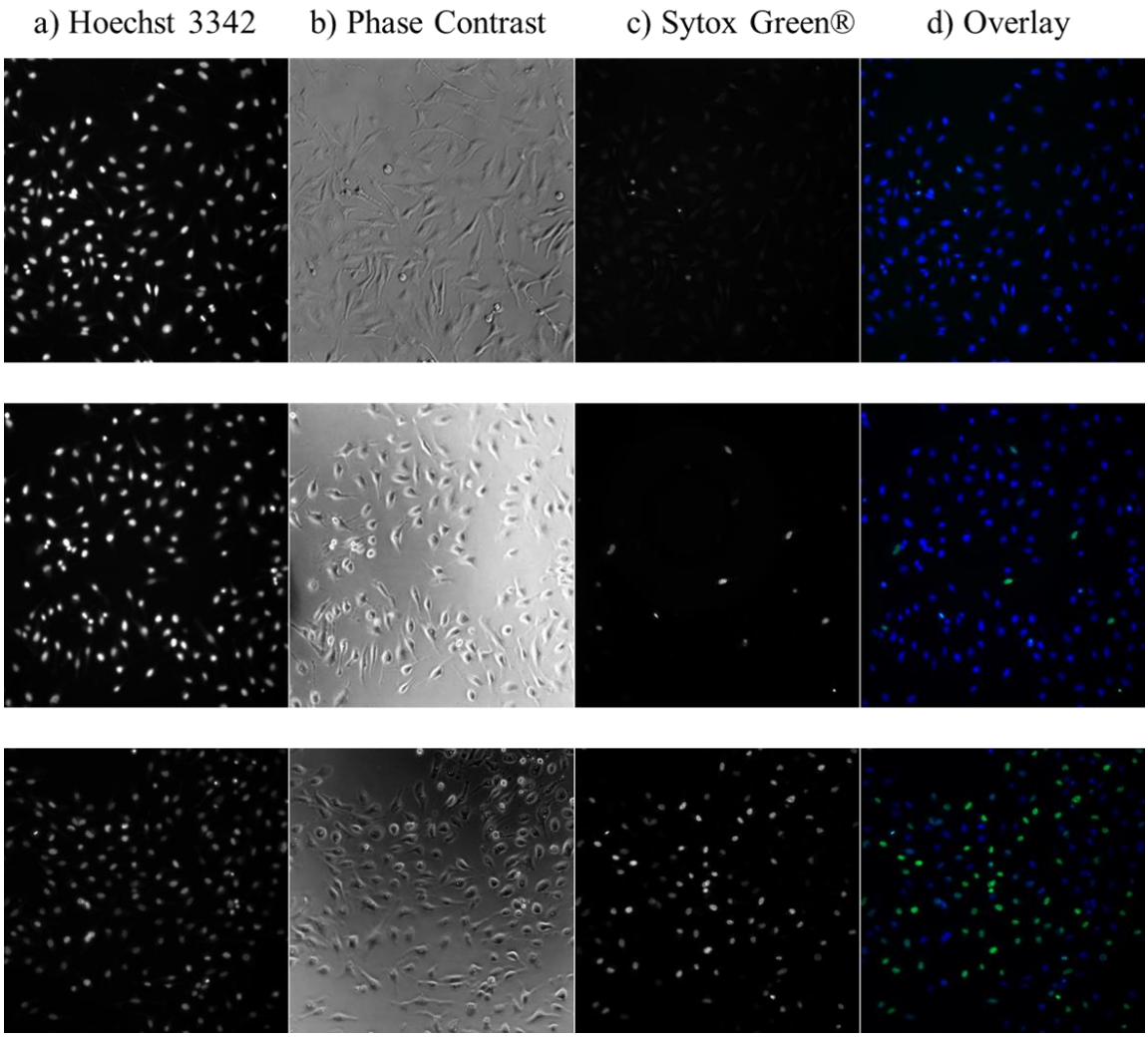

Figure 4.22 Confocal microscopy images of HeLa cells treated with 50 μM solutions of **8** and 100 μM solutions of **9** for 2 h in the dark, irradiated for 1h, followed by treatment with Sytox® Green and Hoechst. Top control after irradiation, middle pane compound **8** and bottom compound **9**. a) Hoechst 33342, blue fluorescence, b) phase contrast, c) SYTOX® Green fluorescence, and d) overlay of blue and green fluorescence.

Mitochondrial Trans-membrane Potential Disruption: JC-1 Assay

The mitochondrial respiratory chain in the inner mitochondrial membrane is responsible for the generation of ROS, which, in the absence of antioxidants, can cause

damage to lipids, proteins and DNA and eventually trigger cell death.[191] It is well understood by the scientific community that accumulation of cationic species inside the mitochondria induces changes in mitochondrial potential ($\Delta\Psi$)[192] which promote the release of pro-apoptogenic factors, which in turn induce cell death.[153] In order to study the changes in mitochondrial potential induced by **9**, the commercially available JC-1 dye was used. JC-1 targets the mitochondria and exhibits two types of fluorescent responses when the $\Delta\Psi$ changes.[193-194] Healthy cells have high $\Delta\Psi$ and in this type of environment JC-1 is in its aggregated form (J-aggregates) which fluoresces red. Conversely when $\Delta\Psi$ is low, the dye adopts a monomeric form which has a green fluorescence.

In order to study the cell death mechanism of compound **9**, HeLa cells were incubated with JC-1 and the ratio of green to red florescence was measured as a function of time (**Figure 4.23**). The changes in mitochondrial potential were monitored for a period of 5 h and it was found that compound **9** induces a decrease in mitochondrial potential with time which plateaus after 4 h. It is possible that the decrease in mitochondrial potential observed in **9** is triggered by an apoptotic response.

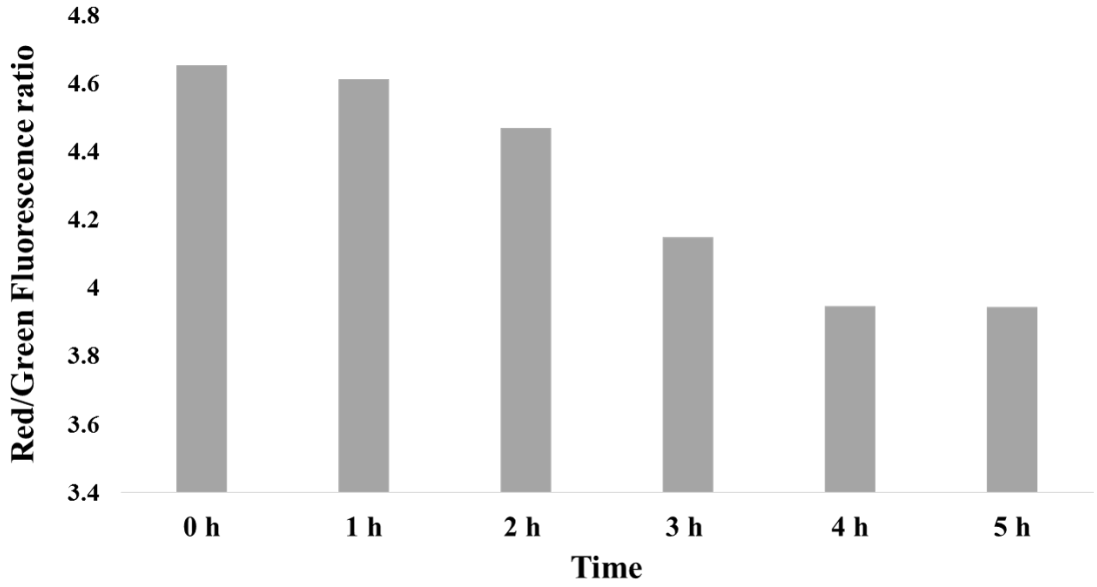

Figure 4.23 Mitochondrial potential changes in HeLa cells as a function of time for compound **9**.

Annexin-V FITC

Programmed cell death, most commonly known as apoptosis triggers a cascade of biological responses that induce cell death.[42] The apoptotic response is characterized by the activation of caspases, chromatin condensation, and exposure of phosphatidyl serine (PS) on the cell surface amongst others.[42] The exposure of PS can be monitored by fluorescence spectroscopy by using Annexin-V FITC. This protein reversibly binds to PS when it is exposed to the outer leaflet of the cell and exhibits a green fluorescence.[195]

In order to determine the mechanism of cell death, HeLa cells were treated with **9**, followed by incubation with Annexin-V FITC for 10 min. The cells treated with compound **9** exhibit green fluorescence localized on the outer side of the cell membrane

(**Figure 4.24**). These results taken in combination with the JC-1 assay support the conclusion that **9** induces apoptotic mediated cell death.

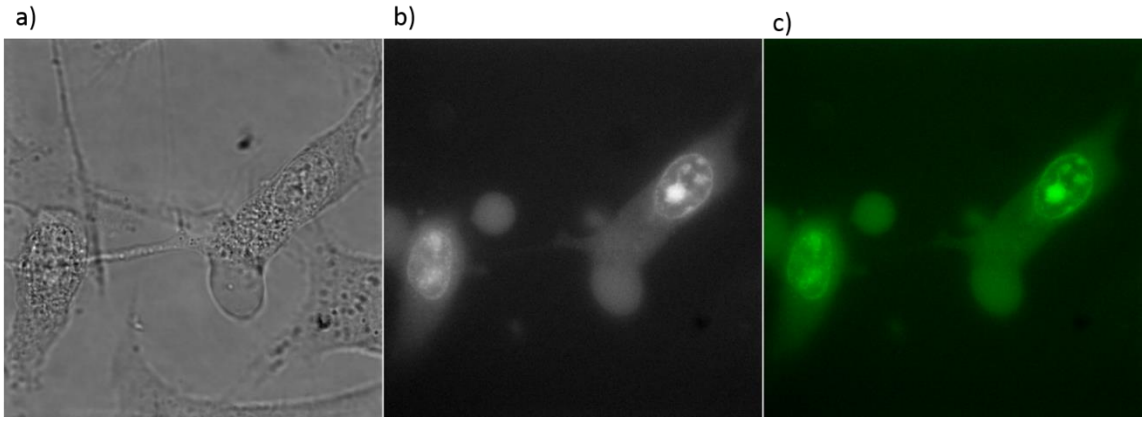

Figure 4.24 Confocal microscopy images of HeLa cells treated with **9** followed by treatment with Annexin V-FITC. a) Phase contrast image, b) Annexin V-FITC, green fluorescence and c) Annexin V-FITC pseudo colored green image.

Concluding Remarks

The head-to-head (H-H) isomers of *cis*-2,2-[Rh_2(μ-NOC_4H_6)$_2$(Hpyrro)(CH_3CN)$_5$](BF_4)$_2$ and *cis*-2,2-[Rh_2(μ-NOC_4H_6)$_2$(pyrrol)(CH_3CN)$_5$]$^{2+}$ along with the oxidized form of *cis*-2,2-[Rh_2(μ-NOC_4H_6)$_4$]$^+$ were synthesized and characterized. Compound **8** has one Hpyrro in the axial position, while **9** has a pyrrol molecule in the equatorial position *trans* to the O bridge as confirmed by X-ray studies. The UV-visible spectrum of **10** exhibits a band at 1033 nm and 1140 nm that was not reported by Bear and according to the TD-DFT results these bands are result of LMCT

and MC transitions, respectively. The ^{1}H NMR studies performed on **8** and **9** show that the axial Hpyrro ligand in **8** exchanges in the dark and that **9** does not exchange the eq pyrrol molecule for the deuterated solvent for up to 3 h. Compound **9** exchanges the CH_3CN^{O} in the dark. Compound **8** is more kinetically stable in the dark than **9** is and does not induce toxicity in HeLa cells upon irradiation with white light. The 22-fold increase in toxicity of compound **9** upon irradiation is expected to be related to the release of the pyrrol molecule and the labilization of the eq CH_3CN monodentate ligands upon irradiation. The TD-DFT calculations indicate that the LUMO+1 orbital in both cases has Rh-Leq (σ*) antibonding character for the eq acetonitrile molecule *trans* to the O bridge which is responsible for the labilization of the eq CH_3CN monodentate ligands. This result supports the findings from ^{1}H NMR spectroscopy studies performed in D_2O in the dark and upon irradiation. Compounds **8** and **9** are the first examples of dirhodium partial paddlewheels bearing photo-labile anticancer active ligands which render them good candidates for cancer therapy. These compounds can be easily tuned and future efforts will be directed towards the design and synthesis dirhodium compounds bearing anticancer ligands and tumor targeting moieties.

CHAPTER V

CONCLUDING REMARKS

Medicinal inorganic chemistry is an attractive field of modern drugs but, in fact, metal compounds have been used for centuries to treat different ailments. Coordination compounds offer a broad array of coordination numbers, ligand environments, and accessible redox states which poises them as good therapeutic agents.[95] Although there are a number of promising and effective transition metal drugs currently in use around the world, there remains a pressing need to discover new therapies that target different organelles and biologically relevant molecules other than DNA. Over the past 20 years, our laboratories have focused their efforts on the development of dirhodium compounds with cytostatic activity. As part of our interest in metal anticancer agents we are exploring dirhodium(II,II) complexes with different types of bridging and chelating ligands in the same molecule,[196] work that has led to the isolation of families of such compounds that are inactive towards cancer cells in the dark but which are toxic upon irradiation has been synthesized and characterized.

In Chapter I, five new complexes with two different bridging ligands ($[O_2CCH_3]^-$ and $[F_2form]^-$) were reported. Formamidinate compounds of the type $[Rh_2(F_2form)(O_2CCH_3)(N\text{-}N)_2][OAc]_2$ with electron accepting chelating ligands (N-N) (N-N = dpq (dipyrido[3,2-f:2',3'-h]-quinoxaline), dppz (dipyrido[3,2-a:2’,3’-c]phenazine) and dppn (benzo[i]dipyrido[3,2-a:2’,3’-h]quinoxaline)) were studied and their anti-proliferative activity was evaluated against ovarian cancer and cervical cancer cell lines

in the dark and also upon irradiation. In addition, the effects of these compounds on mitochondrial potential and type of cell death were studied. Compounds **4** and **5** exhibit the highest activity against ovarian cancer cell lines OVCAR-8 and NCI-ADR/RES respectively, with LC_{50} values in the lower micromolar range after irradiation. This new family of dirhodium compounds induces different types of cell death depending on the nature of the bridging ligands. Earlier we had shown that $[Rh_2(\mu\text{-}O_2CCH_3)_2(dppn)(dppz)]$ and $[Rh_2(\mu\text{-}O_2CCH_3)_2(dppn)_2]$ induce apoptotic and necrotic cell death respectively. Parallel results were not observed for this series of compounds; compound **2** induces an apoptotic response while compounds **3-5** exhibit signs of both apoptosis and necrosis in NCI-ADR/RES cells. Cell death induced by **2-5** occurs in a very short time scale as evidenced by fast mitochondrial potential depletion from the JC-1 studies in HeLa cells. These results suggest that the ability of these compounds to generate ROS may be a key factor for the rapid cell death.

We propose that these compounds may be oxidizing phospholipids or inducing endosomal lysis upon irradiation which would account for the rapid cell death. In the future it would be very interesting to study the how ROS scavengers affect the activity of compounds **4** and **5**. In addition, considering the type of cell death induced by these compounds, a concentration dependent and a time lapse experiment with YO-PRO-1[197] and propidium iodide would help elucidate the mechanism of cell death induced by **4** and **5**. Since most of the compounds in this study induce necrotic cell death to some extent it would be valuable to study how the inhibition of PARP-1 (nuclear enzyme that initiates cell necrosis)[104] could be effected; by doing so necrotic cell death can be prevented and

this may affect the mechanism of cell death imparted by these compounds upon irradiation.

Light induced toxicity by ligand dissociation is another strategy for the metal-based drugs in this study, data that are presented in Chapter III. Partially solvated compounds with two different bridging ligands were synthesized and their activity against HeLa cells was evaluated. Compounds $[Rh_2(F_2form)(\mu\text{-}O_2CCH_3)(CH_3CN)_6]^{2+}$(**6**) and $[Rh_2(PC_6H_4Ph_2)(\mu\text{-}O_2CCH_3)(CH_3CN)_6]^{2+}$ (**7**) showed rapid ligand dissociation in the dark. In particular, compound **6** is unstable although irradiation does not affect the rate of ligand dissociation. The side product **6b** was isolated in which the acetate group is missing. Compound **7** exchanges the eq CH_3CN ligands *trans* to the orthometallated phosphine but the signals corresponding to the eq CH_3CN ligands *trans* to acetate do not exchange in the dark or upon irradiation under the experimental conditions. Cytotoxicity studies reveal that neither of these compounds exhibit carcinostatic activity. Although these compounds are not good candidates for PDT applications, **7** can be used as a precursor for further functionalization and applications in cancer therapy or photocatalytic reduction of H_2O.[134]

The results in Chapter IV focus on the synthesis of dirhodium partial paddlewheel compounds with 2-pyrrolidinone as a bridging ligand. The 2-pyrrolidinone molecule is quite interesting as it has been studied for anticancer properties against HeLa (cervical) cells and PC-3 (prostate) cancer cells.[186] In an effort to synthesize the partially solvated dirhodium compound with 2-pyrrolidinone as a bridging ligand, $[Rh_2(pyrro)_4]$ was used as a precursor and reacted with the alkylating reagent triethyloxonium tetrafluoroborate.

This reaction afforded two different compounds, namely *cis*-2,2-[Rh_2(μ-NOC_4H_6)$_2$(Hpyrro)(CH_3CN)$_5$]$^{2+}$ (**8**) and *cis*-2,2-[Rh_2(μ-NOC_4H_6)$_2$(pyrrol)(CH_3CN)$_5$]$^{2+}$(**9**). Compound **8** has a 2-pyrrolidione ligand in the axial position while in **9** a pyrrole is bound in the equatorial position *trans* to the O. The toxicity of these compounds was evaluated against HeLa cells in the dark and upon irradiation. While compound **8** is not toxic, **9** showed a 22-fold increase in phototoxicity upon irradiation. The toxicity of **9** may be attributed to the release of the eq pyrrole molecule upon irradiation. These compounds do not show high toxicity, this may be due to low internalization in the cells. Che and coworkers showed that functionalization of the 2-pyrrolidinone with lipophilic groups improves toxicity when compared to [Rh_2(pyrro)$_4$].[184] These strategy may be useful with compounds **8** and **9** as well to improve their toxicity. Although the toxicities of these compounds are not high, they are good examples of dirhodium compounds bearing photolabile organic drug molecules for which examples in literature for dirhodium (II,II) compounds are scarce.

Future Directions

In order to prevent side effects caused by chemotherapy many efforts have been devoted to the design of anticancer drugs that can target cancerous cells instead of healthy tissue. Among the more studied systems are nanoparticles, which can be tailored in order to modify shape, size and surface modification to make them more specific towards a particular target.[198-200] Another approach that has been pursued by the scientific community is the functionalization of anticancer agents with folic acid, in order to target

folic acid receptors on the cancerous cells.[201] Folic acid receptors are glycoproteins that are anchored to the cell membrane and facilitate the uptake of folic acid by the cell.[201-202] It has been demonstrated by several research groups that these folic acid receptors are overexpressed in rapidly growing tissues.[203-205] Mouse models of colon carcinoma showed increased proliferation of the cancer in the presence of folic acid.[206] Due to the overexpression of folic acid receptors in many types of cancerous cells the conjugation of this ligand to anticancer agents offers another means of targeting tumors cells selectively.[201]

Dirhodium compounds offer a variety of possible coordination sites that can be available for reactions allowing the synthesis of a great number of derivatives. In order to make our compounds more selective towards cancerous cells, folic acid could be incorporated into the bridging position of the dirhodium core. The acid dissociation constants of folic acid makes the ligand accessible for the functionalization of the dirhodium core through the α carboxylic acid (pK_a=4.7) of the folic acid.[202,207] A dirhodium compound that could be used as a precursor for the synthesis of a targeted pro-drug system can be $[Rh_2(Ph_2P(C_6H_4))(O_2CCH_3)(1,8\text{-naphtyridine})(CH_3CN)_4]^{2+}$ (**7b**) which has been successfully synthesized (**Figure 5.1a**).

The synthesis of **7b** is a great example of controlled functionalization of dirhodium compounds by tuning the ligand environment around the dirhodium core to afford heteroleptic compound **7b**. Since the phosphine is a strong σ-donating ligand, it was predicted that 1 eqv. of 1,8-naphthyridine would bind *trans* to it (**Figure 5.1a**). The reaction takes place at room temperature in CH_3CN to afford **7b** in good yields (75 %).

The purity of the compound was confirmed by ^{1}H-NMR and X-ray crystallography methods (**Figure 5.2**). The ^{1}H NMR spectrum shows the characteristic multiplet resonances four for the phosphine at 6.76 ppm, 7.05 ppm, 7.33 ppm and 7.57 ppm, and four characteristic resonances for the naphthyridine ligand at 8.04 ppm, 8.83 ppm, 9.58 ppm and 9.74 ppm (**Figure 5.1b**). As in the case of **7**, there are three singlet resonances in the aliphatic region corresponding to the bridging acetate (1.40 ppm) and the two eq CH_3CN *trans* to acetate at 1.67 ppm and 1.78 ppm.

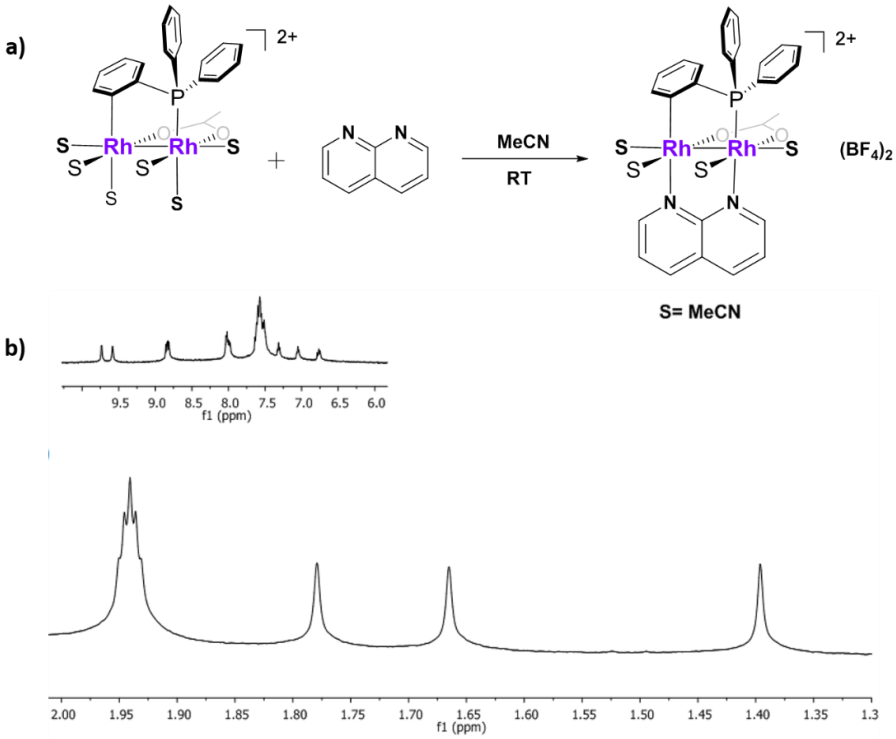

Figure 5.1 a) Reaction scheme of **7** with 1,8-naphthyridine and b) ^{1}H NMR spectrum of $[Rh_2(PC_6H_4Ph_2)(\mu\text{-}O_2CCH_3)(1,8\text{-naphthyridine})(CH_3CN)_4]^{2+}$ in CH_3CN.

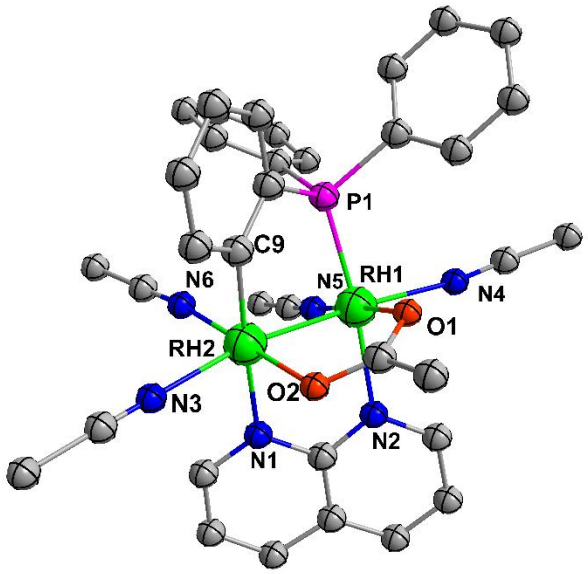

Figure 5.2 Thermal ellipsoid plot of compound **7b** at the 50% probability level. Anions and hydrogen atoms have been omitted for the sake of clarity.

This molecule is of great importance since it poses as a great precursor for selective binding of biomolecules to the dirhodium core. It would be expected that reactions of **7b** with folic acid would afford a folic acid functionalized dirhodium complex that confers specificity to the dirhodium drug by targeting folate receptors in ovarian cancer cells (**Figure 5.3**).[18]

One interesting molecule that could also be used in both cancer treatment and live cell imaging is curcumin ((1*E*,6*E*)-1,7-Bis(4-hydroxy-3-methoxyphenyl)-1,6-heptadiene-3,5-dione).[208] Curcumin is the active ingredient in the turmeric spice, it has been demonstrated that in combination with several chemotherapeutic drugs can elicit synergistic effects in cancer treatment amongst other uses (such as anti-viral and microbial, anti-inflammatory, etc.).[209-210] One disadvantage though is the low

bioavailability due to its poor solubility and low stability in acidic environments.[211] In order to circumvent this problem researchers have coordinated curcumin to transition metals and it has shown improved activity and accumulation in the cell.[208] There is evidence that curcumin can work as a photosensitizer and induce cell death upon irradiation.[208] Dirhodium compounds are very stable and robust compounds that can be used as delivery vehicles for curcumin. The combination of the photochemotherapeutic effects of curcumin with that of the dirhodium compounds would enhance the therapeutic potential of these compounds. The coordination of curcumin to dirhodium compounds like **7b** or the synthesis of a partially solvated dirhodium compound containing curcumin as a bridging ligand should be explored (**Figure 5.3** and **Figure 5.4**).

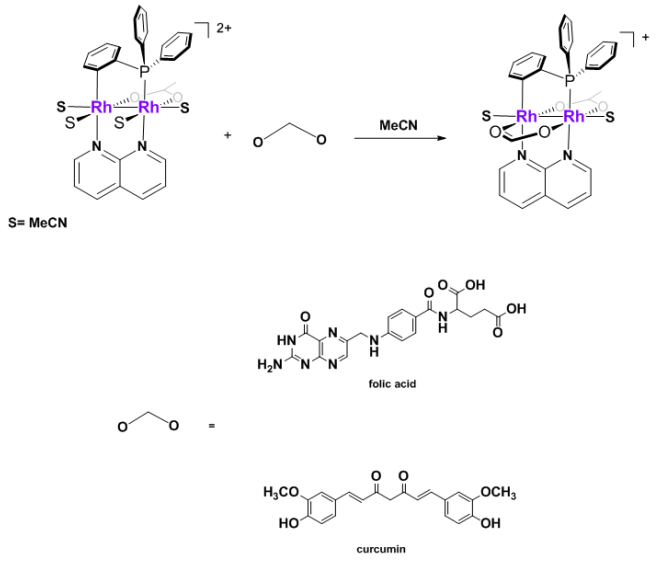

Figure 5.3 Proposed reaction scheme of **7b** with curcumin and folic acid.

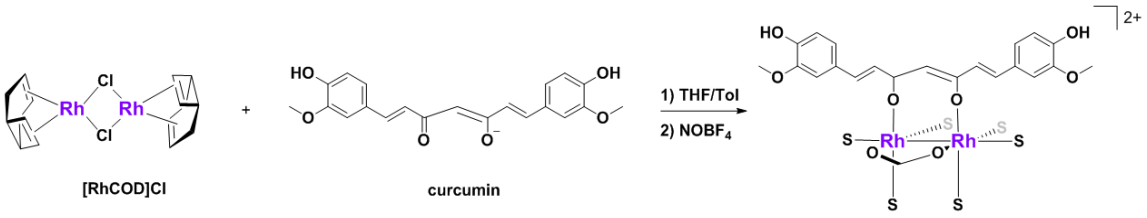

Figure 5.4 Schematic representation of the proposed synthetic patch for the preparation of $[Rh_2(curcumin)_2(CH_3CN)_6]^{2+}$.

The dirhodium compounds in this dissertation expand the knowledge of how different bridging ligands affect the toxicity of these compounds against different cancers and their mechanisms of cell death. The dark stability of the equatorial CH_3CN ligands and their lability upon irradiation are crucial for their potential applications as photodynamic therapy agents. The work described in this thesis helps to expand the database of information available on how to design of dirhodium anticancer agents with new and improved properties.

REFERENCES

(1) Paulmurugan, R. In *Molecular Imaging Probes for Cancer Research* 2012, p 3-27.

(2) Anand, P.; Kunnumakara, A. B.; Sundaram, C.; Harikumar, K. B.; Tharakan, S. T.; Lai, O. S.; Sung, B.; Aggarwal, B. B. *Pharm. Res.* **2008**, *25*, 2097-2116.

(3) *Cancer Facts & Figures 2015*; American Cancer Society: Atlanta, GA, 2015.

(4) David, A. R.; Zimmerman, M. R. *Nat. Rev. Cancer* **2010**, *10*, 728-733.

(5) Chen, L.; Malhotra, A. *Cell Biochem. Biophys.* **2015**, *72*, 637-641.

(6) Bray, F.; Moller, B. *Nat. Rev. Cancer* **2006**, *6*, 63-74.

(7) Correa, P. *Cancer Res.* **1981**, *41*, 3685-3690.

(8) Bradley, P. M.; Angeles-Boza, A. M.; Dunbar, K. R.; Turro, C. *Inorg. Chem.* **2004**, *43*, 2450-2452.

(9) Dunham, S. U.; Chifotides, H. T.; Mikulski, S.; Burr, A. E.; Dunbar, K. R. *Biochemistry* **2004**, *44*, 996-1003.

(10) Bosl, G. J.; Motzer, R. J. *New Engl. J. Med* **1997**, *337*, 242-253.

(11) Todd, R. C.; Lippard, S. J. *J. Inorg. Biochem.* **2010**, *104*, 902-908.

(12) Takahara, P. M.; Frederick, C. A.; Lippard, S. J. *J. Am. Chem. Soc.* **1996**, *118*, 12309-12321.

(13) Timerbaev, A. R.; Hartinger, C. G.; Aleksenko, S. S.; Keppler, B. K. *Chem. Rev.* **2006**, *106*, 2224-2248.

(14) Koeberle, B.; Tomicic, M. T.; Usanova, S.; Kaina, B. *Biochim. Biophys. Acta, Rev. Cancer* **2010**, *1806*, 172-182.

(15) Oliver, T. G.; Mercer, K. L.; Sayles, L. C.; Burke, J. R.; Mendus, D.; Lovejoy, K. S.; Cheng, M.-H.; Subramanian, A.; Mu, D.; Powers, S.; Crowley, D.; Bronson, R. T.; Whittaker, C. A.; Bhutkar, A.; Lippard, S. J.; Golub, T.; Thomale, J.; Jacks, T.; Sweet-Cordero, E. A. *Gene. Dev.* **2010**, 837-852.

(16) Trudu, F.; Amato, F.; Vaňhara, P.; Pivetta, T.; Peña-Méndez, E. M.; Havel, J. *J. Appl. Biomed.* **2015**, *13*, 79-103.

(17) Arnesano, F.; Natile, G. *Coord. Chem. Rev.* **2009**, *253*, 2070-2081.

(18) Ang, W. H.; Myint, M.; Lippard, S. J. *J. Am. Chem. Soc.* **2010**, *132*, 7429-7435.

(19) Gutekunst, M.; Oren, M.; Weilbacher, A.; Dengler, M. A.; Markwardt, C.; Thomale, J.; Aulitzky, W. E.; van der Kuip, H. *PLoS One* **2011**, *6*, e19198.

(20) R.W.Masters, J.; Köberle, B. *Nat. Rev. Cancer* **2003**, *3*, 517-525.

(21) Lovejoy, K. S.; Todd, R. C.; Zhang, S.; McCormick, M. S.; D'Aquino, J. A.; Reardon, J. T.; Sancar, A.; Giacomini, K. M.; Lippard, S. J. *Proc. Natl. Acad. Sci. U. S. A.* **2008**, *105*, 8902-8907.

(22) Ishida, S.; Lee, J.; Thiele, D. J.; Herskowitz, I. *Proc. Natl. Acad. Sci. U. S. A.* **2002**, *99*, 14298-14302.

(23) Kuo, M. T.; Chen, H. H. W.; Song, I.-S.; Savaraj, N.; Ishikawa, T. *Cancer Metastasis Rev.* **2007**, *26*, 71-83.

(24) Nakayama, K.; Kanzaki, A.; Terada, K.; Mutoh, M.; Ogawa, K.; Sugiyama, T.; Takenoshita, S.; Itoh, K.; Yaegashi, N.; Miyazaki, K.; Neamati, N.; Takebayashi, Y. *Clin. Cancer Res.* **2004**, *10*, 2804-2811.

(25) Yoshizawa, K.; Nozaki, S.; Kitahara, H.; Ohara, T.; Kato, K.; Kawashiri, S.; Yamamoto, E. *Oncol. Rep.* **2007**, *18*, 987-991.

(26) Komiya, S.; Gobhardt, M. C.; Mangham, D. C.; Inoue, A. *J. Orthop. Res.* **1998**, *16*, 15-22.

(27) Chen, H. H. W.; Kuo, M. T. *Met-Based. Drugs* **2010**, 430939.

(28) Galluzzi, L.; Senovilla, L.; Vitale, I.; Michels, J.; Martins, I.; Kepp, O.; Castedo, M.; Kroemer, G. *Oncogene* **2012**, *31*, 1869-1883.

(29) Poulogiannis, G.; Frayling, I. M.; Arends, M. J. *Histopathology* **2010**, *56*, 167-179.

(30) Fink, D.; Nebel, S.; Aebi, S.; Zheng, H.; Cenni, B.; Nehme, A.; Christen, R. D.; Howell, S. B. *Cancer Res.* **1996**, *56*, 4881-4886.

(31) Ceppi, P.; Novello, S.; Cambieri, A.; Longo, M.; Monica, V.; Lo Iacono, M.; Giaj-Levra, M.; Saviozzi, S.; Volante, M.; Papotti, M.; Scagliotti, G. *Clin. Cancer Res.* **2009**, *15*, 1039-1045.

(32) Narod, S. A.; Foulkes, W. D. *Nat. Rev. Cancer* **2004**, *4*, 665-676.

(33) Castedo, M.; Coquelle, A.; Vivet, S.; Vitale, I.; Kauffmann, A.; Dessen, P.; Pequignot, M. O.; Casares, N.; Valent, A.; Mouhamad, S.; Schmitt, E.; Modjtahedi, N.; Vainchenker, W.; Zitvogel, L.; Lazar, V.; Garrido, C.; Kroemer, G. *EMBO J.* **2006**, *25*, 2584-2595.

(34) Jain, H. V.; Meyer-Hermann, M. *Cancer Res.* **2011**, *71*, 705-715.

(35) Janson, V.; Johansson, A.; Grankvist, K. *Cell Death Dis.* **2010**, *1*, 1-7.

(36) Feldman, D. R.; Bosl, G. J.; Sheinfeld, J.; Motzer, R. J. *J. Am. Med. Assoc.* **2008**, *299*, 672-684.

(37) Aguirre, J. D.; Angeles-Boza, A. M.; Chouai, A.; Turro, C.; Pellois, J.-P.; Dunbar, K. R. *Dalton Trans.* **2009**, 10806-10812.

(38) Allardyce, C. S.; Dorcier, A.; Scolaro, C.; Dyson, P. J. *Appl. Organomet. Chem.* **2005**, *19*, 1-10.

(39) Qian, Z. M.; Li, H.; Sun, H.; Ho, K. *Pharmacol. Rev.* **2002**, *54*, 561-587.

(40) Gava, B.; Zorzet, S.; Spessotto, P.; Cocchietto, M.; Sava, G. *J. Pharmacol. Exp. Ther.* **2006**, *317*, 284-291.

(41) Hartinger, C. G.; Zorbas-Seifried, S.; Jakupec, M. A.; Kynast, B.; Zorbas, H.; Keppler, B. K. *J. Inorg. Biochem.* **2006**, *100*, 891-904.

(42) Jaeaettelae, M. *Oncogene* **2004**, *23*, 2746-2756.

(43) Kratz, F.; Hartmann, M.; Keppler, B.; Messori, L. *J. Biol. Chem.* **1994**, *269*, 2581-2588.

(44) Marcon, G.; Carotti, S.; Coronnello, M.; Messori, L.; Mini, E.; Orioli, P.; Mazzei, T.; Cinellu, M. A.; Minghetti, G. *J. Med. Chem.* **2002**, *45*, 1672-1677.

(45) Wang, X.; Guo, Z. *Dalton Trans.* **2008**, 1521-1532.

(46) Ward, J. R. *Am. J. Med.* **1988**, *85*, 39-44.

(47) Nordberg, J.; Arner, E. S. J. *Free Radical Biol. Med.* **2001**, *31*, 1287-1312.

(48) Sachweh, M. C. C.; Drummond, C. J.; McCarthy, A. R.; Lain, S.; Stafford, W. C.; Arner, E. S. J.; Higgins, M.; Campbell, J.; Brodin, B. *Oncotarget* **2015**, *6*, 16488-16506.

(49) ClinicalTrials.gov: Westwood, Kansas, United States, 2011, Identifier NCT01419691, A Phase I Phase II Two-Step Study of the Oral Gold Compound Auranofin in Chronic Lymphocytic Leukemia (CLL)/ Small Lymphocytic Lymphoma (SLL)/ Prolymphocytic Lymphoma (PLL). Available from: https://clinicaltrials.gov/ct2/show/NCT01419691 Accessed: 09/17/2015.

(50) Chitambar, C. R. *Future. Med. Chem.* **2012**, *4*, 1257-1272.

(51) Rudnev, A. V.; Foteeva, L. S.; Kowol, C.; Berger, R.; Jakupec, M. A.; Arion, V. B.; Timerbaev, A. R.; Keppler, B. K. *J. Inorg. Biochem.* **2006**, *100*, 1819-1826.

(52) Gogna, R.; Madan, E.; Keppler, B.; Pati, U. *Br. J. Pharmacol.* **2012**, *166*, 617-636.

(53) Madan, E.; Gogna, R.; Keppler, B.; Pati, U. *PLoS One* **2013**, *8*, e71016.

(54) Howard, R. A.; Sherwood, E.; Erck, A.; Kimball, A. P.; Bear, J. L. *J. Med. Chem.* **1977**, *20*, 943-946.

(55) Howard, R. A.; Kimball, A. P.; Bear, J. L. *Cancer Res.* **1979**, *39*, 2568-2573.

(56) Sorasaenee, K.; Fu, P. K. L.; Angeles-Boza, A. M.; Dunbar, K. R.; Turro, C. *Inorg. Chem.* **2003**, *42*, 1267-1271.

(57) Chifotides, H. T.; Fu, P. K. L.; Dunbar, K. R.; Turro, C. *Inorg. Chem.* **2004**, *43*, 1175-1183.

(58) Chifotides, H. T.; Hess, J. S.; Angeles-Boza, A. M.; Galan-Mascaros, J. R.; Sorasaenee, K.; Dunbar, K. R. *Dalton Trans.* **2003**, 4426-4430.

(59) Chifotides, H. T.; Koshlap, K. M.; Pérez, L. M.; Dunbar, K. R. *J. Am. Chem. Soc.* **2003**, *125*, 10714-10724.

(60) Chifotides, H. T.; Koshlap, K. M.; Pérez, L. M.; Dunbar, K. R. *J. Am. Chem. Soc.* **2003**, *125*, 10703-10713.

(61) Aoki, K.; Salam, M. A. *Inorg. Chim. Acta* **2002**, *339*, 427-437.

(62) Kang, M.; Chouai, A.; Chifotides, H. T.; Dunbar, K. R. *Angew. Chem. Int. Ed.* **2006**, *45*, 6148-6151.

(63) Nyst, H. J.; Tan, I. B.; Stewart, F. A.; Balm, A. J. M. *Photodiagn. Photodyn. Ther.* **2009**, *6*, 3-11.

(64) Allison, R. R.; Cuenca, R.; Downie, G. H.; Randall, M. E.; Bagnato, V. S.; Sibata, C. H. *Photodiagn. Photodyn. Ther.* **2005**, *2*, 51-63.

(65) Allison, R. R.; Downie, G. H.; Cuenca, R.; Hu, X.-H.; Childs, C. J. H.; Sibata, C. H. *Photodiagn. Photodyn. Ther.* **2004**, *1*, 27-42.

(66) Castano, A. P.; Mroz, P.; Hamblin, M. R. *Nat. Rev. Cancer* **2006**, *6*, 535-545.

(67) Oleinick, N. L.; Morris, R. L.; Belichenko, I. *Photochem. Photobiol. Sci.* **2002**, *1*, 1-21.

(68) Allison, R. R.; Sibata, C. H. *Photodiagn. Photodyn. Ther.* **2010**, *7*, 61-75.

(69) Jones, L. R.; Grossweiner, L. I. *J. Photochem. Photobiol., B* **1994**, *26*, 249-256.

(70) Steiner, M.-S.; Duerkop, A. *Analyst* **2011**, *136*, 148-154.

(71) Abdel-Shafi, A. A.; Worrall, D. R.; Ershov, A. Y. *Dalton Trans.* **2004**, 30-36.

(72) Knoll, J. D.; Brewer, K. J. In *Prog. Inorg. Chem.*; Karlin, K. D., Ed. 2014; Vol. 59, p 189-243.

(73) Boreham, E. M.; Jones, L.; Swinburne, A. N.; Blanchard-Desce, M.; Hugues, V.; Terryn, C.; Miomandre, F.; Lemercier, G.; Natrajan, L. S. *Dalton Trans.* **2015**, *44*, 16127-16135.

(74) Thompson, M. E.; Djurovich, P. I.; Murphy, D.; Selke, M.; University of Southern California, USA . 2005, p 31.

(75) Abdel-Shafi, A. A.; Bourdelande, J. L.; Ali, S. S. *Dalton Trans.* **2007**, 2510-2516.

(76) Angeles-Boza, A. M.; Bradley, P. M.; Fu, P. K. L.; Shatruk, M.; Hilfiger, M. G.; Dunbar, K. R.; Turro, C. *Inorg. Chem.* **2005**, *44*, 7262-7264.

(77) Lutterman, D. A.; Fu, P. K. L.; Turro, C. *J. Am. Chem. Soc.* **2006**, *128*, 738-739.

(78) Knoll, J. D.; Turro, C. *Coord. Chem. Rev.* **2015**, *282-283*, 110-126.

(79) Burya, S. J.; Palmer, A. M.; Gallucci, J. C.; Turro, C. *Inorg. Chem.* **2012**, *51*, 11882-11890.

(80) Li, Z.; Burya, S. J.; Turro, C.; Dunbar, K. R. *Philos. Trans. R. Soc., A* **2013**, *371*, 20120128.

(81) Li, Z.; Chifotides, H. T.; Dunbar, K. R. *Chem. Sci.* **2013**, *4*, 4470-4485.

(82) Fu, P. K. L.; Bradley, P. M.; Turro, C. *Inorg. Chem.* **2001**, *40*, 2476-2477.

(83) Aguirre, J. D.; Angeles-Boza, A. M.; Chouai, A.; Pellois, J.-P.; Turro, C.; Dunbar, K. R. *J. Am. Chem. Soc.* **2009**, *131*, 11353-11360.

(84) Angeles-Boza, A. M.; Bradley, P. M.; Fu, P. K. L.; Wicke, S. E.; Bacsa, J.; Dunbar, K. R.; Turro, C. *Inorg. Chem.* **2004**, *43*, 8510-8519.

(85) Aguirre, J. D.; Angeles-Boza, A. M.; Chouai, A.; Pellois, J.-P.; Turro, C.; Dunbar, K. R. *J. Am. Chem. Soc.* **2009**, *131*, 11353-11360.

(86) Olive, P. L.; Banath, J. P. *Nat. Protoc.* **2006**, *1*, 23-29.

(87) Balendiran, G. K.; Dabur, R.; Fraser, D. *Cell Biochem. Funct.* **2004**, *22*, 343-352.

(88) Joyce, L. E.; Aguirre, J. D.; Angeles-Boza, A. M.; Chouai, A.; Fu, P. K. L.; Dunbar, K. R.; Turro, C. *Inorg. Chem.* **2010**, *49*, 5371-5376.

(89) Mari, C.; Pierroz, V.; Leonidova, A.; Ferrari, S.; Gasser, G. *Eur. J. Inorg. Chem.* **2015**, *2015*, 3879-3891.

(90) Sgambellone, M. A.; David, A.; Garner, R. N.; Dunbar, K. R.; Turro, C. *J. Am. Chem. Soc.* **2013**, *135*, 11274-11282.

(91) Gentry, G. A.; Morse, P. A., Jr.; Dorsett, M. T. *Cancer Res.* **1971**, *31*, 909-912.

(92) Mari, C.; Pierroz, V.; Leonidova, A.; Ferrari, S.; Gasser, G. *Eur. J. Inorg. Chem.* **2015**, 3879-3891.

(93) Palmer, A. M.; Burya, S. J.; Gallucci, J. C.; Turro, C. *ChemMedChem* **2014**, *9*, 1260-1265.

(94) Guo, Z.; Sadler, P. J. *Angew. Chem. Int. Ed.* **1999**, *38*, 1512-1531.

(95) van Rijt, S. H.; Sadler, P. J. *Drug Discov. Today* **2009**, *14*, 1089-1097.

(96) Hartmann, M.; Keppler, B. K. *Comments Inorg. Chem.* **1995**, *16*, 339-372.

(97) Fimiani, V.; Ainis, T.; Cavallaro, A.; Piraino, P. *J. Chemother.* **1990**, *2*, 319-326.

(98) Howard, R. A.; Spring, T. G.; Bear, J. L. *Cancer Res.* **1976**, *36*, 4402-4405.

(99) Kang, M.; Chifotides, H. T.; Dunbar, K. R. *Biochemistry* **2008**, *47*, 2265-2276.

(100) Bradley, P. M.; Bursten, B. E.; Turro, C. *Inorg. Chem.* **2001**, *40*, 1376-1379.

(101) Berg, K.; Selbo, P. K.; Weyergang, A.; Dietze, A.; Prasmickaite, L.; Bonsted, A.; Engesaeter, B. O.; Angell-Petersen, E.; Warloe, T.; Frandsen, N.; Hogset, A. *J. Microsc.* **2005**, *218*, 133-147.

(102) de, B. E. C.; Medema, J. P. *Cancer Treat. Rev.* **2008**, *34*, 737-749.

(103) Sui, X.; Chen, R.; Wang, Z.; Huang, Z.; Kong, N.; Zhang, M.; Han, W.; Lou, F.; Yang, J.; Zhang, Q.; Wang, X.; He, C.; Pan, H. *Cell Death Dis.* **2013**, *4*, e838.

(104) Zong, W.-X.; Thompson, C. B. *Genes Dev.* **2006**, *20*, 1-15.

(105) Grivennikov, S. I.; Greten, F. R.; Karin, M. *Cell* **2010**, *140*, 883-899.

(106) Apetoh, L.; Ghiringhelli, F.; Tesniere, A.; Criollo, A.; Ortiz, C.; Lidereau, R.; Mariette, C.; Chaput, N.; Mira, J.-P.; Delaloge, S.; Andre, F.; Tursz, T.; Kroemer, G.; Zitvogel, L. *Immunol. Rev.* **2007**, *220*, 47-59.

(107) Apetoh, L.; Ghiringhelli, F.; Tesniere, A.; Obeid, M.; Ortiz, C.; Criollo, A.; Mignot, G.; Maiuri, M. C.; Ullrich, E.; Saulnier, P.; Yang, H.; Amigorena, S.; Ryffel, B.; Barrat, F. J.; Saftig, P.; Levi, F.; Lidereau, R.; Nogues, C.; Mira, J.-P.; Chompret, A.; Joulin, V.; Clavel-Chapelon, F.; Bourhis, J.; Andre, F.; Delaloge, S.; Tursz, T.; Kroemer, G.; Zitvogel, L. *Nat. Med.* **2007**, *13*, 1050-1059.

(108) Rempel, G. A.; Legzdins, P.; Smith, H.; Wilkinson, G. *Inorg. Syn.* **1971**, *13*, 90-91.

(109) Lahuerta, P.; Paya, J.; Peris, E.; Pellinghelli, M. A.; Tiripicchio, A. *J. Organomet. Chem.* **1989**, *373*, C5-C7.

(110) Kuhn, K. M.; Grubbs, R. H. *Org. Lett.* **2008**, *10*, 2075-2077.

(111) Che, G.; Li, W.; Kong, Z.; Su, Z.; Chu, B.; Li, B.; Zhang, Z.; Hu, Z.; Chi, H. *Synth. Commun.* **2006**, *36*, 2519-2524.

(112) Gaussian 09, Revision D.01, Frisch, M. J.; Trucks, G. W.; Schlegel, H. B.; Scuseria, G. E.; Robb, M. A.; Cheeseman, J. R.; Scalmani, G.; Barone, V.; Mennucci, B.; Petersson, G. A.; Nakatsuji, H.; Caricato, M.; Li, X.; Hratchian, H. P.; Izmaylov, A. F.; Bloino, J.; Zheng, G.; Sonnenberg, J. L.; Hada, M.; Ehara, M.; Toyota, K.; Fukuda, R.; Hasegawa, J.; Ishida, M.; Nakajima, T.; Honda, Y.; Kitao, O.; Nakai, H.; Vreven, T.; Montgomery, J. A., Jr.; ; Peralta, J. E.; Ogliaro, F.; Bearpark, M.; Heyd, J. J.; Brothers, E.; Kudin, K. N.; Staroverov, V. N.; Kobayashi, R.; Normand, J.; Raghavachari, K.; Rendell, A.; Burant, J. C.; Iyengar, S. S.; Tomasi, J.; Cossi, M.; Rega, N.; Millam, J. M.; Klene, M.; Knox, J. E.; Cross, J. B.; Bakken, V.; Adamo, C.; Jaramillo, J.; Gomperts, R.; Stratmann, R. E.; Yazyev, O.; Austin, A. J.; Cammi, R.; Pomelli, C.; Ochterski, J. W.; Martin, R. L.; Morokuma, K.; Zakrzewski, V. G.; Voth, G. A.; Salvador, P.; Dannenberg, J. J.; Dapprich, S.; Daniels, A. D.; Farkas, Ö.; Foresman, J. B.; Ortiz, J. V.; Cioslowski, J.; Fox, D. J. Gaussian, Inc., Wallingford CT, 2009.

(113) Adamo, C.; Barone, V. *J. Chem. Phys.* **1998**, *108*, 664-675.

(114) Perdew, J. P.; Chevary, J. A.; Vosko, S. H.; Jackson, K. A.; Pederson, M. R.; Singh, D. J.; Fiolhais, C. *Phys. Rev. B: Condens. Matter* **1992**, *46*, 6671-6687.

(115) Perdew, J. P.; Burke, K.; Wang, Y. *Phys. Rev. B: Condens. Matter* **1996**, *54*, 16533-16539.

(116) Dolg, M.; Stoll, H.; Preuss, H.; Pitzer, R. M. *J. Phys. Chem.* **1993**, *97*, 5852-5859.

(117) Petersson, G. A.; Bennett, A.; Tensfeldt, T. G.; Al-Laham, M. A.; Shirley, W. A.; Mantzaris, J. *J. Chem. Phys.* **1988**, *89*, 2193-2218.

(118) Petersson, G. A.; Al-Laham, M. A. *J. Chem. Phys.* **1991**, *94*, 6081-6090.

(119) Bauernschmitt, R.; Ahlrichs, R. *Chem. Phys. Lett.* **1996**, *256*, 454-464.

(120) Casida, M. E.; Jamorski, C.; Casida, K. C.; Salahub, D. R. *J. Chem. Phys.* **1998**, *108*, 4439-4449.

(121) Stratmann, R. E.; Scuseria, G. E.; Frisch, M. J. *J. Chem. Phys.* **1998**, *109*, 8218-8224.

(122) Van Caillie, C.; Amos, R. D. *Chem. Phys. Lett.* **1999**, *308*, 249-255.

(123) Van Caillie, C.; Amos, R. D. *Chem. Phys. Lett.* **2000**, *317*, 159-164.

(124) Furche, F.; Ahlrichs, R. *J. Chem. Phys.* **2002**, *117*, 7433-7447.

(125) Caricato, M.; Mennucci, B.; Tomasi, J.; Ingrosso, F.; Cammi, R.; Corni, S.; Scalmani, G. *J. Chem. Phys.* **2006**, *124*, 124520.

(126) Tomasi, J.; Mennucci, B.; Cammi, R. *Chem. Rev.* **2005**, *105*, 2999-3093.

(127) Tomasi, J. In *Structure and Reactivity in Aqueous Solution*; American Chemical Society: 1994; Vol. 568, p 10-23.

(128) Agui 9.2.1, Dennington, R. D.; Keith, T. A.; Milliam, J. M. Semichem, Inc. , Shawnee Mission KS, 2008.

(129) Chemissian v4.38, Skripnikov, L. V. 2009.

(130) Cotton, F. A.; Murillo, C. A.; Walton, R. A.; Editors *Multiple Bonds Between Metal Atoms, Third Edition*; Springer, 2005.

(131) Calligaris, M.; Campana, L.; Mestroni, G.; Tornatore, M.; Alessio, E. *Inorg. Chim. Acta* **1987**, *127*, 103-112.

(132) Chifotides, H. T.; Catalan, K. V.; Dunbar, K. R. *Inorg. Chem.* **2003**, *42*, 8739-8747.

(133) Angeles-Boza, A. M.; Bradley, P. M.; Fu, P. K. L.; Shatruk, M.; Hilfiger, M. G.; Dunbar, K. R.; Turro, C. *Inorg. Chem.* **2005**, *44*, 7262-7264.

(134) Li, Z.; Leed, N. A.; Dickson-Karn, N. M.; Dunbar, K. R.; Turro, C. *Chem. Sci.* **2014**, *5*, 727-737.

(135) Sowa, T.; Kawamura, T.; Shida, T.; Yonezawa, T. *Inorg. Chem.* **1983**, *22*, 56-61.

(136) Kataoka, Y.; Kitagawa, Y.; Saito, T.; Nakanishi, Y.; Sato, K.; Miyazaki, Y.; Kawakami, T.; Okumura, M.; Mori, W.; Yamaguchi, K. *Supramol. Chem.* **2011**, *23*, 329-336.

(137) Bueno, C.; Villegas, M. L.; Bertolotti, S. G.; Previtali, C. M.; Neumann, M. G.; Encinas, M. V. *Photochem. Photobiol.* **2002**, *76*, 385-390.

(138) Gonzalez-Pinzon, R.; Haggerty, R.; Myrold, D. D. *J. Geophys. Res.* **2012**, *117*, G00N06.

(139) O'Brien, J.; Wilson, I.; Orton, T.; Pognan, F. *Eur. J. Biochem.* **2000**, *267*, 5421-5426.

(140) Hazen-Martin, D. J.; Garvin, A. J.; Gansler, T.; Tarnowski, B. I.; Sens, D. A. *Am. J. Pathol.* **1993**, *142*, 893-905.

(141) Lin, J. H.; Yamazaki, M. *Clin. Pharmacokinet.* **2003**, *42*, 59-98.

(142) Ke, W.; Yu, P.; Wang, J.; Wang, R.; Guo, C.; Zhou, L.; Li, C.; Li, K. *Med. Oncol. (N. Y., NY, U. S.)* **2011**, *28*, 135-141.

(143) Wilson, A. J.; Liu, A. Y.; Roland, J.; Adebayo, O. B.; Fletcher, S. A.; Slaughter, J. C.; Saskowski, J.; Crispens, M. A.; Jones, H. W., III; James, S.; Fadare, O.; Khabele, D. *Cancer Res.* **2013**, *73*, 4758-4769.

(144) Goyal, G. C.; Blum, A.; Grossweiner, L. I. *Cancer Res.* **1983**, *43*, 5826-5830.

(145) Chen, Y. Q.; Wang, J.; Liu, Y. Z.; Yu, S. Y. *Zhonghua Zhong Liu Za Zhi* **1986**, *8*, 413-416.

(146) Thomas, J. P.; Hall, R. D.; Girotti, A. W. *Cancer Lett.* **1987**, *35*, 295-302.

(147) In *Molecular Probes: The Handbook*; Invitrogen: 2007.

(148) Strasser, A.; O'Connor, L.; Dixit, V. M. *Annu. Rev. Biochem.* **2000**, *69*, 217-245.

(149) Telford, W. G.; Komoriya, A.; Packard, B. Z. *Methods Mol. Biol.* **2004**, *263*, 141-159.

(150) Wang, J.; Yan, H.-c. *Shandong Yiyao* **2014**, *54*, 20-22.

(151) Belmokhtar, C. A.; Hillion, J.; Segal-Bendirdjian, E. *Oncogene* **2001**, *20*, 3354-3362.

(152) Gottlieb, R. *Biol. Signals Recept.* **2001**, *10*, 147.

(153) Modica-Napolitano, J. S.; Aprille, J. R. *Adv. Drug Delivery Rev.* **2001**, *49*, 63-70.

(154) Flewelling, R. F.; Hubbell, W. L. *Biophys. J.* **1986**, *49*, 531-540.

(155) Ross, M. F.; Kelso, G. F.; Blaikie, F. H.; James, A. M.; Cocheme, H. M.; Filipovska, A.; Ros, T.; Hurd, T. R.; Smith, R. A. J.; Murphy, M. P. *Biochemistry (Moscow)* **2005**, *70*, 222-230.

(156) Madak, J. T.; Neamati, N. *Curr. Top. Med. Chem.* **2015**, *15*, 745-766.

(157) Neuzil, J.; Wang, X.-F.; Dong, L.-F.; Low, P.; Ralph, S. J. *FEBS Lett.* **2006**, *580*, 5125-5129.

(158) Ralph, S. J.; Rodriguez-Enriquez, S.; Neuzil, J.; Moreno-Sanchez, R. *Mol. Aspects Med.* **2010**, *31*, 29-59.

(159) De Proost, I.; Pintelon, I.; Brouns, I.; Kroese, A. B. A.; Riccardi, D.; Kemp, P. J.; Timmermans, J.-P.; Adriaensen, D. *Am. J. Respir. Cell Mol. Biol.* **2008**, *39*, 180-189.

(160) Park, J.-W.; Lee, S.-Y.; Yang, J.-Y.; Rho, H.-W.; Park, B.-H.; Lim, S.-N.; Kim, J.-S.; Kim, H.-R. *Biochim. Biophys. Acta* **1997**, *1344*, 132-138.

(161) Abbro, L.; Lanubile, R.; Dini, L. *Ital. J. Zool.* **2004**, *71*, 95-100.

(162) Murphy, M. P. *Biochim. Biophys. Acta, Bioenerg.* **2008**, *1777*, 1028-1031.

(163) Singh, K. *Mitochondrial DNA Mutations in Aging, Disease and Cancer*, 1998.

(164) Suen, D.-F.; Norris, K. L.; Youle, R. J. *Genes Dev.* **2008**, *22*, 1577-1590.

(165) Jung, Y.; Lippard, S. J. *Chem. Rev.* **2007**, *107*, 1387-1407.

(166) Kelland, L. *Nat. Rev. Cancer* **2007**, *7*, 573-584.

(167) Groessl, M.; Dyson, P. J. *Curr. Top. Med. Chem.* **2011**, *11*, 2632-2646.

(168) Erck, A.; Sherwood, E.; Bear, J. L.; Kimball, A. P. *Cancer Res.* **1976**, *36*, 2204-2209.

(169) Pruchnik, F. P.; Starosta, R.; Ciunik, Z.; Opolski, A.; Wietrzyk, J.; Wojdat, E.; Dus, D. *Can. J. Chem.* **2001**, *79*, 868-877.

(170) Li, Z.; David, A.; Albani, B. A.; Pellois, J.-P.; Turro, C.; Dunbar, K. R. *J. Am. Chem. Soc.* **2014**, *136*, 17058-17070.

(171) Chakravarty, A. R.; Cotton, F. A.; Tocher, D. A.; Tocher, J. H. *Organometallics* **1985**, *4*, 8-13.

(172) Tresoldi, G.; Lo Schiavo, S.; Nicolo, F.; Cardiano, P.; Piraino, P. *Inorg. Chim. Acta* **2003**, *344*, 190-196.

(173) Piraino, P.; Bruno, G.; Tresoldi, G.; Lo Schiavo, S.; Zanello, P. *Inorg. Chem.* **1987**, *26*, 91-96.

(174) Pimblett, G.; Garner, C. D.; Clegg, W. *J. Chem. Soc., Dalton Trans.* **1986**, 1257-1263.

(175) Dunbar, K. R.; Majors, S. O.; Sun, J.-S. *Inorg. Chim. Acta* **1995**, *229*, 373-382.

(176) Ren, T.; Lin, C.; Valente, E. J.; Zubkowski, J. D. *Inorg. Chim. Acta* **2000**, *297*, 283-290.

(177) In *Molecular Probes: The Handbook*; Life Technologies: 2005.

(178) Guo, Z.; Sadler, P. J. *Angew. Chem. Int. Ed.* **1999**, *38*, 1512-1531.

(179) Che, C.-M.; Siu, F.-M. *Curr. Opin. Chem. Biol.* **2010**, *14*, 255-261.

(180) Chen, X.; Tang, L.-J.; Sun, Y.-N.; Qiu, P.-H.; Liang, G. *J. Inorg. Biochem.* **2010**, *104*, 379-384.

(181) Von, S.-T.; Seng, H.-L.; Lee, H.-B.; Ng, S.-W.; Kitamura, Y.; Chikira, M.; Ng, C.-H. *JBIC, J. Biol. Inorg. Chem.* **2012**, *17*, 57-69.

(182) Zhu, T. P.; Ahsan, M. Q.; Malinski, T.; Kadish, K. M.; Bear, J. L. *Inorg. Chem.* **1984**, *23*, 2-3.

(183) Bear, J. L.; Lifsey, R. S.; Chau, L. K.; Ahsan, M. Q.; Korp, J. D.; Chavan, M.; Kadish, K. M. *J. Chem. Soc., Dalton Trans.* **1989**, 93-100.

(184) Siu, F.-M.; Lin, I. W.-S.; Yan, K.; Lok, C.-N.; Low, K.-H.; Leung, T. Y.-C.; Lam, T.-L.; Che, C.-M. *Chem. Sci.* **2012**, *3*, 1785-1793.

(185) Walmsley, J. A. *J. Phys. Chem.* **1978**, *82*, 2031-2035.

(186) Thangam, R.; Suresh, V.; Rajkumar, M.; Vincent, J. D.; Gunasekaran, P.; Anbazhagan, C.; Kaveri, K.; Kannan, S. *Phytother. Res.* **2013**, *27*, 1664-1670.

(187) Sowa, T.; Kawamura, T.; Shida, T.; Yonezawa, T. *Inorg. Chem.* **1983**, *22*, 56-61.

(188) Norman, J. G., Jr.; Kolari, H. J. *J. Am. Chem. Soc.* **1978**, *100*, 791-799.

(189) Cotton, F. A.; Feng, X. *Inorg. Chem.* **1989**, *28*, 1180-1183.

(190) Angeles-Boza, A. M.; Bradley, P. M.; Fu, P. K. L.; Shatruk, M.; Hilfiger, M. G.; Dunbar, K. R.; Turro, C. *Inorg. Chem.* **2005**, *44*, 7262-7264.

(191) Victor, V. M.; Rocha, M. *Curr. Pharm. Des.* **2007**, *13*, 845-863.

(192) Murphy, M. P.; Smith, R. A. J. *Annu. Rev. Pharmacol. Toxicol.* **2007**, *47*, 629-656.

(193) Liu, T.; Hannafon, B.; Gill, L.; Kelly, W.; Benbrook, D. *Mol. Cancer Ther.* **2007**, *6*, 1814-1822.

(194) Han, J.; Goldstein, L. A.; Gastman, B. R.; Rabinowich, H. *J. Biol. Chem.* **2006**, *281*, 10153-10163.

(195) van, E. M.; Ramaekers, F. C.; Schutte, B.; Reutelingsperger, C. P. *Cytometry* **1996**, *24*, 131-139.

(196) Piraino, P.; Tresoldi, G.; Lo Schiavo, S. *Inorg. Chim. Acta* **1993**, *203*, 101-105.

(197) Ernst, R. J.; Komor, A. C.; Barton, J. K. *Biochemistry* **2011**, *50*, 10919-10928.

(198) Rubio-Aliaga, I.; Daniel, H. *Trends Pharmacol. Sci.* **2002**, *23*, 434-440.

(199) Shieh, Y.-A.; Yang, S.-J.; Wei, M.-F.; Shieh, M.-J. *ACS Nano* **2010**, *4*, 1433-1442.

(200) Bovis, M. J.; Woodhams, J. H.; Loizidou, M.; Scheglmann, D.; Bown, S. G.; MacRobert, A. J. *J. Controlled Release* **2012**, *157*, 196-205.

(201) Lee, R. J.; Low, P. S. *Methods Mol. Med.* **2000**, *25*, 69-76.

(202) Akhtar, M. J.; Khan, M. A.; Ahmad, I. *J. Pharm. Biomed. Anal.* **1999**, *19*, 269-275.

(203) Toffoli, G.; Cernigoi, C.; Russo, A.; Gallo, A.; Bagnoli, M.; Boiocchi, M. *Int. J. Cancer* **1997**, *74*, 193-198.

(204) Ross, J. F.; Chaudhuri, P. K.; Ratnam, M. *Cancer* **1994**, *73*, 2432-2443.

(205) Toffoli, G.; Russo, A.; Gallo, A.; Cernigoi, C.; Miotti, S.; Sorio, R.; Tumolo, S.; Boiocchi, M. *Int. J. Cancer* **1998**, *79*, 121-126.

(206) Kim, Y.-i. *J. Nutr.* **2003**, *133*, 3731S-3739S.

(207) Poe, M. *J. Biol. Chem.* **1977**, *252*, 3724-3728.

(208) Banerjee, S.; Chakravarty, A. R. *Acc. Chem. Res.* **2015**, *48*, 2075-2083.

(209) Carr, K. R.; Ioffe, Y. J.; Filippova, M.; Duerksen-Hughes, P.; Chan, P. J. *Eur. J. Obstet. Gynecol. Reprod. Biol.* **2015**, *193*, 96-101.

(210) Zhang, C.; Jiang, S.; Li, K.; Wang, M.; Zhu, R.; Sun, X.; Wang, Q.; Wang, S. *Spectrochim. Acta, Part A* **2015**, *150*, 181-186.

(211) Esatbeyoglu, T.; Huebbe, P.; Ernst, I. M. A.; Chin, D.; Wagner, A. E.; Rimbach, G. *Angew. Chem. Int. Ed.* **2012**, *51*, 5308-5332.